Direct numerical simulation of turbulent premixed flames at high Karlovitz numbers: structure and modelling

Nilsson, Thommie

2019

Document Version:
Publisher's PDF, also known as Version of record

Link to publication

Citation for published version (APA):
Nilsson, T. (2019). *Direct numerical simulation of turbulent premixed flames at high Karlovitz numbers: structure and modelling*. Department of Energy Sciences, Lund University.

Total number of authors:
1

LUND UNIVERSITY

PO Box 117
221 00 Lund
+46 46-222 00 00

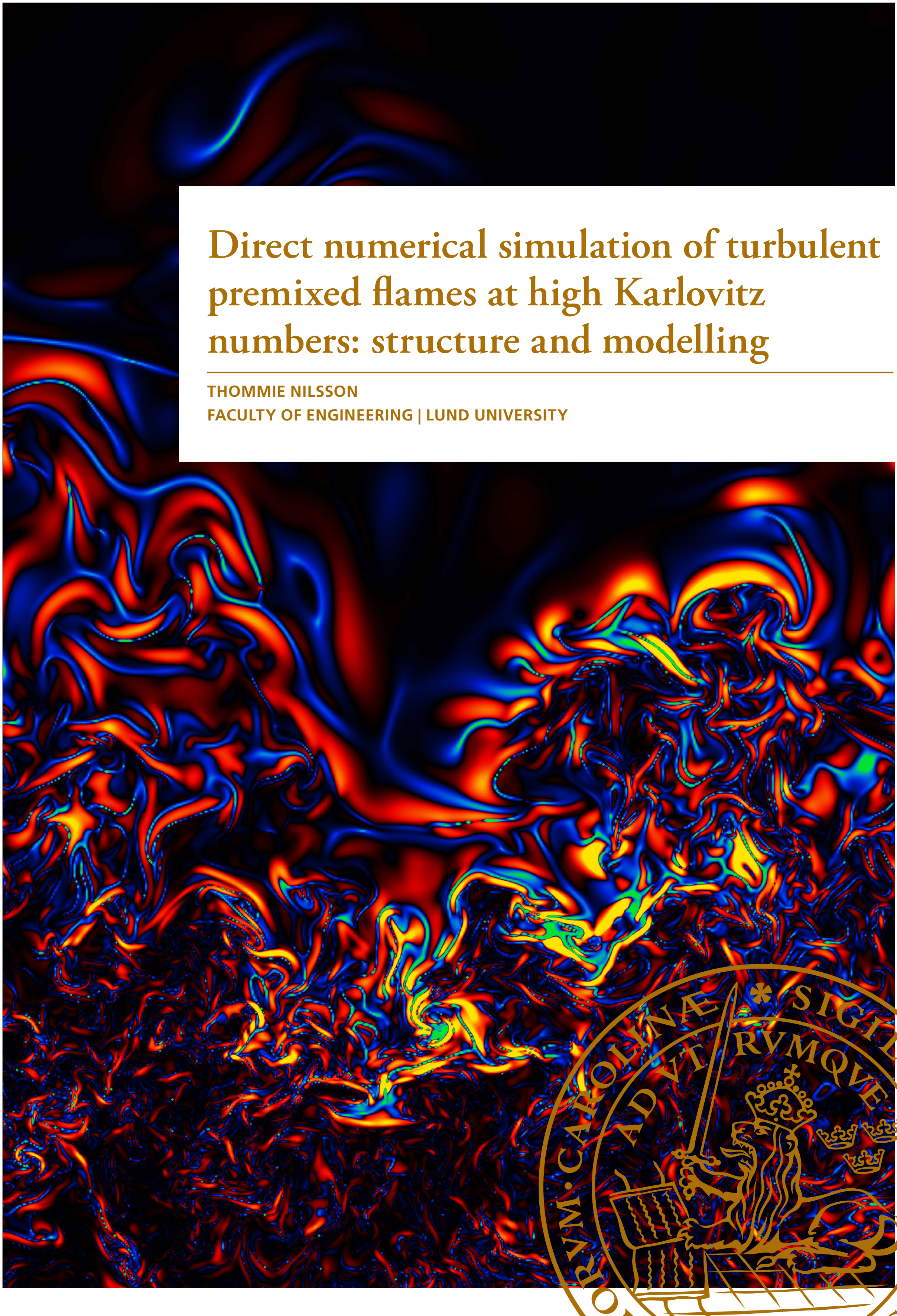

Direct numerical simulation of turbulent premixed flames at high Karlovitz numbers: structure and modelling

THOMMIE NILSSON
FACULTY OF ENGINEERING | LUND UNIVERSITY

Direct numerical simulation of turbulent premixed flames at high Karlovitz numbers: structure and modelling

by Thommie Nilsson

LUND
UNIVERSITY

Thesis for the degree of Philosophy in Engineering
Thesis advisors: Prof. Xue-Song Bai, Dr. Rixin Yu
Faculty opponent: Prof. Nilanjan Chakraborty

To be presented, with the permission of the Faculty of Engineering of Lund University, for public criticism in the lecture hall M:B, M-building, at the Department of Energy Sciences on the 31th of May 2019 at 10:00.

Organization
LUND UNIVERSITY

Department of Energy Sciences
Box 118
SE–221 00 LUND
Sweden

Document name
DOCTORAL DISSERTATION

Date of disputation
2019-05-31

Sponsoring organization

Author(s)
Thommie Nilsson

Title and subtitle
Direct numerical simulation of turbulent premixed flames at high Karlovitz numbers: structure and modelling

Abstract

There has been recent increased interest in premixed flames and in particular for use in gas turbines for power generation. This is a development that follows from increasing demands for high efficiency and low emissions of NOx, which can be achieved by using premixed flames and lean pre-heated mixtures, often close to the lean flammability limit. In combination with high levels of turbulence, which is needed to burn significant amounts of fuel in a limited space, this trend leads to higher Karlovitz numbers. The Karlovitz number is a dimensionless quantity that compares the time scale of flame propagation with the time scale of turbulent micro-mixing. It has been hypothesized, for example in classical regime diagrams, that premixed flames enter a special combustion regime, the distributed reaction zone regime, at high enough Karlovitz numbers and in this regime turbulent mixing would distort all layers of the flame. This has important implications for computational fluid dynamics (CFD) simulation of premixed flames since such simulations rely on models that are often based on the flamelet assumption which states that the internal flame structure should not be distorted. In the recent literature there have been a limited number of reports of flames, simulated and experimental, that are claimed to probe the high Karlovitz regime and observations include changes in the chemical reaction path, low temperature heat release and average broadening of the flame, but also the existence of locally thin or compressed regions and the persistence of a layered structure well above the speculated regime boundary of distributed reactions. In addition to remaining questions about structure changes in high Ka flames, there is the important question about how to model them. In particular, under what conditions can flamelet based models be used, when can they not be used, and is there a need for different models? This thesis is devoted to two main questions. First, the thesis concerns the structure of premixed turbulent flames, in particular at high Karlovitz numbers, and the focus is on the flame thickness, how it evolves in a transient developing flame, and the balance between contributing mechanisms. Direct numerical simulations (DNS) are used to investigate these topics. Second, the thesis concerns modelling in premixed flames in the large eddy simulation (LES) framework which is assessed using filtered DNS data. The focus is on a flamelet-based presumed probability density function (PDF) model for the filtered reaction rate, investigated for a range of premixed flames of varying complexity and Karlovitz number, as well as on the related sub-filter variance equation which is an essential ingredient of the studied flamelet model.

Key words
Computational Fluid Dynamics, Direct Numerical Simulation, Premixed Flame, Turbulence, Combustion Model, Karlovitz Number

Classification system and/or index terms (if any)

Supplementary bibliographical information

Language
English

ISSN and key title
0282-1990

ISBN
978-91-7895-109-3 (print)
978-91-7895-110-9 (pdf)

Recipient's notes

Number of pages
199

Price

Security classification

DOKUMENTDATABLAD enl SIS 61 41 21

I, the undersigned, being the copyright owner of the abstract of the above-mentioned dissertation, hereby grant to all reference sources the permission to publish and disseminate the abstract of the above-mentioned dissertation.

Signature

Date 2019-04-16

Direct numerical simulation of turbulent premixed flames at high Karlovitz numbers: structure and modelling

by Thommie Nilsson

LUND
UNIVERSITY

Funding information: The thesis work was financially supported by the Swedish Research Council (VR) and the national Centre for Combustion Science and Technology (CeCOST).

Cover illustration: Snapshot of $|\nabla c|(a_t - S_d \nabla \cdot \boldsymbol{n})$ from case B4.

Department of Energy Sciences
Faculty of Engineering
Lund University
Box 118
SE–221 00 LUND
Sweden

ISBN: 978-91-7895-109-3 (print)
ISBN: 978-91-7895-110-9 (pdf)
ISSN: 0282-1990
ISRN: LUTMDN/TMHP-19/1149-SE

Printed in Sweden by Media-Tryck, Lund University, Lund 2019

Contents

List of publications

This thesis is based on the following publications, referred to by their Roman numerals:

I **Structures of turbulent premixed flames in the high Karlovitz number regime – DNS analysis**

T. Nilsson, H. Carlsson, R. Yu, X. S. Bai
Fuel 216 (2018), pp. 627–638

II **A priori analysis of sub-grid variance of a reactive scalar using DNS data of high Ka flames**

T. Nilsson, I. Langella, N. A. K. Doan, N. Swaminathan, R. Yu, X. S. Bai
Accepted for publication in Combust. Theory Model. (2019)

III **Filtered reaction rate modelling in moderate and high Karlovitz number flames: an a priori analysis**

T. Nilsson, R.Yu, N. A. K. Doan, I. Langella, N. Swaminathan, X. S. Bai
Submitted to Flow Turbulence Combust. (2019)

IV **On thinning/broadening in turbulent premixed reaction waves**

R.Yu, **T. Nilsson**, X. S. Bai, A. N. Lipatnikov
Submitted to Combust. Flame (2019)

Acknowledgements

This work was carried out at the Department of Energy Sciences, Lund University, Sweden. The work has been financially supported by the Swedish Research Council (VR) and the National Centre for Combustion Science and Technology (CeCOST). PRACE is acknowledged for awarding access to MareNostrum at Barcelona Supercomputing Center (BSC), Spain and SuperMUC at LRZ, Germany. Computational were also performed on resources provided by the Swedish National Infrastructure for Computing (SNIC) at PDC and HPC2N.

I would like to thank my advisor professor Xue-Song Bai for giving me the opportunity to work on this project. Thank you for all valuable advice, discussions and for everything I learned about research. I also like to thank my co-advisor Rixin Yu for all helpful and interesting discussions we had. My gratitude also goes to professor Nedunchezhian Swaminathan, Nguyen Anh Khoa Doan and Ivan Langella for the great collaboration. Finally, I like to thank all my colleges, current and former, for the fantastic environment and for always being supportive.

Popularvetenskaplig sammanfattning

Lite förenklat handlar det här arbetet om hur en gaslåga samverkar med virvelströmmar. Eller mer specifikt, hur man kan använda datorer för att räkna ut det. Datorsimuleringar av det här slaget kan vara användbara om man till exempel vill förbättra brännaren i en gasturbin, minska risken för detonation vid gasläckor i gruvor, eller studera hur snabbt vissa exploderande stjärnor brinner. En av de stora fördelarna med simuleringar är att man har full kontroll över det man studerar och kan göra perfekta 'mätningar', utan många av de begränsningar och mätosäkerheter som ofta förekommer i riktiga experiment. Simuleringar gör det också möjligt att till exempel studera idealiserade och förenklade förhållanden som inte går att uppnå experimentellt. Många av de simuleringar som utförs, till exempel i denna avhandling, kan dock tyckas märkliga: varför skulle man vilja studera en gasflamma som saknar värme, eller turbulenta strömvirvlar som uppstår ur tomma intet? För att svara på denna fråga, låt oss titta lite på bakgrunden.

Navier-Stokes ekvationer beskriver rörelser i gaser och vätskor och har varit kända sedan tidigt 1800-tal. Under samma århundrade upptäcktes även Arrhenius ekvation som säger hur snabb en kemisk reaktion är. Tillsammans utgör de här ekvationerna, samt några ytterligare tekniska detaljer, en modell som i detalj beskriver bland annat förblandade gasflammor. Betyder det att problemet redan är löst, att vi har en tillräckligt noggrann modell som bara är att använda? Svaret är både ja och nej. Problemet är att modellen är för detaljerad. Den går helt enkelt inte att använda i praktiken på grund av den enorma beräkningskraft som skulle krävas för att räkna ut något. För att kunna använda simuleringar i studier av praktiska flammor behöver vi skapa enklare modeller som har en lägre beräkningskostnad. Informationen från en sådan modell behöver inte vara perfekt, alla detaljer om varenda liten virvel är inte relevanta, men det är viktigt att informationen är tillräcklig för ändamålet. För att konstruera en förenklad modell krävs därför information. Man behöver veta vilka delar av en ekvation som är viktiga, vilka förenklingar som är rimliga i olika situationer.

Inom ramverket som på engelska kallas ”Large Eddy Simulation” (LES) är tanken att man behåller allt som är stort i modellen och försummar sådant som är smått. Motiveringen är att mycket av detaljerna (som är kostsamma att räkna ut) är småskaliga medan majoriteten av energin finns i stora virvlar och strömmar. Metoden kan liknas vid ett grovt såll där bara de största bitarna fastnar och alla små detaljer filtreras bort. Tyvärr är verkligheten inte alltid så simpel, fenomen som händer på stora och små skalor är inte isolerade från varandra och de bortsållade små skalorna måste därför ersättas med något slags gissning. En av de stora utmaningarna när det gäller flammor är att inte bara de små strömvirvlarna, utan även själva flamfronten, ofta faller genom 'sållet'. Här kan man givetvis invända att LES kanske inte är rätt väg att gå, men tyvärr finns inte många alternativ idag som inte bygger på något liknande såll. Det här betyder inte att allt hopp om en realistisk simulering är förlorat, en hel del är fortfarande möjligt att göra och resultatet beror på hur bra 'gissningar' man kan göra. Men hur vet man vad som är en bra gissning?

Här kommer anledningen till att man vill studera idealiserade och förenklade fall, som en flamma utan värme eller en flamma in en oändlig periodisk låda. Om ett system bara är tillräckligt simpelt så är det möjligt att använda en detaljerad modell direkt, utan något såll. Den enkelheten ger oss en möjlighet att testa och förbättra våra 'filtrerade' modeller (utförda inom ramverket för LES) mot de 'ofiltrerade' modellerna. Dessutom kan detaljerade simuleringar av enkla system ge oss ny information som ökar kunskapen och som kan ligga till grund för nya modeller.

Arbetet i den här avhandlingen bygger på simuleringar av enkla flammor med detaljerade modeller och har i huvudsak två delar. Flammorna som studeras är förblandade vilket innebär att bränsle och luft har blandats innan de bränns. Förblandade flammor har ofta en specifik tjocklek och rör sig med en specifik hastighet. Det första delen av arbetet handlar om hur en flammas inre struktur påverkas av turbulenta strömvirvlar. Om det finns många små och starka virvlar så kan dessa göra att flamman blir tjockare. Hur tjock flamman blir beror på ett samspel mellan värmefrigörelsen och virvlarna. Vid väldigt stark turbulens kan även de kemiska reaktionerna påverkas, något som kan vara av stort intresse om man vill tillverka brännare med låga utsläpp. En studie gjordes även om hur flammans hastighet kan påverkas av de turbulenta virvlarna, och ett försök har gjorts att separera olika processer som påverkar hastigheten.

Den andra delen av avhandlingen knyter an till den första och handlar om hur förenklade modeller fungerar vid olika stark turbulens. En modell som undersökts bygger på att skatta hur vanligt förekommande olika bortfiltrerade tillstånd är, och sedan slå upp i en förberäknad tabell vad reaktionshastigheten ska vara. Metoden bygger på antaganden om hur de bortfiltrerade tillstånden är fördelade och vad som ska finnas i tabellen.

Chapter 1

Introduction

Before high-speed digital computers became commonly available there were essentially two ways that research on fluid dynamics could be done: experimentally or theoretically. Computational fluid dynamics (CFD) now provides a third option, which is based on finding approximate solutions to the system of partial differential equations (PDEs) governing fluid flow using numerical methods. While CFD has several merits in terms of cost and flexibility it also comes with some drawbacks related to turbulence models and boundary conditions. CFD can therefore be viewed as a tool in fluid dynamics research that can be used alongside experimental and theoretical methods in order to provide a more complete picture of a flow situation. The direct method of using CFD is to numerically solve the governing equations without further modification. As long as the schemes are stable and consistent [1] the result will be an approximate solution to the flow problem defined by the equations together with their boundary and initial conditions (assuming that the problem is well-posed). This method is referred to as direct numerical simulation (DNS) and is straight forward to apply to laminar flow. In most turbulent flows of interest, however, DNS is not practical due to the large range of length and time scales present and the associated high cost in terms of computation time and memory. The solution is to manipulate the governing equations in a way that reduces the number of scales and thereby the computational cost. The two most common approaches are the Reynolds-averaged Navier-Stokes (RANS) and the large eddy simulation (LES). These resulting equations however contain unclosed terms that are related to the scales that were removed, and they need to be modelled. To find good closure models is one of the main challenges of CFD.

The topic of this thesis is CFD simulation of turbulent premixed deflagration flames which is a combustion mode where gaseous fuel and oxidizer are mixed prior to combustion. Many other modes of combustion exist, including non-premixed diffusion flames, auto-ignition, detonation waves and surface oxidation of solid fuels. The distinguishing features of a premixed deflagration flame is that the unburned reactant mixture (fuel and oxidizer) is separated from the burned product mixture by a thin flame, and that the flame propagates into the reactant mixture with a characteristic speed controlled by a balance of reaction and diffusion. Premixed flames are further classified as either laminar or turbulent based on the local flow conditions. In virtually all industrial applications of premixed flames the flow conditions are turbulent. Laminar premixed flames are mostly found in laboratory burners where they are used to study fundamental properties of flames such as combustion chemistry. Turbulent premixed flames on the other hand are found in a diverse range of topics including gas turbine engines for power generation, spark ignited piston engines, gas stoves, accidents after gas leaks in factories or mines, various laboratory burners, and possibly type Ia supernovae [2].

1.1 Regime diagram of premixed combustion

Turbulent flows contain motions covering a large spectrum of length and time scales. In terms of length scales, the largest motions are characterized by an integral length scale ℓ_0, often defined as the integrated longitudinal autocorrelation of velocity, L_{11}. The smallest motions, where viscosity is important, are characterized by the Kolmogorov length scale, $\eta = \nu^{3/4}\varepsilon^{1/4}$, where ε is the dissipation rate of turbulent kinetic energy and ν is the kinematic viscosity. Corresponding integral and Kolmogorov time scales τ_0 and τ_η can also be constructed. One of the central non-dimensional numbers in turbulent flow is the Reynolds number,

$$\mathrm{Re} = \frac{\ell_0 u'}{\nu} \tag{1.1}$$

where U' is a large scale characteristic velocity. Re is related to the ratio of integral and Kolmogorov scales. For further details on the scales of turbulence, see for example ref. [3].

When a premixed flame interacts with a turbulent flow there are more scales to consider, and these lead to more non-dimensional numbers that can be used to characterize the flow/flame interaction. In particular, the laminar flame speed, S_L, laminar thermal flame thickness, $\delta_{th} \propto \min(1/|\nabla T|)$, and laminar flame residence time, $\tau_F = \delta_{th}/S_L$, are commonly used flame scales. Comparing the flame time scale with the large and small time scales of turbulence gives the Damköhler and Karlovitz numbers, respectively. These are defined as

$$\mathrm{Da} = \frac{\tau_0}{\tau_F} = \frac{S_L \ell_0}{\delta_{th} U'} \tag{1.2}$$

and

$$\mathrm{Ka} = \frac{\tau_F}{\tau_\eta} = \frac{U'^{3/2}\delta_{th}^{1/2}}{S_L^{3/2}\ell_0^{1/2}} \tag{1.3}$$

where the estimates $\varepsilon = U'^3/\ell_0$ and $\nu = S_L\delta_{th}$ have been used. (An alternative approach is to define the Ka using the time scale of the inertial sub-range of turbulence, $1/\varepsilon = \ell_0/U'^3$ [4], which yields the same formula (1.3) without the need to involve the viscosity).

Dimensionless numbers have been used to classify premixed flames into different regimes and several regime diagrams can be found in the literature [5–10]. Such diagrams would

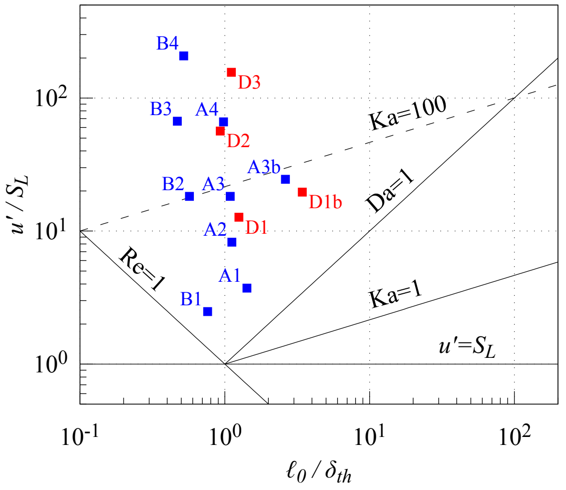

Figure 1.1: Regime diagram of turbulent premixed combustion. The location of all flames simulated in this work are indicated with symbols.

be of great value if they could allow the general behaviour of a flame to be predicted from knowledge of only a few non-dimensional numbers that can be estimated before any experiment or simulation is carried out. Shown in Fig. 1.1 is the diagram by Borghi and Peters [7, 9]. All the DNS simulations performed for this thesis are marked in the diagram and, according to the diagram, span from the thin reaction zone regime (TRZ) to the distributed reaction zone regime (DRZ). It is clear, however, that a single regime diagram with only the two parameters ℓ_0/δ_{th} and u'/S_L cannot account for all situations since there are more parameters that affect the flame/turbulence interaction.

In a premixed flame the reactions are confined to a narrow layer which is usually thinner than the thermal flame thickness. The distinction between the TRZ and DRZ regimes is that, in the TRZ the small turbulent scales are able to disturb the pre-heat layer (essentially the thermal thickness) but not the thinner reaction layer, while in the DRZ regime the turbulent scales are small enough to disturb both layers. The DRZ regime has been predicted [9] to occur when the reaction layer Karlovitz number, $\mathrm{Ka}_\delta = \delta_r^2/\eta^2$, is grater than 1. If the reaction layer is one tenth of the thermal thickness this criterion can be written in terms of the regular Karlovitz number as $\mathrm{Ka} > 100$, a well-known prediction that is often depicted in regime diagrams. However, recent studies [4, 11–14] have shown that the Karlovitz number of the predicted regime boundary is massively under-predicted for flames in practical fuel/air mixtures and that thin reaction layers can be observed well above the predicted boundary.

A notable phenomenon that the regime diagram does not consider is the volume dilatation present in flames with non-zero heat release and the effect this has on the turbulence. Heat release is quantifiable by the non-dimensional density ratio $R = \rho_u/\rho_b = T_b/T_u$. As an illustration of this effect, Fig 1.2 shows two example flames with different density ratio R. These flames are based on a single-step chemical reaction, they have been constructed to have the same laminar flame speed and thermal thickness and they evolve in initially the same turbulent flow thus having the same location on the regime diagram. In both flames the Karlovitz number is 150 and u'/S_L is 30. The density ratio is $R = 10$ for the flame on the right and $R = 1.2$ for the one on the left. Indeed a very different behaviour is seen as a result of this difference.

The above example shows how different flames can be despite them having the same Karlovitz, Damköhler and Reynolds numbers. In flames with multi-step chemistry there are even more parameters. Every additional species adds a Lewis number and each reaction rate adds more reaction parameters. As a result there are many more scales available in a multi-species flame than in a single-species one. Figure 1.3 shows profiles of a few selected species mass fractions and reaction rates in a one-dimensional premixed methane/air flame, simulated with the chemical model of Smooke and Giovangigli [15]. In this flame δ_{th} is about 1 mm, while the intermediate species OH and H_2 occupy much wider zones and the reaction rates $\dot{\omega}_{\mathrm{H2O}}$ and $\dot{\omega}_{\mathrm{CH4}}$ are confined to a more narrow zone. Using alternative length and time scales it is possible to define, for example, a reaction layer Karlovitz number [9] and species-specific Karlovitz numbers [16]. The bottom line is that there are many effects to consider in turbulent premixed combustion and simple two-dimensional regime diagrams, as useful as they might be, cannot accommodate the complete picture of flame/flow interaction. Much is yet to be understood about this interaction, especially at high Karlovitz numbers.

1.2 The need for combustion models

In simulations of reacting flow, such as combustion, in the RANS or LES frameworks there are additional unclosed terms due to unresolved fluxes and source terms of the reactive scalars. The averaged or filtered reaction rates are noticeably difficult to model and in practical LES of premixed flames the flame front is often thinner than the filter or grid size, making the reactions entirely a sub-filter process. The purpose of a combustion model is to work around this issue and many different strategies have been proposed in the literature. Some of them are general but most are specific to a certain combustion regime. Combustion models can be classified according to ref. [17] as PDF-like or flamelet-like, where flamelet-like models restrict the degrees of freedom to a low dimensional space while PDF-like models do not make such a restriction. In ref. [18] combustion models are classified based on the concept used to describe flame/flow interaction (surface, statistical or mixing) and by the type of chemical description (fast, single-step, tabulated or detailed). Reviews of many of the common modelling approaches can be found in refs. [18–20].

Many models for premixed flames are based on the 'flamelet' assumption [21–24]. It states that the internal structure of the flame, and in particular the reaction layer, is the same as in a corresponding laminar flame. This is a reasonable assumption if there exists some scale separation between turbulence and the flame. There are however many circumstances where the flamelet assumption does not hold. This may be the case when the flame is in the distributed reaction zone regime that was mentioned earlier. In the DRZ regime turbulent mixing is able to disrupt the inner flame structure if the relevant turbulent time scale is shorter than the flame time scale. It is not clear how such a distributed flame should be modelled in RANS or LES, but it is expected that flamelet type models may not be suitable due to the constraints they put on the accessible chemical state space. However, as mentioned before, studies of distributed flames are rare and the transition to distributed burning seems to happen at much higher Ka than predicted. One of the reasons for the high value of the critical Ka required for the DRZ regime pertains to the two-way coupling between turbulent flow and the flame: heat release causes volume dilatation that increases the length scales of turbulence, effectively lowering the Karlovitz number inside the reaction layer. This implies that the range of applicability of models based on the flamelet assumption may be extended to rather high Karlovitz numbers.

1.3 Objectives and outline

The objectives of this thesis can be summarized as follows:

- Investigate the structure and transient evolution of premixed flames at Karlovitz numbers around and above 100 while generating an extensive database of such flames using direct numerical simulation. Particular focus is put on the flame thickness and different flame thickness metrics are analysed under different flow and flame conditions.

- Perform an *a priori* evaluation of a presumed-PDF flamelet model for premixed flames of varying complexity. This includes one and three dimensions, single and multi-step chemistry and varying Karlovitz numbers.

- Analyse the sub-filter scalar variance transport equation, find out how the balance of different terms in this equation changes with increasing Karlovitz number, and investigate how this affects the applicability of model closures.

The thesis is organized as follows. In chapter 2 the governing equations of reactive fluid flow are summarized. Chapter 3 describes the numerical methods that were used as well as all the simulations that were performed. In chapters 4 and 5 the theory related to the flame thickness, flame propagation, presumed PDF modelling and sub-filter variance transport is presented. Some of the key results of the research papers as well as a discussion of well-stirred reactors at high Karlovitz numbers are also presented. A future outlook is given in chapter 6. At the end the research papers are attached.

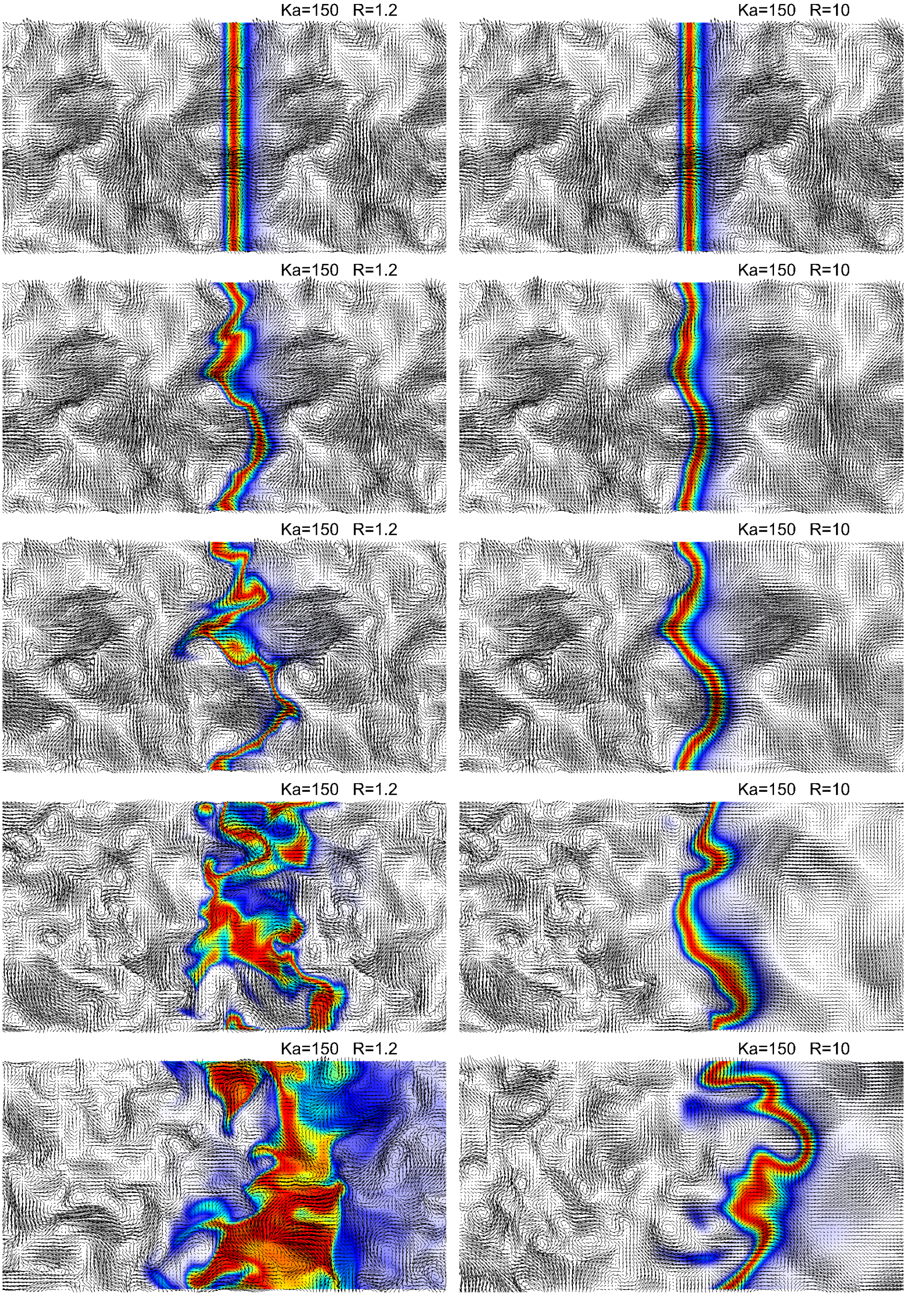

Figure 1.2: Transient evolution of two flames with the same Karlovitz number. The flame on the left has a density ratio of $R = 1.2$ while the one on the right has $R = 10.0$. The colour shows reaction rate and vectors show velocity and time increases from top to bottom, $t/\tau_0 = 0, 0.18, 0.41, 1.2$ and 12.

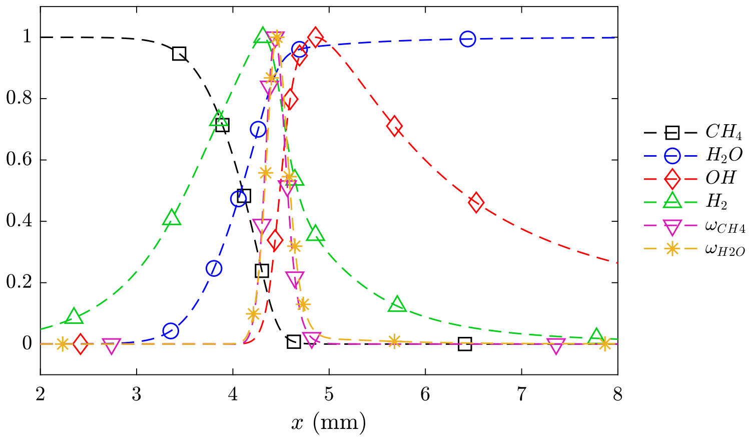

Figure 1.3: Selected species mass fractions and reaction rates in a simulated 1D planar premixed methane/air flame using the mechanism by Smooke and Giovangigli [15].

Chapter 2

Mathematical description of reactive flow

Fluid flow is commonly modelled by a system of partial differential equations (PDEs). The appropriate set of equations to use depends on the problem studied and what assumptions are made. In this work the flows considered are reacting, single-phase, multi-component flows at low Mach number. These are described by conservation equations for mass, momentum, energy and species.

2.1 Mass, momentum and energy conservation

The flow of a single-phase Newtonian fluid with variable density is modelled by the continuous conservation equations for mass, momentum and energy. The mass and momentum equations, known as the Navier-Stokes equations, can be formulated as

$$\frac{\partial \rho}{\partial t} + \frac{\partial u_i \rho}{\partial x_i} = 0 \tag{2.1}$$

$$\frac{\partial \rho u_i}{\partial t} + \frac{\partial \rho u_i u_j}{\partial x_j} = -\frac{\partial P}{\partial x_i} + \frac{\partial}{\partial x_j}\left[\rho\nu\left(S_{ij} - \frac{2}{3}\delta_{ij}\frac{\partial u_k}{\partial x_k}\right)\right] \tag{2.2}$$

where ρ is the density, u is the velocity, P is the pressure, ν is the kinematic viscosity and $S_{ij} = \left(\frac{\partial u_i}{\partial x_j} + \frac{\partial u_j}{\partial x_i}\right)$ is the strain rate tensor. Repeated indexes imply summation. For the energy equation many different forms exist. The variant most relevant for this work is

$$\rho C_p \frac{\partial T}{\partial t} + \rho u_i C_p \frac{\partial T}{\partial x_i} = \frac{\partial}{\partial x_i}\left(\rho C_p D_T \frac{\partial T}{\partial x_i}\right) + E_T + \dot{\omega}_T. \tag{2.3}$$

where T is the temperature, C_p is the heat capacity at constant pressure, D_T is the thermal diffusivity, E_T represents heat transfer due to the diffusion of individual species and $\dot{\omega}_T$

represents heat released from chemical reactions. Additional effects, such as compression, radiation and dissipation of kinetic energy, are not relevant for this work and have been excluded in Eq. (2.3).

2.2 Chemically reacting flow and scalar transport

In order to simulate a flame, a description of the combustion process has to be selected and coupled with the flow equations (2.1)-(2.3). This can be done with various levels of complexity. The flame can for example be described as an infinitely thin sheet with a prescribed propagation velocity, or as a wave of finite thickness whose propagation is driven by one or more chemical reactions. Depending on the choice of description of the flame, one or more scalar transport equations has to be added to the system of PDEs. The transport equation for a typical scalar ϕ can be written in the general form

$$\frac{\partial \rho \phi}{\partial t} + \frac{\partial \rho u_i \phi}{\partial x_i} = \mathcal{D}_\phi + \dot{\omega}_\phi \tag{2.4}$$

where $\mathcal{D}_\phi$ is a diffusion term and $\dot{\omega}_\phi$ is a source term. A useful distinction can be made between active and passive scalars: a scalar is passive if it exerts no influence on the velocity field (one-way coupling) and active if it does influence the velocity field (two-way coupling). The type and number of scalars for which transport equations has to be solved depends on the details of the combustion model.

2.2.1 Single-step chemical model

In a few of the simulations presented in this thesis the chemistry is described by a single reaction of the form $R \rightarrow P$ where R and P denote reactant and product, respectively. In this case it is conventional to describe the local chemical state by a single scalar c, called a reaction progress variable, which takes the value 0 for pure reactant and 1 for pure product. In the single reaction simulations, c is transported by equation (2.4) with diffusion and reaction terms given by Fick's law and by an Arrhenius expression, respectively:

$$\mathcal{D}_c = \frac{\partial}{\partial x_i}\left(\rho D_c \frac{\partial c}{\partial x_i}\right) \tag{2.5}$$

$$\dot{\omega}_c = \rho \frac{(1-c)^n}{\tau_R} \exp\left(-\frac{E_a}{RT}\right) \tag{2.6}$$

In these equations, D_c is the diffusivity, n is the reaction order, E_a is the activation energy, R is the universal gas constant and τ_R is a constant time scale. Here, the quantity ρD_c is considered to be constant. The corresponding terms to be used in the temperature equation (2.3) are $E_T = 0$ and $\dot{\omega}_T = C_p(T_b - T_0)\dot{\omega}_c$. For later reference, the c-equation can now be written as

$$\frac{\partial \rho c}{\partial t} + \frac{\partial \rho u_i c}{\partial x_i} = \frac{\partial}{\partial x_i}\left(\rho D_c \frac{\partial c}{\partial x_i}\right) + \dot{\omega}_c \tag{2.7}$$

Note that if the Lewis number is unity, i.e. $\mathrm{Le} = D_T/D_c = 1$, and there are no other sources of heat than the chemical reactions, then the transport equations for T and c are equivalent and one of them can be discarded. This can be useful to save on the computational cost.

2.2.2 Multi-step chemical model

In the other set of DNS simulations in this work a chemical model based on multiple species and reactions is used. The transported scalars are the mass fractions Y_α of each individual species. The diffusion term for a mass fraction, to be used in Eq. (2.4), has the form

$$\mathcal{D}_\alpha = \frac{\partial \rho V_{\alpha,i} Y_\alpha}{\partial x_i} \tag{2.8}$$

where V_α is the velocity at which species α diffuses in the mixture. The diffusion velocity is modelled using the Curtiss-Hirschfelder approximation [25] (note: no implied summation over α and β):

$$V_{\alpha,i} Y_\alpha = D_\alpha \frac{\partial Y_\alpha}{\partial x_i} + D_\alpha \frac{Y_\alpha}{\overline{W}} \frac{\partial \overline{W}}{\partial x_i} - Y_\alpha \sum_{\beta=1}^{N_{sp}} D_\beta \frac{\partial Y_\beta}{\partial x_i} - \frac{Y_\alpha}{\overline{W}} \frac{\partial \overline{W}}{\partial x_i} \sum_{\beta=1}^{N_{sp}} Y_\beta D_\beta \tag{2.9}$$

In Eq. (2.9) D_α is the diffusivity of species α and $\overline{W}$ is the mixture averaged molecular weight. The first term on the right hand side is analogous to Fick's law for binary diffusion, the second term appears due to gradients in the mean molecular weight, and the third and fourth terms are corrections to ensure the constraint $\sum_\alpha V_{\alpha,i} Y_\alpha = 0$ is fulfilled. If all diffusivities were equal, terms two and four would cancel and term three would be zero.

The chemical source term of a mass fraction Y_α is a sum of contributions from all reactions that involve this species and has the following form:

$$\dot{\omega}_\alpha = \rho W_\alpha \sum_{r=1}^{N_R} (\gamma_{\alpha r}^b - \gamma_{\alpha r}^f) \left[k_r^f \prod_{\beta=1}^{n} \left(\frac{\rho Y_\beta}{W_\beta} \right)^{\gamma_{\beta r}^f} - k_r^b \prod_{\beta=1}^{n} \left(\frac{\rho Y_\beta}{W_\beta} \right)^{\gamma_{\beta r}^b} \right] \tag{2.10}$$

In Eq. (2.10) N_R is the number of (reversible) reactions, b and f denote backward and forward reaction and $\gamma_{\alpha r}$ is the stoichiometric coefficient of species α in reaction r. The forward and backward reaction rates k_r^f and k_r^b are given by the Arrhenius law

$$k_r = A_r T^{n_r} \exp(-\frac{E_r}{RT}) \tag{2.11}$$

where A_r, n_r and E_r are reaction-specific constants and R is the universal gas constant.

The corresponding terms to be used in the temperature equation are

$$E_T = \frac{\partial T}{\partial x_i} \sum_{\alpha=1}^{N} \rho C_{p,\alpha} V_{\alpha,i} Y_\alpha \tag{2.12}$$

and

$$\dot{\omega}_T = -\sum_{\alpha=1}^{N} h_\alpha \dot{\omega}_\alpha \tag{2.13}$$

where h_α and $C_{p,\alpha}$ are the enthalpy and heat capacity of species α, respectively. In addition, fluid properties ν, C_p and D_T in equations (2.2) and (2.3) depend on the local mixture composition and on the temperature.

The number of species contained in CFD simulations, including DNS, is usually a small set of all the species that occur in a real flame. State-of-the-art detailed reaction mechanisms do provide a more complete picture but they simply contain too much detail and using them in CFD would make the computational cost intractable. Also, in DNS the purpose of a simulation is usually not to mimic the flow in a specific practical device, but rather to probe a certain physical process. Thus it is usually not needed to use a detailed chemical model as long as the model used can produce the necessary results for the process that is studied.

2.3 Filtered equations for large eddy simulation

In large eddy simulation filtered versions of the governing equations are solved. This is necessary when the full problem contains too many scales to be computationally affordable. There are different approaches to LES [26, 27], ranging from the 'pure' filtering view where a convolution filter is applied to obtain a set of modified governing equations that are to be solved with high accuracy, to the numerical view where no 'explicit' filter is used and scales too small to resolve are eliminated by a dissipative numerical scheme. For the purpose of the *a priori* studies in this thesis, the view is adopted that LES is a solution to a set of filtered PDEs with some model for each unclosed term. Note however that different DNS realizations that have the same filtered field at time $t = 0$, but different sub-filter fields, will disperse with time and the filtered fields will also be different for time $t > 0$. This means that the filtered field is a 'random field' and a deterministic LES can only match filtered DNS in a statistical sense (p.613 in [3]).

In flows with density variation it is convenient to make use of density weighted filtering, so-called Favre filtering. A Favre filtered quantity is defined by $\tilde{\phi} = \overline{\rho\phi}/\bar{\rho}$. For example, the filtered reaction progress variable transport equation reads

$$\frac{\partial \bar{\rho}\tilde{c}}{\partial t} + \frac{\partial \bar{\rho}\tilde{u}_i\tilde{c}}{\partial x_i} = \overline{\mathcal{D}_c} - \frac{\partial}{\partial x_i}\left(\overline{\rho u_i c} - \bar{\rho}\tilde{u}_i\tilde{c}\right) + \overline{\dot{\omega}_c} \tag{2.14}$$

which is obtained by applying a filter on each term in Eq. (2.7). It should also be noted that the Favre filter is not homogeneous or isotropic and does not commute with the spatial derivatives, i.e.

$$\frac{\partial \widetilde{\phi}}{\partial x_i} \neq \widetilde{\frac{\partial \phi}{\partial x_i}}. \tag{2.15}$$

This inequality is critically important in the derivation of the sub-filter variance equation which is discussed in section 5.2.3 and in paper 2.

In Eq. (2.14) the terms $\overline{\mathcal{D}_c}$, $\partial(\overline{\rho u_i c})/\partial x_i$ and $\overline{\dot{\omega}_c}$ cannot be computed with knowledge of only the filtered fields, i.e. $\overline{\rho}, \tilde{u}_i$ and $\tilde{c}$. These terms are therefore unclosed in LES and they have to be modelled. Similar unclosed terms appear in the filtered momentum equation, and in all species equations in case of a multi-species chemical model. It is a major challenge to find accurate and cost efficient models for all unclosed terms in LES. In paper 3 a modelling approach for $\overline{\dot{\omega}_c}$ is investigated. That approach depends on the sub-filter variance σ^2, and a method for modelling σ^2 is investigated in paper 2. These specific models will be described in detail in chapter 5.

2.4 Displacement speed of a scalar

For any convection-diffusion-reaction equation with the form of Eq. (2.4) a local displacement speed S_d can be defined. For a progress variable c it is given by

$$S_{d,c} = \frac{1}{|\nabla c|}\left(\frac{\partial c}{\partial t} + u_i \frac{\partial c}{\partial x_i}\right) = \frac{\mathcal{D}_c + \dot{\omega}_c}{\rho|\nabla c|} \tag{2.16}$$

The displacement speed is a local quantity that tells the self-propagation speed of the local scalar iso-surface. The concept is used extensively in paper 4 and in section 4.3. It is also possible to define a displacement speed for a filtered quantity. For example, by writing Eq. (2.14) in non-conservative form the displacement speed of $\tilde{c}$ is found to be

$$S_{d,\tilde{c}} = \frac{1}{|\nabla \tilde{c}|}\left(\frac{\partial \tilde{c}}{\partial t} + \tilde{u}_i \frac{\partial \tilde{c}}{\partial x_i}\right) = \frac{\overline{\mathcal{D}_c} + \overline{\dot{\omega}_c} - \frac{\partial}{\partial x_i}\left(\overline{\rho u_i c} - \overline{\rho}\tilde{u}_i\tilde{c}\right)}{\overline{\rho}|\nabla \tilde{c}|} \tag{2.17}$$

where the last term is due to the sub-filter flux.

Chapter 3

Methods for direct numerical simulation

Direct numerical simulations (DNS) are used in this work which means that the governing equations are solved numerically without the use of filtering or averaging. Turbulent motions are resolved down to the Kolmogorov length scale and species or other scalars are resolved down to their smallest structures. The numerical methods and case set-ups are described in the following sections, but first the computational cost and the associated Reynolds number restriction on this type of simulation is discussed.

The computational cost of a flow simulation (using an explicit time-marching solver) in terms of CPU time is proportional to the number of computational cells and the number of time steps, $cost \propto N_{steps} \times sN_{cells}$. Say that the integral length and velocity scales are L and U, the Kolmogorov length scale is η and the smallest scales of any scalar field is δ_l. The size of the computational domain is taken to be proportional to L. Additionally, for premixed flames there are velocity and length scales S_L and δ_L associated with the flame propagation. The computational cost can be written as $cost \propto T/\Delta t \times (L/\Delta x)^3$ where the time duration to be simulated, T, is a multiple of L/U or δ_L/S_L, whichever is largest, giving $T = \max(L/U, \delta_L/S_L)$. The Kolmogorov scale is considered to be resolved if $\Delta x \leq 2\eta \propto L \times \mathrm{Re}^{-3/4}$ [3] so a suitable grid resolution is $\Delta x \propto \min(L\mathrm{Re}^{-3/4}, \delta_l)$. An explicit method is used for time-marching and the time step size Δt is limited by the Courant–Friedrichs–Lewy (CFL) condition, $\Delta t \leq \Delta x/U$, and by the stability of diffusion, $\Delta t \leq (\Delta x)^2/D$, giving $\Delta t \propto \min(\Delta x/U, (\Delta x)^2/D)$. These estimates lead to the following scaling of the simulation cost:

$$\begin{aligned} cost &\propto \frac{\max(\frac{L}{U}, \frac{\delta_L}{S_L})}{\min\left(\frac{\min(L\mathrm{Re}^{-3/4}, \delta_l)}{U}, \frac{(\min(L\mathrm{Re}^{-3/4}, \delta_l))^2}{D}\right)} \cdot \frac{L^3}{\min(L^3\mathrm{Re}^{-9/4}, \delta_l^3)} \\ &= \max\left(1, \frac{1}{\mathrm{Da}}\right) \cdot \max\left(\mathrm{Re}^{3/4}, \frac{L}{\delta_l}, \mathrm{Re}^{1/2}, \frac{1}{\mathrm{Re}} \frac{L^2}{\delta_l^2}\right) \cdot \max\left(\mathrm{Re}^{9/4}, \frac{L^3}{\delta_l^3}\right) \end{aligned} \tag{3.1}$$

where $\mathrm{Da} = \frac{\delta_L U}{S_L L}$ is the Damköhler number. In all cases considered within this work $\mathrm{Re} > 1$ and in most cases $\mathrm{Da} < 1$ leading to the simpler expression

$$cost \propto \mathrm{Da}^{-1} \cdot \max\left(\mathrm{Re}^{3/4}, \frac{L}{\delta_l}, \frac{L^2}{\mathrm{Re}\,\delta_l^2}\right) \cdot \max(\mathrm{Re}^{9/4}, \frac{L^3}{\delta_l^3}) \tag{3.2}$$

In Eq. (3.2) the Damköhler number represents the normalized flame residence time, the second factor represents the time step (limited by either the CFL condition or diffusion stability) and the last factor represents the grid resolution (limited by either the Kolmogorov scale or the flame scales). If the turbulent scales is the limiting factor then Eq. (3.1) reduces to the well-known Re^3-scaling [3], but if flame scales are limiting then other scalings are possible.

In addition to the CPU time there may also be constraints on computer memory. The amount of memory needed is proportional to the number of computational cells and is therefore given by the last factor of Eq. (3.2) alone. It follows from Eqs. (3.1) and (3.2) that DNS of turbulent premixed flames is limited to low Reynolds numbers and small ratios L/δ_l, both can typically be no more than a few hundred. It is often desired to make these two numbers as large as possible and it is therefore desirable to use high order numerical methods which offers to maintain accuracy while keeping Δx and Δt manageable.

3.1 Numerical methods

The solver used for all DNS in this work is based on the governing equations for conservation of mass, momentum, energy and chemical species at low Mach number. A detailed description and validation has previously been published, see Yu et al. [28]. The solver uses explicit time stepping and a uniform staggered Cartesian grid with pressure and scalars represented at cell centres and velocity represented at cell faces. For most spatial derivatives a 6th-order central difference scheme is used. The exception is the convective terms for which a 5th-order weighted essentially non-oscillatory (WENO) finite difference method [29] is used to avoid numerical over-shooting in regions with large density gradients that may otherwise lead to spurious oscillations. The variable-coefficient Poisson equation for pressure difference is solved using a multi-grid method [30].

For time discretisation a second-order operator splitting scheme [31] is employed by performing integration of the chemical source terms between two half time-step integrations of the diffusion and convection. The overall time step of the operator splitting scheme is limited by the CFL condition. Since diffusion under some conditions requires a shorter time step to be stable (see Eq. (3.1)) the integration of the diffusion term is further split into smaller explicit time steps using a combined Runge-Kutta and Adam-Bashforth scheme as described in ref. [32]. In cases with multi-step chemistry the time integration of the chemical source term is typically stiff and also needs to be sub-stepped. This is done using the stiff ODE solver DVODE [33].

For the analysis of LES-related filtered quantities, such as $\bar{\dot{\omega}}$, explicit spatial filtering has to be performed by computing convolution products of the form $\int G(r')f(r-r')dr'$ where G is a filter kernel and f is the function to be filtered. For large filter kernels this becomes prohibitively expensive to compute in physical space. The standard solution is to first apply a Fourier transform and then compute the convolution product in wave space as

$$\int G(r')f(r-r')dr' = \hat{G}(k)\hat{f}(k). \tag{3.3}$$

where $\hat{G}$ and $\hat{f}$ are the transformed kernel and function, respectively. However, it is required that the data is periodic when the transform is applied, and the data studied here is in most cases only periodic in two of the three dimensions. This is overcome by attaching a mirrored copy of the data in the non-periodic direction. Also, mirroring does not have to be carried out explicitly in practice since the desired effect can be obtained more easily by removing all odd terms from the Fourier transform in the non-periodic direction, resulting in a cosine transform.

3.1.1 Turbulence forcing

In order to study turbulent flames it is necessary to generate turbulence. While it would in principle be possible to include turbulence-generating geometries such as solid objects or shear layers in the simulations, the excessive computational cost makes such strategies impractical in DNS. Instead, different methods can be used to generate and maintain turbulence through an artificial source term in the momentum equation. The most common methods seen in the literature are linear forcing [34, 35] and low-wavenumber forcing [36]; in this work the latter is used.

Low-wavenumber forcing injects energy to the large scales at the same rate, $\varepsilon = 2\nu S_{ij}S_{ij}$, at which energy is dissipated. This way the amount of turbulent kinetic energy is maintained. A new source term $\mathbf{f}$ is added on the right hand side of the momentum equation (2.2). For wavenumber κ the Fourier transform of the source term is

$$\hat{\mathbf{f}}_\kappa(t) = \frac{\langle\varepsilon\rangle I^R_{\kappa\leq\kappa_f}}{2k_f(t)}\frac{\rho}{\rho_u}\hat{\mathbf{u}}_\kappa(t) \tag{3.4}$$

where $\langle\varepsilon\rangle$ is the space-average of the dissipation rate, $\hat{\mathbf{u}}_\kappa$ is the Fourier transform of the velocity and $k_f = \sum_{|\kappa|\leq\kappa_f}\hat{\mathbf{u}}_\kappa\cdot\hat{\mathbf{u}}_\kappa/2$ is the kinetic energy contained in the modes with wavenumbers $|\kappa| \leq \kappa_f$. The cut-off wavenumber κ_f is is the largest wavenumber that will receive energy from forcing. The function $I^R_{\kappa\leq\kappa_f}$ is stochastic; at every time step it is 1 for a randomly selected wavenumber in the shell $|\kappa| \leq \kappa_f$ and 0 for all others. The source term in physical space is finally obtained by inverse Fourier transform of Eq. (3.4). Further details on the low wavenumber forcing method are given in refs. [37, 38].

3.1.2 Parallelization

Parallelization of the DNS solver is done within a distributed-memory framework where processes communicate using the Message Passing Interface (MPI). The computational domain is decomposed into rectangular blocks of equal size with six cells overlap, with one block for each parallel process. High-order spatial derivatives can be computed by keeping the overlapping cells synchronized.

In simulations employing multi-step chemistry the majority of computational work is spent on solving the stiff system of ODEs in the chemical step. The time it takes to integrate the chemical sources varies from block to block depending on how stiff the equations are. In general, a block with no flame segments inside it will be solved faster than a block with many flame segments. A simple method is used to balance this: the computational time spent on solving chemistry is measured for each block every time step. The measured times from the previous step is used rank the blocks from fastest to slowest, and each slower block is allowed to send a set of cells to a faster block. The time saved for the cases studied was found to be about 10-25% and the method was considered a reasonable trade-off between speed-up and communication complexity.

3.2 DNS database

Within this work a new database of DNS of turbulent premixed flames has been generated. The database contains two sets of flames. Apart from the chemistry and transport properties the two sets of flames share the same configuration and the following description of geometry, initial and boundary conditions is valid for both.

All flames are adiabatic and premixed without stratification, and the geometry is a rectangular box discretized on a uniform Cartesian grid. Periodic boundary conditions are used in the transverse directions while inflow and convective outflow conditions are used in the stream-wise directions. Planar flames are initially released at the centre of the domain together with pre-computed homogeneous isotropic turbulence. During the simulation the turbulence level is maintained by forcing as described in section 3.1.1, and pre-computed turbulence is also fed into the domain via the inlet. Figure 3.1 illustrates the set-up for the representative case D2. Further details on the set-up are given in the attached papers.

The first set of flames (set 1) is based on a rather realistic description of premixed methane/air combustion. It includes 16 chemical species with temperature-dependent transport properties, differential diffusion effects and the multi-step reaction scheme by Smooke and Giovangigli [15] which contains of 35 chemical reactions. The stiff system of ODEs for the chemistry and the multi-species diffusion (especially the highly diffusive H and H_2 species) makes these cases computationally demanding and limits the amount of statistics that can be obtained. All cases of set 1 are summarized in Table 3.1. The Reynolds, Damköhler and Karlovitz numbers are defined by Eqs. (1.1), (1.2) and (1.3), respectively. The integral length scale L_{11} is the integral of the longitudinal auto-correlation function.

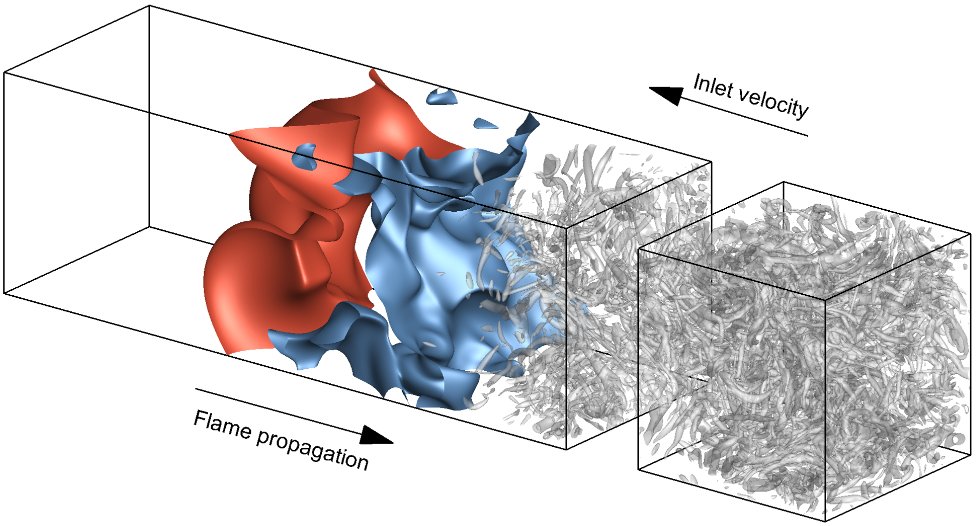

Figure 3.1: Illustration of a typical simulation set-up. The small box to the right shows the pre-generated turbulence used to feed the inlet, and the longer box to the left is the actual computational domain. Gray contours show vortices using the λ_2-method and red and blue contours show the $c = 0.2$ and $c = 0.95$ iso-surfaces.

The second set (set 2), on the contrary, is intended to have lower complexity than the first set. These flames are based on a chemical model with only two species (reactant and product) with a single reaction step. Transport properties are kept constant so there is no differential diffusion. The relevant parameters of the cases in set 2 are summarized in Table 3.2 where the Lewis, Prandtl and Zeldovich numbers are defined as Le $= D_T/D_c$, Pr $= \nu/D_T$ and Ze $= E_a(T_b - T_u)/(RT_b^2)$.

In paper 1 five transient DNS cases are investigated. These were originally set up by Carlsson [39] to explore the transition to the distributed burning regime. Three of these cases, namely K65, K550 and K3350, were in this work extended from a simulation duration of about $2\tau_0$ to at least $20\tau_0$ and are referred to as cases B2, B3 and B4 in Table 3.1. The reported Karlovitz numbers in paper 1 are lower because the integral length scale was estimated in a different way. For paper 2 these cases were complemented by the low Ka case B1. For paper 3 the cases denoted by A were constructed. These use a cut-off wavenumber κ_f of 1 instead of 3 resulting in an almost doubled integral length scale and Reynolds number. Case A3b has the same Ka as A3 but the domain size is increased to yield the same Re as A4 which allowed the sensitivity to Re to be tested under conditions of constant Ka. Case B4 was also used to provide a very high Ka flame, and case D1 was constructed to provide a flame that is free from the complexity of multi-step chemistry. For paper 4 case D2 was also added to provide a single-step chemistry case with higher Ka. The remaining case D1b was constructed as a single-step analogue to A3b.

Table 3.1: Data set 1: DNS of flames with methane-air chemistry.

Case	A1	A2	A3	A3b	A4	B1	B2	B3	B4
u'/S_L	3.7	8.3	18	24	66	2.5	18	67	210
Ka	6.0	22	74	75	540	4.5	103	800	4100
Da	0.38	0.14	0.060	0.11	0.01	0.31	0.031	0.0070	0.0025
Re	32	57	120	390	396	12	63	190	660
L_{11}/δ_{th}	1.4	1.1	1.1	2.6	0.98	0.75	0.58	0.46	0.52
δ_{th}/Δ_x	23.5	23.5	23.5	16.8	47.0	23.5	23.5	47.0	93.9
η/Δ_x	2.5	1.4	0.83	0.63	0.64	2.3	0.67	0.48	0.43

Table 3.2: Data set 2: DNS of flames with single-step chemistry.

Case	D1	D1b	D2
u'/S_L	12.7	19.6	56.5
Ka	40	47	440
Da	0.098	0.18	0.017
Re	80	340	260
L_{11}/δ_{th}	1.2	3.4	0.93
δ_{th}/Δ_x	11.7	12.8	46.6
η/Δ_x	0.62	0.69	0.82
Le	1.0	1.0	1.0
Pr	0.3	0.3	0.3
Ze	7.4	7.4	7.4

Instantaneous snapshots of each case are shown in Fig. 3.2 for comparison. Note that higher Karlovitz numbers lead to more disturbances in the flame front and these disturbances are more pronounced near the unburned side (blue colour in the figures) than near the burned side. At high Karlovitz numbers the flame structure tends to be altered. Conditional averages of species mass fractions and reaction rates deviate from their respective profiles of a one-dimensional flame. Many of the mass fractions are however seen to approach the profiles of a one-dimensional flame with unity Lewis number when the Karlovitz number is increased. This is shown for the mass fractions of the three species H_2, H_2O_2 and CO_2 in Fig. 3.3 using cases A1-3. This observation seems to support the use of a turbulent diffusivity to model small-scale turbulent transport at high Ka. However, the mass fraction of the radical HCO is seen to behave differently and it shows increased activity in the low temperature region at high Karlovitz numbers, which is contrary to the behaviour of the unity Lewis number flame. Figure 3.4 shows conditional profiles of HCO for cases A1-3 and elevated concentration is seen for $c \leq 0.5$ where c is based on the H_2O mass fraction. Furthermore, at the highest Karlovitz number, $\mathrm{Ka} = 4100$ in case B4, local regions with high HCO mass fraction are seen in the pre-heat zone. This is in the right panel of Fig. 3.4

where two such regions are marked by A and B.

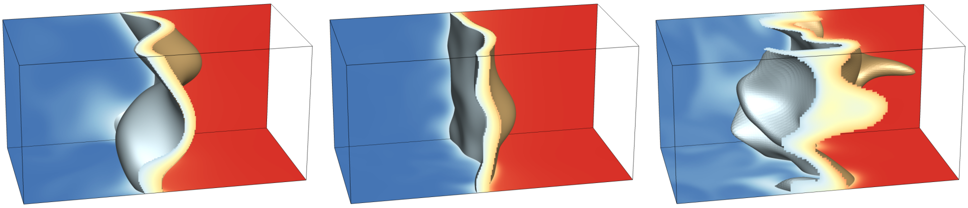

(a) Case A1 **(b)** Case B1 **(c)** Case D1

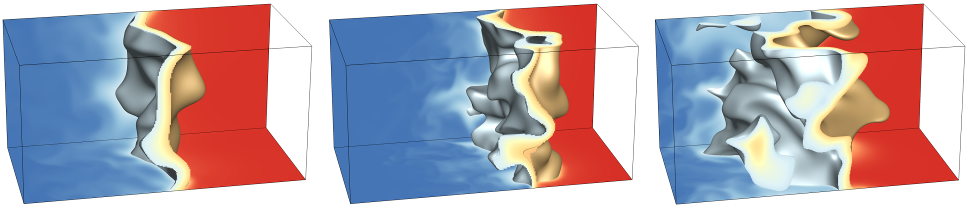

(d) Case A2 **(e)** Case B2 **(f)** Case D2

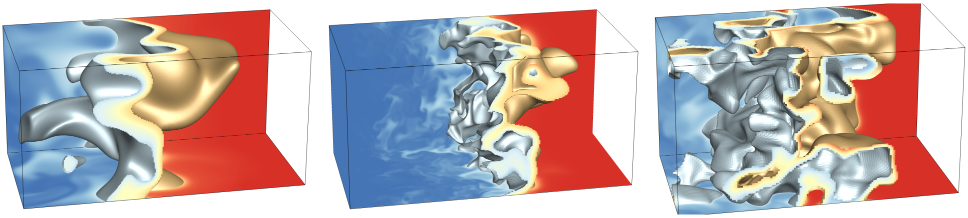

(g) Case A3 **(h)** Case B3 **(i)** Case D1b

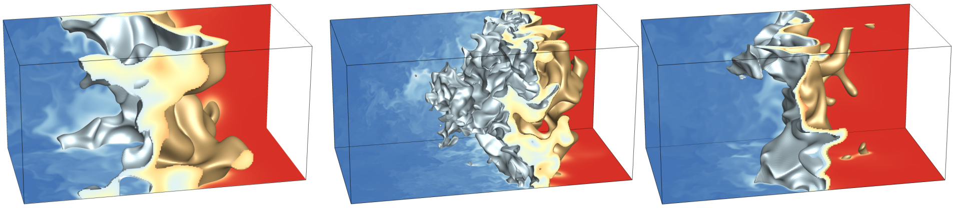

(j) Case A4 **(k)** Case B4 **(l)** Case A2b

Figure 3.2: Flame geometry in the DNS cases. Coloured slices shows the reaction progress variable c with iso-surfaces drawn at $c = 0.3$ and $c = 0.7$. For cases with multi-step chemistry c is based on $\mathrm{H_2O}$ mass fraction.

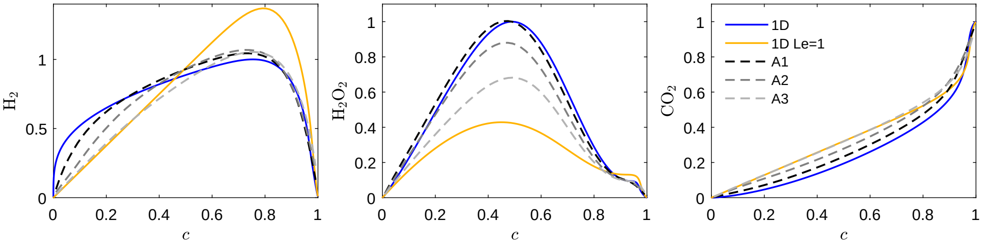

Figure 3.3: Conditional averages of three selected species mass fractions. Dashed lines show cases A1, A3 and A4 which have three different Karlovitz numbers, the blue line shows a one-dimensional flame and the orange line shows a one-dimensional flame with unity Lewis number.

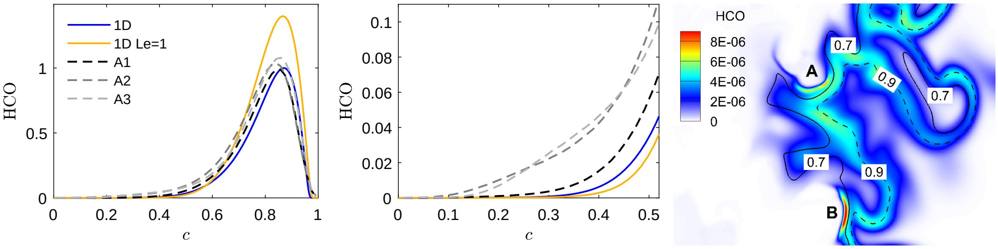

Figure 3.4: The left and middle figures show conditional average of HCO mass fraction. Dashed lines show cases A1, A3 and A4 which have three different Karlovitz numbers, the blue line shows a one-dimensional flame and the orange line shows a one-dimensional flame with unity Lewis number. The right figure shows contours of the HCO mass fraction (colour) and reaction progress (two lines) for case B4.

Chapter 4

Structure and propagation of premixed flames

In this chapter some of the results related to flame structure and propagation speed are summarized. Papers 1 and 4 focuses on the structure and transient evolution of premixed turbulent flames, and in particular the flame thickness. In paper 1 the discussion is centred around the transient evolution from an initially planar flame to a turbulent flame under moderate and high Karlovitz numbers. The multi-step chemistry flames B1 to B4 from data set 1 (see Table 3.1) were used. In paper 4 the discussion of flame thickness is expanded and precise evolution equations for three different metrics of averaged flame thickness are analysed. The latter analysis is outlined in the following section 4.1. An analysis from paper 1 about alignment of the flame surface normal, which is related to the evolution of thickness, is shortly summarized in section 4.2. The chapter is then concluded with some results for the evolution equation for averaged displacement speed in section 4.3.

4.1 Thickness analysis

In paper 4 the dynamics of flame thickening and thinning are investigated by analysis of evolution equations for the three conditionally averaged thickness metrics. These equations were recently derived in ref. [40]. The analysis is based on the concepts of surface averages and the iso-surface following derivative. A surface average $\langle \cdot \rangle_s$ is defined as

$$\langle \phi \rangle_s = \frac{1}{M} \sum_{i=1}^{M} \frac{\oiint_S \phi \, \mathrm{ds}}{\oiint_S \, \mathrm{ds}} \tag{4.1}$$

where S is a surface, ds is a surface element and M is the number of realizations. Letting S be an iso-surface defined by $c = \hat{c}$ gives a definition of conditional average $\langle \phi \rangle_s |_{c=\hat{c}}$ that is weighted by surface area. More details including the relation to volume weighted averages $\langle \cdot \rangle_v$ are given in ref. [40] and in paper 4.

The concept of an iso-surface following derivative is related to the conventional 'flow-following' material derivative and is defined as

$$\frac{\partial^* \phi}{\partial^* t} = \frac{\partial \phi}{\partial t} + u_i^* \frac{\partial \phi}{\partial x_i} \tag{4.2}$$

where $u_i^* = u_i - n_i S_d$ is the sum of local flow velocity and self-propagation velocity. The normal direction is $n_i = \nabla c / |\nabla c|$ and the self-propagation speed S_d is given by Eq. (2.16). For example, the iso-surface following derivative of the thickness marker $|\nabla c|$ is

$$\frac{\partial^* |\nabla c|}{\partial^* t} = |\nabla c| \left(n_i \frac{\partial S_d}{\partial x_i} - a_n \right) \tag{4.3}$$

where $a_n = n_i n_j \partial u_i / \partial x_j$ is the normal strain rate. Equation (4.3) describes the local balance of thickening and thinning forces on a flame front and it is discussed in paper 1 and also by refs. [41–44].

In addition to the local flame thickness it might be of interest to know how the average thickness evolves. It has been shown [40] that the time rate of change of a surface averaged quantity is related to the iso-surface following derivative by

$$\frac{\partial \left\langle \phi \right\rangle_s}{\partial t} = \left\langle \frac{\partial^* \phi}{\partial^* t} \right\rangle_s + \left\langle \phi \mathcal{K} \right\rangle_s - \left\langle \phi \right\rangle_s \left\langle \mathcal{K} \right\rangle_s \tag{4.4}$$

where

$$\mathcal{K} = S_d \frac{\partial n_i}{\partial x_i} + \frac{\partial u_i}{\partial x_i} - a_n \tag{4.5}$$

is the stretch rate. Substituting Eq. (4.3) into eq. (4.4) and rearranging yield an expression for the time evolution of the surface-averaged flame thickness marker $|\nabla c|$ as

$$\frac{\partial \left\langle |\nabla c| \right\rangle_s}{\partial t} = \left\langle |\nabla c| n_i \frac{\partial S_d}{\partial x_i} \right\rangle_s - \left\langle |\nabla c| \frac{\partial u_i}{\partial x_i} \right\rangle_s + 2 \left\langle |\nabla c| \mathcal{K} \right\rangle_s - \left\langle |\nabla c| \right\rangle_s \left\langle \mathcal{K} \right\rangle_s \tag{4.6}$$

In paper 4 Eq. (4.6) and similar equations for the evolution of two other averaged thickness markers, are used to study the dynamics of flame thickness. The three averaged markers $\left\langle |\nabla c| \right\rangle_s$, $\left\langle |\nabla c| \right\rangle_v$ and $\exp(\left\langle \ln(|\nabla c|) \right\rangle_s)$ are used to analyse a set of 6 flames of different complexity. The first one is a passive reaction wave (flame without heat release) with a single reaction. This wave propagates in a forced turbulent flow and has a high Karlovitz number. Then there are the two single-step chemistry flames D1 and D2 from table 3.2 and the two multi-step chemistry flames A3 and B4 from table 3.1. Finally there is a one-dimensional laminar flame with multi-step chemistry.

It was found that the three thickness metrics can give quite different results. It was shown that the inequality $\left\langle |\nabla c| \right\rangle_v \leq \left\langle |\nabla c| \right\rangle_s$ always holds, and the numerical results show that under some circumstances the metrics $\left\langle |\nabla c| \right\rangle_s$ and $\left\langle |\nabla c| \right\rangle_v$ can give opposite results as to whether the flame is thinned or broadened (compared to the laminar thickness). This is most clearly seen for the passive flame and in the pre-heat zone of the other flames. Mathematically the only difference between these two metrics is that one is weighted by the iso-surface area while the other is weighted by volume. This result highlights the importance of how flame thickness is defined since the chosen definition can significantly affect the result. Indeed, there have been many possibly contradicting reports of both thinned [13, 45–47] and broadened [48–53] turbulent premixed flames in the literature, both experiments and simulations, and it is known that locally thin segments exist even if a flame is broadened on average.

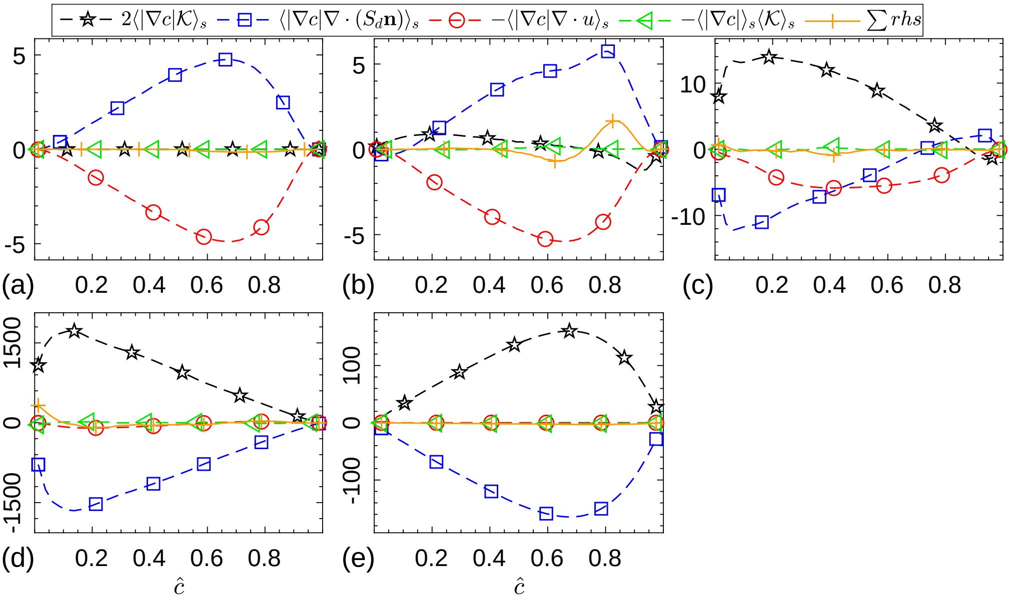

Figure 4.1: Conditional surface-averaged terms in the evolution equation for $|\nabla c|$. Shown in (a-e) are, respectively, the laminar flame, case A1, case A3, case B4 and the passive reaction wave.

In the flames that have non-zero heat release and associated density variations, the terms in the thickness evolution equations that contain the volume dilatation rate can become important and change the balance in the equations. A trend was however observed with the Karlovitz number. Consider the equation for $\langle|\nabla c|\rangle_s$ given by Eq. (4.6), the terms of which are shown in Fig. 4.1. The last term contains $\langle\mathcal{K}\rangle_s$, the surface averaged mean stretch rate, and this term is zero since the flame is in a statistically stationary state. For the passive reaction wave the second term on the right hand side is also zero because it contains the velocity divergence. This leaves a balance between the first and third terms, $\langle|\nabla c|n_i\partial S_d/\partial x_i\rangle_s$ and $2\langle|\nabla c|\mathcal{K}\rangle_s$, the former being negative and the latter positive. This balance was also seen for other passive reaction waves, both laminar and turbulent. Another limiting case is the one-dimensional flame with heat release. For that case $\mathcal{K} = 0$ so that the first term in Eq. (4.6) disappears. Secondly, the velocity divergence is non-zero and positive, giving a negative term $\langle|\nabla c|\partial u_i/\partial x_i\rangle_s < 0$. This leaves the remaining term $\langle|\nabla c|n_i\partial S_d/\partial x_i\rangle_s$ as a positive term, which is opposite compared with the passive wave case. Finally, when three-dimensional turbulent flames with heat release are studied, the observed balance seems to change from that of the one-dimensional case for low Karlovitz numbers to that of the passive wave case for high Karlovitz numbers as seen in Fig. 4.1.

Concerning Fig. 4.1 it can be noted that the sum of right hand side terms does not entirely vanish for case A1. The cause of this is an effect of the relatively large time step that was used in this simulation. This is not a problem for most analyses since the resulting error is very small for most statistics, but since Eq. (4.6) contains some rather sensitive terms involving gradients of the displacement speed the error turns out to be observable in this case. This however does not change the general conclusion discussed above which has been verified for multiple cases. Another observation from the figure is that in cases A3 and B4 the dominating terms decay with increasing c, something which is not seen for the passive wave. This is related to the two-way coupling between flow and flame in cases with heat release: the velocity divergence reduces the effective Karlovitz number with increasing c.

In Fig. 4.2 the spatial distribution of the three terms $2|\nabla c|\mathcal{K}$, $|\nabla c|n_i\partial S_d/\partial x_i$ and $|\nabla c|\partial u_i/\partial x_i$ is shown for cases A1 and A4. The figure shows that the velocity divergence term becomes negligible at high Ka. It can also be seen that the stretch term, $2|\nabla c|\mathcal{K}$, has significant magnitude also in the low Ka case A1 meaning that the surface-averaged value of zero previously seen in Fig. 4.1 must have resulted from cancellation of positive and negative contributions. Finally, the last panel of Fig. 4.2 shows the thickness marker $|\nabla c|$. In case A1 a rather even distribution of $|\nabla c|$ is seen while the distribution in case A4 is broad but spotty with appearance of locally compressed flame segments with large values of $|\nabla c|$.

4.2 Alignment of the flame surface normal

In the analysis of flame thickness it was found that the presence of heat release and associated density variation can have a significant effect on the dynamics. In cases with low Ka the heat release can completely change the balance in the thickness equations and some terms even change sign. Another manifestation of the effect of heat release can be seen in the alignment characteristics of the flame surface normal vector, n_i.

It is known that the iso-surface normal of a passive scalar aligns preferentially with the eigenvecor of the strain rate tensor S_{ij} that corresponds to the most compressive direction [54]. It is also known that the iso-surface normal of a progress variable in a low Ka flame with significant heat release aligns with the extensive eigenvector [55, 56]. The latter case is easily confirmed in the limit of a planar laminar flame: if there is no turbulence then the only source of strain is due to the heat release.

It was shown in ref. [55] that, as the Karlovitz number increases, the alignment of the surface normal changes in the pre-heat zone and becomes aligned with the compressive direction. In paper 1 this trend was confirmed and it was shown that, for very high Ka,

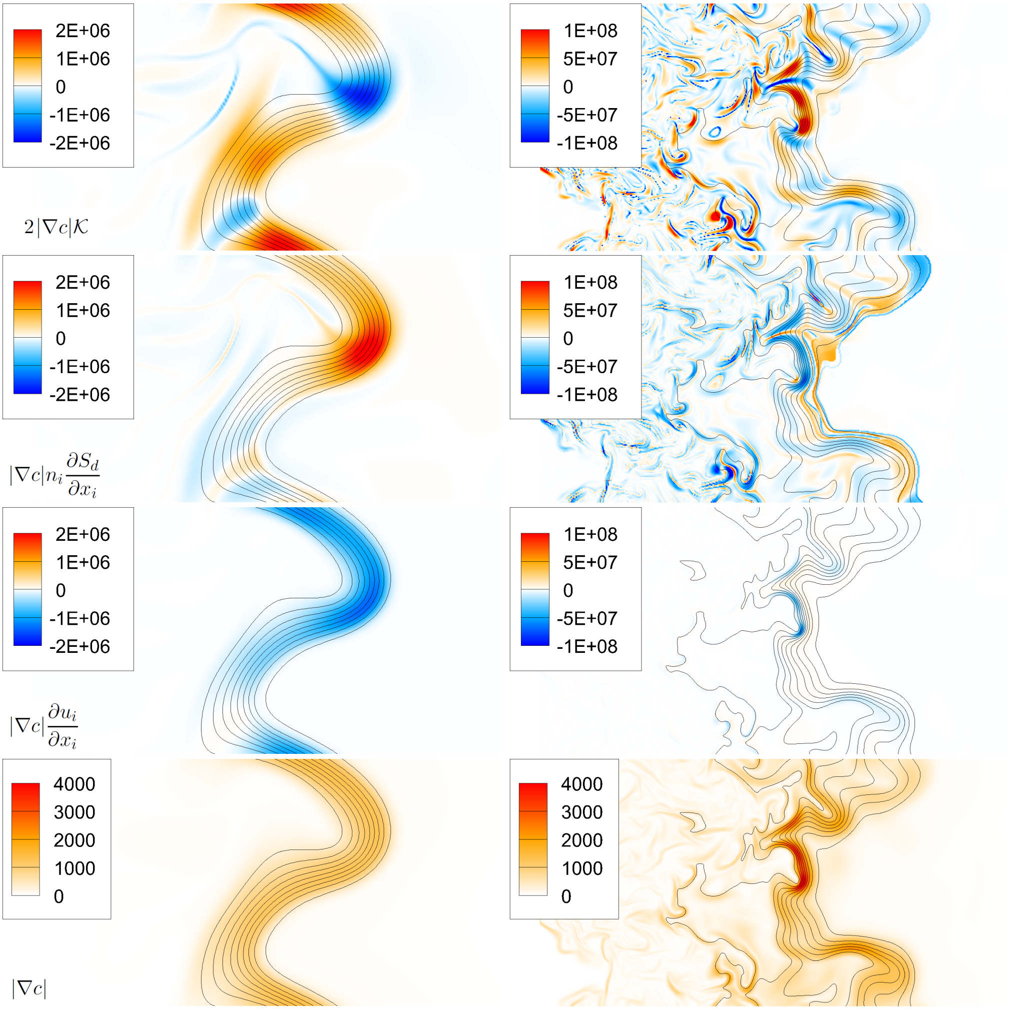

Figure 4.2: Spatial distribution of the three dominating terms in the evolution equation for $|\nabla c|$ (top three rows) and $|\nabla c|$ itself (bottom row). Two cases are shown: case A1 with $\mathrm{Ka} = 6$ (left) and case A4 with $\mathrm{Ka} = 540$ (right).

alignment with the compressive direction is seen in the entire flame including the reaction zone. The preferential alignment with the compressive eigenvector is of interest because it provides a possible mechanism that can explain flame thinning that is observed (at least locally) in highly turbulent premixed flames. In Fig. 4.3 the conditional average of five different alignment angles are shown for cases B1 and B3. In the legend the symbol N refers to the surface normal, C, E and 2 refer to the compressive, extensive and intermediate strain rate eigenvectors, and ω refers to the vorticity vector.

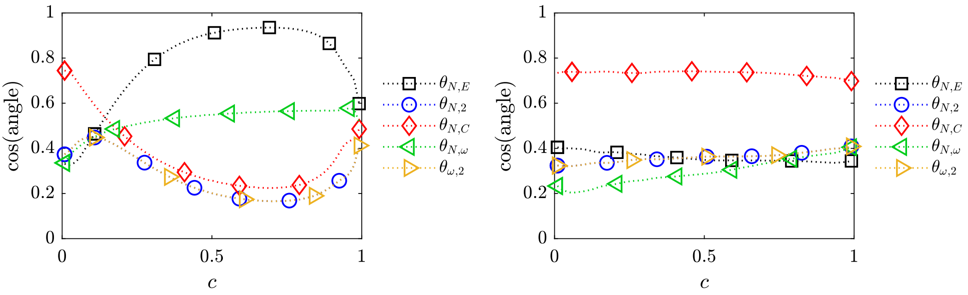

(a) Case B1, Ka = 4

(b) Case B3, Ka = 800

Figure 4.3: Conditional average of alignment angles between the flame surface normal, the three strain rate eigenvectors and the vorticity vector.

4.3 Displacement speed evolution equation

In ref. [40] it was shown that Eq. (4.4) can be used to obtain an evolution equation for the average displacement speed $\langle S_d \rangle_s$ for the case of an isothermal reaction wave with constant diffusivity. The equation can be extended to flames with density variation and single step chemistry if the diffusion term is given by Eq. (2.5). If it is also assumed that the quantity ρD_c is constant (as is the case for the flames in set 2) the equation becomes

$$\begin{aligned}\frac{\partial \langle S_d \rangle_s}{\partial t} = &\left\langle S_d \frac{\partial u_i}{\partial x_i} \right\rangle_s - \left\langle S_d \frac{\partial S_d n_i}{\partial x_i} \right\rangle_s - \left\langle \frac{D_c}{|\nabla c|} \frac{\partial c}{\partial x_i} \frac{\partial^2 u_i^*}{\partial x_j \partial x_j} \right\rangle_s \\ &- 2 \left\langle \frac{D_c}{|\nabla c|} \frac{\partial^2 c}{\partial x_i \partial x_j} \frac{\partial u_i^*}{\partial x_j} \right\rangle_s - \langle S_d \rangle_s \langle \mathcal{K} \rangle_s\end{aligned} \tag{4.7}$$

where u_i^* is the 'effective' iso-surface velocity that was defined in section 4.1. The derivation of Eq. (4.7) is straight-forward starting from the definition of S_d and making use of the fact that the iso-surface following derivative of a quantity that only depends on c is zero. The full details are given in [40].

In ref. [57] Eq. (4.7) was analysed for both laminar and turbulent flames without density variation. At the time of this writing the analysis of the displacement speed equation is still ongoing but some results are shown in Fig. 4.4. This figure shows conditional averages of all terms for three cases. The first case is a laminar one-dimensional flame, and the second and third are cases D1 and D2. In the plots in the bottom row the iso-surface velocity u_i^* has been decomposed as $u_i^* = u_i - n_i S_d$. First, it can be observed that the sum of all terms, $\sum rhs$, is close to zero and since these flames are known to be in a statistically stationary state this indicates that all terms have been computed with sufficient accuracy. Terms involving gradients of the displacement speed are particularly sensitive to the numerical accuracy and it has been seen that even a small inconsistency can disrupt the balance. Secondly, the velocity divergence term loses significance when turbulence intensity is increased similarly to the observations made for the thickness equation in section 4.1. Third, the components of the two terms that were decomposed in the bottom row of the figure mostly mirror each other. Finally, in the laminar case the iso-surface velocity u_i^* is constant due to the stationary state leading to exact balances between the pairs of terms.

In discussions of the displacement speed it is common to use a decomposition that separates S_d into three components as was also done in paper 1. These pertain to reaction, normal diffusion and tangential diffusion (curvature) and are given by

$$S_d = \underbrace{D\frac{\partial n_i}{\partial x_i}}_{S_d^C} + \underbrace{\frac{n_i}{\rho|\nabla c|}\frac{\partial \rho D|\nabla c|}{\partial x_i}}_{S_d^N} + \underbrace{\frac{\dot{\omega}_c}{|\nabla c|}}_{S_d^R} \tag{4.8}$$

where the same assumptions of single-step chemistry and constant ρD have been used. A discussion of the decomposition is given in paper 4. From Eq. (4.4) it is possible to obtain evolution equations analogous to Eq. (4.7) for each of these components. A related equation for the local curvature was recently published by Cifuentes et al. [58]. Further analysis of how the evolution equations for the different components are affected by heat release, Karlovitz number etc. is a topic for future study.

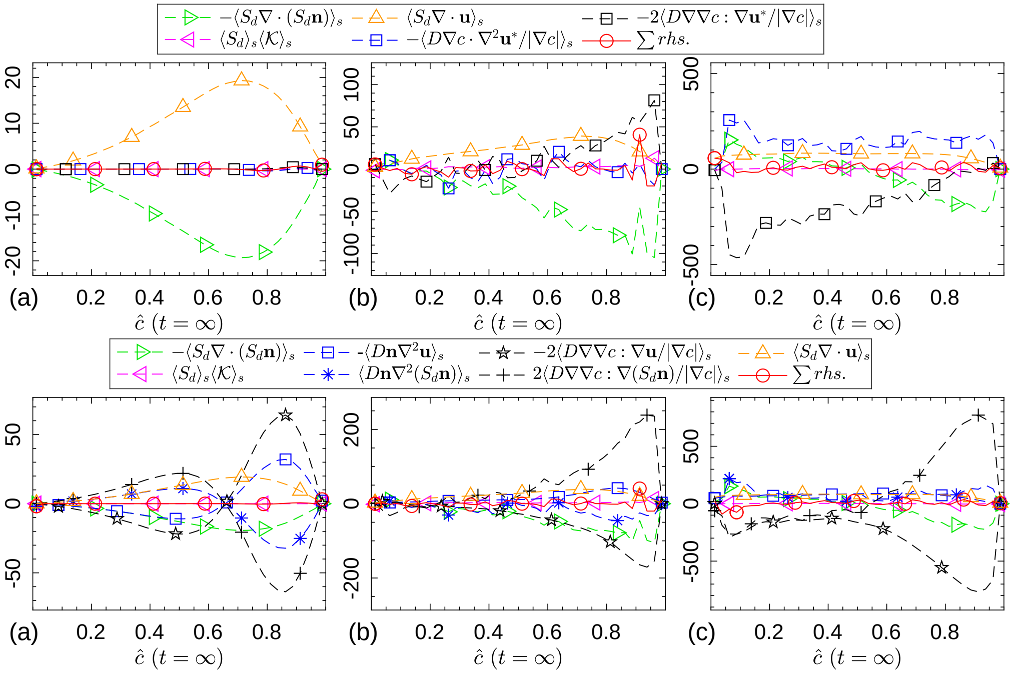

Figure 4.4: Conditionally averaged terms in the displacement speed evolution equation. The top row shows the form used in Eq. (4.7) while in the bottom row two terms have been expanded by decomposing the effective velocity $u_i^* = u_i - n_i S_d$. The cases are, from left to right, a laminar one-dimensional flame, case D1 and case D2.

Chapter 5

Modelling of turbulent premixed flames

In this chapter some theory and results related to modelling of turbulent premixed flames are presented. The chapter begins with a discussion of the well-stirred reactor assumption in the context of high Karlovitz number flames in section 5.1. Then in section 5.2 presumed PDF modelling and the sub-filter variance equation are discussed.

5.1 Well-stirred reactors at high Ka

A modelling concept that is sometimes discussed for high Ka combustion is the so-called well-stirred reactor (WSR). When the Kolmogorov time scale is sufficiently smaller compared to any reaction time scale, i.e. at sufficiently high Karlovitz number, then there should exist a length scale below which all scalars are 'well mixed'. If the LES filter size Δ is smaller than this length scale then the flame is resolved and the sub-grid distribution can be approximated by a delta-function which leads to the model

$$\overline{\dot{\omega}}(T, Y_i) \approx \dot{\omega}(\widetilde{T}, \widetilde{Y_i}) \tag{5.1}$$

Equation (5.1) will be referred to as the well-stirred reactor model in the following. The use of Eq. (5.1) at low Ka is known to be problematic due to the non-linear dependence of $\dot{\omega}$ on T and Y_i, see Eqs. (2.6) and (2.10), and it is not clear how intense the turbulence needs to be in practice for Eq. (5.1) to be a good approximation. Referring to Fig. 4.2 and the results of [4, 11–14] it is known that thin flame segments with large scalar gradients exist in turbulent premixed flames at very high Ka, even in the case of a constant density flow, and this might impede the accuracy of a WSR model. Therefore it is of interest to know how quickly the error of WSR decreases when the Karlovitz number is increased.

The WSR model represent a class of combustion models where multi-step chemistry can be used directly without restricting the chemical state space to a low dimension, as it is done in flamelet models. On the other hand, this means that pre-tabulation of reaction rates cannot be used and that transport equations have to be solved for all filtered species mass fractions implying a higher computational cost compared to pre-tabulated models. It should be noted that several related models exist in the literature where different measures are taken to make them applicable in other combustion regimes and for different combustion modes [59–62]. Most of these variants are based on arguments involving turbulent and chemical time or length scales. A thorough investigation of such models is outside the scope of this work and they are not discussed further here.

An effect of the well-stirred assumption is that unburned and burned gases that were separated on the sub-grid are artificially ”mixed” by the model, often with too large reaction rates as a result. If the filter size goes to zero the WSR model becomes exact, i.e. it is consistent in the DNS limit, but the error grows rapidly with increasing filter size. When multi-step chemistry is used a further issue will arise. If Eq. (5.1) is applied to the filtered rates of all reactions, the error in each individual reaction rate will be different. These differences can be significant and makes it difficult to correct for the error since every reaction has to be treated differently [63]. The WSR model can therefore not be easily ’fixed’ by introducing a global scaling factor for the reaction rates.

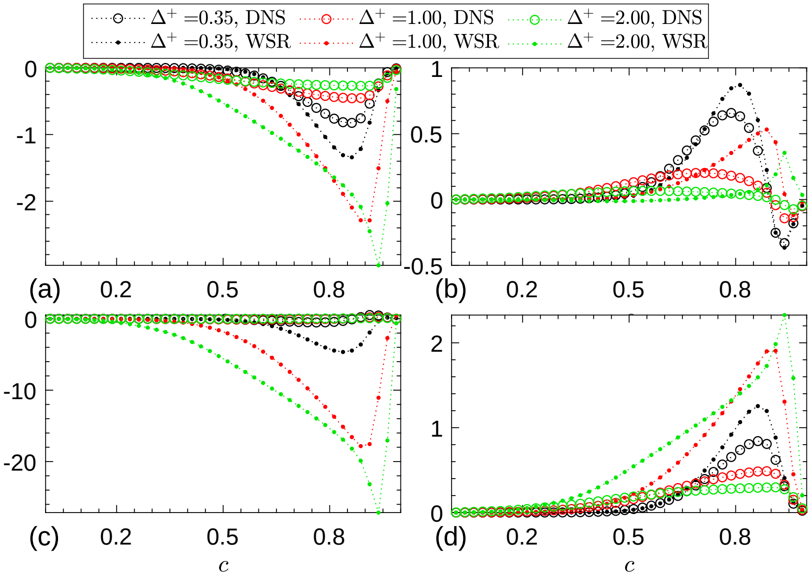

Figure 5.1: Conditionally averaged filtered reaction rates from filtering of DSN data (circles) and the WSR model (dots). The data is for case A3.

In Fig. 5.1 filtered net reaction rates of four selected species (CH_4, H_2, OH and H_2O) are shown for case A3 which has a relatively low Ka of 74. Rates are normalized by the maximum magnitude of the corresponding rate in a one-dimensional flame. Conditioning is done on the reaction progress variable c which is based on the H_2O mass fraction. Three filter sizes are used, $\Delta^+ = \Delta/\delta_{th} = 0.35$, 1.0 and 2.0, shown by different colours in the figure. Circles show the filtered rates $\overline{\dot{\omega}}$ obtained by direct filtering of $\dot{\omega}$ and the dots show the WSR rates obtained through Eq. (5.1). When the filter size is increased the magnitude of the filtered rates (circles) are seen to decrease for all four species. The WSR rates are generally over-predicted and for three of the species shown the rate even increases with filter size. For the OH radicals (Fig. 5.1.c) the WSR rate is 25 times the laminar peak value when the filter size is twice the laminar flame thickness.

In the following, the effect of Karlovitz number and filter size on the WSR assumption is investigated statistically. Following the analysis in paper 3, an integrated error metric and a weighted correlation coefficient [64] are used. These are defined as

$$E = \frac{\sum_i |\overline{\dot{\omega}}_i - \overline{\dot{\omega}}_i^{WSR}|}{\sum_i |\overline{\dot{\omega}}_i|} \tag{5.2}$$

and

$$r = \frac{\sum_i \overline{\dot{\omega}}_i(\overline{\dot{\omega}}_i - \langle\overline{\dot{\omega}}\rangle)(\overline{\dot{\omega}}_i^{WSR} - \langle\overline{\dot{\omega}}^{WSR}\rangle)}{(\sum_i \overline{\dot{\omega}}_i(\overline{\dot{\omega}}_i - \langle\overline{\dot{\omega}}\rangle)^2)^{1/2}(\sum_i \overline{\dot{\omega}}_i(\overline{\dot{\omega}}_i^{WSR} - \langle\overline{\dot{\omega}}^{WSR}\rangle)^2)^{1/2}} \tag{5.3}$$

where i runs over a large number of samples (computational cells). Since WSR is equivalent to perfect mixing on the sub-grid scale it is expected that the error made by this model will decrease as the flame becomes increasingly stirred by turbulence. In Fig. 5.2 the correlation coefficient r and error E evaluated for the WSR model, Eq (5.1), are shown for cases A1, A3, A4, B4, D1 and D2 as well as a one-dimensional flame (1D). In the cases with multi-step chemistry the net rate of H_2O formation is used to evaluate r and E while in the single-step chemistry cases D1 and D2 the rate of c is used.

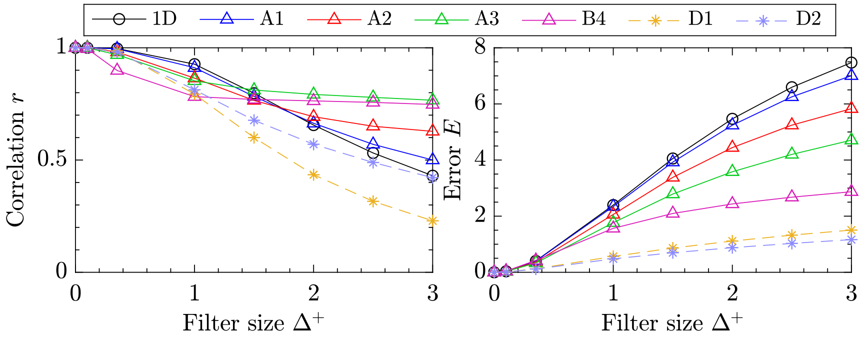

Figure 5.2: Correlation coefficient and error of the WSR model for different cases.

Considering the multi-step chemistry cases A1, A3, A4 and B4 the results confirm that the error increases with filter size and decreases with Ka and the correlation does the opposite just as expected. For the error E there is no significant difference between cases A1, A3 and the 1D laminar flame but some improvement with Ka is seen in the correlation coefficient for the larger filter sizes. Moving to case A4 yields a significant reduction in E and further increase in r for large filters. Finally, case B4 represents another significant drop in E while r actually decreases for small filters but levels out around $r = 0.8$ for larger filters. It should be kept in mind though that case B4 is not fully developed into a statistically stationary state which might have some effect on the metrics.

The situation is a bit different for the cases that use single-step chemistry, D1 and D2. These have lower error than all multi-step cases, but yet they have the lowest correlation. A likely explanation for this can be found: In the case of simplified chemistry and transport, $\dot{\omega}$ only depends on c and there exists a maximum value $\dot{\omega}(c_{\max})$ that occurs for a certain value $c_{\max}$. This puts a constraint on how much the rate can be over-predicted. In the case of complex chemistry and transport the chemical phase space is no longer one-dimensional and the maximum possible reaction rate does not occur on the manifold accessed in a typical turbulent flame. Thus, there is no clear constraint on the reaction rate, and the artificial mixing in the WSR model due to filtering can result in chemical states located far from the usual manifold where the reaction rates can be extremely large [65]. This provides an explanation why the error is larger in flames with complex chemistry compared with the flame with simplified chemistry, despite the higher correlation in the complex chemistry flames.

Finally, Fig. 5.3 shows E and r computed for 14 different species mass fractions in cases A1 and A4 to further illustrate the effect on multi-step chemistry. The figure shows that the difference between species is, for the most part, much larger than the difference between Karlovitz numbers. The right-most sub-figures also show a scaling factor defined as

$$\frac{\int |\bar{\dot{\omega}}| \, \mathrm{d}\mathbf{x}}{\int |\bar{\dot{\omega}}^{WSR}| \, \mathrm{d}\mathbf{x}} \tag{5.4}$$

which gives a sense of the error in the total consumption/production of the various species. It can be noted that the reactant and product species (CH_4, O_2, H_2O and CO_2) often have smaller errors than the radical and intermediate species, both as measured by E and by the scaling factor.

In summary the WSR model is exact in the limit of zero filter size, has a high correlation coefficient for small filters ($\Delta^+ \ll 1$), has a smaller error with increasing Ka and does not restrict the degrees of freedom in the chemical phase space. Thus, in a case with a combination of small filter size and high Karlovitz number, it seems that the WSR model (or at least a scaled variation of it) could perform well. This can be compared with flamelet models of the type discussed in papers 2 and 3 which tend to give large error for the combination of small filters and complex chemistry.

As a final remark it is stressed that the analysis presented here is an *a priori* evaluation of the WSR model, meaning that the chemical states that are accessed have all been obtained from filtering of DNS data with no feedback from the WSR model. A filtered DNS case could in principle be converted to an LES and allowed to develop with filtered rates

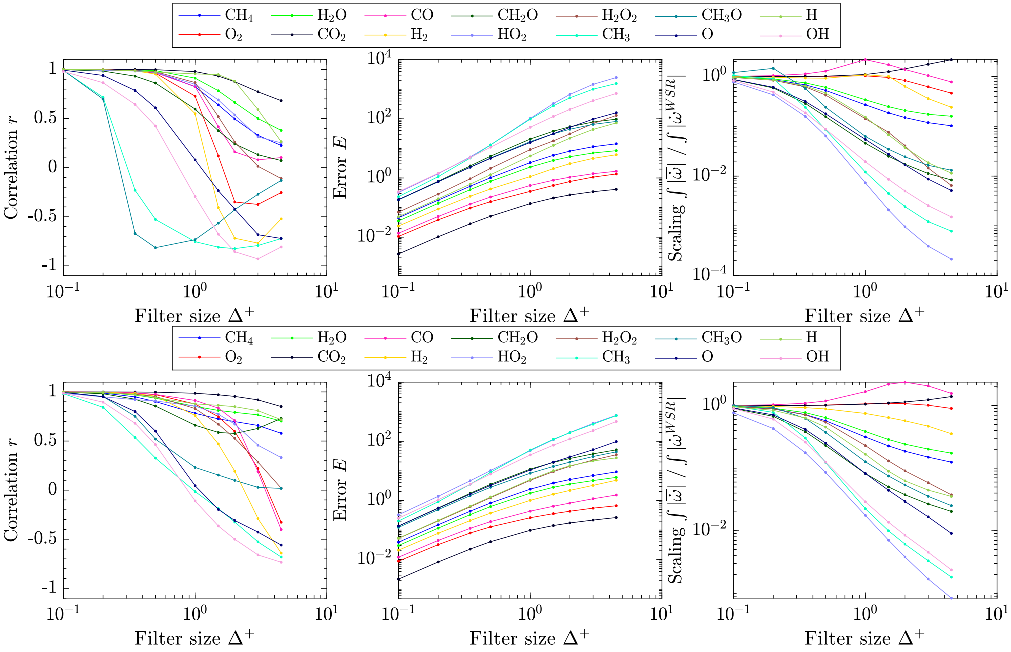

Figure 5.3: Correlation coefficient, error and scaling of the net reaction rate from the WSR model for different species. The top row shows case A1 (low Ka) and the bottom row case A4 (high Ka).

provided by the WSR model. Due to the large errors in WSR rates, the existing chemical states would start to move away from their correct locations in the chemical state space. This can be visualized in terms of the chemical state manifolds. In a premixed flame all the accessed states Y_α in the chemical state space lie on a low-dimensional manifold that connect the unburned and burned state [65]. In a filtered flame, where the filter is larger than the smallest flame structures, the filtered states $\widetilde{Y}_\alpha$ form a different manifold between the burned and unburned states. This manifold of filtered states is different from the unfiltered one because of the combination of the smearing property of the filter and the layered structure of the flame, which together results in overlap of species in the filtered flame that do not overlap in the unfiltered flame. When the WSR rate of Eq. (5.1) is used, the filtered chemical states are bound to rapidly and incorrectly move towards the manifold of an unfiltered flame (the large magnitudes of certain rates observed in Figs. 5.1 indicate that this is indeed what happens). A new equilibrium state would eventually be settled but how accurate this state will be in terms of both species mass fractions and global properties such as flame speed cannot be determined by an *a priori* analysis. The errors in the reaction rates and the above discussion only tells that the new chemical sates will be different from those in the filtered DNS.

5.2 Presumed PDF modelling

The topic of paper 3 is modelling of the filtered reaction rate term in the c-equation, Eq. (2.14), with a presumed PDF approach. The methodology that is discussed is based on two assumptions: that the local reaction rate is a function of only c, $\dot{\omega}_c = \dot{\omega}_c(c)$, and that the sub-filter distribution of c follows a presumed functional form parametrized by its mean and variance. The relevant theory and some of the key results are outlined in sections 5.2.1 and 5.2.2. The model approach depends on the sub-filter variance. The transport equation for sub-filter variance, which is the topic of paper 2, is discussed in the final section 5.2.3.

5.2.1 Sub-filter PDF

In filtered scalar fields, the smallest scales are not resolved and statistical measures of the unresolved (or sub-filter) distribution, such as the variance, are therefore useful in the formulation of model closures. Before discussing the reaction rate model in detail, the sub-filter probability density function (PDF) is introduced. The name filtered density function (FDF) is sometimes used instead to emphasize the connection to the filter.

The filter operation is, as mentioned before, defined as a convolution product of the unfiltered variable, for example $c(\mathbf{x}, t)$, and a normalized filter kernel G. If G is non-zero on Ω then the filtered $\overline{c}(\mathbf{x}, t)$ is defined by

$$\overline{c}(\mathbf{x}, t) = \int_\Omega G(\mathbf{r}) c(\mathbf{x} - \mathbf{r}, t) \, \mathrm{d}\mathbf{r} \tag{5.5}$$

The sub-filter PDF is a distribution $P(c = \varsigma; \mathbf{x}, t)$ that describes how much $c = \varsigma$ has contributed to the filtered value $\overline{c}(\mathbf{x}, t)$. Formally the PDF can be introduced in a fine-grained sense as [66–68]

$$P(\varsigma; \mathbf{x}, t) = \int_\Omega G(\mathbf{r}) \delta(c(\mathbf{x} - \mathbf{r}, t) - \varsigma) \, \mathrm{d}\mathbf{r} \tag{5.6}$$

where δ is the Dirac delta-function. In this work the filter kernel is always a normal distribution,

$$G(\mathbf{r}) = \left(\frac{6}{\pi \Delta^2}\right)^{-\frac{1}{2}} \exp\left(-6 \frac{|\mathbf{r}|^2}{\Delta^2}\right) \tag{5.7}$$

where Δ is the filter width. The first moment of the PDF recovers the filtered variable:

$$\int_0^1 \varsigma P(\varsigma; \mathbf{x}, t) \, \mathrm{d}\varsigma = \int_\Omega G(\mathbf{r}) \int_0^1 \varsigma \delta(c(\mathbf{x} - \mathbf{r}, t) - \varsigma) \, \mathrm{d}\varsigma \mathrm{d}\mathbf{r} = \overline{c}(\mathbf{x}, t) \tag{5.8}$$

In LES, only the Favre filtered $\tilde{c}(\mathbf{x}, t)$ is available and, for the purpose of modelling, it will be necessary to use a Favre PDF. This is defined as

$$\widehat{P}(\varsigma;\mathbf{x},t) = \int_\Omega \frac{\rho(\mathbf{x}-\mathbf{r},t)G(\mathbf{r})}{\overline{\rho}(\mathbf{x},t)}\delta(c(\mathbf{x}-\mathbf{r},t)-\varsigma)\,\mathrm{d}\mathbf{r} \tag{5.9}$$

$$= \int_\Omega \widehat{G}(\mathbf{r},\mathbf{x},t)\delta(c(\mathbf{x}-\mathbf{r},t)-\varsigma)\,\mathrm{d}\mathbf{r} \tag{5.10}$$

where the modified filter kernel $\widehat{G}$ has been introduced. Again, the first moment recovers the filtered variable, this time $\tilde{c}(\mathbf{x},t)$:

$$\int_0^1 \varsigma\widehat{P}(\varsigma;\mathbf{x},t)\,\mathrm{d}\varsigma = \int_\Omega \frac{\rho(\mathbf{x}-\mathbf{r},t)G(\mathbf{r})}{\overline{\rho}(\mathbf{x},t)}\int_0^1 \varsigma\delta(c(\mathbf{x}-\mathbf{r},t)-\varsigma)\,\mathrm{d}\varsigma\mathrm{d}\mathbf{r} = \tilde{c}(\mathbf{x},t) \tag{5.11}$$

5.2.2 Reaction rate modelling by presumed PDF and flamelet tabulation

In paper 3 a model for $\overline{\dot{\omega}_c}$ within the framework of LES is studied. It is representative for a class of statistical models for premixed combustion that has been discussed and applied in many previous studies, from early developments [69–71] to more recent works [72–78].

The model is first expressed for the simple case of single-step chemistry where both $\dot{\omega}_c$ and T are only dependent on c. The idea of the model is to use an approximate form of the sub-filter PDF, $P(\varsigma;\mathbf{x},t)$, to compute an approximation for the filtered reaction rate $\overline{\dot{\omega}_c}$ as

$$\overline{\dot{\omega}_c}(\mathbf{x},t) = \int_0^1 \dot{\omega}_c(\varsigma)P(\varsigma;\mathbf{x},t)\,\mathrm{d}\varsigma. \tag{5.12}$$

For modelling convenience this expression has to be rewritten in terms of the Favre PDF. This can be done using the relation $\overline{\dot{\omega}_c} = \overline{\rho}\widetilde{\dot{\omega}_c/\rho}$ and results in

$$\overline{\dot{\omega}_c}(\mathbf{x},t) = \overline{\rho}(\mathbf{x},t)\int_0^1 \frac{\dot{\omega}_c(\varsigma)}{\rho(\varsigma)}\widehat{P}(\varsigma;\mathbf{x},t)\,\mathrm{d}\varsigma. \tag{5.13}$$

Finally the Favre PDF is approximated with a β-distribution parametrized by its mean and variance, which yields

$$\overline{\dot{\omega}_c}(\mathbf{x},t) \approx \overline{\rho}(\mathbf{x},t)\int_0^1 \frac{\dot{\omega}_c(\varsigma)}{\rho(\varsigma)}P_\beta\left(\tilde{c}(\mathbf{x},t),\sigma^2(\mathbf{x},t)\right)\,\mathrm{d}\varsigma. \tag{5.14}$$

Here, $\sigma^2 = \widetilde{cc} - \tilde{c}\tilde{c}$ is the sub-filter variance. The model is complete if an estimate for σ^2 can be provided, and that is the topic of paper 2 and of section 5.2.3. In Fig. 5.4 a comparison is made between the actual sub-filter PDF extracted from DNS (and averaged over all data points with $\tilde{c} = 0.5$) and the corresponding β-distribution with σ^2 taken as the average from the DNS data. It appears from the figure that the β-distribution does represent the functional form of the PDF quite well given the appropriate value of σ^2. Whether or not this is good enough to accurately predict $\overline{\dot{\omega}_c}$ is, however, a different question.

In paper 3 the discussion is centred around the following two questions:

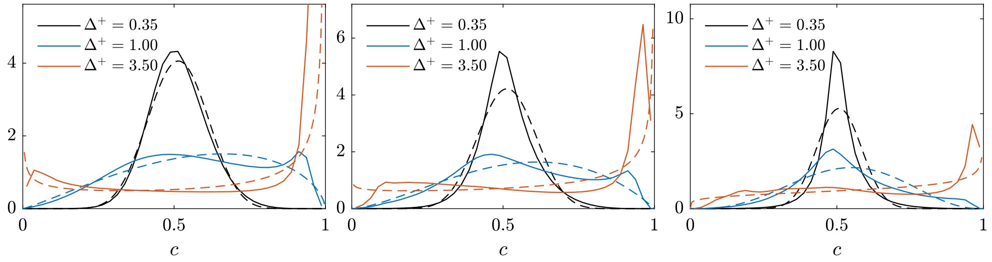

Figure 5.4: Sub-filter PDFs of c for three flames with different Karlovitz numbers. The PDFs have been averaged over many data samples with the same filtered value $\tilde{c} = 0.5$.

- How well does the presumed PDF approach work in cases where the flamelet assumption holds?
- How well can a flame with multi-step chemistry be modelled using the presumed PDF approach and a complementary flamelet assumption that provides the value of $\dot{\omega}_c/\rho$ as function of c?

The DNS data set 2, summarized in table 3.2, contains cases that fulfil all constraints of Eq. (5.14). Specifically, case D1 is used to investigate the first question. For the second question, more complex flames from data set 1 are used. For these multi-species flames a representative reaction progress variable c needs to be constructed and there are many possible choices. Further, in order to use Eq. (5.14) an additional model assumption is needed, namely that the local value of $\dot{\omega}_c/\rho$ depends only on c. Note that the validity of this assumption will depend on the choice of c. It is also convenient to select a c that has a transport equation of the form of Eq. (2.4), which can be achieved by making c a linear function of either temperature or a product or reactant species mass fraction. Finally, the value of $\dot{\omega}_c/\rho$ as function of c is provided by a one-dimensional steady flame simulation (a flamelet). The name 'flamelet assumption' in this work pertains to the assumption that $\dot{\omega}_c/\rho$ depends only on c and is provided by a flamelet calculation.

One of the main advantages of a model with the form of Eq. (5.14) is that the integral on the right hand side can be pre-computed and tabulated as a function of c and σ^2. The computational cost of using the model is therefore low since chemical reaction rates need not be evaluated at runtime of a LES. Note also that all flames under consideration here are adiabatic and have constant pressure and equivalence ratio. However, it is straightforward to extend Eq. (5.14) by adding for example unburned temperature, $T_u(\mathbf{x}, t)$, as an additional dependency for $\dot{\omega}_c/\rho$, and is accounted for by an extra dimension in the table. Such complications will however not be considered further in this work.

In cases with multi-step chemistry one has to make a choice of the definition of the reaction progress variable as mentioned earlier. Different definitions may be more or less suitable to use in the presumed PDF framework. The effect of different choices of c has not been studied in detail in this work but Fig. 5.5 shows how the sub-filter PDF can differ

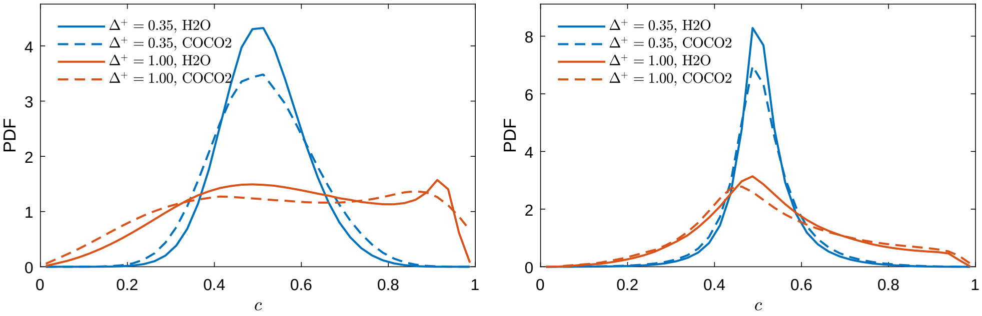

Figure 5.5: Sub-filter PDFs of c using two different definitions of c and for two filter sizes. Left and right shows case A1 and A4, respectively.

when the definition is changed. Here, c has been based on H_2O (as in the paper) and on CO_2 for comparison. The difference is significant and it is possible that the distribution of some progress variables can be fitted better with a β-distribution than others. Further investigation of this should be performed.

Selected joint PDFs of the exact reaction rate $\overline{\dot{\omega}_c}$ from filtered DNS and modelled ones computed from Eq. (5.14) are shown in Fig. 5.6. Three filter sizes ($\Delta^+ = 0, 0.35$ and 2) and three cases (D2, A3 and A4) are shown. For the single-step chemistry case D2 the model is exact when the filter size is zero, but as the filter size is increased the scatter is seen to grow. In the two multi-step chemistry cases on the other hand the scatter is largest when $\Delta^+ = 0$ and decreases when the filter size is increased. This is related to the flamelet assumption and is further discussed in the paper where also the correlation between modelled and exact rates is studied. Finally one can observe some differences between the two cases A3 and A4 at small filter sizes. In case A3, which has the lower Ka, the scatter seems to be larger and two branches can be seen. It was found that the upper branch, which is farthest from the diagonal, corresponds to places near the burned side of the reaction zone and the model error here correlates with flame curvature. Such an effect is not seen in cases with higher Ka or in planar unstrained flames.

In paper 3 a correction factor is proposed for Eq. (5.14) based on the fact that filtering the flame does not affect the consumption speed. This provides a constraint that the model should fulfil. In one dimension this constraint can be written as

$$\int_{-\infty}^{\infty} \dot{\omega}(x)\, \mathrm{d}x = \int_{-\infty}^{\infty} \overline{\dot{\omega}}(x)\, \mathrm{d}x \tag{5.15}$$

which follows from the definition of the filter and the requirement that the filter kernel G is normalized. If $\overline{\dot{\omega}}$ is computed according to the model Eq. (5.14) the constraint may not be fulfilled, and can in fact be far from fulfilled for filter sizes larger than the flame thickness as shown in ref. [79] as well as in paper 3. In principle, the constraint can be imposed on the modelled $\overline{\dot{\omega}}$ from Eq. (5.14) by multiplying it with a correction factor, but that factor would be both time and case dependent. The method suggested is to compute the factor

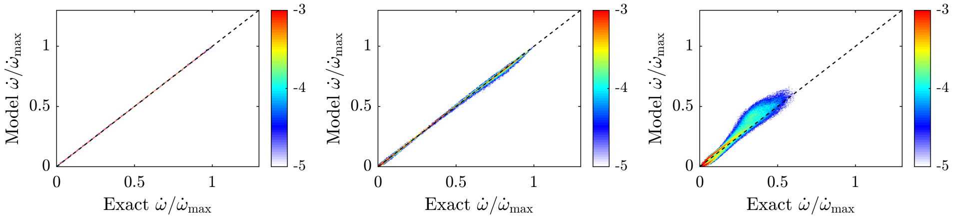

(**a**) Case D2, $\Delta^+ = 0$ (**b**) Case D2, $\Delta^+ = 0.35$ (**c**) Case D2, $\Delta^+ = 2$

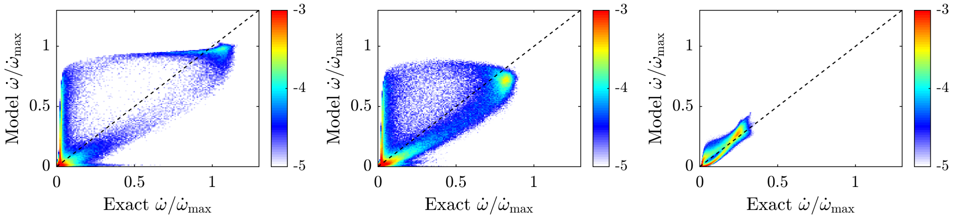

(**d**) Case A3, $\Delta^+ = 0$ (**e**) Case A3, $\Delta^+ = 0.35$ (**f**) Case A3, $\Delta^+ = 2$

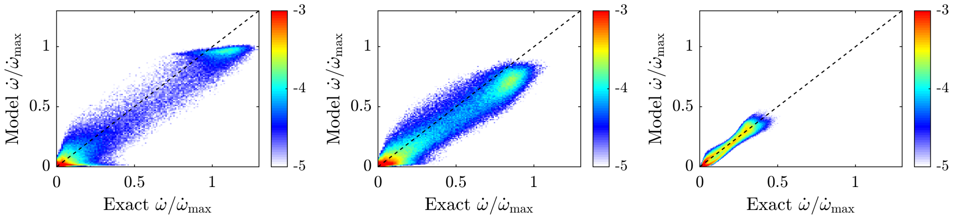

(**g**) Case A4, $\Delta^+ = 0$ (**h**) Case A4, $\Delta^+ = 0.35$ (**i**) Case A4, $\Delta^+ = 2$

Figure 5.6: Joint PDF of exact filtered reaction rate and modelled filtered reaction rate.

as a function of only filter size for a one-dimensional flame and then use that same factor for all cases. This will not impose the constraint exactly, but in most of the investigated cases it was found to significantly improve the model for filter sizes larger than δ_{th}. As an example, Fig. 5.7 shows the correction factor computed using single-step chemistry. The figure also shows the correlation coefficient between modelled and exact $\bar{\dot{\omega}}$ and a measure of the model error before and after scaling with the correction factor. The definition of this error metric is given by Eq. (5.2). As can be seen from the figure the correction factor is near 1 for $\Delta^+ < 1$ and smaller than 1 otherwise.

5.2.3 Sub-filter scalar variance

The sub-filter variance was introduced in the last section where it was used in the parametrization of the approximate PDF. Note that the two filtered variables $\bar{c}$ and $\tilde{c}$ have different associated variances, here referred to as s^2 and σ^2, respectively. The variance of a distribution, here the sub-filter distribution of c, is defined as the second central moment of

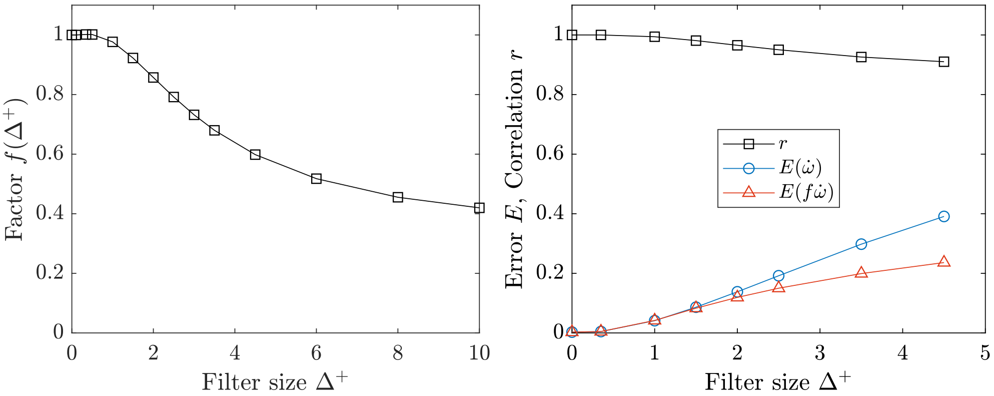

Figure 5.7: Left: Scaling factor computed with single-step chemistry. Right: Correlation coefficient (squares) and error of the model, with and without correction factor (triangles and circles) for case D1b.

the distribution function. This leads to the following formulas for the two variances [68]:

$$s^2(\mathbf{x},t) = \int_0^1 \left(\bar{c}(\mathbf{x},t) - \varsigma\right)^2 P(\varsigma;\mathbf{x},t)\,\mathrm{d}\varsigma = \overline{c(\mathbf{x},t)^2} - \bar{c}(\mathbf{x},t)^2 \tag{5.16}$$

and

$$\sigma^2(\mathbf{x},t) = \int_0^1 \left(\tilde{c}(\mathbf{x},t) - \varsigma\right)^2 \hat{P}(\varsigma;\mathbf{x},t)\,\mathrm{d}\varsigma = \widetilde{c(\mathbf{x},t)^2} - \tilde{c}(\mathbf{x},t)^2 \tag{5.17}$$

The sub-filter variance is often referred to as the sub-grid scale (SGS) variance in the context of LES and this naming convention is used in papers 2 and 3.

In the case of conserved scalars (no source terms) there exist algebraic models for the variance. By assuming local equilibrium between production and dissipation of variance [80] a model of the form

$$s^2 = C\Delta^2|\nabla c|^2 \tag{5.18}$$

can be obtained. However, this type of model may not be suitable for reactive scalars if the reaction is found to have a significant effect on the variance [73]. An alternative modelling approach, one that avoids the equilibrium assumption, is to solve an approximate transport PDE for σ^2. Such equations have been discussed extensively in the literature for non-reactive scalars in the context of LES, see for example refs. [26, 68] and references therein. For reactive scalars, such as c, most of the literature has this far been focused on the RANS context [19, 81, 82] and only few studies exist for LES [73]. In the following, an outline of the derivation of the σ^2-equation for LES is given. This equation and the modelling of some of its terms is the topic of paper 2.

Starting from the unfiltered c-equation, Eq. (2.7), an equation for $\widetilde{c^2}$ is obtained by first multiplying with c and then applying the unweighted filter to all terms. This yields

$$\begin{aligned}\frac{\partial \overline{\rho}\widetilde{c^2}}{\partial t} + \frac{\partial \overline{\rho}\tilde{u}_i\widetilde{c^2}}{\partial x_i} = 2\overline{\dot{\omega}_c c} + \frac{\partial}{\partial x_i}\left(\overline{\rho}\widetilde{D\frac{\partial c^2}{\partial x_i}}\right) - 2\overline{\rho}\widetilde{D\frac{\partial c}{\partial x_i}\frac{\partial c}{\partial x_i}} \\ -\frac{\partial}{\partial x_i}\left(\overline{\rho}\widetilde{u_i c^2} - \overline{\rho}\tilde{u}_i\widetilde{c^2}\right)\end{aligned} \tag{5.19}$$

Similarly, staring from the filtered c-equation, Eq. (2.14), and multiplying by $\tilde{c}$ gives

$$\frac{\partial \overline{\rho}\tilde{c}^2}{\partial t} + \frac{\partial \overline{\rho}\tilde{u}_i\tilde{c}^2}{\partial x_i} = 2\overline{\dot{\omega}_c}\tilde{c} + 2\tilde{c}\frac{\partial}{\partial x_i}\left(\rho D\frac{\partial c}{\partial x_i}\right) - 2\tilde{c}\frac{\partial}{\partial x_i}\left(\overline{\rho}\widetilde{u_i c} - \overline{\rho}\tilde{u}_i\tilde{c}\right) \tag{5.20}$$

Subtracting Equations (5.19) and (5.20) gives after simplification

$$\begin{aligned}\underbrace{\frac{\partial \overline{\rho}\sigma^2}{\partial t}}_{T_1} + \underbrace{\frac{\partial \overline{\rho}\tilde{u}_i\sigma^2}{\partial x_i}}_{T_2} = \underbrace{2(\overline{\dot{\omega}_c c} - \overline{\dot{\omega}_c}\tilde{c})}_{T_{\text{chem}}} \underbrace{-2\overline{\rho}\left(\widetilde{D\frac{\partial c}{\partial x_i}\frac{\partial c}{\partial x_i}} - \tilde{D}\frac{\partial \tilde{c}}{\partial x_i}\frac{\partial \tilde{c}}{\partial x_i}\right)}_{T_{\text{diss}}} \\ + \underbrace{\frac{\partial}{\partial x_i}\left(\overline{\rho}\widetilde{D\frac{\partial c^2}{\partial x_i}} - \overline{\rho}\tilde{D}\frac{\partial \tilde{c}^2}{\partial x_i}\right) + 2\tilde{c}\frac{\partial}{\partial x_i}\left(\overline{\rho}\tilde{D}\frac{\partial \tilde{c}}{\partial x_i} - \overline{\rho}\widetilde{D\frac{\partial c}{\partial x_i}}\right)}_{T_{\text{diff}}} \\ \underbrace{-\frac{\partial}{\partial x_i}\left(\overline{\rho}\widetilde{u_i c^2} - \overline{\rho}\tilde{u}_i\widetilde{c^2}\right) + 2\frac{\partial}{\partial x_i}\left(\overline{\rho}\widetilde{u_i c}\tilde{c} - \overline{\rho}\tilde{u}_i\tilde{c}^2\right)}_{T_{\text{tran}}} \underbrace{-2\frac{\partial \tilde{c}}{\partial x_i}\left(\overline{\rho}\widetilde{u_i c} - \overline{\rho}\tilde{u}_i\tilde{c}\right)}_{T_{\text{prod}}}\end{aligned} \tag{5.21}$$

The terms on the right hand side essentially represent, from left to right, reaction, dissipation, diffusion, sub-filter transport and production. Due to the use of density-weighted filtering, however, this description of the terms is not entirely accurate. It has for example been found in paper 2 that the production term T_{diss} can be negative under certain conditions. However, the above designations are still used here for consistency with previous works [68, 73].

When deriving Eq. (5.21) the c-equation (2.7) was used as starting point. If the progress variable is instead defined from a species mass fraction in a multi-species simulation, the detailed diffusion term in Eq. (2.9) should be used in the derivation. It is straight-forward to modify Eq. (5.21) to account for the detailed diffusion term, resulting in a more lengthy expression for T_{diff}. For the progress variable based on H_2O used for the methane/air flames in paper 2 the difference was found to be negligible as seen in Fig. 5.8a where the combined diffusion and dissipation term $T_{\text{diff+diss}}$ from Eq. (5.21) is compared with $T^*_{\text{diff+diss}}$ which is computed using the detailed diffusion term, both extracted from case B3. As demonstrated by the figure, expression (5.21) can safely be used without modification also for multi-step chemistry flames. However, in cases where the mean molecular weight has large gradients or when the diffusivity of c differs significantly from the mixture average the detailed diffusion term might be needed. In such cases, detailed diffusion would also have to be accounted for in an LES model for T_{diff}.

As a verification that the numerical accuracy is sufficient, both the left and right hand sides of Eq. (5.21) are extracted and compared for one of the high Ka cases, B3. Figure 5.8b shows all the terms and there is a good match between the left hand side $T_1 + T_2$ (circles) and the right hand side (dots).

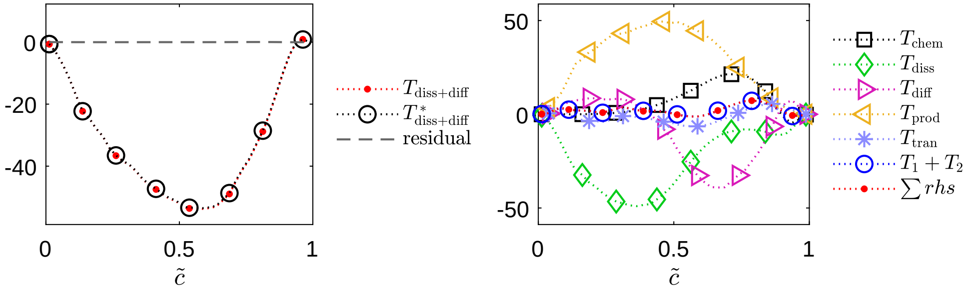

Figure 5.8: Sub-filter variance equation for case B3 using c based on H_2O mass fraction and using a filter size of $\Delta^+ = 0.35$. Left: Dots shows the combined diffusion and dissipation term computed according to Eq. (5.21) while circles shows the corresponding terms resulting when the full diffusion expression in Eq. (2.9) is used. The dashed line shows the difference. Right: Balance of all terms in Eq. (5.21).

In paper 2 it is discussed how the relative importance of the different terms changes with both filter size and with Karlovitz number. When Ka increases (for a fixed filter size) the variance equation tends to change from a balance of T_{chem}, T_{diss} and T_{diff} to a balance of T_{diss}, T_{tran} and T_{prod}. This is illustrated in Fig. 5.9 which shows all the terms on a two-dimensional cut for cases B1, B2 and B4. The most notable effect of the filter size is that the relative importance of the chemical term, T_{chem}, increases with increasing Δ. This trend was verified for Ka from 4 to 4100. It is thus the combination of Ka and Δ that determines whether T_{chem} is important. This is different from the situation in the RANS framework where there is no filter size and the chemical term will be small in the distributed reaction zone regime as discussed in ref. [82].

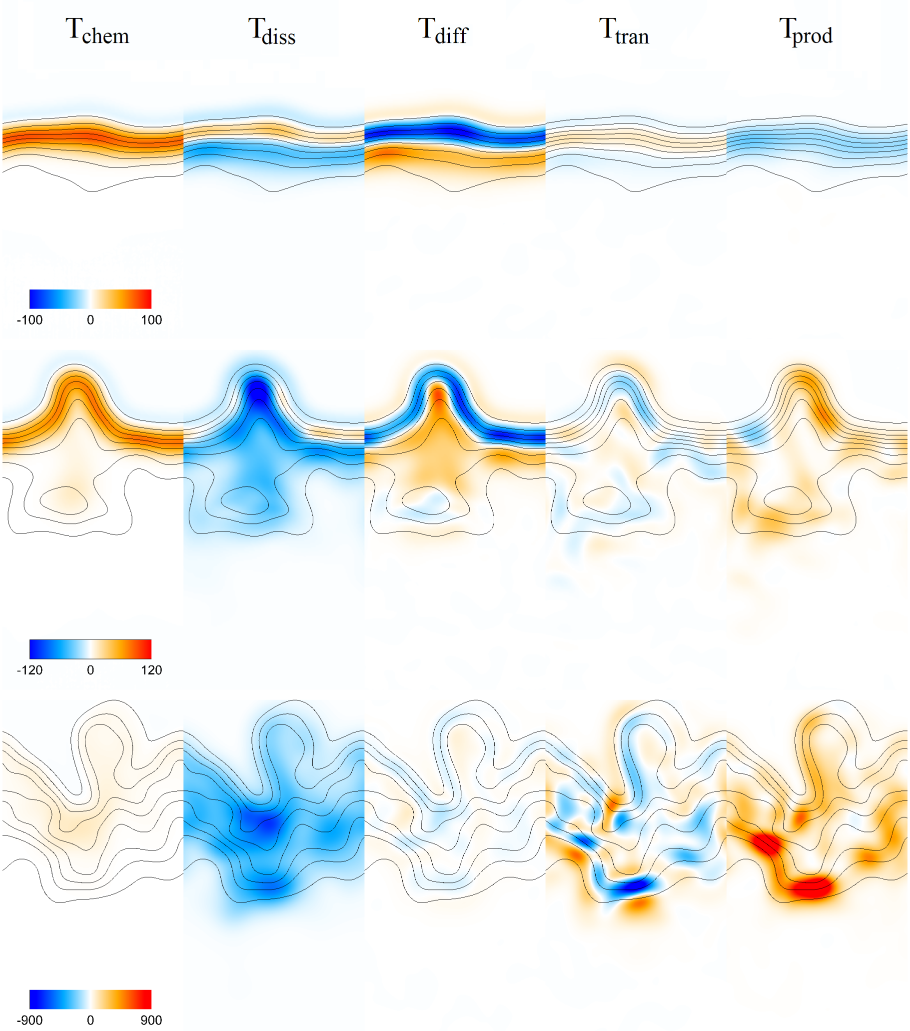

Figure 5.9: Terms in the sub-filter variance equation for cases B1 (top), B2 (middle) and B4 (bottom). The lines show iso-contours of c.

Chapter 6

Conclusions and future outlook

In this thesis direct numerical simulations of turbulent premixed flames have been studied. There have been two main goals of this work. The first goal was to deepen the understanding of turbulent premixed flames, in particular concerning the flame thickness and its evolution at high Karlovitz numbers. This is done in papers 1 and 4 which discuss both developing and statistically stationary flames, different metrics of flame thickness, how different definitions can lead to seemingly different conclusions, and how the evolution of thickness is related to different processes. The second goal of this work was to perform *a priori* investigations of models for turbulent premixed flames. This includes a study of a presumed PDF model for the reaction rate in the LES framework for flames of varying complexity, which was presented in paper 3. A study of the sub-filter variance transport equation, which is relevant for the aforementioned presumed PDF model, was presented in paper 2 and the modelling of certain terms in this equation was investigated. Some of the main conclusions of this thesis are:

- Distributed reaction zones are not observed near the traditionally predicted regime boundary $\mathrm{Ka}_\delta = 1$ for flames with significant heat release. The two-way coupling between flame and flow inhibits the turbulence intensity in the pre-heat layer, leading to a much lower effective Karlovitz number inside the reaction zone. For flames without heat release the traditional prediction appears to be more accurate.

- At high Karlovitz numbers, locally thin structures with large gradients are commonly found, even if the flame is broadened on average. This can have implications for modelling these flames, for example concerning the usefulness of the ’well-stirred reactor’ assumption at high Ka. Preferential alignment of the flame surface normal with the compressive strain rate eigenvector provides a mechanism for the formation of these structures.

- The transient evolution of a planar flame into a fully developed turbulent flame follows a trend of fast early thinning driven by compressive stretch, followed by a slower re-broadening process driven by diffusion. This trend is seen for all investigated turbulent flames, including a wide range of Karlovitz numbers, single- and multi-step chemistry and with and without heat release.

- The presumed PDF model with flamelet assumption, applied to model the reaction rate of premixed flames in LES, shows a strong dependency on filter size. The model error also relates to the filter size and can, in many cases, be reduced by a simple filter size dependent correction factor.

- After filtering DNS data it was seen that the unstrained flamelet assumption works better at very high Karlovitz numbers (> 500) than at moderate Karlovitz numbers (< 100). The effect seems to be related to inability of strain and curvature to change the flame structure when the turbulent time scale is very small.

- Based on the above conclusions, it may be possible to apply flamelet based LES models at Karlovitz number well above the traditionally predicted transition to the distributed reaction zone regime. This is also supported by the *a priori* analysis in paper 3.

- In the sub-filter variance equation the relative importance of the chemical term decreases with Ka as expected, but it also increase with filter size. The chemical term can therefore not be neglected based only on considerations of the Karlovitz number without accounting for the filter size.

From here there are many questions that deserve further investigation and can be potential topics of future work. There has recently been an increasing interest in DNS of highly turbulent premixed flames in the literature with many published studies. Chemistry-wise these studies cover a wide range including single-step chemistry at varying Karlovitz and Zeldovich numbers, hydrogen, methane and more complex fuels, and varying Lewis numbers. Concerning the type of turbulence generation most studies have used either homogeneous isotropic turbulence forcing (as was done in this work) or shear turbulence generated from a fuel/air jet. A topic that might deserve attention is a systematic study of the interaction between flames and non-isotropic turbulence which can be generated in a well-controlled way by use of anisotropic forcing. This topic can be of interest, in particular from a modelling perspective, since the turbulence experienced by flames in many practical applications is not isotropic.

The study of the displacement speed evolution equation briefly mentioned in section 4.3 is only just started. Further analysis of this equations, and its decomposition into evolution equations for the reaction, curvature and normal diffusion components, is straightforward to perform and can form a basis for further studies. Such investigations might lead to new insights into flame propagation that can guide the design of models.

On the modelling part, the natural path to extend this work is to perform an *a posteriori* analysis of the presumed PDF model with the studied closure for reaction rate (with and without correction factor) and the terms in the variance equation. Some LES of experimental flames have already been published with the modelling strategy [73] but to bridge the gap between practical LES and the *a priori* analysis performed in this work it is suggested that the same cases be simulated both in DNS and with various model closures in LES. In order to provide a good test environment the LES should use the exact same case set-up and numeric schemes as the DNS. Such a study would allow not only instantaneous values and conditional averages of various modelled terms to be compared, but also global properties such as mean turbulent flame speed and flame brush thickness. Further, it was found in paper 2 that the production term in the variance equation was difficult to model, so analysis of alternative models or development of a new model for that term will be of particular relevance.

On the wider topic of combustion research, we are still lacking a complete regime diagram for premixed flames. If a new regime diagram could be constructed which accounts for all relevant parameters in a pure premixed flame, including length or time scale ratios, Lewis number, density ratio, Zeldovich number and possibly Mach number, it might be a significant addition to the general understanding of flame-turbulence interaction. For such work DNS will be a suitable tool due to its flexibility when it comes to adjusting parameters independently of each other.

Chapter 7

Summary of publications

Paper i: Structures of turbulent premixed flames in the high Karlovitz number regime – DNS analysis

T. Nilsson, H. Carlsson, R. Yu, X. S. Bai
Fuel 216 (2018), pp. 627–638

This paper discusses the structure of methane/air flames at moderate and high Karlovitz numbers, and the focus is on the transient development from an initially planar flame to a distorted turbulent flame. The thickness of the flames is quantified by different metrics and a trend of early thinning followed by slow re-broadening is seen for all flames. It was seen that local regions with large gradients exist even at very high Karlovitz numbers. The evolution equation for the local gradient magnitude is studied and the balance of terms is seen to be affected by the Karlovitz number. Finally, the alignment between the flame surface normal vector and the eigenvectors of the strain rate tensor is studied and the alignment was found to change when the Karlovitz number is increased.

The candidate performed the analysis and wrote the manuscript with advice from the co-authors. Simulations were performed by H.C.

Paper ii: A priori analysis of sub-grid variance of a reactive scalar using DNS data of high Ka flames

T. Nilsson, I. Langella, N. A. K. Doan, N. Swaminathan, R. Yu, X. S. Bai
Accepted for publication in Combust. Theory Model. (2019)

A transport equation for sub-filter variance in the LES framework was analysed using DNS data. It was found that the relative importance of many of the terms in the equation are dependent on LES filter size. In particular, the chemical term gains importance with increasing filter size, a conclusion that is supported both by the DNS data and an order-of-magnitude analysis of the terms. Some model closures were also evaluated for the chemical, turbulent production and dissipation terms. Two models were tested for the dissipation term; a simple linear relaxation model, developed for non-reactive scalars and an alternative model that accounts for the reactive nature of the progress variable. The former model was found to under-predict the dissipation term by an order of magnitude. Additionally, the production term was found to be difficult to model and its importance increases with increasing Karlovitz number.

The candidate performed the simulations and most of the analysis. The candidate wrote the manuscript with input from the co-authors. I.L. contributed significantly to the order-of-magnitude analysis.

Paper III: Filtered reaction rate modelling in moderate and high Karlovitz number flames: an a priori analysis

T. Nilsson, R.Yu, N. A. K. Doan, I. Langella, N. Swaminathan, X. S. Bai
Submitted to Flow Turbulence Combust. (2019)

A presumed PDF approach with flamelet assumption was investigated for modelling the filtered reaction rate of the progress variable in LES of premixed flames. The model uses a one-dimensional flamelet to represent the reaction rate as function of the local progress variable, and a beta-distribution is used to model the sub-filter PDF. A set of flames of varying complexity was used for the analysis, including one-dimensional laminar and three-dimensional turbulent flames, single-step and multi-step chemistry, and a range of Karlovitz numbers. It was found the in flames with single-step chemistry the model error increases monotonously with increasing filter size, while in multi-step chemistry flames non-monotonic behaviour was found. A correction factor was proposed to make the model consistent with the laminar flame speed in the limit of a one-dimensional planar flame, and this was seen to reduce the model error in most cases.

The candidate performed the simulations and the analysis. The manuscript was written by the candidate with input from the other co-authors.

Paper IV: On thinning/broadening in turbulent premixed reaction waves

R.Yu, **T. Nilsson**, X. S. Bai, A. N. Lipatnikov
Submitted to Combust. Flame (2019)

DNS simulations were used to analyse flame thickness and its transient evolution. Three different metrics of surface-averaged flame thickness are defined. Equations that describe the time evolution of these averages have recently been published. In this paper, these equations are used to quantitatively analyse the contributing effects of stretch, self-propagation and volume dilatation on the evolution of the thickness metrics. It was found that, in some cases, it is possible to obtain opposite trend regarding if the flame is thinned or broadened depending on which metric is used. Findings also show that transient flames, developing from initially planar to fully developed turbulent, undergo an early stage of rapid thinning related to flow stretch, followed by a later stage of slow re-broadening driven by diffusion related processes. Further, it was also found that the volume dilatation can have a significant effect on the balance in the thickness equations for with heat release, but this effect was also seen to diminish as the Karlovitz number was increased.

The candidate performed the simulations of all flames with variable density (cases D, E, F, G) and R.Y. performed the simulation of the constant density reaction wave (case C). The candidate contributed to the analysis as well as to the writing of the manuscript. R.Y. and A.N.L. performed most of the theoretical derivations related to surface averages.

References

[1] R.H. Pletcher, J.C. Tannehill, and D. Anderson. *Computational Fluid Mechanics and Heat Transfer, Third Edition*. Taylor & Francis, 2012.

[2] Röpke, F. K. and Hillebrandt, W. “Full-star type Ia supernova explosion models”. In: *A&A* 431 (2005), pp. 635–645.

[3] S. B. Pope. *Turbulent Flows*. Cambridge: Cambridge University Press, 2000.

[4] A. J. Aspden. “A numerical study of diffusive effects in turbulent lean premixed hydrogen flames”. In: *Proc. Combust. Inst.* 36 (2017), pp. 1997–2004.

[5] R Borghi. “On the Structure and Morphology of Turbulent Premixed Flames”. In: *Recent Advances in the Aerospace Sciences*. Ed. by Corrado Casci and Claudio Bruno. 1985, pp. 117–138.

[6] F. A. Williams. *Combustion Theory*. 2nd ed. The Benjamin/Cummins Publishing Company Inc., 1985.

[7] R. Borghi. “Turbulent combustion modelling”. In: *Prog. Energy Combust. Sci.* 14 (1988), pp. 245–292.

[8] N. Peters. “Laminar flamelet concepts in turbulent combustion”. In: *Symposium (International) on Combustion* 21 (1988), pp. 1231 –1250.

[9] N. Peters. “The turbulent burning velocity for large-scale and small-scale turbulence”. In: *Journal of Fluid Mechanics* 384 (1999), pp. 107–132.

[10] T. Poinsot, D Veynante, and S Candel. “Quenching Processes and Premixed Turbulent Combustion Diagrams”. In: *Journal of Fluid Mechanics* 228 (July 1991), pp. 561–606.

[11] R. Sankaran et al. “Response of flame thickness and propagation speed under intense turbulence in spatially developing lean premixed methane-air jet”. In: *Combust. Flame* 162 (2015), pp. 3294–3306.

[12] B. Savard, B. Bobbitt, and G. Blanquart. “Structure of a high Karlovitz n-C7H16 premixed turbulent flame”. In: *Proc. Combust. Inst.* 35 (2015), pp. 1377–1384.

[13] T. M. Wabel et al. “Measurements to determine the regimes of premixed flames in extreme turbulence”. In: *Proceedings of the Combustion Institute* 36 (2017), pp. 1809 –1816.

[14] T. Nilsson et al. “Structures of turbulent flames in the high Karlovitz number regime - DNS analysis”. In: *Fuel* 216 (2018), pp. 627–638.

[15] M.D. Smooke and V. Giovangigli. *Reduced Kinetic Mechanisms and Asymptotic Approximation for methane-air Flames*. Springer-Verlag, Berlin, 1991.

[16] H. Carlsson, R. Yu, and X. S. Bai. “Flame structure analysis for categorization of lean premixed CH4/air and H2/air flames at high Karlovitz numbers: Direct numerical simulation studies”. In: *Proc. Combust. Inst* 35 (2015), pp. 1425–1432.

[17] S. B. Pope. “Small scales, many species and the manifold challenges of turbulent combustion”. In: *Proc. Combust. Inst.* 34 (2013), pp. 1–31.

[18] B. Fiorina, D. Veynante, and S. Candel. “Modeling combustion chemistry in large eddy simulation of turbulent flames”. In: *Flow Turbulence Combust.* 94 (2015), pp. 3–42.

[19] D. Veynante and L. Vervisch. “Turbulent combustion modeling”. In: *Progress in Energy and Combustion Science* 28 (2002), pp. 193–266.

[20] T. Echekki and E. Mastorakos. *Turbulent combustion modeling: Advances, new trends and perspectives*. Springer Netherlands, 2011.

[21] P. A. Libby and K.N.C. Bray. “Implications of the laminar flamelet model in premixed turbulent combustion”. In: *Combustion and Flame* 39 (1980), pp. 33 –41.

[22] K. C. N. Bray, P. A. Libby, and J. B. Moss. “Unified modeling approach for premixed turbulent combustion – part I: General formulation”. In: *Combust. Flame* 61 (1985), pp. 87–102.

[23] N. Peters. *Turbulent Combustion*. Cambridge University Press, 2000.

[24] H. Pitsch. “A consistent level set formulation for large-eddy simulation of premixed turbulent combustion”. In: *Combust. Flame* 143 (2005), pp. 587–598.

[25] V. Giovangigli. “Convergent iterative methods for multicomponent diffusion”. In: *IMPACT of Computing in Science and Engineering* 3 (1991), pp. 244–276.

[26] P. Sagaut and C. Meneveau. *Large Eddy Simulation for Incompressible Flows: An Introduction*. Springer, 2006.

[27] S. B. Pope. “Ten questions concerning the large-eddy simulation of turbulent flows”. In: *New Journal of Physics* 6 (2004), p. 35.

[28] R. Yu, J. Yu, and X. S. Bai. “An improved high-order scheme for DNS of low Mach number turbulent reacting flows based on stiff chemistry solver”. In: *J. Comp. Phys.* 231 (2012), pp. 5504–5521.

[29] G. S. Jiang and C. W. Shu. "Efficient Implementation of Weighted ENO Schemes". In: *Journal of Computational Physics* 126 (1996), pp. 202–228.

[30] R. Yu and X. S. Bai. "A semi-implicit scheme for large Eddy simulation of piston engine flow and combustion". In: *Int. J. Numerical Methods in Fluids* 71 (2013), pp. 13–40.

[31] G. Strang. "On the construction and comparison of difference schemes". In: *Siam J. on Num. Anal.* 5 (1968), pp. 506–517.

[32] O. M. Knio, H. N. Najm, and P. S. Wyckoff. "A Semi-implicit Numerical Scheme for Reacting Flow: II. Stiff, Operator-Split Formulation". In: *Journal of Computational Physics* 154 (1999), pp. 428 –467.

[33] P. N. Brown, G. D. Bryne, and A. C. Hindmarsch. "VODE, A variable-coefficient ODE solver". In: *Siam J. Sci. Stat. Comp.* 10 (1989), pp. 1038–1051.

[34] T. S. Lundgren. "Linearly Forced Isotropic Turbulence". In: *Annual Research Briefs* (2003), pp. 461–473.

[35] C. Rosales and C. Meneveau. "Linear forcing in numerical simulations of isotropic turbulence: Physical space Implementations and convergence properties". In: *Physics of Fluids* 17 (2005), pp. 1–8.

[36] V. Eswaran and S.B. Pope. "An examination of forcing in direct numerical simulations of turbulence". In: *Computers & Fluids* 16 (1988), pp. 257–278.

[37] R. Yu and N. Lipatnikov. "DNS study of dependence of bulk consumption velocity in a constant-density reacting flow on turbulence and mixture characteristics". In: *Phys. Fluids* 29 (2017), p. 065116.

[38] S. Ghosal et al. "A dynamic localization model for large-eddy simulation of turbulent flows". In: *J. Fluid Mech.* 286 (1995), pp. 229–255.

[39] H. Carlsson. "Detailed numerical simulations of turbulent premixed flames at moderate and high Karlovitz numbers". PhD thesis. Lund University, 2014.

[40] R. Yu and A. N. Lipatnikov. "Surface-averaged quantities in turbulent reacting flows and relevant evolution equations". In: *Submit. to Phys. fluids* (2019).

[41] L. Vervisch et al. "Surface density function in premixed turbulent combustion modeling, similarities between probability density function and flame surface approaches". In: *Phys. Fluids* 7 (1995), pp. 2496–2503.

[42] C. Dopazo et al. "Strain rates normal to approaching iso-scalar surfaces in a turbulent premixed flame". In: *Combust. Flame* 162 (2015), pp. 1729–1736.

[43] R. Sankaran et al. "Structure of a spatially developing turbulent lean methane-air Bunsen flame". In: *Proc. Combust. Inst.* 31 (2007), pp. 1291–1298.

[44] H. Wang et al. “Direct numerical simulations of a high Karlovitz number laboratory premixed jet flame – an analysis of flame stretch and flame thickening”. In: *J. Fluid Mech.* 815 (2017), pp. 511–536.

[45] F. Dinelacker et al. “Structure of locally quenched highly turbulent lean premixed flames”. In: *Proc. Combust. Inst.* 27 (1998), pp. 857–865.

[46] A. Soika, F. Dinkelacker, and A. Leipertz. “Measurement of the resolved flame structure of turbulent premixed flames with constant reynolds number and varied stoichiometry”. In: *Symposium (International) on Combustion*. 1. 1998, p. 785.

[47] D. Thévenin. “Three-dimensional direct simulations and structure of expanding turbulent methane flames”. In: *Proc. Combust. Inst.* 30 (2005), pp. 629–637.

[48] A. Y. Poludnenko and E. S. Oran. “The interaction of high-speed turbulence with flames: Global properties and internal flame structure”. In: *Combust. Flame* 162 (2010), pp. 995–1011.

[49] R. Sankaran et al. “Structure of a spatially developing turbulent lean methane-air Bunsen flame”. In: *Proc. Combust. Inst.* 1 (2007), p. 1291.

[50] A. J. Aspden, M. S. Day, and J. B. Bell. “Turbulence-flame interactions in lean premixed hydrogen: transition to the distributed burning regime”. In: *J. Fluid Mech.* 680 (2011), pp. 287–320.

[51] B. Zhou et al. “Development and application of CN PLIF for single-shot imaging in turbulent flames”. In: *Combust. Flame* 162 (2015), pp. 368–374.

[52] S. Lapointe, B. Savard, and G. Blanquart. “Differential diffusion effects, distributed burning, and local extinctions in high Karlovitz premixed flames”. In: *Combust. Flame* 162 (2015), pp. 3341–3355.

[53] A. W. Skiba et al. “Premixed flames subjected to extreme levels of turbulence part I: Flame structure and a new measured regime diagram”. In: *Combust. Flame* 189 (2018), p. 407.

[54] W. T. Ashurst et al. “Alignment of vorticity and scalar gradient with strain rate in simulated Navier-Stokes turbulence”. In: *Phys. Fluids* 30 (1987), pp. 2345–2353.

[55] N. Chakraborty and N. Swaminathan. “Influence of the Damköhler number on turbulence-scalar interaction in premixed flames. I. Physical insight”. In: *Phys. Fluids* 19 (2007), p. 045103.

[56] L. Cifuentes et al. “Local flow topologies and scalar structures in a turbulent premixed flame”. In: *Phys. Fluids* 26 (2014), p. 065108.

[57] R. Yu, T. Nilsson, and A. Lipatnikov. “Assessment of an evolution equation for the averaged displacement speed of a reaction scalar field”. In: *Submit. to 11th Mediterranean Combustion Symposium*. 2019.

[58] L. Cifuentes et al. “Analysis of flame curvature evolution in a turbulent premixed bluff body burner”. In: *Physics of Fluids* 30 (2018), p. 095101.

[59] O. Colin et al. “A thickened flame model for large eddy simulations of turbulent premixed combustion”. In: *Phys. Fluids* 12.2000 (2000), pp. 1843–1863.

[60] B. F. Magnussen. “On the Structure of Turbulence and a Generalized Eddy Dissipation Concept for Chemical Reaction in Turbulent Flow”. In: *19th AIAA Aerospace Science Meeting, St.Louis, Missouri* (1981).

[61] E. Giacomazzi, C. Bruno, and B. Favini. “Fractal modelling of turbulent combustion”. In: *Combust. Theory Model.* 4 (2000), pp. 391–412.

[62] M. Berglund et al. “Finite Rate Chemistry Large-Eddy Simulation of Self-Ignition in a Supersonic Combustion Ramjet”. In: *AIAA J.* 48 (2010), pp. 540–550.

[63] A.J. Aspden, N. Zettervall, and C. Fureby. “An a priori analysis of a DNS database of turbulent lean premixed methane flames for LES with finite-rate chemistry”. In: *Proc. Combust. Inst.* (2018).

[64] J. M. Bland and D. G. Altman. “Calculating correlation coefficients with repeated observations: Part 2—correlation between subjects”. In: *BMJ* 310 (1995), p. 633.

[65] U. Maas and S.B. Pope. “Simplifying chemical kinetics: Intrinsic low-dimensional manifolds in composition space”. In: *Combustion and Flame* 88 (1992), pp. 239 – 264.

[66] F. Gao and E. E. O’Brien. “A large-eddy simulation scheme for turbulent reacting flows”. In: *Physics of Fluids A: Fluid Dynamics* 5 (1993), pp. 1282–1284.

[67] S. B. Pope. “PDF methods for turbulent reactive flows”. In: *Prog. Energy Combust.* 11 (1985), pp. 119–192.

[68] C. Jimenez et al. “Subgrid scale variance and its dissipation of a scalar field in large eddy simulations”. In: *Phys. Fluids* 13 (2001), pp. 1748–1754.

[69] R. Borghi and P. Moreau. “Turbulent combustion in a premixed flow”. In: *Acta Astronautica* 4 (1977), pp. 321–341.

[70] D. Bradley et al. “Laminar flamelet modeling of recirculating premixed metahne and propane-air combustion”. In: *Combust. Flame* 71 (1988), pp. 109–122.

[71] A. W. Cook and J. J. Riley. “A subgrid model for equilibrium chemistry in turbulent flows”. In: *Phys. Fluids* 6 (1994), pp. 2868–2870.

[72] J. A. van Oijen et al. “State-of-the-art in premixed combustion modeling using flamelet generated manifolds”. In: *Progress in Energy and Combustion Science* 57 (2016), pp. 30–74.

[73] I. Langella and N. Swaminathan. “Unstrained and strained flamelets for LES of premixed combustion”. In: *Combust. Theory Model.* 20 (2016), pp. 410–440.

[74] P. Domingo, L. Vervisch, and D. Veynante. “Large-eddy simulation of a lifted methane jet flame in a vitiated coflow”. In: *Combust. Flame* 152 (2008), pp. 415–432.

[75] J. Floyd et al. “A simple model for the filtered density function for passive scalar combustion LES”. In: *Combust. Theory Model.* 13 (2009), pp. 559–588.

[76] S. Nambully et al. “A filtered-laminar-flame PDF sub-grid scale closure for LES of premixed turbulent flames. Part I: Formalism and application to a bluff-body burner with differential diffusion”. In: *Combust. Flame* 161 (2014), pp. 1756–1774.

[77] I. Langella, N. Swaminathan, and R. W. Pitz. “Application of unstrained flamelet SGS closure for multi-regime premixed combustion”. In: *Combust. Flame* 173 (2016), pp. 161–178.

[78] S. Lapointe and G. Blanquart. “A priori filtered chemical source term modeling for LES of high Karlovitz number premixed flames”. In: *Combust. Flame* 176 (2017), pp. 500–510.

[79] B. Fiorina et al. “A filtered tabulated chemistry model for LES of premixed combustion”. In: *Combustion and Flame* 157 (2010), pp. 465 –475.

[80] C. D. Pierce and P. Moin. “A dynamic model for subgrid-scale variance and dissipation rate of a conserved scalar”. In: *Physics of Fluids* 10 (1998), pp. 3041–3044.

[81] O. R. Darbyshire, N. Swaminathan, and S. Hochgreb. “The Effects of Small-Scale Mixing Models on the Prediction of Turbulent Premixed and Stratified Combustion”. In: *Combustion Science and Technology* 182 (2010), pp. 1141–1170.

[82] A. J. Aspden, M. S. Day, and J. B. Bell. “Turbulence–flame interactions in lean premixed hydrogen: transition to the distributed burning regime”. In: *J. Fluid Mech.* 680 (2011), pp. 287–320.

Paper 1

Structures of turbulent premixed flames in the high Karlovitz number regime - DNS analysis

Thommie Nilsson[a], Henning Carlsson[a], Rixin Yu[a], Xue-Song Bai[a]

[a]*Div. of Fluid Mechanics, Dep. of Energy Sciences, Lund University, Sweden*

Abstract

Lean premixed turbulent methane-air flames have been investigated using direct numerical simulations (DNS) for different Karlovitz numbers (Ka), ranging from 65 to 3350. The flames are imposed to a high intensity small-scale turbulent environment, corresponding to high Ka conditions, and the effect on the flame structure is investigated during the transition from initial laminar flame to highly distorted turbulent flame. The focus is on the internal structure of different sub-layers of these flames. The preheat layer, fuel consumption layer and oxidation layer are characterized by the distribution of formaldehyde, the fuel consumption rate and the CO consumption rate, respectively. Different measures that quantify sub-layer thickness for turbulent flames have been defined and analyzed. The flame brush is broadened with time while the local thickness (excluding large scale wrinkling) of all three layers initially show thinning due to the interaction of the flame with the turbulent flow field. As time passes, the local thickness of the preheat layer and fuel consumption layer are restored while the oxidation layer remains thinned due to suppression of CO consuming reactions. As Ka increases there is an increasing probability of finding thinned, large gradient regions in each of these sub-layers. The contribution to the evolution of flame thickness from normal strain rate, chemical reaction and normal and tangential diffusion is analyzed in terms of a gradient transport equation. The relative size of the terms changes as Ka increase and, in particular, the term due to chemical reactions loses its relative significance. The observed thinning of the local flame structure is attributed to the preferential alignment of the flame normal with the compressive strain rate eigenvectors. Such alignment provides a mechanism for the flame thinning, consistent with the behavior of non-reacting scalars. A preferred angle of about 20 degrees is observed between the flame normal and the compressive strain rate eigenvector.

Keywords: Direct numerical simulation, Turbulent premixed flames, Flame-turbulence interaction, High Karlovitz number

1. Introduction

The structure of a premixed flame is affected by its interaction with turbulence. Based on the Karlovitz number (Ka), which is the ratio of the characteristic time scale of chemical reactions to the smallest time scale of turbulence (the Kolmogorov time scale), turbulent premixed flames can be classified into different regimes [1–3]. In the laminar and corrugated flamelet regimes ($\mathrm{Ka} \leq 1$) the intensity of turbulence is low and the Kolmogorov length scale is larger than the thickness of a laminar flame; the inner structure of such a flame is similar to that of a laminar flame. This feature has been widely used in the development of models for simulation of turbulent premixed flames in the laminar flamelet regime [3, 4].

Premixed flames under the conditions of high intensity and small length scale turbulence, typically at high Ka, are commonly used in engineering combustion devices, e.g., in gas turbines and internal combustion engines. The structures of flames under these conditions are however less well understood. The thin reaction zones regime, where turbulence micro-scales are small enough to penetrate and perturb the preheat layer of the flame but not the reaction layer, is considered to occur for $1 < \mathrm{Ka} \lesssim 100$. At Ka well above 100 it is expected that turbulence micro-scales can penetrate also the reaction zone leading to distributed or broken reaction zones.

The small time and length scales in high Ka flames poses a great challenge to both experiments and numerical simulations due to the fine spatial and temporal resolution required. Planar laser induced fluorescence (PLIF) experiments of various species using fine resolution (< 50 μm), e.g. OH, and 2D temperature measurements [4–9], indicated that the structures of turbulent premixed hydrocarbon flames in the thin-reaction zone regime ($\mathrm{Ka} \sim 10$) are rather similar to those of laminar flames. At $\mathrm{Ka} \geq 100$ the structure of the flames can become highly distorted [10, 11] but the results are not always consistent. CH/HCO PLIF measurements indicated that the reaction zones in high Ka flames became significantly distorted and broadened [11] while other studies show that a layered flame structure still remains at $\mathrm{Ka} > 100$ [12, 13], indicating that the regime boundary between the thin and distributed reaction zone regimes is not as low as $\mathrm{Ka} = 100$ when based on upstream turbulence conditions. Thinning of the local flame structure has also been observed [14].

Due to the limitation of the spatial and temporal resolution (especially in measurements of turbulence using particle image velocimetry, PIV) and due to the 2D nature of most of todays experiments, direct numerical simulation (DNS) can play an important role in the further investigation of high Ka flames. DNS, however, is limited to small Reynolds numbers, i.e. only a narrow range of length scales in the vicinity of the flame thickness may be resolved. Thus, DNS studies of high Ka flames are restricted to use small integral length scales, typically a few times the laminar flame thickness. In experiments on the other hand the integral scale is usually related to the geometry and is considerably larger than the flame thickness. This means that for a DNS simulation to match the small scale turbulence-flame interaction (i.e. the Karlovitz number) of an experiment or application, the large scales have to be excluded. Consequently, when comparing with experiments, DNS should not be viewed as a simulation of an entire flame but rather as a zoom-in on a small segment of a larger flame. In this view, the turbulence forcing term usually applied in DNS should be seen as a model for the cascading of turbulent energy from larger scales.

Several authors have recently reported DNS of high Ka premixed flames [12, 15–32] and interesting phenomena have been observed. Typical ratios of integral length scale to thermal flame thickness of these studies range from 0.5 to 4, generally smaller for higher Ka, and turbulent Reynolds numbers range from around 50 to 400. Aspden et al. [24] showed that at high Ka conditions (Ka $\sim$ 400) the reaction zone is highly distorted and local phenomena such as differential diffusion becomes less important in a statistical sense. Carlsson et al. [15, 16] reported that the highly energetic small scale turbulence can transport the radicals (e.g. H) from the reaction zone to the low temperature unburned fuel/air region within the time scale of the radical recombination reactions. Such transport can give rise to a highly broadened zone with chemical reactions, e.g., radical recombination reactions, active even at temperatures as low as 500 K. Recent studies by Lapointe et al. [19, 20] of turbulent flame speed show that the turbulent flame speed at high Karlovitz numbers is determined by the turbulent to laminar area ratio just as it is for corrugated flamelets.

It has been shown for example by Ashurst et al. [33] that the normal of a passive scalar surface (a zero heat release flame) aligns preferentially with the most compressive principal strain rate (the eigenvector of the symmetric strain rate tensor that corresponds to the most negative eigenvalue). In the presence of strong heat release the flame normal aligns with the most extensive principal strain rate since the largest source of extensive strain is the thermal expansion. It is expected that, as u'/S_L increases, the thermal expansion becomes less dominating and the flame front will instead align with the compressive principal strain rate. Indeed, Chakraborty and Swaminathan [34] reported that at Ka $\sim$ 10 the flame surface normal starts to show preferential alignment with the most compressive principal strain rate eigenvector in the preheat layer. The preferential alignment with the compressive strain rate increases the scalar gradient (thinning of the flame) until balanced by the thickening processes. Thinning and thickening processes compete and it has been suggested that the balance of these processes varies with the combustion regime defined by the Damköhler and Karlovitz numbers [12, 18]. A balance equation can be derived for the scalar gradient magnitude [35] and applied to reactive scalars in a flame the equation can be used to investigate the thickening/thinning process. A few analyses of the involved terms have been reported [36, 28, 30].

In recent studies [15, 16] the responses of different intermediate species layers to high Ka were investigated and an attempt for global quantification by means of a species specific Karlovitz number was presented. However, systematic investigations of the successive variation of the structures of turbulent premixed flames under various Ka is needed to reconcile the different experimental and numerical results and hypotheses and to develop a better understanding of the structures of turbulent premixed flames.

In this work, DNS of turbulent premixed methane/air flames is carried out for Ka ranging from 65 to 3350. This regime is selected because of the trend in engineering applications towards high intensity and lean mixtures which results in high Karlovitz numbers. The focus of this work is on the not-so-well explored high Ka regime; typical Ka may not be higher than a few hundred in most current gas turbines but this may change in the future due to the use of ultra lean mixtures and alternative fuels like hydrogen or ammonia. Also, since a transition to distributed combustion is expected somewhere above Ka=100, we have considered a case well above Ka=100.

The focus of the analysis is on the interaction between the sub-layers of a flame and small-scale homogeneous isotropic turbulence, a process that is difficult to investigate experimentally. It is a study of the transient process of sub-layer structures of an initially laminar flame that is exposed to a high Ka turbulent environment. The sub-layers are the preheat layer, the inner layer and the oxidation layer. The flame thickness and gradient are important parameters for premixed flame modeling. To analyze the thickness of different sub-layers a quantitative measure is needed and it is non-trivial to define such a measure. Two different approaches to define sub-layer thickness are presented and employed. The variation of the thickness is then explained by means of a gradient transport equation and the preferential alignment of the flame normal with principal strain rate eigenvectors.

2. Analysis methods

2.1. Thickness measures for sub-layers

To identify the sub-layers of the flame, three layer markers are defined. The preheat layer is represented using the CH_2O mass fraction Y_{CH2O} [8, 19], the inner layer using the fuel consumption rate $\dot{\omega}_{\mathrm{CH4}}$ [3, 37], and the oxidation layer using the CO consumption rate $\dot{\omega}_{\mathrm{CO},c}$ [37]. In this work the CO consumption rate is defined from the CO consuming reactions only; reactions that produce CO are left out when computing $\dot{\omega}_{\mathrm{CO},c}$. For reversible reactions the forward and backward directions are considered as separate reactions. To quantify the widths of the sub-layers a "mean brush thickness" denoted by δ_B and a "conditional mean thickness" denoted by δ_V are defined. Both thickness measures are to be applied to all three layers.

Let ϕ be a layer marker, c a reaction progress variable and $\langle\cdot\rangle$ the volume-weighted spatial average of an instantaneous three-dimensional field. The conditional mean $\langle\phi \mid c\rangle$ for a simulated case is estimated by sorting data points into bins of suitable sizes. A reference value ϕ^* is defined as the maximum of the conditional mean, $\phi^* = \max\langle\phi \mid c\rangle$. A corresponding reference value of the progress variable, c^*, is defined at the location of ϕ^* in c-space such that $\langle\phi \mid c = c^*\rangle = \phi^*$. These reference values are used in the following thickness definitions.

The mean brush thickness of a layer, δ_B, is defined by averaging the layer marker in the cross-stream directions and measuring the width of the resulting profile at 1/10 of the peak value:

$$\delta_B = \int H(\langle\phi \mid x\rangle - 0.1\phi^*)dx \tag{1}$$

In Eq. (1) $H(x)$ is a Heaviside function defined by $H(x \geq 0) = 1$ and $H(x < 0) = 0$ and x is the stream-wise coordinate. The measure δ_B tells how broad region the wrinkled brush occupies. The threshold value, chosen as $0.1\phi^*$, is defined as a fraction of ϕ^* rather than in terms of laminar flame properties because of observed differences in the magnitude of layer markers when the Karlovitz number is varied. No qualitative difference was observed in the results if the factor 0.1 was changed to 0.5.

A volume-based conditional mean layer thickness, δ_V, is defined by comparing the volume of the layer with the area $A_{c=c^*}$ of the representative iso-surface defined by $c = c^*$:

$$\delta_V = \frac{\int_V H(\phi(\boldsymbol{x}) - 0.1\phi^*)dV}{A_{c=c^*}} \tag{2}$$

An iso-surface of the layer marker is not used in the definition of δ_V because the layer markers do not vary monotonically from unburned to burned mixtures; all markers have their peak value at intermediate c which would lead to a "double" iso-surface. Instead, the iso-surface defined by $c = c^*$ is used.

The conditional mean thickness, δ_V, measures the local layer broadening/thinning while excluding the wrinkling of the layer while the mean brush thickness, δ_B, represents the ensemble averaged mean thickness of the layer, including both the wrinkling and broadening/thinning of the layer.

2.2. Gradient transport equation

To analyze the local dynamics of flame thickness the gradient $|\nabla Y_k|$, where k is either a reactant or product species, is studied. A transport equation for $|\nabla Y_k|$ can be obtained [28, 36] and the relative importance of the contributing terms will be quantified. The starting point is the transport equation for the species mass fraction Y_k,

$$\frac{DY_k}{Dt} = \mathbb{D}_k + \frac{\dot{\omega}_k}{\rho} \tag{3}$$

Here, D/Dt is the material derivative, $\mathbb{D}$ is the diffusion rate and $\dot{\omega}_k$ is the reaction rate. The diffusion term, modeled using the Curtiss-Hirschfelder approximation and expressed in terms of mass fractions and using implicit summation over repeated i, is

$$\begin{aligned}\mathbb{D}_k = &\underbrace{\frac{1}{\rho}\frac{\partial}{\partial x_i}\left(\rho D_k \frac{\partial Y_k}{\partial x_i}\right)}_{F_1} + \underbrace{\frac{1}{\rho}\frac{\partial}{\partial x_i}\left(\rho D_k \frac{Y_k}{\overline{W}}\frac{\partial \overline{W}}{\partial x_i}\right)}_{F_2} \\ &\underbrace{-\frac{1}{\rho}\frac{\partial}{\partial x_i}\left(\rho Y_k \sum_{m=1}^{N_{sp}} D_m \frac{\partial Y_m}{\partial x_i}\right)}_{C_1} \underbrace{-\frac{1}{\rho}\frac{\partial}{\partial x_i}\left(\frac{\rho Y_k}{\overline{W}}\frac{\partial \overline{W}}{\partial x_i}\sum_{m=1}^{N_{sp}} Y_m D_m\right)}_{C_2}\end{aligned} \tag{4}$$

In Eq. (4) D_k is the diffusivity of species k and $\overline{W}$ is the mixture averaged molecular weight. The F_1 term is analogous to Fick's law for binary diffusion, the F_2 term appears due to gradients in the mean molecular weight and the C_1 and C_2 terms are minor corrections in the model and included to fulfill the constraint $\sum_k Y_k = 1$. Note that $F_2 = C_2$ if all diffusivities are equal.

Defining the iso-surface normal as $\mathbf{n} = -\nabla Y_k / |\nabla Y_k|$ the leading term F_1 of Eq. (4) can be separated into two contributions due to curvature and diffusion in the normal direction:

$$F_1 = \frac{1}{\rho}\frac{\partial}{\partial x_i}\left(\rho D_k \frac{\partial Y_k}{\partial x_i}\right) = -D_k |\nabla Y_k| \frac{\partial n_i}{\partial x_i} - \frac{1}{\rho}\frac{\partial}{\partial x_n}(\rho D_k |\nabla Y_k|) \tag{5}$$

The normal derivative is defined as $\partial\psi/\partial x_n = n_i \partial\psi/\partial x_i$ for any scalar field ψ.

By applying the gradient to Eq. (3) a balance equation for $|\nabla Y_k|$ can be derived. This equation can be written

$$\frac{D^*|\nabla Y_k|}{D^* t} = -|\nabla Y_k| \frac{\partial S_d}{\partial x_n} - |\nabla Y_k| a_N \tag{6}$$

In Eq. (6) the iso-surface following derivative $D^*\psi/D^*t = \partial\psi/\partial t + (u_i + S_d n_i)\partial\psi/\partial x_i$ has been introduced and it describes the rate of change in a point that moves with the combined velocity of the flow and the self-propagation of the iso-surface. The term $a_N = n_i S_{ij} n_j$ is the normal strain rate, $S_{ij} = (\partial u_i/\partial x_j + \partial u_j/\partial x_i)/2$ is the symmetric strain rate tensor and $S_d = (DY_k/Dt)/|\nabla Y_k|$ is the local displacement speed due to self-propagation of the iso-surface. Combining equations (3)-(6) the balance equation for $|\nabla Y_k|$ can be expanded as

$$\begin{aligned}\left(\frac{D^*|\nabla Y_k|}{D^* t}\right) = {} & \underbrace{|\nabla Y_k| \frac{\partial}{\partial x_n}\left(D_k \frac{\partial n_i}{\partial x_i}\right)}_{A_{curv}} + \underbrace{|\nabla Y_k| \frac{\partial}{\partial x_n}\left(\frac{1}{\rho|\nabla Y_k|}\frac{\partial}{\partial x_n}(\rho D_k |\nabla Y_k|)\right)}_{A_{norm}} \\ & \underbrace{-|\nabla Y_k| \frac{\partial}{\partial x_n}\left(\frac{\dot{\omega}_k}{\rho|\nabla Y_k|}\right)}_{A_R} \underbrace{-|\nabla Y_k| \frac{\partial}{\partial x_n}\left(\frac{F_2 - C_1 - C_2}{|\nabla Y_k|}\right)}_{A_{corr}} \underbrace{-|\nabla Y_k| a_N}_{A_N}\end{aligned} \tag{7}$$

According to Eq. (7) the gradient magnitude, and thus the distance between iso-surfaces, is governed by the five terms on the RHS: the flow normal strain rate term A_N, the curvature term A_{curv}, the normal diffusion term A_{norm}, the chemical reaction term A_R and finally the A_{corr} term that is due to gradients in $\overline{W}$ and the species conservation correction in the diffusion model. The time evolution of $|\nabla Y_k|$ and the relative importance of the terms will be investigated in section 4.3.

2.3. Alignment with principal strain rate eigenvectors

Further insight into the behavior of the normal strain rate a_N can be obtained by studying alignment of the flame normal with principal strain rate eigenvectors. The symmetrical strain rate tensor S_{ij} has three real eigenvalues. The smallest, largest and intermediate eigenvalues are referred to as λ_-, λ_+ and λ_2. In incompressible flow the corresponding eigenvectors can be referred to as the compressive, extensive and intermediate eigenvector, respectively. It is a well-known behavior that the gradient of non-reactive scalars aligns with the most compressive eigenvector [33]. For flames in weak to moderate turbulence (Ka $\leq$ 1) the flame itself generates considerable thermal expansion and the gradients align instead with the extensive eigenvector [34, 18, 38]. It is expected that for intensive turbulence, e.g.

high Ka, the expansion due to combustion will be overwhelmed by turbulence and the non-reactive result may be recovered. This has been reported for example by Chakraborty and Swaminathan [34] where alignment with the compressible eigenvector at the unburned side of the flame for Ka $\sim$ 10 was observed. In section 4.4 it is shown that, at higher Ka, the alignment with the compressive eigenvector persists throughout the flame structure, from $c = 0$ to $c = 1$.

3. Numerical method and problem setup

The governing equations for conservation of mass, momentum, energy and chemical species at low Mach number are solved using a DNS solver, see Yu et al. [39] for a detailed description of the implementation and validation. A 5th order weighted essentially non-oscillating (WENO) finite difference scheme is used for convective terms in the species and temperature equations and a 6th order central difference scheme is used for all other terms. A second order operator splitting scheme [40] is employed by performing integration of the chemical source terms between two half time-step integrations of the diffusion term. The diffusion term integration is further divided into smaller explicit time steps to ensure stability. Chemical source terms are integrated using the stiff DVODE solver [41]. The variable coefficient Poisson equation for pressure difference is solved using a multigrid method [42].

The current DNS is on the transient development stage of the flame from its initial laminar state to a highly perturbed flame, within the period of around 2 integral time scales of turbulence. The computational setup is a 10×5×5 mm box in an inlet-outlet configuration with a statistically planar lean premixed flame propagating toward the inlet. Initial conditions are set by superimposing a steady one-dimensional laminar flame, computed with the same kinetics and transport properties as in the DNS, on a pre-calculated statistically stationary turbulence field.

At the inlet a constant mean velocity and temperature of 2 m/s and 298 K are used. The flame position remains within the center region of the domain during the time simulated. Periodic boundary conditions are applied in the cross-stream directions. The domain is discretized on a uniform grid of 1024×512×512 cells. Low wave number turbulence forcing [43, 44] is used in the unburned mixture to maintain the turbulence intensity and length scales. To avoid forcing of the flame the forced region ends one laminar flame thickness upstream of the leading edge of flame; the forcing term was not applied to the flame zone and downstream to avoid direct interference of forcing with the flame structure. The same forcing was also used to generate statistically stationary homogeneous isotropic turbulence in a periodic cubic box of the size 5×5×5 mm, starting from an initial artificially synthesized turbulence [45]. This solution was used to set the initial condition and to feed stationary turbulence through the inlet in the flame simulations.

Three DNS cases with different turbulence intensity u' and inlet/initial conditions have been simulated. The fuel is methane, the equivalence ratio of the mixture is $\phi = 0.6$ and the pressure is 1 bar. The methane/air chemistry is described with the skeletal mechanism of Smooke and Giovangigli [46], which contains 16 species and 35 reactions. The transport

Table 1: Time and length scales and dimensionless numbers for the computed cases. ℓ is given in mm, τ in ms, η in µm and ν in m^2/s.

Case	Ka	Da	Re	Re$_t$	u'/S_L	ℓ	τ	η	ν
K65	65	0.051	11	76	15	0.68	0.38	110	$1.6 \cdot 10^{-5}$
K550	550	0.016	75	510	68	0.99	0.12	39	$1.6 \cdot 10^{-5}$
K3350	3350	0.0062	429	2900	260	1.47	0.047	16	$1.6 \cdot 10^{-5}$

properties, i.e., species diffusion coefficients, thermal conductivity, and viscosity, are mixture averaged based on the detailed properties for individual species obtained from the CHEMKIN thermodynamic database.

Table 1 shows the initial Karlovitz (Ka), Damköhler (Da) and Reynolds (Re) numbers, turbulent intensity (u'/S_L), integral length scale (ℓ), integral time scale (τ) and Kolmogorov length scale (η) of the unburned mixtures for the DNS cases. The Karlovitz, Damköhler, and two different Reynolds numbers are defined as $\mathrm{Ka} = (u'/S_L)^{3/2}(\delta_L/\ell)^{1/2}$, $\mathrm{Da} = \ell S_L/(\delta_L u')$, $\mathrm{Re} = \ell u'/(\delta_L S_L)$ and $\mathrm{Re}_t = u'\ell/\nu$, where u' is the root mean square velocity fluctuation, $\delta_L = (T_{max} - T_{min})/|\nabla T|_{max} = 0.9$ mm is the laminar thermal flame thickness and $S_L = 0.12$ m/s is the laminar flame speed calculated with the Smooke-Giovangigli mechanism. The integral length scale is defined as $\ell = u'^3/\varepsilon$ where $\varepsilon = 2\nu S_{ij}S_{ij}$ is the dissipation rate and ν is the kinematic viscosity. The integral time scale is computed as $\tau = \ell/u'$ and the Kolmogorov length scale as $\eta = \ell/\mathrm{Re}^{3/4}$. All turbulence quantities in Table 1 are evaluated in the homogeneous turbulence field in the cube used to set the initial condition.

The Ka numbers indicate that this series of flames ranges from the thin reaction zones regime to what has historically been predicted to be the distributed or broken reaction zones regime. It should be noted that the integral length scale chosen is on the same order as the flame thickness; this is not seen as a major restriction since the focus is on the interaction of flames with turbulence that is smaller than the flame thickness, thus a direct modification of the inner reaction zone structures. Inclusion of large scales would require a larger domain, which would not only require more computational time but also introduce more complex events such as flame/flame interaction due to large scale folding of the flame. Such large scale interaction is not the focus of this study and for these reasons it was decided to keep the same domain size across all cases. The ratio of integral scale to thermal flame thickness and the turbulent Reynolds numbers are of the same order as have been used in other DNS studies of this type of flames [12, 15–29].

4. Results and discussion

4.1. Overview of the flame structure

Instantaneous snapshots of the K65 and K3350 cases after about 2 integral times are presented in Fig. 1. Three subfigures are dedicated to each of these two cases. The subfigures show mass fractions and net formation rates of CH_2O, CH_4 and CO on two separate slices through the domain. Iso-lines of a reaction progress variable c are drawn at $c = 0.3$ and $c = 0.9$. The progress variable is defined as $c = (T - T_u)/(T_b - T_u)$ where $T_u = 298$ K

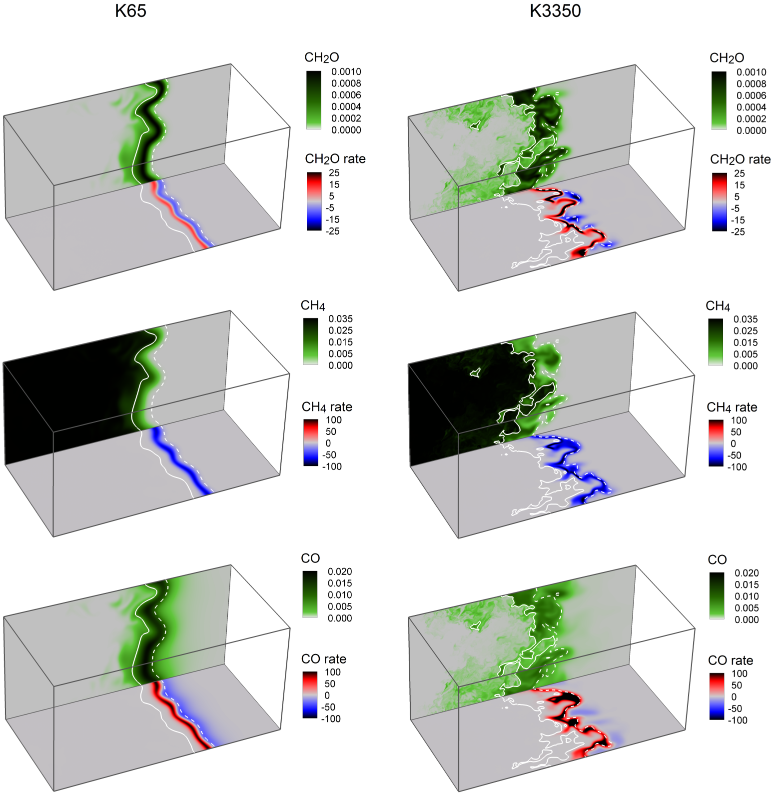

Figure 1: Overview of the K65 (left) and K3350 (right) cases. Mass fraction and net formation rate [1/s] after two integral times are shown for the species CH_2O, CH_4 and CO. Each picture shows the domain with inlet on the left. Iso-lines are drawn at $c = 0.3$ (solid) and $c = 0.9$ (dashed).

and $T_b = 1667$ K are the unburned and burned gas temperatures, respectively. In the K65 case both reaction rates and mass fraction distributions maintain a layered structure without major distortions. In the K3350 case it can be seen that the reaction rates are still confined to relatively narrow zones while the mass fractions of CH_2O and CO are broader and extend into the unburned and burned zones. The distribution of these two stable intermediate species mass fractions appears much broader than their corresponding consumption rates, which is reasonable because the reaction rates of stable species vanish below a limiting temperature where the diffusion of these species can still take place.

In Figs. 2 and 3 iso-lines of the instantaneous reaction rates for CH_2O, CH_4 and CO are shown in a 2D plane at five different times for the K65 and K3350 cases, respectively. The grayscale indicates the enstrophy $E = \omega^2$ (logarithmic scale). Regions with temperature between 400 K and 1600 K are shaded with green to indicate the thermal thickness. For both cases, the enstrophy field in the unburned mixture remains similar at all times shown in the figures, while the enstrophy fields in the burned mixture evolve rapidly with time. The magnitude of enstrophy in the burned gas decreases with time, owing mainly to the dilatation effect. The evolution of the flame structures can also be seen in Figs. 2 and 3. At $t = 0.1\tau$, the three layers are only slightly disturbed from its initial laminar flame state; at $t = 1.7\tau$, large scale wrinkling of the layers can be seen in the K65 case, while both large scale wrinkling and small scale distortion of the layers can be seen in the K3350 case.

Flow scales are smaller in the K3350 case and the flame brush appears to be more broadened compared with the K65 case, especially from the axial line-of-sight viewpoint. The flame brush in this context is the range on the x-axis where the flame can be found. As seen in the figure, a broadened flame brush does not necessarily mean a broadened local flame structure. In fact, one can see local broadening as well as local thinning of the layers. It should be pointed out that any statements about sub-layer thickness based on 2D data such as Figs. 2 and 3 can be misleading since the plot only shows a slice cut through a three-dimensional flame and the mean angle between the flame front and the plotted slice changes with increased wrinkling.

Regions with large gradients may be observed in the K3350 case (Fig. 3) in the form of iso-line clusters, which means local flame thinning. This is related to the mixing process of passive scalars in turbulent flows where large gradient regions are formed at converging-diverging saddle-points [47]. The statistical abundance of large gradient regions can be seen in Fig. 4. This figure shows the joint probability density function (JPDF) of the reaction progress variable c and its normalized gradient magnitude $|\nabla c|/|\nabla c|_{\mathrm{L,max}}$ where $|\nabla c|_{\mathrm{L,max}}$ is the peak magnitude of the gradient in the corresponding unstretched laminar flame. Shown in the figure is also the conditional mean and the corresponding laminar profile. The JPDF shows a large span of gradient magnitudes, both larger and smaller than the laminar reference, which shows that both thinned and broadened regions are present. In the K3350 case a larger skew towards large gradients is seen, especially for c between 0.1 and 0.5, and the gradient magnitude can locally be more than 10 times the laminar peak value. The co-existence of both thinning and broadening of the reaction zone structures in high Ka flames poses a challenge to turbulent combustion models for LES and RANS

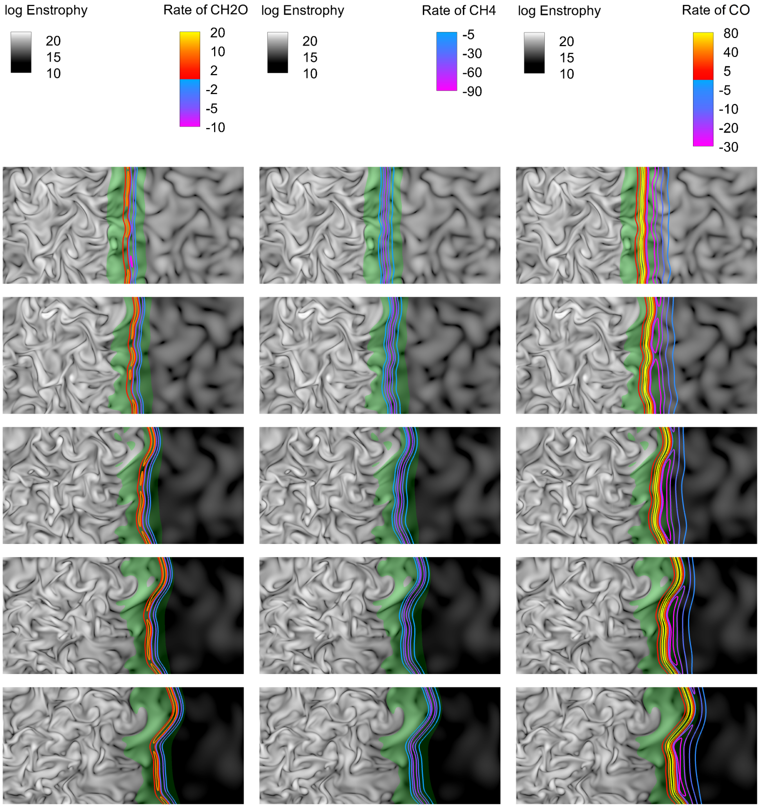

Figure 2: Case K65. Instantaneous reaction rates (lines) of CH_2O, CH_4 and CO and natural logarithm of enstrophy (gray-scale) at five different times, $t = 0.1\tau$, 0.4τ, 0.9τ, 1.3τ and 1.7τ. Regions with temperature between 400 K and 1600 K are shaded green. The rates are in units of s^{-1} of mass fraction. The unit of enstrophy is s^{-2}.

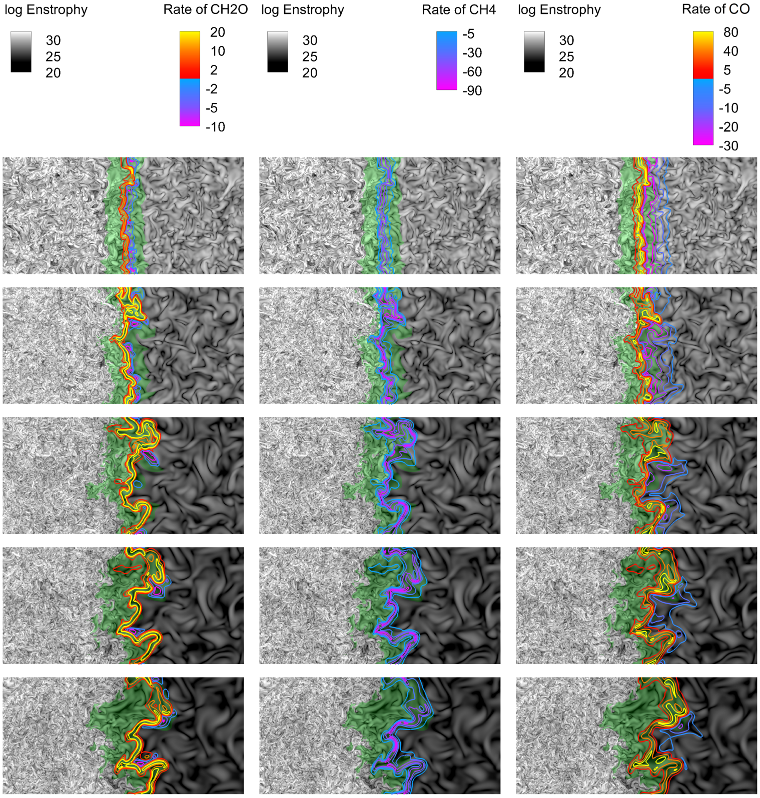

Figure 3: Case K3350. Instantaneous reaction rates (lines) of CH_2O, CH_4 and CO and natural logarithm of enstrophy (gray-scale) at five different times, $t = 0.1\tau$, 0.4τ, 0.9τ, 1.3τ and 1.7τ. Regions with temperature between 400 K and 1600 K are shaded green. The rates are in units of s^{-1} of mass fraction. The unit of enstrophy is s^{-2}.

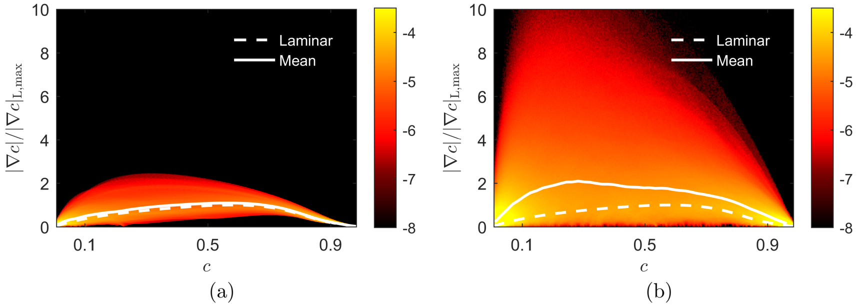

(a) (b)

Figure 4: Joint probability density function of c and its gradient magnitude. (a) Case K65 and (b) case K3350. A logarithmic color scale is used; the numbers indicate the exponent. Dashed lines show the corresponding values of a laminar flame and solid lines the conditional mean of the turbulent flame cases.

simulations. The large span of high and low gradients in the reaction zone, which is not only due to the enhancement/suppression of the reactions but to a large extent due to distortion by turbulence, implies that models based on stretched flamelets or thickening of the reaction zone may require revision for high Ka flames.

In section 4.3 the gradient and its dynamics are analyzed further.

4.2. Sub-layer thickness

Figure 5 shows the joint PDFs of c with the three sub-layer markers computed at the final time. These markers are CH_2O mass fraction (Y_{CH2O}), CH_4 consumption rate ($\dot{\omega}_{\mathrm{CH4}}$) and CO consumption rate ($\dot{\omega}_{\mathrm{CO},c}$). Note that $\dot{\omega}_{\mathrm{CO},c}$ contains CO consuming reactions only. The corresponding profiles of a one-dimensional unstretched laminar flame are included in the figure as reference. Data is normalized by the maximum laminar values. In laminar flames Y_{CH2O} reaches significant values already around $c = 0.1$ and can therefore be considered a preheat zone marker. In both the K65 and K3350 cases the JPDF of Y_{CH2O} and c follows a narrow manifold for $c < 0.5$, as both CH_2O and c are transported by turbulence at a similar rate. Furthermore, in the K65 case $\dot{\omega}_{\mathrm{CH4}}$ and $\dot{\omega}_{\mathrm{CO},c}$ both closely follow the laminar flame manifold and the flame structure can therefore be considered similar to that of a laminar flame. In the K3350 case the scattering around the conditional means increases significantly for both $\dot{\omega}_{\mathrm{CH4}}$ and $\dot{\omega}_{\mathrm{CO},c}$ for $c > 0.5$. In the K3350 case the positioning of the peak value of all layer markers have shifted toward higher c and $\dot{\omega}_{\mathrm{CO},c}$ decreases to half the laminar value, indicating that CO oxidation is slowed down in high Ka flames.

The temporal evolution of the mean brush thickness is shown in Fig. 6. The mean brush thickness increases with time for all cases and layer markers, and it increases with the Ka number as well. A statistically stationary state, where the brush thickness on average does not change, is not reached during the simulated time of two integral time scales, consistent with previous DNS e.g. Ref. [48]. One explanation may be that, due to thermal expansion and the associated enlargement of vortices, the integral time scale inside the flame is longer

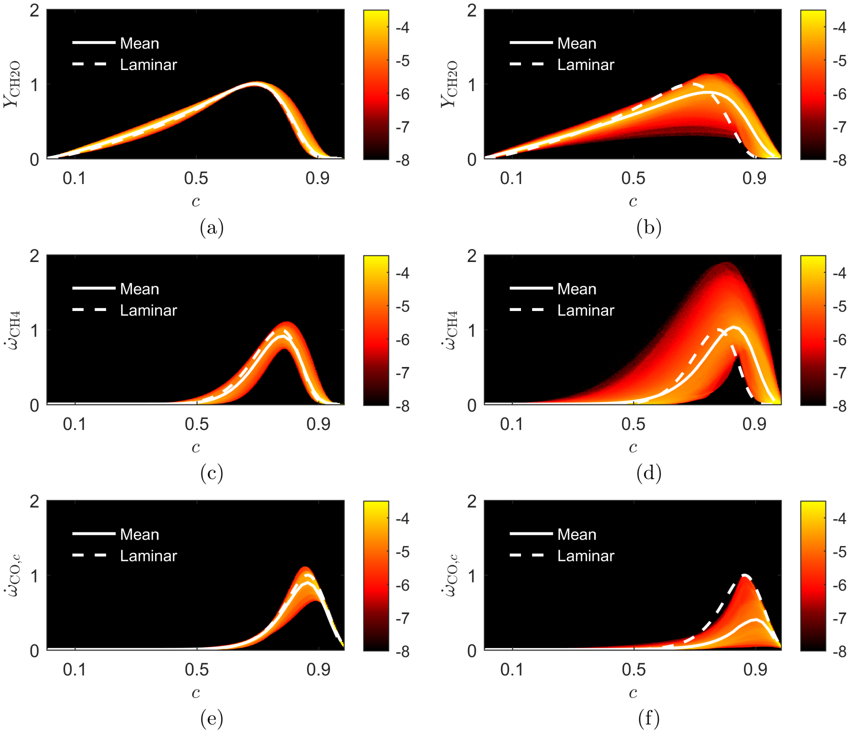

(a) (b) (c) (d) (e) (f)

Figure 5: Joint PDF of progress variable c and $Y_{\mathrm{CH_2O}}$ (a-b), $\dot{\omega}_{\mathrm{CH_4}}$ (c-d), and $\dot{\omega}_{\mathrm{CO},c}$ (e-f). Case K65 is shown in (a,c,e) and case K3350 in (b,d,f). A logarithmic color scale is used; the numbers indicate the exponent. The dashed lines show laminar profiles. The data is normalized by the maximum of the laminar profiles. Mean values conditioned on c from DNS simulations are shown as solid lines.

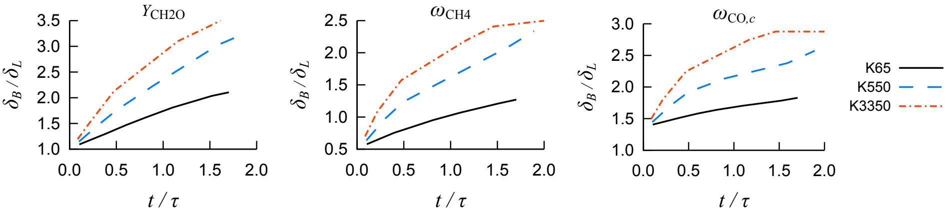

Figure 6: Mean brush thickness δ_B as function of time.

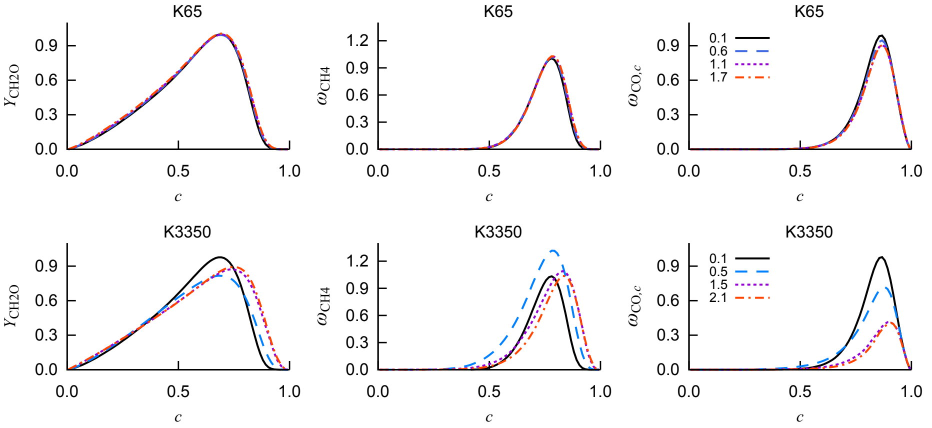

Figure 7: Profiles of the layer markers in c-space. Evaluated at four different times indicated in the legend in units of t/τ.

than that ahead of the flame, so longer time is required for the flame to reflect the disturbance due to turbulence.

From Figs. 2 and 3 it is clear that the broadening of the profiles and the decrease of the peaks of the profiles are due to the large-scale wrinkling of the flame, as well as the small-scale turbulent distortion of the layers. For the lower Ka number case, K65, the broadening of the layers, in particular the fuel consumption layer ($\dot{\omega}_{\mathrm{CH4}}$) and the CO oxidation layer ($\dot{\omega}_{\mathrm{CO},c}$), is mainly due to the large scale wrinkling, while the small-scale turbulent distortion effect is less significant.

To discriminate the broadening in c-space from the broadening of c itself, the mean profiles of layer markers conditioned on c are shown in Fig. 7 for different times. For the lower Ka flame, case K65, the mean profiles are nearly the same at all times (the $\dot{\omega}_{\mathrm{CO},c}$ profile shows a minor decrease in the peak values with time). This indicates that the broadening of the mean profiles shown in Fig. 6 is essentially due to broadening of c, while the internal flame structures are similar to the laminar flame. The high Ka flame, K3350, shows however a significant modification of the internal flame structures. The $\dot{\omega}_{\mathrm{CO},c}$ profile shows a substantial decrease of the peak, due to the suppression of the CO oxidation reactions (cf. also Fig.5). The $\dot{\omega}_{\mathrm{CH4}}$ and Y_{CH2O} profiles show a shift towards large c.

In contrary to δ_B, the conditional mean layer thickness, measured by δ_V (Fig. 8) and which excludes the large scale wrinkling effects, becomes thinner with increasing Ka for all layers. For the lower Ka number flame, K65, the thickness of the preheat zone decreases slightly in the earlier transient stage, while the layer becomes thicker at later time. The fuel consumption and the CO consumption layer become thinner with time. For the higher Ka flames, e.g., K3350, the preheat zone and the fuel consumption zone first experience a rapid thinning with time and after 0.4τ the layers become thicker with time. The CO oxidation

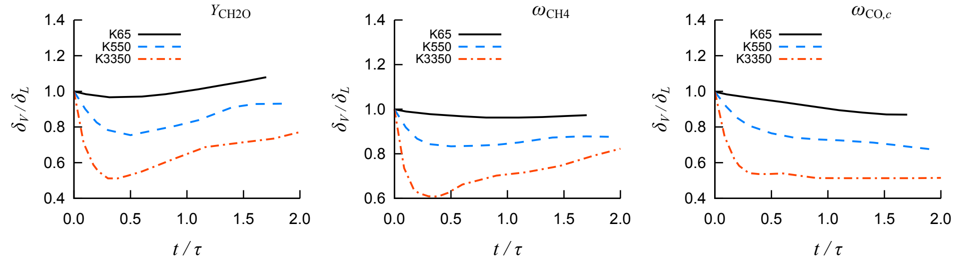

(a) (b) (c)

Figure 8: Time evolution of the mean conditional layer thickness δ_V of (a) the CH_4 consumption layer, (b) the CH_2O layer and (c) the CO consumption layer.

layer stays thinned and does not recover its thickness during the time studied. The thinning of the CO oxidation layer is a result of the suppressed oxidation rate of CO, which also results in a higher leakage of CO in the postflame zone, and a broader CO layer in the domain, cf. Fig. 3.

It should be pointed out that in practical flames there will often be regions in the flame undergoing flame-flame interaction. Such regions will reduce both the mean gradient and the wrinkled area. To study the thickness of a freely propagating flame segment, regions undergoing flame interaction could be filtered out. In practice, however, flame interaction is important [49, 50]. In the present case flame interaction is rare due to the small length scale and no attempt has thus been made to filter out any regions and still the flame structure appears to be thinned for the time simulated. The situation may be different if a larger integral scale, as is seen in many practical flames, was used allowing for increased flame-flame interaction.

In the literature most studies have reported thickening of lean methane flames at high Karlovitz numbers, but there are reports of thinning as well. In the experimental studies by Dinkelacker et al. [14] and by Goey and Peters [6], thinned lean natural gas flames were observed on swirl burners. In these studies the thickness was quantified by temperature gradients obtained from both 2D and double-sheet 3D measurements. There have been many observations of thickened flames. Lapointe and Savard [19] reported, for freely propagating n-heptane flames, broadening of the flame brush (similar measure to δ_B) and broadening of the preheat layer (visually from temperature iso-lines). Broadening of the reaction zone is also reported, quantified by the percentage of fuel consumed more than half a laminar flame thickness away from the isotherm of maximum consumption rate. No considerable broadening was found in temperature space; the broadening observed was attributed to decreasing temperature gradients. Thevenin [22] used a gradient-based thickness for a spherically expanding methane flame and observed thinning to dominate but largely thickened regions also occur. Sankaran, Hawkes and Chen [12, 28] observed thickening of a methane-air slot Bunsen flame using a gradient-based thickness as well as distance from an iso-surface of c.

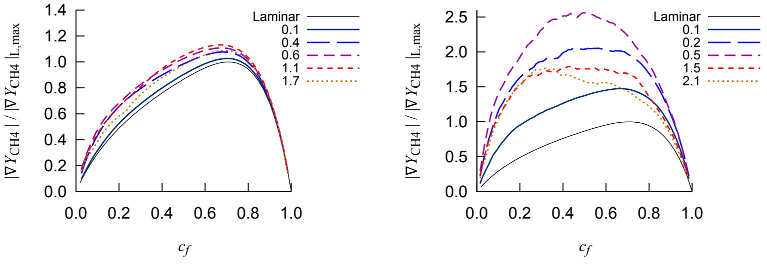

(a) (b)

Figure 9: Fuel gradient $|\nabla Y_{\mathrm{CH4}}|$ as function of c_f at different times. (a) Case K65. (b) case K3350.

The thickening saturates at high Ka. Local thinning was observed in regions of large positive tangential strain rate. Wabel et al. reported that the CH layer of a methane jet flame was not broadened even at very high turbulent intensities [13], while Zhou et al. reported substantial broadening of the CH layers at high Ka flames [10, 11]. Clearly there are differences in the observed behaviour of the flame thickness. This may be attributed to the differences in flame geometry, such as flat, jet or swirl flames with varying amounts of history effects and mean curvatures, to the use of different fuels that result in different reaction zone structures, or to the different integral length scales affecting the extent of flame-flame interactions. To understand the dynamic development of the flame structures the fuel-consumption layer is further analyzed in the following section.

4.3. Transient development of the gradient

The temporal evolution of flame thickness in terms of the gradient of the fuel mass fraction is described by Eq. (7) which was formulated in section 2.2. Figure 9 shows the conditional mean of the gradient $|\nabla Y_{\mathrm{CH4}}|$ conditioned on the normalized fuel mass fraction ($c_f = 1 - Y_{\mathrm{CH4}}/Y_{\mathrm{CH4},u}$, which represents the progress of the fuel consumption reactions). Initially, the gradient increases (thinning of the flame) and later starts to decrease (thickening of the layer) in the same way as the mean conditional layer thickness discussed in section 4.2.

A breakdown of the terms contributing to $D^*|\nabla Y_{\mathrm{CH4}}|/D^*t$ as defined in Eq. (7) is shown in Fig. 10. These are the flow normal strain rate term A_N, the normal diffusion term A_{norm}, the curvature term A_{curv}, the reaction term A_R and the correction term A_{corr}. The plot shows the budget at two different times. In the K65 case the laminar structure with a balance of reaction and normal diffusion dominates while curvature and flow strain only have significance outside the reaction zone. In the K3350 the dominating terms are the flow strain, the normal diffusion and the curvature. The reaction term loses its relative significance at high Ka since its magnitude does not increase with turbulent intensity as the other terms do.

For both Karlovitz numbers the A_N term always has a thinning effect (gradient creation) while the diffusion and reaction terms are responsible for any thickening effect (gradient

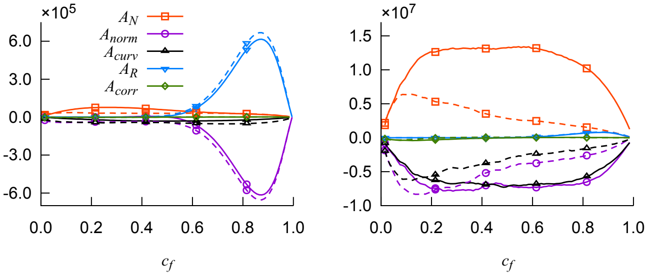

Figure 10: Balance of terms in the gradient equation. (a) shows case K65 at $t = 0.1\tau$ (solid) and $t = 1.7\tau$ (dashed). (b) shows case K3350 at $t = 0.2\tau$ (solid) and $t = 2.1\tau$ (dashed).

destruction). In a laminar flame the A_N term is always negative and created by the acceleration due to thermal expansion; e.g. in one dimension $a_N = \nabla \cdot \mathrm{u}$. Under high Ka condition, however, the A_N term is mostly generated by turbulence and, as seen in Fig. 10, is positive. The role of A_N is thus reversed from thickening to thinning in these high Ka cases. The thinning effect of A_N is attributed to the preferential alignment of iso-scalar surface normals with the compressive strain rate eigenvector which is discussed in section 4.4. Since preferential alignment is an always occurring phenomenon it is unlikely that the conclusions here are dependent on the particular cases or the transient stage of the flame considered here.

Figure 11 shows the joint PDF of normal strain rate a_N and tangential strain rate $a_T = \nabla \cdot \boldsymbol{u} - a_N$ conditioned on $0.7 < c < 0.9$. The dilatation rate $\nabla \cdot \boldsymbol{u}$ is the sum of a_N and a_T. It can be seen in Fig. 11 that, for the K3350 case, the magnitude of dilatation rate is rather small compared with a_N and a_T and that the incompressible relation $a_N = -a_T$ is a good approximation. It is also seen that negative a_N and positive a_T is the more common configuration.

4.4. Alignment with principal strain rate eigenvectors

It has been seen in Fig. 10 that large negative normal strain rates, a_N, exist in these high Ka flames and that it can cause thinning of the local flame structure. Figure 12 shows the PDF of the cosine of the alignment angle between the flame normal, $n = -\nabla c/|\nabla c|$, and the three eigenvectors corresponding to the (i) smallest, (ii) largest and (iii) intermediate real eigenvalues of the symmetrical strain rate tensor $S_{ij} = (\partial u_i/\partial x_j + \partial u_j/\partial x_i)/2$ (note that in incompressible flow they can be referred to as the compressive, extensive and intermediate eigenvectors, respectively). The cosine is used rather than the angle itself since the cosine has a flat distribution for randomly oriented vectors. In incompressible flows [33] the normal to an iso-surface of a passive scalar aligns with the compressive strain rate eigenvector. Such alignment causes negative a_N and increases the scalar gradient. The data in Fig. 12 is conditioned on $0.7 < c < 0.9$ (where the heat release is significant) and sampled at the final time. At all Karlovitz numbers investigated the flame normal aligns preferentially with the most compressive eigenvector (i.e. the angle is small), whereas the extensive and intermediate

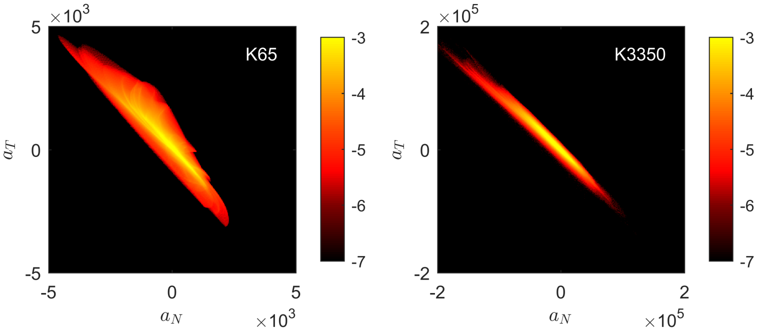

(a) (b)

Figure 11: Joint PDF of normal strain rate and tangential strain rate. (a) shows case K65 and (b) shows case K3350. The data is conditioned on $0.7 < c < 0.9$. A logarithmic color scale is used; the numbers indicate the exponent.

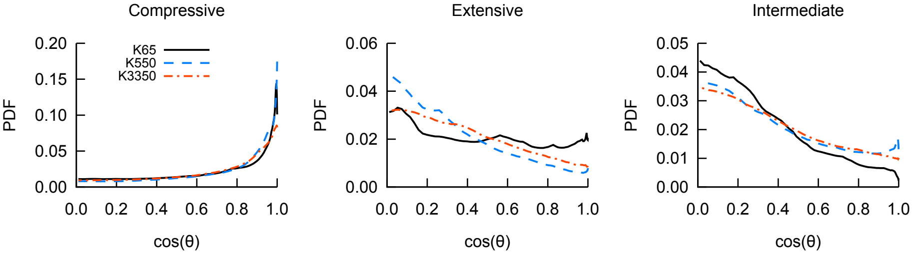

Figure 12: PDF of cosine of the alignment angle θ of the flame normal with principal strain rate eigenvectors conditioned on c corresponding to the heat release region. 1 means aligned and 0 means not aligned.

eigenvectors are mostly tangential of the flame (with the angle close to 90 degrees). Thus, the result resembles that of passive scalars.

Chakraborty and Swaminathan [34] reported that, for Ka $\sim$ 10, the alignment with the compressive eigenvector is strongest in the preheat layer and decreases toward the burned side. Fig. 13 shows that for Ka $\gtrsim$ 65 the observed alignment is not confined to any particular layer but persists throughout all layers of the flame, almost independent of c. This indicates that the effect due to thermal expansion is small when compared with the flow induced strain rate. From Figures 12 and 13 it appears that the alignment with the most compressive strain rate eigenvector is the likely mechanism behind large negative flow strain rates a_N that creates locally thinned regions.

In Fig. 14 the time evolution of the alignment with compressive and extensive strain rate eigenvectors is shown for the K65 case conditioned on $0.7 < c < 0.9$. The figure shows that preferential alignment develops quickly; in the beginning there is no alignment since

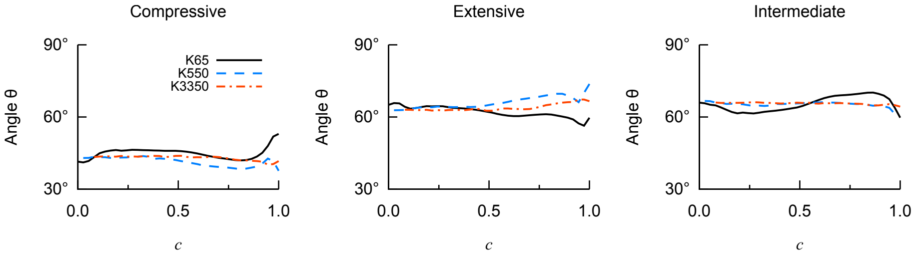

Figure 13: Mean alignment of the flame normal with compressive, extensive and intermediate principal strain rate eigenvectors as function of c.

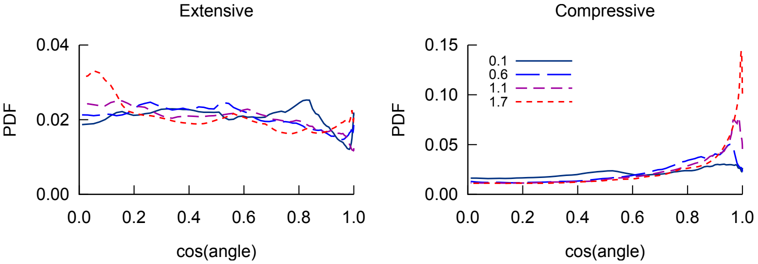

Figure 14: PDF of cosine of the alignment of the flame normal with compressive and extensive strain rate eigenvectors for Ka = 65 after 0.1, 0.6, 1.1 and 1.7 integral times.

the imposed turbulence is random but already after half an integral time the the alignment with the compressive strain rate eigenvector can be seen. The time scale to establish the alignment is thus of the order of the integral time scale.

5. Conclusions

Direct numerical simulations have been performed to study the transient evolution of statistically planar premixed lean methane/air flames exposed to high intensity small-scale turbulence under atmospheric conditions. Karlovitz numbers ranging from 65 to 3350 are considered. Turbulence forcing is employed on the unburned reactant side to maintain intensity and length scales. Different measures have been proposed to quantify the thickness of the preheat layer, the fuel consumption layer and the CO oxidation layer. The dynamics of flame thickness has then been analyzed by comparing contributing terms in the scalar gradient transport equation. Alignment of the flame normal with principal eigenvectors of the strain rate tensor has also been investigated to provide an explanation of the observed compressive normal strain rate responsible for flame-thinning.

It is seen that, as the high Karlovitz (and Reynolds) number turbulence is encountered, the flow induced strain rate overwhelms the thermal expansion, the flame normal then aligns preferentially with the compressible strain rate eigenvector and regions with locally very large gradients start to appear. With time the thickness starts to recover, but not equally for all layers.

The main conclusions are summarized as follows:

1. The proposed measure of mean conditional layer thickness show initial thinning of all three investigated sub-layers (representative of the preheat zone, the fuel consumption zone, and the CO oxidation zone) as the Karlovitz number is increased. The preheat layer (CH_2O) and the fuel consumption layer both show some recovery of thickness with time while the CO oxidation layer remains considerably thinned. The mean flame brush, however, is broadened.
2. The fuel mass fraction gradient, representing the local thickness, is governed by a balance of normal strain rate, reaction and diffusion. At all simulated Karlovitz numbers, 65 to 3350, the normal strain rate is compressive (rather than extensive as it is in the corresponding laminar flame). At Ka 65 the budget of the gradient transport equation shows mainly a balance between the reaction (compressive) and normal diffusion (extensive) terms characteristic of laminar flames and that persists during the simulated time. At Ka 3350 the reaction term has lost its relative significance and the gradient equation budget is dominated by normal strain rate (compressive) and diffusion (extensive). The magnitude of these terms decreases with time as turbulence adapts to the thermal expansion.
3. Preferential alignment between the flame normal and the most compressive principal strain rate eigenvector is observed. The extent of the alignment is essentially the same from Karlovitz number 65 up to 3350. The observed alignment is opposite to what has been reported for the flamelet combustion regime but consistent with the behavior of passive scalars. The alignment was also seen to develop quickly and it persists for all layers in the flame.

An explanation for preferential alignment with compressive flow structures and the resulting shift toward compressive normal strain rates is provided by the mechanism for passive scalars. The observation of decreasing thickness of various sub-layers show that the compressive mechanism dominates over any thickening mechanism in this series of flames. However, even though the compressed structures dominate, broadened low-gradient regions also appear locally.

Acknowledgments

This work was supported by the Swedish Research Council (VR) and the national Centre for Combustion Science and Technology (CeCOST). We acknowledge PRACE for awarding access to computer resources via LRZ based in Germany. We acknowledge the Swedish National Infrastructure for Computing (SNIC) for awarding access to resources via the Center for High Performance Computing (PDC) and High Performance Computing Center North (HPC2N). The authors would like to thank prof. César Dopazo for valuable discussions.

[1] R. Borgi, Turbulent combustion modelling, Prog. Energy Combust. Sci. 14 (1988) 245–292.

[2] F. A. Williams, Combustion Theory, 2nd Edition, The Benjamin/Cummins Publishing Company Inc., 1985.

[3] N. Peters, Turbulent combustion, Cambridge Univ. Press, 2000.

[4] I. G. Shepherd, R. K. Cheng, T. Plessing, C. Kortschik, N. Peters, Premixed flame front structure in intense turbulence, Proc. Combust. Inst. 29 (2002) 1833–1840.

[5] P. Tamadonfar, Ö. L. Gülder, Experimental investigation of the inner structure of premixed turbulent methane/air flames in the thin reaction zones regime, Combust. Flame 162 (2015) 115–128.

[6] L. P. H. de Goey, T. Plessing, R. T. E. Hermannas, N. Peters, Analysis of the thickness of turbulent flamelets in the thin reaction zones regime, Proc. Combust. Inst. 30 (2005) 859–866.

[7] M. J. Dunn, A. R. Masri, R. W. Bilger, A new piloted premixed jet burner to study strong finite-rate chemistry effects, Combust. Flame 151 (2007) 46–60.

[8] Z. S. Li, B. Li, Z. W. Sun, X. S. Bai, M. Aldén, Turbulence and combustion interaction: High resolution local flame front structure visualization using simultaneous single-shot PLIF imaging of CH, OH, and CH2O in a piloted premixed jet flame, Combust. Flame 157 (2010) 1087–1096.

[9] J. Sjöholm, J. Rosell, B. Li, M. Richter, Z. Li, X. S. Bai, M. Aldén, Simultaneous visualization of OH, CH, CH2O and toluene PLIF in a methane jet flame with varying degrees of turbulence, Proc. Combust. Inst. 34 (2013) 1475–1482.

[10] B. Zhou, C. Brackmann, Z. Li, M. Aldén, X. S. Bai, Simultaneous multi-species and temperature visualization of premixed flames in the distributed reaction zone regime, Proc. Combust. Inst. 35 (2015) 1409–1416.

[11] B. Zhou, C. Brackmann, Z. Li, M. Aldén, Development and application of CN PLIF for single-shot imaging in turbulent flames, Combust. Flame 162 (2015) 368–374.

[12] R. Sankaran, E. R. Hawkes, C. S. Yoo, J. H. Chen, Response of flame thickness and propagation speed under intense turbulence in spatially developing lean premixed methane-air jet, Combust. Flame 162 (2015) 3294–3306.

[13] T. M. Wabel, A. W. Skiba, J. E. Temme, J. F. Driscoll, Measurements to determine the regimes of turbulent premixed flames in extreme turbulence, Proc. Combust. Inst. 36 (2017) 1809–1816.

[14] F. Dinkelacker, A. Soika, D. Most, D. Hofmann, A. Leipertz, W. Polifke, K. Döbbeling, Structure of locally quenched highly turbulent lean premixed flames, Proc. Combust. Inst. 27 (1998) 857–865.

[15] H. Carlsson, R. Yu, X. S. Bai, Direct numerical simulation of lean premixed CH4/air and H2/air flames at high Karlovitz numbers, Int. J. Hydrogen Energy 39 (2014) 20216–20232.

[16] H. Carlsson, R. Yu, X. S. Bai, Flame structure analysis for categorization of lean premixed CH4/air and H2/air flames at high Karlovitz numbers: Direct numerical simulation studies, Proc. Combust. Inst 35 (2015) 1425–1432.

[17] N. Chakraborty, M. Klein, N. Swaminathan, Effect of Lewis number on the reactive scalar gradient alignment with local strain rate in turbulent premixed flames, Proc. Combust. Inst. 32 (2009) 1409–1417.

[18] N. Chakraborty, N. Swaminathan, Comparison of displacement speed statistics of turbulent premixed flames in the regimes representing combustion in corrugated flamelets and thin reaction zones, Phys. Fluids 19 (2007) 045103.

[19] S. Lapointe, B. Savard, G. Blanquart, Differential diffusion effects, distributed burning, and local extinctions in high Karlovitz premixed flames, Combust. Flame 162 (2015) 3341–3355.

[20] S. Lapointe, G. Blanquart, Fuel and chemistry effects in high Karlovitz premixed turbulent flames, Combust. Flame 167 (2016) 294–307.

[21] B. Savard, B. Bobbitt, G. Blanquart, Structure of a high karlovitz n-C7H16 premixed turbulent flame, Proc. Combust. Inst. 35 (2015) 1377–1384.

[22] D. Thévenin, Three-dimensional direct simulations and structure of expanding turbulent methane flames, Proc. Combust. Inst. 30 (2005) 629–637.

[23] A. J. Aspden, M. S. Day, J. B. Bell, Turbulence-chemistry interaction in lean premixed hydrogen combustion, Proc. Combust. Inst. 35 (2015) 1321–1329.

[24] A. J. Aspden, M. S. Day, J. B. Bell, Lewis number effects in distributed flames, Proc. Combust. Inst. 33 (2011) 1473–1480.

[25] E. R. Hawkes, O. Chatakonda, H. Kolla, A. R. Kerstein, J. Chen, A petascale direct numerical simulation study of the modelling of flame wrinkling for large-eddy simulations in intense turbulence, Combust. Flame 159 (2012) 2690–2703.

[26] E. R. Hawkes, J. H. Chen, Comparison of direct numerical simulation of lean premixed methane-air flames with strained laminar flame calculations, Combust. Flame 144 (2006) 112–125.

[27] D. Cecere, E. Giacomazzi, N. M. Arcidiacono, F. R. Picchia, Direct numerical simulation of a turbulent lean premixed CH4/H2-air slot flame, Combust Flame 165 (2016) 384–401.

[28] R. Sankaran, E. R. Hawkes, J. H. Chen, T. Lu, C. K. Law, Structure of a spatially developing turbulent lean methane-air bunsen flame, Proc. Combust. Inst. 31 (2007) 1291–1298.

[29] P. E. Hamlington, A. Y. Poludnenko, E. S. Oran, Interactions between turbulence and flames in premixed reacting flows, Phys. Fluids 23 (2011) 125111.

[30] H. Wang, E. R. Hawkes, J. H. Chen, B. Zhou, Z. Li, M. Aldén, Direct numerical simulations of a high Karlovitz number laboratory premixed jet flame - an analysis of flame stretch and flame thickening, J. Fluid Mech. 815 (2017) 511–536.

[31] R. Yu, A. N. Lipatnikov, Direct numerical simulation study of statistically stationary propagation of a reaction wave in homogeneous turbulence, Phys. Rev. E 95 (2017) 063101.

[32] R. Yu, A. N. Lipatnikov, DNS study of dependence of bulk consumption velocity in a constant-density reacting flow on turbulence and mixture characteristics, Phys. Fluids 29 (2017) 065116.

[33] W. T. Ashurst, A. R. Kerstein, R. M. Kerr, C. H. Gibson, Alignment of vorticity and scalar gradient with strain rate in simulated Navier-Stokes turbulence, Phys. Fluids 30 (1987) 2345–2353.

[34] N. Chakraborty, N. Swaminathan, Influence of the Damköhler number on turbulence-scalar interaction in premixed flames. I. Physical insight, Phys. Fluids 19 (2007) 045103.

[35] L. Vervisch, E. Bidaux, K. N. C. Bray, W. Kollmann, Surface density function in premixed turbulent combustion modeling, similarities between probability density function and flame surface approaches, Phys. Fluids 7 (1995) 2496–2503.

[36] C. Dopazo, L. Cifuentes, J. Martin, C. Jimenez, Strain rates normal to approaching iso-scalar surfaces in a turbulent premixed flame, Combust. Flame 162 (2015) 1729–1736.

[37] K. Seshadri, N. Peters, The inner structure of methane-air flames, Combust. Flame 81 (1990) 96–118.

[38] L. Cifuentes, C. Dopazo, J. Martin, C. Jimenez, Local flow topologies and scalar structures in a turbulent premixed flame, Phys. Fluids 26 (2014) 065108.

[39] R. Yu, J. Yu, X. S. Bai, An improved high-order scheme for DNS of low mach number turbulent reacting flows based on stiff chemistry solver, J. Comp. Phys. 231 (2012) 5504–5521.

[40] G. Strang, On the construction and comparison of difference schemes, Siam J. on Num. Anal. 5 (1968) 506–517.

[41] P. N. Brown, G. D. Bryne, A. C. Hindmarsch, VODE, a variable-coefficient ode solver, Siam J. Sci. Stat. Comp. 10 (1989) 1038–1051.

[42] R. Yu, X. S. Bai, A semi-implicit scheme for large eddy simulation of piston engine flow and combustion, Int. J. Numerical Methods in Fluids 71 (2013) 13–40.

[43] R. Yu, X. S. Bai, A. Lipatnikov, A direct numerical simulation study of interface propagation in homogeneous turbulence, J. Fluid Mech. 772 (2015) 127–164.

[44] S. Ghosal, T. S. Lund, P. Moin, K. Akselvoll, A dynamic localization model for large-eddy simulation of turbulent flows, J. Fluid Mech. 286 (1995) 229–255.

[45] R. Yu, X. S. Bai, A fully divergence-free method for generation of inhomogeneous and anisotropic turbulence with large spatial variation, J. Comp. Phys. 256 (2014) 234–253.

[46] M. Smooke, V. Giovangigli, Reduced Kinetic Mechanisms and Asymptotic Approximation for methane-air Flames, Springer-Verlag, Berlin, 1991.

[47] R. A. Antonia, A. J. Chambers, D. Britz, L. W. B. Browne, Organized structures in a turbulent plane jet: topology and contribution to momentum and heat transport, J. Fluid Mech. 172 (1986) 211–229.

[48] A. J. Aspden, M. S. Day, J. B. Bell, Three-dimensional direct numerical simulations of turbulent lean premixed methane combustion with detailed kinetics, Combust. Flame 166 (2016) 266–283.

[49] A. A. Burluka, M. A. Gorokhovski, R. Borghi, Statistical model of turbulent premixed combustion with interacting flamelets, Combust. Flame 109 (1997) 173–187.

[50] T. D. Dunstan, N. Swaminathan, K. N. C. Bray, N. G. Kingsbury, Flame interactions in turbulent premixed twin V-flames, Combust. Sci. Technol. 185 (2013) 134–159.

Paper II

A priori analysis of sub-grid variance of a reactive scalar using DNS data of high Ka flames

Thommie Nilsson[a], Ivan Langella[b,c], Nguyen Anh Khoa Doan[b],
Nedunchezhian Swaminathan[b], Rixin Yu[a], Xue-Song Bai[a]

[a]*Department of Energy Sciences, Lund University, Lund, Sweden*
[b]*Department of Engineering, University of Cambridge, Cambridge, United Kingdom*
[c]*Department of Aeronautical and Automotive Engineering, Loughborough University, United Kingdom*

Abstract

Direct numerical simulations (DNS) of low and high Karlovitz number (Ka) flames are analysed to investigate the behaviour of the reactive scalar sub-grid scale (SGS) variance in premixed combustion under a wide range of combustion conditions (regimes). An order of magnitude analysis is performed to assess the importance of various terms in the variance evolution equation and the analysis is validated using the DNS results. This analysis sheds light on the relative behaviour among turbulent transport and production, scalar dissipation and chemical processes involved in the evolution of the SGS variance at different Ka. The common expectation is that the variance equation shifts from a reaction-dissipation balance at low Ka to a production-dissipation balance at high Ka with diminishing reaction contribution. However, in large eddy simulation (LES), a high Ka alone does not make the reaction term negligible, as the relative importance of the reaction term has a concurrent increase with filter size. The filter size can be relatively large compared with the Kolmogorov length scale in practical LES of high Ka flames, and as a consequence a reaction-production-dissipation balance may prevail in the variance equation even in a high Ka configuration, and this possibility is quantified using the DNS analysis in this work. This has implications from modelling perspectives, and therefore two commonly used closures in LES for the SGS scalar dissipation rate are investigated *a priori* to estimate the importance of the above balance in LES modelling. The results are explained to highlight the interplay among turbulence, chemistry and dissipation processes as a function of Ka.

Keywords: Scalar variance, Scalar dissipation rate, Turbulent premixed flame, Direct numerical simulation, High Karlovitz number

---

1. Introduction

Fuel lean premixed combustion has potential to improve thermal efficiency and reduce NO_x emissions [1, 2] but it is highly susceptible to combustion instability, blowout and flashback [3]. To enable its use, a better understanding of its physics is required. The presence of intense turbulence with lean flames in practical applications such as gas turbines typically yields high Karlovitz numbers, Ka, which is defined as the ratio between the chemical time scale and the smallest turbulence time scale. This situation of strong turbulence and lower reactivity yields complex physics with reaction zones broadening [4, 5] and local extinction [6, 5]. Thus, it is imperative to gain better understanding of high Ka flames and their modelling for the design of future lean-burn combustors.

Given the difficulty of performing measurements under high Ka conditions, direct numerical simulation (DNS) provides the necessary physical insights and an opportunity for a priori analysis of sub-grid scale (SGS) models for large eddy simulation (LES). Several recent DNS studies of high Ka flames have highlighted how the structure of the flame is broadened and disturbed [7–10], but it has also been shown that, probably due to thermal expansion effects [11], the transition to the broken reaction zone regime happens at a much higher Karlovitz number than the traditionally predicted value of 100 [12–17]. There have also been published studies that have investigated the effect of flame stretch and mean shear [18, 19], differential diffusion and non-unity Lewis number [20, 7, 16] and Soret and Dufour effects [20] on the flame. It is known that small scale turbulence can enter and disturb the reaction zone if the Ka is large enough, and that differential diffusion can affect the flame structure at high Ka.

In LES, large scale turbulent eddies are resolved down to a cut-off scale while the effect of sub-grid scales requires modelling. For turbulent premixed combustion, this modelling becomes more important as most of the chemical reactions occur at the sub-grid scale. LES models that are based on a reaction progress variable, c, [21–25], and are of interest in our a priori analysis, describe the flame using a resolved reaction progress variable, $\tilde{c}$, and its SGS variance, $\sigma_c^2 = \widetilde{c^2} - \tilde{c}^2$. For example, Lapointe et al. [26] showed in an a priori analysis that tabulated chemistry with presumed probability density function (PDF) parameterized by $\tilde{c}$ and σ_c^2 was able to provide a reasonable prediction of the reaction rate for high Ka flames. That study included flames up to Ka = 740.

Indeed, the sub-grid variance of the reaction progress variable has been shown to be strongly influenced by reaction, diffusion, dissipation, convection and their interactions at the SGS level [2] and the intense turbulence/flame interaction could greatly affect the evolution of σ_c^2 in high Ka flames. It is not fully understood how the relative importance of the various terms appearing in the transport of SGS variance changes in different regimes, an important question for the $\tilde{c}$-based models. Thus, the objective of this work is to investigate the behaviour of the SGS variance equation and its modelling in high Karlovitz number flames. For this purpose, DNS data of lean premixed methane-air flames with complex chemistry having Ka ranging from 4 up to 4100 is analysed. First, the importance of the various terms in the SGS variance equation is assessed and their behaviours with Ka is studied. Second, the existing models for the closure of the reaction, production and dissipation terms in the SGS variance equation are analysed and compared.

In section 2 the DNS data and numerical procedures are presented. In Section 3 the transport equation of SGS variance of the reaction progress variable and related models are introduced, and the behaviour of various terms involved in the equation at different Ka are assessed using an order-of-magnitude analysis. Section 4.1 presents DNS analysis of the terms in the SGS variance equation, and Section 4.2 presents a priori evaluation of the related models.

2. Numerical Simulations and Data Processing

Four DNS cases of statistically planar premixed flames of methane-air mixture at fuel-lean ($\phi = 0.6$), atmospheric pressure, and different turbulence intensity (Karlovitz numbers) are studied. Three out of the four cases (K100, K800 and K4100) are the same as those presented in [27], but with an increased simulation time. Thus, the quantitative results presented in [27] are relevant also for the current data set. The fourth case, K4, is new but uses the exact same configuration as the other cases except for the smaller turbulence intensity.

The simulation configuration involves an initially flat flame propagating in a rectangular channel of dimensions 10×5×5 mm. Figure 1 illustrates the set-up for the highest Ka number case: the flame region is highlighted by an ensemble of translucent iso-surfaces of H_2O mass fraction and vortical structures are identified by an iso-surface of λ_2 which is the intermediate eigenvalue of the strain rate tensor, S_{ij} [28].

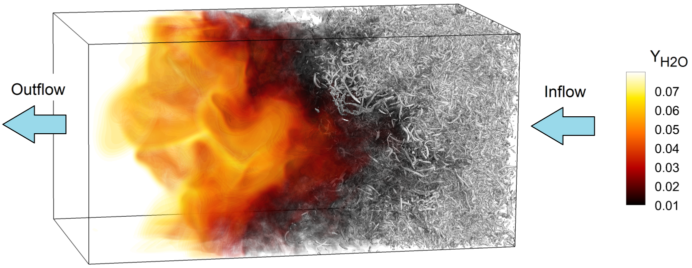

Figure 1: Illustration of case K4100. Translucent iso-surfaces of H_2O shows the flame brush and the iso-surface of $\lambda_2 = -4 \times 10^{11}$ s^{-1} shows vortical structures.

Periodic boundary conditions are imposed in the cross-stream directions and a zero-gradient boundary condition is imposed on the outlet boundary. For the inlet boundary, constant values of temperature ($T = 298$ K) and species are imposed while a turbulence boundary condition is used for the velocity components as described below.

To keep the flame near the centre of the domain the mean velocity $u_{in}(t)$ perpendicular to the inlet is adjusted such that the domain average fuel mass fraction is 50 % of the inlet value. On average this yields $u_{in} = X_L d(\langle Y_F \rangle / Y_{F,in})/dt$ where $\langle Y_F \rangle$ is the domain average fuel mass fraction, $Y_{F,in}$ is the fuel mass fraction at the inlet boundary and X_L is the domain length (distance from inlet to outlet). A lower limit of zero needs to be adopted for u_{in} to avoid numerical instabilities that can otherwise result from negative mean inlet velocity. The reason this is needed is that, in the early time of the simulation, the pre-heat zone is being broadened. This causes thermal expansion in the pre-heat zone which pushes the flame toward the outlet. The fluctuating velocity is given by extracting a section from a pre-generated turbulence field and the location where this section is extracted is moved through the pre-generated field at the speed u_{in} during the simulation. A homogeneous isotropic turbulence field for this purpose is generated as follows: A flow field with desired turbulence intensity and length scale is synthesized in a fully periodic cubic box by sampling sine waves of suitable wave numbers and amplitudes. The flow in this box is then simulated until a statistically stationary state is reached, quantified by convergence of the energy spectrum and the energy dissipation rate. Durring this simulation the turbulence intensity and length scale is maintained by low wavenumber forcing. The computed field is then stored and later used for the inlet boundary as well as the initial condition. The low-wavenumber forcing strategy used to pre-generate turbulence, which is also enabled during reactive simulations to maintain the turbulence intensity, works by injecting energy to low wavenumber modes through the addition of a source term in the momentum equation. Further details on this forcing method are provided in [29, 30].

All reactive flow simulations were initiated by a flat flame profile centred in the domain. This profile was obtained from a one-dimensional laminar freely propagating flame computed using the same thermochemical parameters and the same numerical solver that were used for the turbulent flames. Initial condition for the velocity field is set to the pre-generated turbulence field.

The governing equations for conservation of mass, momentum, energy and chemical species at low Mach number are discretized on a uniform cartesian grid and solved using a DNS solver, see Yu et al. [31] for a detailed description of the implementation and validation. The use of a low Mach number formulation is acceptable since the velocities are small compared to the sound speed everywhere in the domain. A 5th order weighted essentially non-oscillating (WENO) method is used for convective terms in the species and temperature equations while a 6th order central difference scheme is used for all other terms. The WENO method is used to improve the numerical stability in regions of strong gradients, such as across a flame. For time discretization a second order operator splitting scheme [32] is employed by performing integration of the chemical source terms between two half time-step integrations of the diffusion term. The integration of the diffusion term is further divided into smaller explicit steps to ensure stability and the overall time step is set to ensure a CFL number less than 0.1. Chemical source terms are integrated using the stiff DVODE solver [33]. The variable coefficient Poisson equation for pressure difference is solved using a multigrid method [34]. The skeletal chemical kinetic mechanism of Smooke and Giovangigli [35], which involves 16 species and 35 reactions, is used to model the combustion chemistry. Species diffusion coefficients, thermal conductivity and viscosity are mixture averaged based on the detailed properties for individual species obtained from the CHEMKIN thermodynamic database.

Important parameters for the different cases are summarized in Table 1. These include the turbulent intensity u'/S_L, Karlovitz number $\mathrm{Ka} = (u'^3/S_L^3 \cdot \delta_{th}/\ell_0)^{1/2}$, Damköhler number $\mathrm{Da} = \ell_0 S_L/(\delta_{th} u')$, the turbulence Reynolds number $\mathrm{Re}_0 = u'\ell_0/\nu_u$ and the flame Reynolds number $\mathrm{Re} = \mathrm{Ka}^2\mathrm{Da}^2$. Here, u' is the root mean square velocity fluctuation, ℓ_0 is the integral length scale, $S_L = 0.121$ m/s is the laminar flame speed, $\delta_{th} = (T_b - T_u)/|\nabla T|_{\max} = 0.917$ mm is the laminar thermal flame thickness where b and u denote burned and unburned states,

Table 1: Properties of the DNS data set: Integral length scale ℓ_0, Kolmogorov length scale η, velocity fluctuation u', turbulence intensity u'/S_L, Karlovitz number Ka, Damköhler number Da, Reynolds number Re_0, flame Reynolds number Re, ratio of flame thickness to Kolmogorov length scale, grid spacing h and number of grid cells N.

Case	K4	K100	K800	K4100
ℓ_0 (mm)	0.70	0.52	0.43	0.48
η (μm)	90	26	9.4	4.2
u' (m/s)	0.30	2.2	8.1	25
u'/S_L	2.5	18	67	210
Ka	4.5	100	800	4100
Da	0.30	0.032	0.0069	0.0025
Re_0	12	63	190	660
Re	1.9	11	31	110
δ_{th}/η	10	35	98	220
h (μm)	39.1	39.1	19.5	9.77
N	256×128^2	256×128^2	512×256^2	1024×512^2

respectively, and $\eta = (\nu^3/\varepsilon)^{1/4}$ is the Kolmogorov length scale of the unburned mixture. The laminar flame properties were evaluated in the same one-dimensional steady flame that was used for the initial condition. The quantities shown in Table 1 are evaluated using time averaged turbulence properties from the pre-generated turbulence fields used for boundary and initial conditions. The number of mesh cells N used to discretize the domain is also reported in Table 1 for each of the cases; these were chosen such that $h \lesssim \delta_{th}/20$ and $h \lesssim 2.1\eta$ [36] to ensure that both the flame and the turbulence are adequately resolved. The regime diagram for premixed flames [37] is shown in Fig. 2 illustrating that the cases span the regions traditionally considered to be the thin reaction zone and broken reaction zone regimes.

For the following analysis filtered quantities need to be computed from the DNS data. A LES filtered quantity, $\overline{\psi}$, is obtained by convolution with a Gaussian filter kernel as:

$$\overline{\psi}(\mathbf{x},t) = \iiint_V \psi(\mathbf{r},t) G_\Delta(\mathbf{x}-\mathbf{r})\ \mathrm{d}\mathbf{r} \tag{1}$$

where ψ is the quantity to be filtered, V is the computational domain and $G_\Delta(\mathbf{r})$ is a Gaussian filter kernel with filter width Δ. Filter width is conventionally defined by $\Delta^2 = s^2/12$ where s^2 is the variance of the Gaussian function [36]. For computation reasons, and to minimize truncation errors, the convolution product is performed using a Fourier transform as $\widehat{\overline{\psi}}(\mathbf{k}) = \widehat{\psi}(\mathbf{k})\widehat{G}(\mathbf{k})$ where $\widehat{}$ denotes Fourier transform and $\mathbf{k}$ is the wave vector. To be able to use Fourier transform the domain first needs to be made fully periodic. This is accomplished by mirroring the domain in the non-periodic x-direction, which makes the data periodic. Density weighted (Favre) filtered quantities will also be needed and these are computed as $\widetilde{\psi} = \overline{\rho\psi}/\overline{\rho}$.

A reaction progress variable based on H_2O mass fraction, $c = Y_{\mathrm{H2O}}/Y_{\mathrm{H2O,b}}$, is used

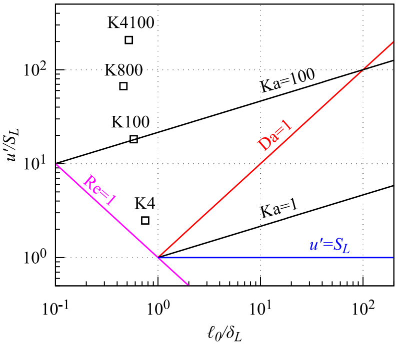

Figure 2: Regime diagram for premixed flames showing the condition of the present DNS simulations.

to describe the flame, where b denotes burned mixture. Instantaneous fields of c and its reaction rate $\dot{\omega}$ are shown for the four cases in Fig. 3, taken near the end of each simulation. As Ka increases, the flame and in particular its pre-heat zone become more perturbed and broadened as observed in the figure. Consistent with previous studies [12–17] it takes a Karlovitz number much above 100, or a reaction layer Ka much above 1, before the reaction layer is disturbed by turbulence. At Ka = 800 the flame is folded at smaller scales, and curved regions with radius of curvature comparable to the flame thickness become common. At a Ka of 4100 the internal structure is seen to be perturbed and the geometry of the reaction layer is complex. Extensive flame folding can potentially lead to formation of islands, and small scale mixing and straining create both broadened and thinned flame segments where reaction rates can locally be much higher than the peak value of its laminar counterpart. Large scale flame folding can also happen at low Karovitz numbers but is restricted in these simulations due to domain size. All this complexity is a manifestation of the interaction between reaction, convection and diffusion as described by the transport equations, thus, a successful LES simulation depends on this balance being mimicked well.

The transport equation for SGS variance of c, which is needed in the reaction progress variable based models of interest here, is also the result of interaction among reaction, convection and diffusion, and it is imperative to investigate this equation and its various terms in detail. This analysis is conducted in the next section.

3. Modelling of SGS variance

The transport equation for the SGS variance, $\sigma_c^2 = \widetilde{c^2} - \tilde{c}^2$, can be derived from the equation for c. This is done by first obtaining equations for $\widetilde{c^2}$ and $\tilde{c}^2$ and then subtracting them [38]. Following this method the transport equation for σ_c^2 in the LES framework is

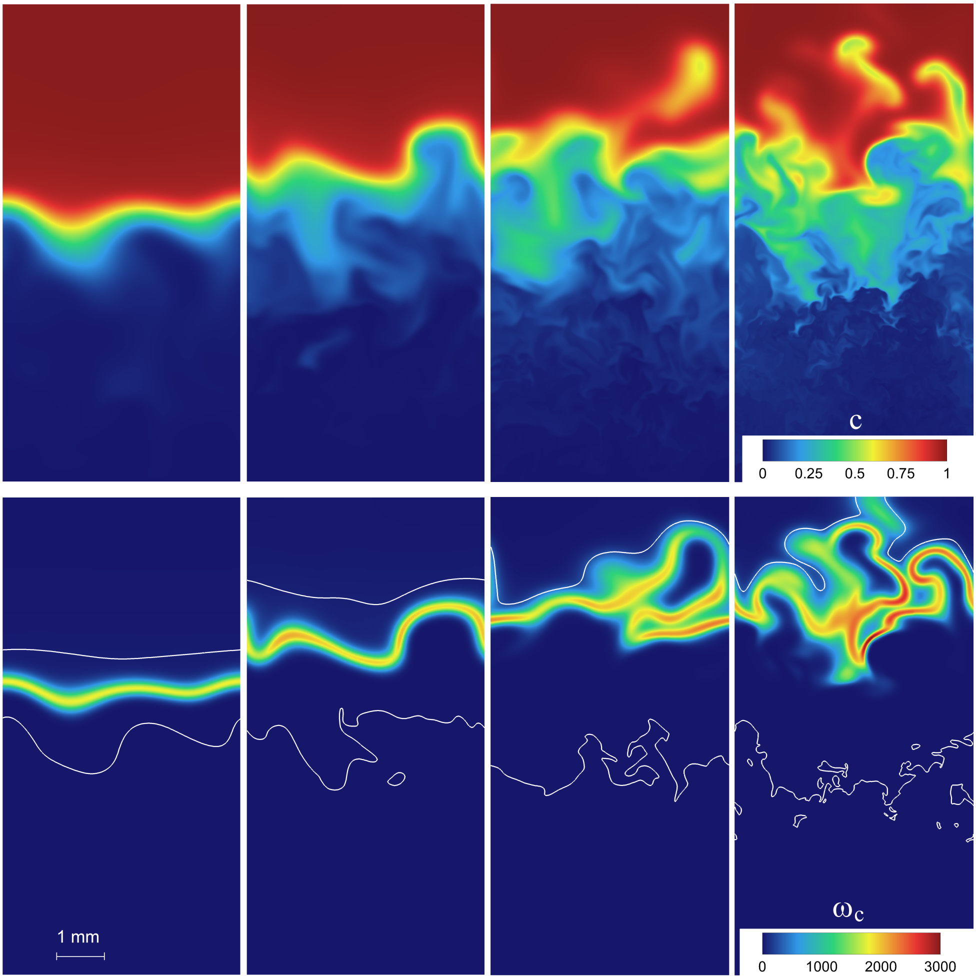

Figure 3: Progress variable c (top) and its reaction rate $\dot{\omega}_c$ [kg/m^3/s] (bottom). Cases from left to right: K4, K100, K800 and K4100. Lines show iso-contours corresponding to $c = 0.1$ and $c = 0.98$.

obtained as

$$\begin{aligned}\underbrace{\frac{\partial\overline{\rho}\sigma_c^2}{\partial t}}_{T_1} + \underbrace{\nabla\cdot\overline{\rho}\widetilde{\mathbf{u}}\sigma_c^2}_{T_2} = \underbrace{2(\overline{\dot{\omega}c} - \overline{\dot{\omega}}\tilde{c})}_{T_{\mathrm{chem}}} \underbrace{-2\left(\overline{\rho D\nabla c\cdot\nabla c} - \overline{\rho}\widetilde{D}\nabla\tilde{c}\cdot\nabla\tilde{c}\right)}_{T_{\mathrm{diss}}} \\ + \underbrace{\nabla\cdot\left(\overline{\rho D\nabla c^2} - \overline{\rho D}\nabla\tilde{c}^2\right) + 2\tilde{c}\nabla\cdot\left(\overline{\rho D}\nabla\tilde{c} - \overline{\rho D\nabla c}\right)}_{T_{\mathrm{diff}}} \\ \underbrace{-\nabla\cdot\left(\overline{\rho\mathbf{u}c^2} - \overline{\rho}\widetilde{\mathbf{u}}\widetilde{c^2}\right) + 2\nabla\cdot\left(\overline{\rho}\widetilde{\mathbf{u}c}\tilde{c} - \overline{\rho}\widetilde{\mathbf{u}}\tilde{c}^2\right)}_{T_{\mathrm{tran}}} \underbrace{-2\nabla\tilde{c}\cdot\left(\overline{\rho}\widetilde{\mathbf{u}c} - \overline{\rho}\widetilde{\mathbf{u}}\tilde{c}\right)}_{T_{\mathrm{prod}}}\end{aligned} \tag{2}$$

where $\mathbf{u}$ is velocity vector, $\dot{\omega}$ is the chemical source term of c and D is the diffusion coefficient of c. The two terms on the left hand side (LHS) are unsteady and advective terms, while the terms on the right hand side (RHS) represent SGS chemical processes, dissipation of σ_c^2, diffusion, and SGS transport and production of σ_c^2 through interaction of the SGS scalar flux and the gradient of $\tilde{c}$. The dissipation term will be expressed here for convenience as $T_{\mathrm{diss}} = -2\overline{\rho}\widetilde{\varepsilon}_c$, where $\widetilde{\varepsilon}_c$ is the SGS scalar dissipation rate (SDR).

The terms on the RHS of Eq. (2) need model closure in LES frameworks. The focus here is on the importance of the SDR and how this quantity balances out the chemical, production and transport terms at high Karlovitz numbers. Exact forms of all terms will be computed directly from DNS, while T_{diss}, T_{chem} and T_{prod} will also be compared with existing model closures in order to assess how these capture the related physics at different Karlovitz numbers and filter sizes.

The production term T_{prod} is often closed using a gradient hypothesis, $\overline{\rho}\widetilde{\mathbf{u}c} - \overline{\rho}\widetilde{\mathbf{u}}\tilde{c} \approx -\nu_{SGS}\nabla\tilde{c}/\mathrm{Sc}$, where ν_{SGS} is the SGS viscosity and $\mathrm{Sc} \approx 0.7$ is the SGS Schmidt number. The SGS viscosity is modelled using the Smagorinsky model,

$$\nu_{SGS} = C_s^2\Delta^2(\overline{S}_{ij}\overline{S}_{ij})^{1/2} \tag{3}$$

where $C_s = 0.17$ is a model constant [39, 36]. The reaction term will be compared with that obtained using a tabulated chemistry model [25]

$$\overline{\dot{\omega}c} - \overline{\dot{\omega}}\tilde{c} \approx \overline{\rho}\int_0^1 \frac{\dot{\omega}_L\zeta}{\rho}\widetilde{P}(\zeta;\tilde{c},\sigma_c^2)\,\mathrm{d}\zeta - \overline{\rho}\tilde{c}\int_0^1 \frac{\dot{\omega}_L}{\rho}\widetilde{P}(\zeta;\tilde{c},\sigma_c^2)\,\mathrm{d}\zeta \tag{4}$$

Here, $\dot{\omega}_L$ is the reaction rate of c in a one-dimensional unstrained laminar flame, ζ is the sample space variable for c and the PDF $\widetilde{P}$ is presumed using a β-distribution as in [25].

The modelling of the SGS scalar dissipation rate, $\widetilde{\varepsilon}_c$, is particularly challenging as the dissipation rate is related to reaction and is influenced by turbulence in premixed combustion. A first straightforward approach to close this term is to use a linear relaxation model:

$$\widetilde{\epsilon}_c = \frac{\nu_{SGS}}{\mathrm{Sc}A\Delta^2}\sigma_c^2 \tag{5}$$

where $A = 0.5$ is a model constant [40] and Δ is the LES filter width. This model is derived by assuming local equilibrium corresponding to a balance between dissipation and turbulent production of the SGS variance and thus it does not account for the effect of chemical reaction. This may result in an underestimation of $\widetilde{\varepsilon}_c$ as was observed in [25]. However, at large Karlovitz numbers T_{prod} becomes large and thus a linear relaxation model may be justified. This is investigated using an order of magnitude analysis (OMA) discussed in the next section. An alternative model for $\widetilde{\varepsilon}_c$ which takes into account both turbulent production and chemical reaction in the balance was proposed in [41] and successfully used in the past LES works (see for example [42–44]). This model is written as

$$\widetilde{\varepsilon}_c = \left[1 - \exp\left(-0.75\frac{\Delta}{\delta_{th}}\right)\right]\left[(2K_c - \tau C_4)\frac{S_L}{\delta_{th}} + C_3'\frac{\epsilon_k}{k}\right]\frac{\sigma_c^2}{\beta_c} \tag{6}$$

where k is the SGS turbulent kinetic energy with a dissipation rate ϵ_k, and it is computed directly from DNS in this work, and $K_c = 0.79\tau$, where $\tau = (T_b - T_u)/T_u$ is the heat release parameter. Laminar flame speed, S_L, thermal thickness, δ_{th}, and the heat release parameter, τ, are obtained from unstretched laminar flame calculations. The model constants in Eq. (6) are derived from DNS studies [41] and are non-tuneable, with the possible exception of β_c. The sub-grid SDR must also be proportional to a sub-grid flow dissipation time scale and this is given by the term involving $C_3' \approx 1.2\sqrt{\mathrm{K}_\Delta}/(1+\sqrt{\mathrm{K}_\Delta})$ in Eq. (6), where the parameter $\mathrm{K}_\Delta = \sqrt{\epsilon_k\,\delta_{th}}/S_L^{3/2}$. The factor C_4 also depends on K_Δ as $C_4 = 1.1/(1+\mathrm{K}_\Delta)^{0.4}$ and β_c is a model parameter with the value 2.4. The term in the first bracket of Eq. (6) ensures that $\widetilde{\varepsilon}_c$ disappears in the limit of small filters while the first and second term in the second bracket represent chemical and turbulent processes, respectively. The presented models for the reaction and SDR terms are evaluated in section 4.

3.1. Order of Magnitude Analysis

Order-of-magnitude analysis of the variance equation was performed in the RANS context in [45, 46], and in the LES context in [25]. These analyses found that, at large Da, the reaction and dissipation terms are the leading terms, while in the low Da limit turbulence production and dissipation are leading. The analysis in [45] and [46] was performed using flame scales and turbulence integral scales. However, in the LES context, gradients of filtered quantities should be considered to scale with the filter size Δ, as was done in [25], and the relative magnitude of several of the terms are found to depend on Δ.

In the OMA presented in [25] the various terms in Eq. (2) were scaled by $\rho_u S_L/\delta_{th}$ to enlighten the dependence on Da_Δ, the Damköhler number at the filter scale. For the scope of this work the OMA is re-written in terms of the Karlovitz number in order to highlight the dependence on this parameter. Following the arguments in [25] the terms in Eq. (2) are scaled as follows: The density, spatial derivatives of filtered quantities, the time derivative and the molecular diffusivity are scaled by ρ_u, Δ, Δ/U_{ref} and $S_L\delta_{th}$, respectively, where U_{ref} is a reference velocity associated to the large scales. The chemical reaction rate is scaled with $\rho_u S_L/\delta_{th}$ and the velocity in the turbulent transport and production terms is scaled with u'_Δ. Here $u'_\Delta = \sqrt{2k_\Delta/3}$ is a velocity associated to the filter scale and k_Δ is the sub-grid turbulent kinetic energy.

To bring Ka into the analysis, Ka has to be expressed in terms of the quantities used for the scaling. To derive a suitable expression it is assumed that the Reynolds number is sufficiently large for the inertial range to exist, and that the filter width Δ is within this range. In this case the Kolmogorov time scale scales as $\tau_k \sim \tau_0 \mathrm{Re}^{-1/2}$ and the chemical time scale scales as $\tau_c \sim \delta_{th}/S_L$. The time scale associated to the filter scale, $\tau_\Delta = \Delta/u'_\Delta$, can be related to the integral scales by $\tau_\Delta \sim \tau_0(\Delta/\ell_0)^{2/3}$ [36] where τ_0 and ℓ_0 are the time and length scales associated to the integral scale. The integral time scale can then be related to the filter scales by $\tau_0 \sim (\Delta/u'_\Delta)(\ell_0/\Delta)^{2/3}$. Now the Karlovitz number can be expressed as

$$\mathrm{Ka} = \frac{\tau_c}{\tau_k} \sim \frac{\delta_{th}\mathrm{Re}^{1/2}}{S_L \tau_0} \sim \frac{\delta_{th}}{S_L}\mathrm{Re}^{1/2}\frac{u'_\Delta}{\Delta}\left(\frac{\Delta}{\ell_0}\right)^{2/3} \tag{7}$$

By using $\eta \sim \mathrm{Re}^{-3/4}\ell_0$ where η is the Kolmogorv length scale [36] one finally obtains

$$\mathrm{Ka} \sim \frac{\delta_{th}u'_\Delta}{S_L\Delta}\left(\frac{\Delta}{\eta}\right)^{2/3} = \frac{\delta_{th}u'_\Delta}{S_L\Delta}\Delta_k^{2/3} \tag{8}$$

where a normalized filter size has been defined as $\Delta_k = \Delta/\eta$. In order to expose the dependence on Ka in Eq. (2) it is convenient to bring out the factor $\rho_u S_L/(\delta_{th}\Delta_k^{2/3})$ from all the terms, rather than $\rho_u S_L/\delta_{th}$ as was done in [25]. Using the previously described scalings and Eq. (8) one obtains the following order of magnitudes (after dropping the leading factor $\rho_u S_L/(\delta_{th}\Delta_k^{2/3})$):

$$\begin{aligned}
T_1 \sim T_2 &\sim \mathcal{O}\left(\frac{U_{\mathrm{ref}}}{u'_\Delta}\mathrm{Ka}\right) & T_{\mathrm{diff}} &\sim \mathcal{O}\left(\frac{\mathrm{Ka}}{\mathrm{Re}_\Delta}\right) \\
T_{\mathrm{diss}} &\sim \mathcal{O}\left(\Delta_k^{2/3}\right) & T_{\mathrm{chem}} &\sim \mathcal{O}\left(\Delta_k^{2/3}\right) \\
T_{\mathrm{tran}} &\sim \mathcal{O}\left(\mathrm{Ka}\right) & T_{\mathrm{prod}} &\sim \mathcal{O}\left(\mathrm{Ka}\right)
\end{aligned} \tag{9}$$

where $\mathrm{Re}_\Delta = u'_\Delta\Delta/(\delta_{th}S_L)$ is the Reynolds number at the filter scale. In Eq. (9) the sub-grid scalar dissipation rate in T_{diss} is scaled using the chemical time scale, $1/\widetilde{\varepsilon}_c \sim \delta_{th}/S_L$. In case the turbulent time scale τ_Δ is used instead, which may be appropriate at very high Ka, T_{diss} would instead scale as

$$T_{\mathrm{diss}} \sim \mathcal{O}\left(\frac{\rho_u S_L}{\delta_{th}\Delta_k^{2/3}} \cdot \mathrm{Ka}\right) \tag{10}$$

Due to the use of the filter size Δ_k in the scaling the terms in the above OMA should only be evaluated in relation to one another. For example, if Δ_k is increased and everything else is fixed, Eq. (9) predicts that the relative importance of T_{diss} and T_{chem} compared with the other terms increases, while the absolute magnitude of T_{diss} and T_{chem} is unaffected. The following comments are made with this in mind.

The appearance of Re_Δ in the scaling for T_{diff} implies that, for a fixed Ka, this term is negligible with respect to the turbulent transport term T_{tran} as one would expect. Unsteady and advective terms are instead never negligible even at small Ka unless the characteristic velocity of the flow is very small. Furthermore, the following points can be made using Eq. (9): (i) the reaction term, T_{chem}, does not increase with Ka like many other terms do, and it becomes negligible only when Ka is large and Δ_k is small. This means that, for a fixed Ka, T_{chem} can be neglected only if the LES resolution is high enough. As will be seen in the next section, at Ka=800 a filter size much smaller than the flame thickness is required for this to happen. (ii) The turbulent production and transport terms become large at high Ka as one would expect. This implies that the dissipation term mainly balances the reaction term at low Ka, while at intermediate and high Ka regimes the dissipation must balance the production, transport and chemical reaction terms, whose relative importance depends on Δ_k and Ka.

It is worth to note that all of the terms in Eq (2) must necessarily disappear as $\Delta \to 0$, indicating that the scaling above may only be valid at sufficiently large Δ_k where the filter operation has a significant effect.

After predicting the behaviour of the various terms by means of the above order of magnitude analysis, it would be interesting to observe the behaviour of the various terms in Eq. (2) while varying Ka and Δ when the length scale (η or ℓ_0 for example) is fixed, and in particular to observe the behaviour of term T_{diss} from DNS and how it compares to its modelling when different assumptions are made. This is the topic of the next section.

4. Results and Discussion

DNS data is used in the first half of this section to compare the behaviour and relative importance of the various terms in Eq. (2) at different Karlovitz numbers and filter sizes in the light of the observations made in OMA. In the second part of this section the models described in Section 3 are evaluated.

When various quantities ψ are presented as conditional averages on $\tilde{c}$ the following definition is used:

$$\langle \psi \mid \tilde{c} = c^* \rangle = \frac{\int_{t_1}^{t_2} \iiint_V \psi(\mathbf{x}, t) \cdot I_{c,\delta} \, \mathrm{d}\mathbf{x} \, \mathrm{d}t}{\int_{t_1}^{t_2} \iiint_V I_{c,\delta} \, \mathrm{d}\mathbf{x} \, \mathrm{d}t} \tag{11}$$

In Eq. (11), t_1 and t_2 are the times at which the sampling starts and ends, V is the computational domain and $I_{c,\delta} = H(\tilde{c} - c^* + \delta) - H(\tilde{c} - c^* - \delta)$ is a rectangular window function where H is the Heaviside function. The parameter δ, representing half the bin size, has a finite value of $\delta = 1/80$ resulting in a coarse-grained average.

When different filter sizes are used the largest meaningful filter is limited by the cross-stream domain size. Since the domain size is fixed at 5.5 times δ_{th} for all simulations presented here, the largest filter corresponds to a fixed value of $\Delta^+ = \Delta/\delta_{th} \approx 5$ for all cases. However, the largest meaningful filter size in terms of Δ_k, which is normalized by the Kolmogorov scale, is case dependent and ranges from about 50 for case K4 to about 1200 for case K4100. I tis sometimes convenient to use Δ^+ but the two filter sizes are simply related by $\Delta^+ = \Delta_k \cdot \eta/\delta_{th}$ (cf. Table 1 for the values of η/δ_{th}). For a fixed Ka, an increase of Δ^+ corresponds to an increase of Δ_k. An increase in Ka for a fixed Δ^+ also results in an increase of Δ_k. For example, the filter size of $\Delta^+ = 3.5$ corresponds roughly to a Δ_k of 35, 130, 300 and 700 for cases K4, K100, K800 and K4100, respectively.

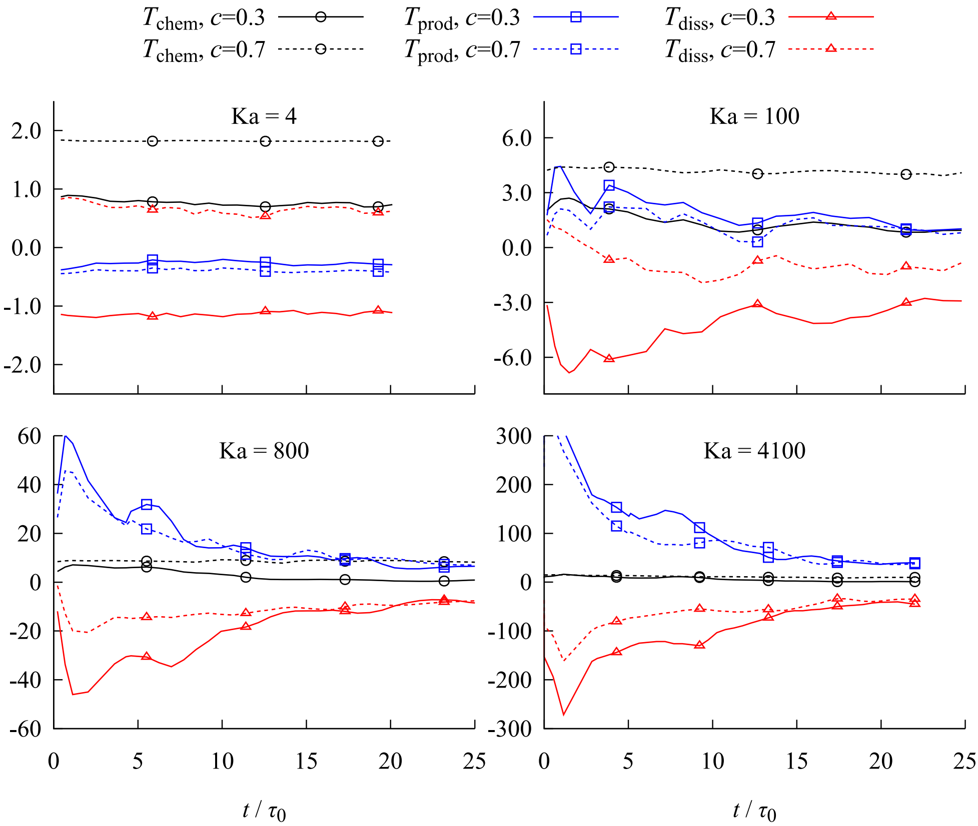

Figure 4: Time evolution of T_{chem}, T_{prod} and T_{diss} conditioned on $c = 0.3$ and $c = 0.7$ for $\Delta^+ = 1.0$. The terms are normalized by $\rho_u S_L/\delta_{th}/\Delta_k^{2/3}$.

Each of the simulations was performed over at least 20 integral time scales τ_0, and t_1 and t_2 were set to include only the last 10 integral time scales of each simulation to remove the initial transient stage from the statistical analysis. This was decided based on the time evolution of the terms T_{chem}, T_{prod} and T_{diss}, which is shown in Fig. 4 for $\Delta^+ = 1.0$ and conditioned on $c = 0.3$ and $c = 0.7$. The integral time scale is estimated as $\tau_0 = \ell_0/u'$. As a verification of the numerical accuracy of the post-processing, all terms of Eq. (2) were computed independently to calculate the imbalance (difference between left and right hand side of the equation). This maximum imbalance occurs for the K4100 case and is not larger than 5% of the peak value of T_{diss}.

4.1. DNS analysis of the variance equation

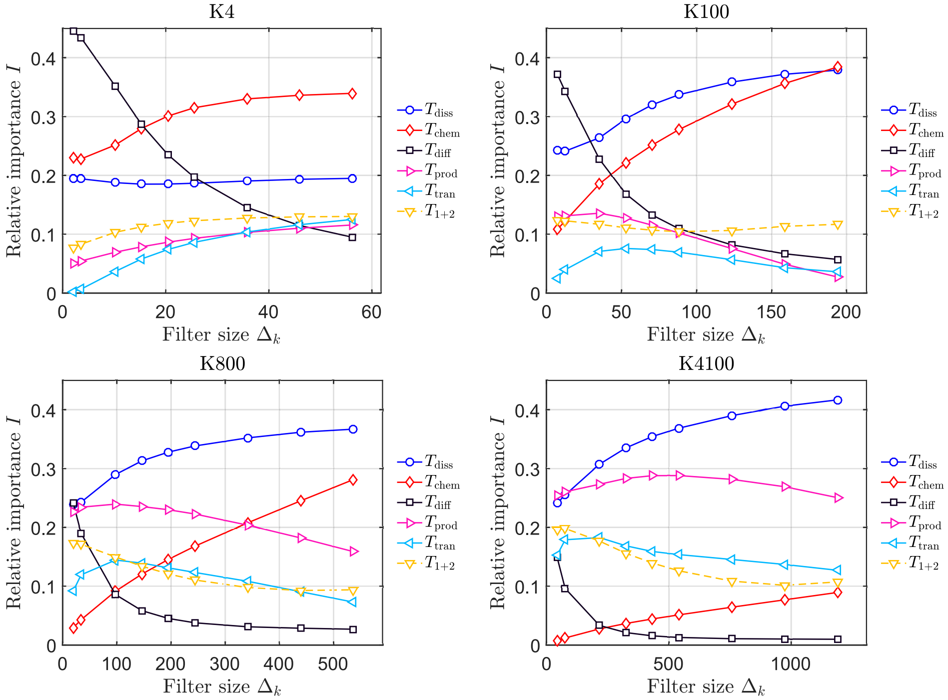

Figure 5: Relative importance of all terms in the variance equation as function of the filter size Δ_k for the four cases.

The exact form of the RHS terms of Eq. (2) computed from the four DNS flames is shown in Figure 6 as conditional averages. Three filter sizes are shown for each Ka, which are $\Delta^+ = 0.35$, 1.0 and 3.5. Note that the unsteady and advective terms, T_1 and T_2, which are in closed form in Eq. (2), are excluded for clarity. To provide a direct measure of the

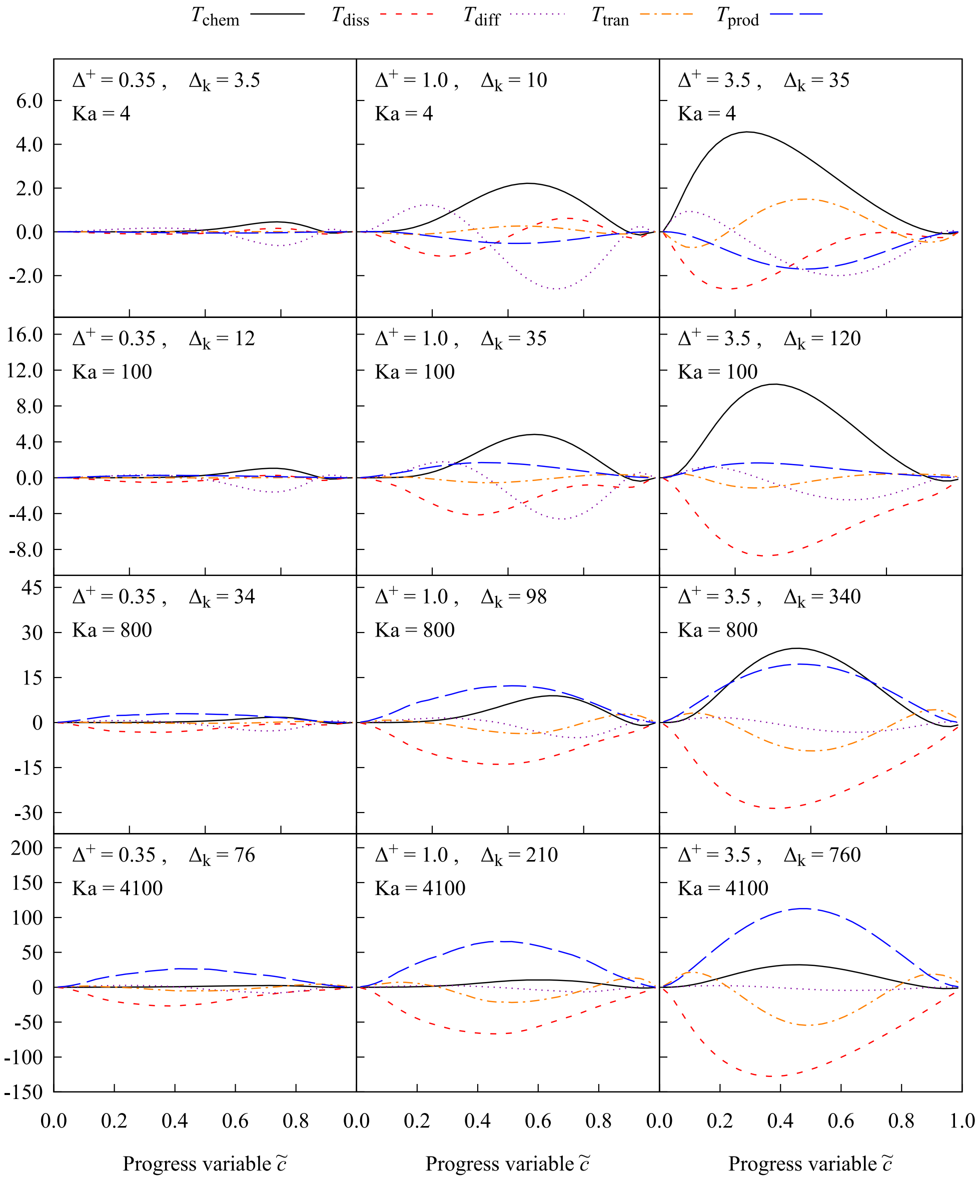

Figure 6: Conditional averages of the terms in variance equation. Four cases (top to bottom: K4, K100, K800, K4100) and three filter sizes (left to right: $\Delta^+ = 0.35$, 1.0 and 3.5) are shown. All terms are normalized by $\rho_u S_L/\delta_{th}/\Delta_k^{2/3}$.

relative importance of the different terms in Eq. (2), in addition to the conditional averages, Fig. 5 shows the integrated magnitude of each term normalized by the total magnitude of all terms as function of filter size Δ_k. This measure will be referred to as I and for a term T_k it is defined by

$$I_k = \frac{\int_{t_1}^{t_2} \iiint_V |T_k| \, \mathrm{d}\mathbf{x} \, \mathrm{d}t}{\sum_i \int_{t_1}^{t_2} \iiint_V |T_i| \, \mathrm{d}\mathbf{x} \, \mathrm{d}t} \tag{12}$$

In Eq (12) the sum is taken over all the terms T_{diff}, T_{chem}, T_{diss}, T_{prod}, T_{tran} and T_{1+2} where $T_{1+2} = T_1 + T_2$ is the sum of the transient and advective terms. Figure 5 and 6 are complementary; Fig. 5 shows which of the unclosed terms makes the largest contributions to the budget, and are therefore most important to model, under different conditions while Fig. 6 shows how the terms vary with c.

The molecular diffusion term, T_{diff}, is found to be important for small filter sizes but loses its importance as the filter size is increased. In the parameter range accessed by the present data T_{diff} is one of the terms that shows the largest variations. For example, for small filters in cases K4 and K100 it is the dominating term while for large filters in cases K800 and K4100 it is the smallest term and contributes less than 5% of the budget (as measured by the relative importance I defined above). The decrease with filter size is explained by the appearance of Re_Δ in the scaling as seen in the order of magnitude analysis. In Fig. 6 it is seen that the diffusion term T_{diff} acts as a source term for $\tilde{c} < 0.5$ and as a sink term for $\tilde{c} > 0.5$.

The chemical term, T_{chem}, is seen to increase in importance with increasing filter size for all cases. This is consistent with the Δ_k-scaling predicted by the OMA in Eq. (9). When discerning the trend with changing Ka at a fixed filter size the comparison is limited to values of Δ_k that are available for several of the plots in fig. 5. Comparison at fixed Δ_k shows that the chemical term T_{chem} loses importance with increasing Ka but remains important up to Ka = 800 for the filter sizes investigated. This suggests that, for any given Ka, there exists a filter size above which T_{chem} will be important when modelling the sub-grid variance equation.

For the dissipation term, T_{diss}, the situation is similar to that of T_{chem}. The relative importance increases with increasing Δ_k but with the exception of case K4 in which the importance is constant. The dissipation term gains importance going from case K4 to case K100 but apart from that there is no clear trend with increasing Ka. Furthermore, it is seen in both Figs. 6 and 5 that T_{diss} remains one of the most important terms at almost all investigated Ka and filter sizes; it is notable that its relative importance does not drop lower than $\sim 20\%$ for any investigated combination of Ka and Δ_k while all other terms do at least at some point drop below 10%. This observation gives some support to the alternative scaling presented in Eq. (10) where it was predicted that T_{diss} scales with Ka if the chemical time scale is long. If T_{diss} did not scale with Ka then it would lose importance to other terms that do have this scaling.

It may be expected that T_{diss} should be everywhere negative, as it is for constant density flow. This is not the case when density weighted Favre filtering is used, however, and this is seen in Fig. 6 for small filter sizes in mainly the K4 case where the appearance of positive values of the dissipation term is evident. This can be understood by inspecting $T_{\rm diss}$ which is of the form $\widetilde{\nabla c \nabla c} - \nabla \tilde{c} \nabla \tilde{c}$. If the filter operator were to commute with the gradient in the second term in this expression, as an unweighted filter does, then the positiveness of the expression follows from Cauchy-Schwarz inequality. However, since the density-weighted filter operation, which does not commute with the gradient, is used here there is no mathematical guarantee of the positiveness of this term. Thus, positive values of $T_{\rm diss}$ does occur in some cases and are mainly seen in laminar or weakly turbulent flames for small filters.

The remaining terms $T_{\rm prod}$, $T_{\rm tran}$ and T_{1+2} were all predicted to scale as Ka in the OMA with no particular dependence on Δ_k. The relative importance of these terms, however, does drop for large filter sizes due to the concurrent increase of the dissipation and reaction terms as seen in Fig. 5. At low Ka (cases K4 and K100) the three terms are of comparable importance but at high Ka (K800 and K4100) the production term $T_{\rm prod}$ stands out as the largest and it can reach an importance I above 25% for case K4100. This shows that modelling of the production term is especially relevant at high Ka.

From Fig. 6 it is also seen that the profiles of turbulent transport ($T_{\rm tran}$) and turbulent production ($T_{\rm prod}$) have opposite sign at small Ka compared with that at high Ka. In fact, the production term acts as a sink term at Ka = 4, although the sum of $T_{\rm prod}$ and $T_{\rm tran}$ remains positive. The changing sign of the production term does make it more challenging to model.

From the modelling perspective it is important to know which of the unclosed terms dominates for different flames and filter sizes. Referring to the order-of-magnitude analysis (Eqs. (9-10)) as well as Fig. 5, the following can be concluded: In the limit of large Δ_k, for a fixed Ka, there will be a balance of dissipation and chemical reaction (as well as transient and advective terms T_1 and T_2). In the limit of large Ka, for a fixed Δ_k, there will be a balance of dissipation and production. It should be kept in mind, however, that the latter limit may not be practically realizable since the resolution requirement, e.g. in terms of the 80% resolved kinetic energy criterion [36], to maintain Δ_k constant with increasing Ka would imply refining the grid and thus increase the computational cost. In most practical LES the filter size is larger than the flame thickness, $\Delta^+ > 1$, and $T_{\rm chem}$ will be non-negligible except in the case of both very high Ka and high resolution (small Δ_k). For most LES the filter size also fulfils $\Delta_k \gg 1$ so that, at high Ka, all terms except molecular diffusion ($T_{\rm diff}$) will have significant contributions.

Some further insight can be found for the dissipation term $T_{\rm diss}$ in Fig. 6. This term, which is the main sink in Eq. (2), must balance the contributions coming from turbulent production and chemical reaction, which are the main source terms. According to the observed relative magnitude between $T_{\rm chem}$ and $T_{\rm prod}$, the dissipation term increases in magnitude with the filter size and becomes rather independent of Ka for low and intermediate values of Ka. This is because at these Ka the SGS scalar dissipation rate $\widetilde{\varepsilon}_c$, appearing in $T_{\rm diss}$, is more likely to scale with the inverse of a chemical time scale, as discussed in section 3.1. At very high Ka, in combination with small Δ^+, the turbulent time scale τ_Δ becomes a more relevant scale for $\widetilde{\varepsilon}_c$ and eventually $T_{\rm diss}$ is balanced entirely by the production term $T_{\rm prod}$. This suggests that a linear relaxation model for T_{diss} would be appropriate in the limit of very high Ka.

4.2. Modelling of the variance equation

As discussed in the previous subsection, the relative magnitudes of the production, dissipation and chemical reaction terms (T_{prod}, T_{diss} and T_{chem}) in the SGS variance equation, Eq. (2), depend on Ka and at high Ka they can all be significant. This has to be captured in LES modelling and it is thus of interest to explore how common LES closures for these three terms perform at different Ka and filter sizes.

4.2.1. Modelling of the dissipation term

The dissipation term, T_{diss}, is seen to always be of significant magnitude. A comparison of two common LES closures, defined in Eqs. (5) and (6), for T_{diss} in the context of $\tilde{c}$-modelling is presented next. In Fig. 7 the dissipation term T_{diss} (square symbols) obtained from DNS is compared with those computed using the linear relaxation model, Eq. (5) (dash-dotted lines), and that proposed by Dunstan et al. [41], Eq. (6) (short-dashed lines). The terms are shown as conditional averages for the four different cases and two filter sizes, $\Delta^+ = 1.0$ and 3.5. In the figure the filter size is also given in terms of Δ_k based on η in the upstream turbulence in the unburned mixture for each case. First, one can notice that the dissipation term is severely under-predicted by the linear relaxation model for all Karlovitz numbers and both filter sizes; this may be explained by the fact that this model was not intended for reactive scalars and an adjustment of the model constant A can therefore be motivated. Comparison of the short-dashed lines and squares in Fig. 7 indicates that the model given by Eq. (6) does capture the right order of magnitude for the larger filter size, although under-prediction occurs for small filters and to some extent also for larger Ka. This shows that scaling of the model constants, β_c and A, is relevant for practical LES. The models depend on Δ and Ka and they have to be chosen carefully in a LES. Their value can be found using, when possible, a dynamic approach as was done for β_c in [25], or choosing the constant from a DNS database. How to optimally scale these constants is not the focus here and will be the topic of a future study.

The ability of the dissipation term closures to reproduce the right profile in the $\tilde{c}$-coordinate is instead explored next. In order to compare the shape of the profiles the modelled dissipation terms are scaled to match the peak magnitude of T_{diss} from the DNS. The scaled terms are denoted T^*_{diss} and are shown as solid and long-dashed lines in Fig. 7. From the plots it is seen that both models predict the shape well, except at the combination of low Ka and small filter where both models fail and the combination of large filter and very high Ka where Eq. (5) tends to predicts a peak position shifted towards higher $\tilde{c}$. Overall the functional form of Eq. (5) seems to be more prone to error and predictions from the scaled Eq. (6) remain more accurate as this model accounts for chemical processes.

For the scaled plots of Eq. (6) in Fig. 7 it can be inferred that the model constant, β_c, depends on Δ^+ and Ka. Figure 8 shows how the model constants β_c and A vary with Ka, Δ^+ and Δ_k. It is seen that β_c increases with increasing Δ^+ and Δ_k; this trend is true for the full range of Δ^+ and Ka accessible by the current data. Also, for filter sizes $\Delta^+ > 1$ the

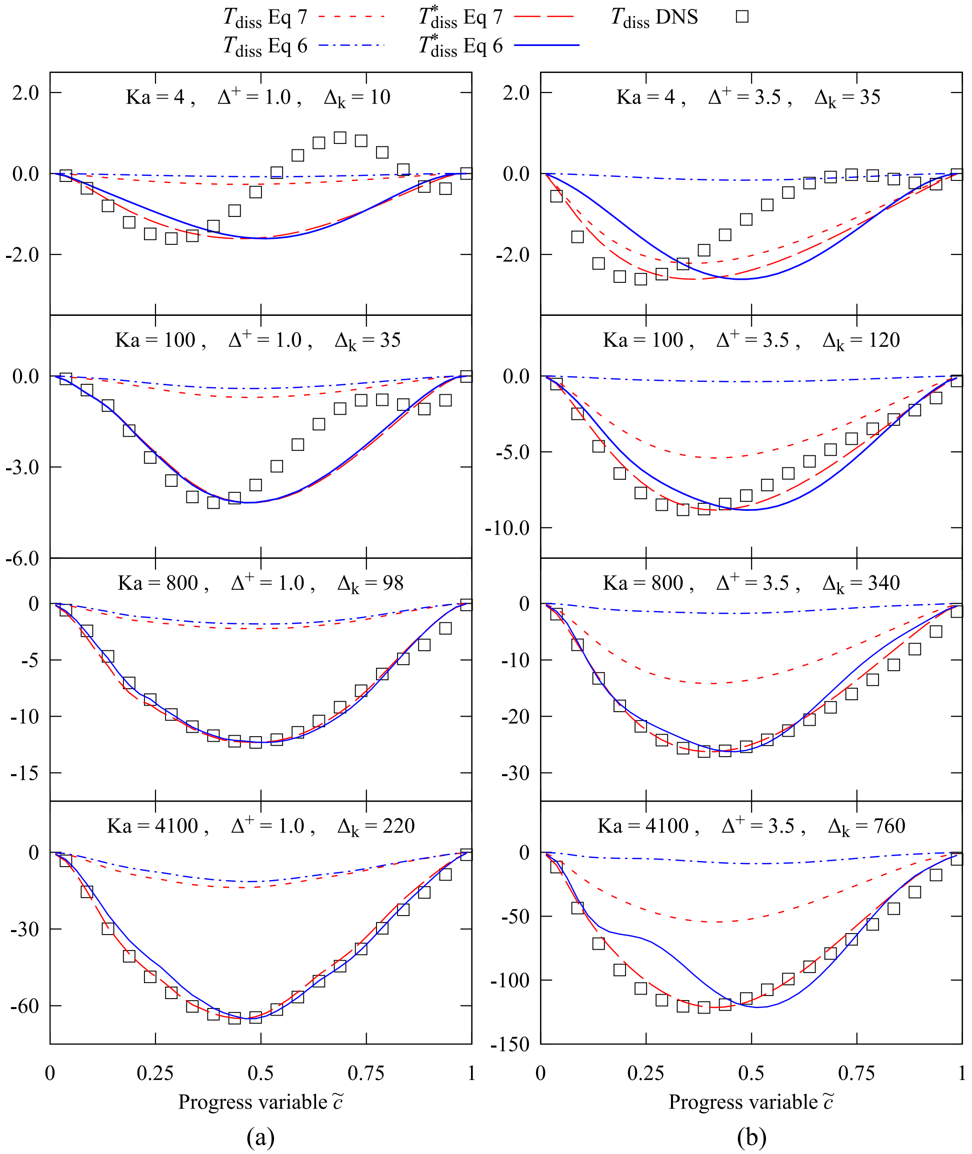

Figure 7: Conditional variations of T_{diss} (squares) compared with the models of Eq. (5) and (6) (dashed lines). The solid lines show scaled versions of the models, normalised to match the DNS peak value. The filter size is (a)$\Delta^+ = 1.0$ and (b) $\Delta^+ = 3.5$. Corresponding values of Δ_k are given in the figure. The terms are normalized by $\rho_u S_L/\delta_{th}/\Delta_k^{2/3}$.

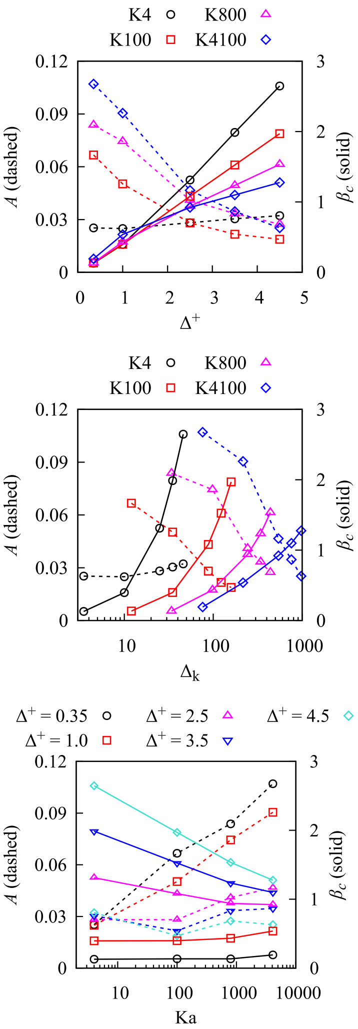

Figure 8: Values of the model constants β_c (solid lines) and A (dashed lines) after scaling to match the peak value to the DNS result. The figure shows the dependence of these model constants on Δ^+, Δ_k and Ka.

value of β_c decreases with increasing Ka. This trend of β_c is consistent with the physical definition of this parameter. Indeed, β_c can be defined as [47, 48]:

$$\beta_c \frac{\bar{\rho}\tilde{\epsilon}_c^2}{\sigma_c^2} = -\underbrace{2\mathcal{D}(\nabla c \cdot \nabla \dot{\omega}_c)}_{T_4} + \underbrace{2\rho\mathcal{D}^2(\nabla\nabla c : \nabla\nabla c)}_{D_2} \tag{13}$$

Thus, β_c is strongly influenced by the curvature of the flame (through D_2) and ∇c and $\nabla\dot{\omega}_c$. As Ka increases, the curvature of the flame increases due to the intense turbulence which leads to an increase in D_2, while the flame thickness induces a decrease in T_4 (as ∇_c and $\nabla\dot{\omega}_c$ decreases). This then leads to a decrease in β_c. The corresponding trends for the parameter A in Eq. (5) are not as regular, in particular the K4 case shows a deviating behaviour, but it can be seen that A does decrease with Δ^+ and Δ_k for Ka ≥ 100. As a function of Ka, A is decreasing for large filters and remains constant or slowly increasing for small filters. For the most part, A shows an opposite trend to β_c variations.

4.2.2. Modelling of the chemical reaction term

For practical values of Δ^+ the magnitude of the dissipation term, T_{diss}, is strongly influenced by the reaction term at low Ka and by a combination of reaction and turbulent production at higher Ka as discussed in Section 4.1. Modelling the dissipation term accurately is not sufficient if the reaction term is not modelled with similar accuracy, as the balance between dissipation, turbulent production and chemical reaction would be affected by an incorrect estimation of T_{chem}. In Fig. 9 a comparison between the reaction term T_{chem} from DNS (squares) and that obtained using the tabulation approach of Eq. (4) (dashed line) is shown. This closure seems to predict the term T_{chem} well at high Ka but a discrepancy can be observed for Ka 4 and 100 for the larger filter size. The maximum error is observed to be about 25% near the peak at Ka $= 4$ and 100 for $\Delta^+ = 3.5$. Past studies ([49, 50]) showed that higher errors due to the beta-PDF can be expected for low Ka. However, the error is again lower for larger Ka (800 and 4100), suggesting that this evaluation is not straightforward. Additional studies will be needed to shed light on this non-trivial behaviour.

4.2.3. Modelling of the turbulent production term

Finally, the modelling of the turbulent production term T_{prod} is assessed using a gradient hypothesis. In Fig. 9 conditional averages are shown for T_{prod} obtained from DNS (circles) as well as the gradient hypothesis model (dot-dashed lines). In case K4 this hypothesis does not work and the model ends up predicting the wrong sign due to negative correlation. In case K100 the model seems to work well. For even higher Ka considerable under-prediction is observed.

However, at the higher Ka, 800 and 4100, the model prediction does improve when the filter size is decreased and the best match is observed for the combination $\Delta^+ \leq 1$ and Ka$\geq$ 100. While it is not certain why the prediction is poor with a large filter size, some reasons that may play a role include: over-estimation of the turbulent Schmidt number that leads to too small production, and the use of filter sizes comparable to the integral scale. It is possible that dynamic approaches for ν_{SGS} and Sc may improve the prediction of T_{prod}, a topic that deserves further study.

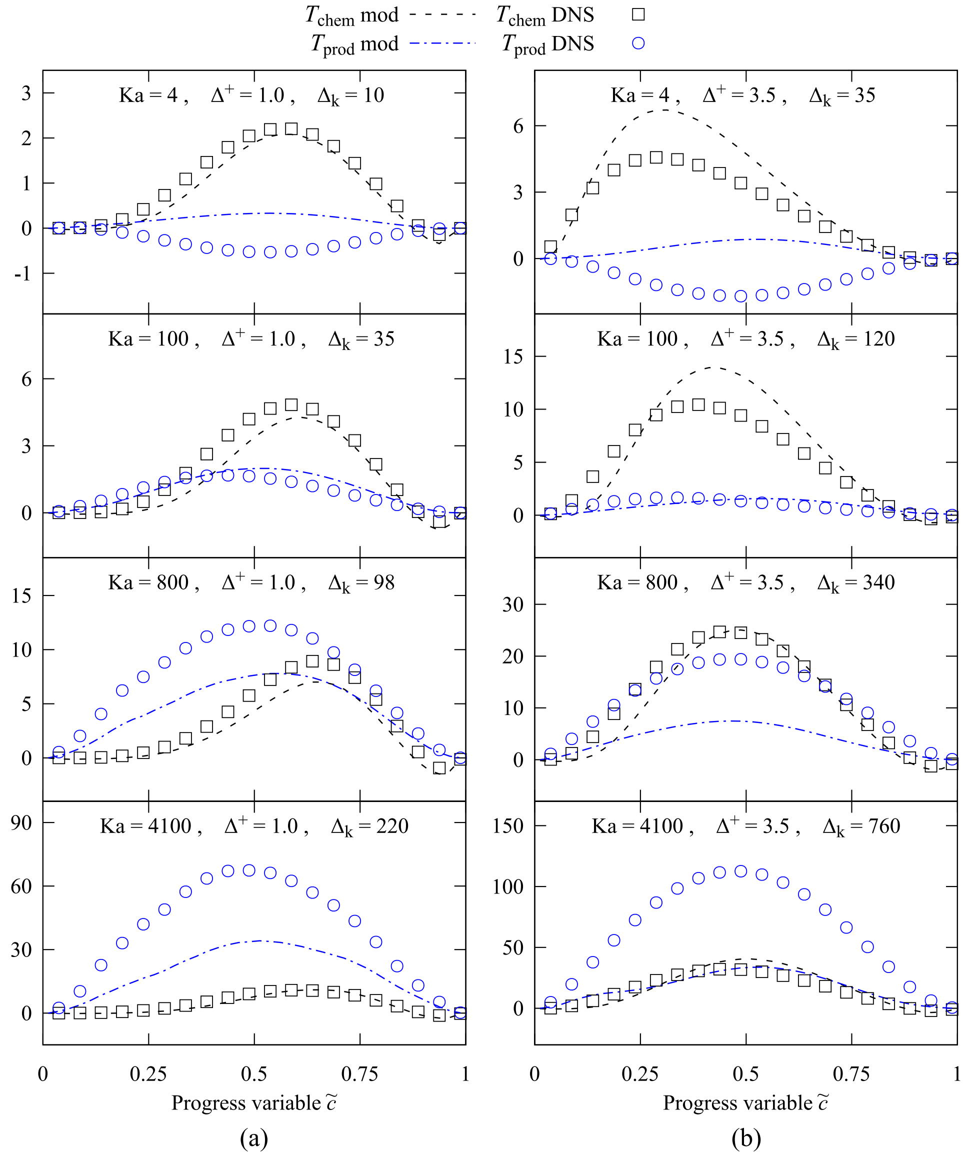

Figure 9: Conditional variations of T_{chem} (squares) and T_{prod} (circles) compared with corresponding models (dashed lines). The filter size is (a) $\Delta^+ = 1.0$ and (b) $\Delta^+ = 3.5$. Corresponding values of Δ_k are given in the figure. The terms are normalized by $\rho_u S_L/\delta_{th}/\Delta_k^{2/3}$.

5. Conclusions

Direct numerical simulations of premixed methane-air flames for low and high Ka have been performed to investigate the behaviour of different terms in the transport equation for progress variable SGS variance in different combustion regimes. This equation is of particular relevance for progress variable based models in LES frameworks. The relative scaling of these terms was also analysed by an order-of-magnitude analysis. Moreover, the accuracy of two common LES closures of the scalar dissipation term as well as closures for the chemical reaction and turbulent production terms, were assessed at both low and high Ka for different normalized filter sizes Δ_k. The main results are summarized in the following.

- The relative importance of the chemical term decreases with Ka and increases with Δ_k. Both the DNS data and the order-of-magnitude analysis supports this result. The importance of the chemical term must be considered in relation with LES resolution and under a combination of both high Ka and large Δ_k this term can be important. It is observed that, at a Ka of 800, the chemical term is one of the largest terms for filter sizes of the order of the laminar flame thickness or larger. At Ka as high as 4100, the chemical term is still seen to gain significance with Δ for all filter sizes accessible with the current data. It is implied that the chemical term is non-negligible for most practical combinations of Ka and Δ. It was also seen that a simple tabulation approach can model the chemical term well at all investigated filter sizes and Karlovitz numbers.

- Molecular diffusion in the variance equation is an important term only for small filters and low Ka. The term was observed to contribute as much as 40% of the budget in a case with small filter and low Ka, while it made a negligible contribution in a case with large filter and high Ka.

- The turbulent transport and production terms gains higher relative importance when Ka increases. This conclusion is supported by the DNS data and the OMA. It was also found, however, that the production term changes sign and becomes a sink term at small Ka. Modelling of the production term by a gradient transport approximation with the sub-grid viscosity estimated by a constant coefficient Smagorinsky model was found to be insufficient in most cases. Further studies, including dynamic modelling approaches, will be needed for this term.

- The dissipation term is the main sink term in the variance equation, except in some cases with small filters where molecular diffusion can also be an important sink. Since the dissipation term on average has to balance the sources due to turbulent production and chemical reaction, the dissipation term ends up being always one of the leading terms. At high Ka, when the Kolmogorov time scale is short compared with the chemical time scale, the relative importance of the dissipation term also changes from a scaling with filter size at low Ka to a scaling with Ka at high Ka. The modelling of the dissipation term is therefore crucial and needs to account for both turbulent and chemical processes. Two different closures were compared for the dissipation term, including the model proposed in [41] which is developed for reactive scalars, and a linear relaxation model which is commonly used for passive scalars. It was found that, while both models require their constants to be selected with care, the linear relaxation model is less likely to predict the right functional form of the conditionally averaged dissipation term. The adjusted model constant in the model from [41] also appears to follow a more consistent trend with Ka and Δ compared with the model constant of the linear relaxation model.

To conclusively confirm the trends observed in this paper, and in particular the behaviour of models, further work is needed including studies of a wider range filter sizes Δ^+, length scales ℓ_0 and flame parameters S_L, δ_{th} and τ. Dynamic approaches exist for the model constants β_c and C_s which may improve the prediction of the dissipation and production terms and reduce the need for calibration, and future work should also consider such approaches.

Acknowledgements

The authors at LU acknowledges funding from the Swedish Research Council (VR) and the national Centre for Combustion Science and Technology (CeCOST). We acknowledge PRACE for awarding us access to MareNostrum at Barcelona Supercomputing Center (BSC), Spain and SuperMUC at GCS@LRZ, Germany. Computations were also performed on resources provided by the Swedish National Infrastructure for Computing (SNIC) at PDC and HPC2N. IL and NS acknowledge funding from the Clean Sky 2 Joint Undertaking under the European Union's Horizon 2020 Research and Innovation Programme under grant agreement No 686332. NAKD acknowledges the support of the Qualcomm European Research Studentship Fund in Technology.

[1] D. Dunn-Rankin, P. Therkelsen, Lean combustion: technology and control, Academic Press, 2016.

[2] N. Swaminathan, K. N. C. Bray, Turbulent Premixed Flames, Cambridge University Press, 2011.

[3] T. Lieuwen, V. McDonell, E. Petersen, D. Santavicca, Fuel Flexibility Influences on Premixed Combustor Blowout, Flashback, Autoignition, and Stability, J. Eng. Gas Turbines Power 130 (2008) 011506.

[4] R. W. Bilger, Future progress in turbulent combustion research, Prog. Energy Combust. Sci. 26 (2000) 367–380.

[5] B. Zhou, C. Brackmann, Q. Li, Z. Wang, P. Petersson, Z. Li, M. Aldén, X. S. Bai, Distributed reactions in highly turbulent premixed methane/air flames. Part I. Flame structure characterization, Combust. Flame 162 (2015) 2937–2953.

[6] M. J. Dunn, A. R. Masri, R. W. Bilger, A new piloted premixed jet burner to study strong finite-rate chemistry effects, Combust. Flame 151 (2007) 46–60.

[7] B. Savard, B. Bobbitt, G. Blanquart, Structure of a high Karlovitz n-C7H16 premixed turbulent flame, Proc. Combust. Inst. 35 (2015) 1377–1384.

[8] S. Lapointe, G. Blanquart, Fuel and chemistry effects in high Karlovitz premixed turbulent flames, Combust. Flame 167 (2016) 294–307.

[9] A. J. Aspden, J. B. Bell, S. E. Woosley, Distributed flames in type Ia supernovae, The Astrophysical Journal 710 (2010) 1654–1663.

[10] H. Carlsson, R. Yu, X. S. Bai, Direct numerical simulation of lean premixed CH4/air and H2/air flames at high Karlovitz numbers, Int. J. Hydrogen Energy 39 (2014) 20216–20232.

[11] A. J. Aspden, A numerical study of diffusive effects in turbulent lean premixed hydrogen flames, Proc. Combust. Inst. 36 (2017) 1997–2004.

[12] W. L. Roberts, J. F. Driscoll, M. C. Drake, L. P. Goss, Images of the quenching of a flame by a vortex—to quantify regimes of turbulent combustion, Combustion and Flame 94 (1993) 58–69.

[13] M. J. Dunn, A. R. Masri, R. W. Bilger, R. S. Barlow, G. H. Wang, The compositional structure of highly turbulent piloted premixed flames issuing into a hot coflow, Proc. Combust. Inst. 32 (2009) 1779–1786.

[14] A. Y. Poludnenko, E. S. Oran, The interaction of high-speed turbulence with flames: Global properties and internal flame structure, Combust. Flame 162 (2015) 995–1011.

[15] S. Srinivasan, S. Menon, Linear eddy mixing model studies of high Karlovitz number turbulent premixed flames, Flow, Turbul. Combust. 93 (2014) 189–219.

[16] S. Lapointe, B. Savard, G. Blanquart, Differential diffusion effects, distributed burning, and local extinctions in high Karlovitz premixed flames, Combust. Flame 162 (2015) 3341–3355.

[17] R. Sankaran, E. R. Hawkes, C. S. Yoo, J. H. Chen, Response of flame thickness and propagation speed under intense turbulence in spatially developing lean premixed methane-air jet, Combust. Flame 162 (2015) 3294–3306.

[18] H. Wang, E. R. Hawkes, J. H. Chen, B. Zhou, Z. Li, M. Aldén, Direct numerical simulations of a high Karlovitz number laboratory premixed jet flame – an analysis of flame stretch and flame thickening, J. Fluid Mech. 815 (2017) 511–536.

[19] S. Chaudhuri, H. Kolla, H. L. Dave, E. R. Hawkes, J. H. Chen, C. K. Law, Flame thickness and conditional scalar dissipation rate in a premixed temporal turbulent reacting jet, Combust. Flame 184 (2017) 273–285.

[20] A. J. Aspden, M. S. Day, J. B. Bell, Turbulence-chemistry interaction in lean premixed hydrogen combustion, Proc. Combust. Inst. 35 (2015) 1321–1329.

[21] O. Colin, F. Ducros, D. Veynante, T. Poinsot, A thickened flame model for large eddy simulations of turbulent premixed combustion, Phys. Fluids 12 (2000) 1843–1863.

[22] C. D. Pierce, P. Moin, Progress-variable approach for large-eddy simulation of non-premixed turbulent combustion, J. Fluid Mech. 504 (2004) 73–97.

[23] G. Wang, M. Boileau, D. Veynante, K. Truffin, Large eddy simulation of a growing turbulent premixed flame kernel using a dynamic flame surface density model, Combust. Flame 159 (2012) 2742–2754.

[24] V. Moureau, B. Fiorina, H. Pitsch, A level set formulation for premixed combustion LES considering the turbulent flame structure, Combust. Flame 156 (2009) 801–812.

[25] I. Langella, N. Swaminathan, Unstrained and strained flamelets for LES of premixed combustion, Combust. Theory Model. 20 (2016) 410–440.

[26] S. Lapointe, G. Blanquart, A priori filtered chemical source term modeling for LES of high Karlovitz number premixed flames, Combust. Flame 176 (2017) 500–510.

[27] T. Nilsson, H. Carlsson, R. Yu, X. S. Bai, Structures of turbulent flames in the high Karlovitz number regime - DNS analysis, Fuel 216 (2018) 627–638.

[28] J. Jeong, F. Hussain, On the identification of a vortex, J. Fluid Mech. 285 (1995) 69–94.

[29] R. Yu, N. Lipatnikov, DNS study of dependence of bulk consumption velocity in a constant-density reacting flow on turbulence and mixture characteristics, Phys. Fluids 29 (2017) 065116.

[30] S. Ghosal, T. S. Lund, P. Moin, K. Akselvoll, A dynamic localization model for large-eddy simulation of turbulent flows, J. Fluid Mech. 286 (1995) 229–255.

[31] R. Yu, J. Yu, X. S. Bai, An improved high-order scheme for DNS of low mach number turbulent reacting flows based on stiff chemistry solver, J. Comp. Phys. 231 (2012) 5504–5521.

[32] G. Strang, On the construction and comparison of difference schemes, Siam J. on Num. Anal. 5 (1968) 506–517.

[33] P. N. Brown, G. D. Bryne, A. C. Hindmarsch, VODE, a variable-coefficient ode solver, Siam J. Sci. Stat. Comp. 10 (1989) 1038–1051.

[34] R. Yu, X. S. Bai, A semi-implicit scheme for large eddy simulation of piston engine flow and combustion, Int. J. Numerical Methods in Fluids 71 (2013) 13–40.

[35] M. Smooke, V. Giovangigli, Reduced Kinetic Mechanisms and Asymptotic Approximation for methane-air Flames, Springer-Verlag, Berlin, 1991.

[36] S. B. Pope, Turbulent Flows, Cambridge University Press, Cambridge, 2000.

[37] N. Peters, The turbulent burning velocity for large-scale and small scale turbulence, J. Fluid Mech. 384 (1999) 107–132.

[38] C. Jimenez, F. Ducros, B. Cuenot, B. Bedat, Subgrid scale variance and its dissipation of a scalar field in large eddy simulations, Phys. Fluids 13 (2001) 1748–1754.

[39] D. K. Lilly, The representation of small-scale turbulence in numerical experiments, Proc. IBM Scientific Computing Symp. on Environmental Sciences (1967) 195–210.

[40] H. Pitsch, Large-eddy simulation of turbulent combustion, Annu. Rev. Fluid Mech. 38 (2006) 453–482.

[41] T. D. Dunstan, Y. Minamoto, N. Chakraborty, N. Swaminathan, Scalar dissipation rate modelling for large eddy simulation of turbulent premixed flames, Proc. Combust. Inst. 34 (2013) 1193–1201.

[42] I. Langella, N. Swaminathan, R. W. Pitz, Application of unstrained flamelet SGS closure for multi-regime premixed combustion, Combust. Flame 173 (2016) 161–178.

[43] I. Langella, N. Swaminathan, Y. Gao, N. Chakraborty, Assessment of dynamic closure for premixed combustion large eddy simulation, Combust. Theory Model. 19 (2015) 628–656.

[44] Z. Chen, S. Ruan, N. Swaminathan, Large Eddy Simulation of flame edge evolution in a spark-ignited methane–air jet, Proc. Combust. Inst. 36 (2017) 1645–1652.

[45] O. R. Darbyshire, N. Swaminathan, S. Hochgreb, The Effects of Small-Scale Mixing Models on the Prediction of Turbulent Premixed and Stratified Combustion, Combustion Science and Technology 182 (2010) 1141–1170.

[46] A. J. Aspden, M. S. Day, J. B. Bell, Turbulence–flame interactions in lean premixed hydrogen: transition to the distributed burning regime, J. Fluid Mech. 680 (2011) 287–320.

[47] N. Swaminathan, K. N. C. Bray, Turbulent Premixed Flames, Cambridge University Press, 2011.

[48] G. Ghiasi, N. A. K. Doan, N. Swaminathan, B. Yenerdag, Y. Minamoto, M. Tanahashi, Assessment of sgs closure for isochoric combustion of hydrogen-air mixture, Int. J. Hydrogen Energy 43 (2018) 8105–8115.

[49] B. Fiorina, R. Vicquelin, P. Auzillon, N. Darabiha, O. Gicquel, D. Veynante, A filtered tabulated chemistry model for les of premixed combustion, Combust. Flame 157 (2010) 465–475.

[50] I. Langella, N. Swaminathan, F. A. Williams, J. Furukawa, Large-Eddy Simulation of Premixed Combustion in the Corrugated-Flamelet Regime, Combustion Science and Technology 188 (2016) 1565–1591.

Paper III

Filtered reaction rate modelling in moderate and high Karlovitz number flames: an a priori analysis

Thommie Nilsson[a], Rixin Yu[a], Nguyen Anh Khoa Doan[b], Ivan Langella[c], Nedunchezhian Swaminathan[d], Xue-Song Bai[a]

[a]*Department of Energy Sciences, Lund University, Lund, Sweden*
[b]*Institute for Advanced Study and Department of Mechanical Engineering, Technical University of Munich, Germany*
[c]*Department of Aeronautical and Automotive Engineering, Loughborough University, United Kingdom*
[d]*Department of Engineering, University of Cambridge, United Kingdom*

Abstract

Direct numerical simulations (DNS) of statistically planar flames at moderate and high Karlovitz number (Ka) have been used to perform an a priori evaluation of a presumed-PDF model approach for filtered reaction rate in the framework of large eddy simulation (LES) for different LES filter sizes. The model is statistical and uses a presumed shape, based here on a beta-distribution, for the sub-grid probability density function (PDF) of a reaction progress variable. Flamelet tabulation is used for the unfiltered reaction rate. It is known that presumed PDF with flamelet tabulation may lead to over-prediction of the modelled reaction rate. This is assessed in a methodical way using DNS of varying complexity, including single-step chemistry and complex methane/air chemistry at equivalence ratio 0.6. It is shown that the error is strongly related to the filter size. A correction function is proposed in this work which can reduce the error on the reaction rate modelling at low turbulence intensities by up to 50 %, and which is obtained by imposing that the consumption speed based on the modelled reaction rate matches the exact one in the flamelet limit. A second analysis is also conducted to assess the accuracy of the flamelet assumption itself. This analysis is conducted for a wide range of Ka, from 6 to 4100. It is found that at high Ka this assumption is weaker as expected, however results improve with larger filter sizes due to the reduction of the scatter produced by the fluctuations of the exact reaction rate.

Keywords: Turbulent premixed flame, Direct numerical simulation, Combustion model, High Karlovitz number, Probability density function

---

1. Introduction

Flow simulations of practical combustion devices are often based on the LES paradigm, as this methodology has the potential to be accurate and to capture unsteady phenomena at affordable computational effort. Since the LES equations are filtered in space, they contain unclosed terms, and further modelling is therefore required in respect to the Navier-Stokes equations from which they are derived. In flows with combustion one of the key terms to model is the filtered chemical reaction rate and this is the purpose of a combustion model. Combustion models for LES of premixed flames can be roughly classified by their main concepts [1] as either geometrical (such as level-set models [2, 3] and thickened flame models [4]), mixing-based (such as eddy dissipation concept [5], partially stirred reactors [6] and the linear eddy model [7]) or statistical (such as transported probability density function (PDF) models [8] and presumed-PDF models [9–11]). Some of these models are combined with a simplified description of the chemistry, realized through tabulation, such as the flamelet generated manifolds (FGM) method [12] and the flame prolongation of ILDM (FPI) method [13].

A central parameter for classifying regimes of premixed combustion is the Karlovitz number, Ka, which is defined as the ratio of a chemical time scale to the smallest turbulence (Kolmogorov) time scale. Most combustion models mentioned previously have been developed and validated for regimes where the chemical time scale is shorter than the turbulent one, which corresponds to a low Karlovitz number. Future combustion devices are however expected to involve more intense turbulence and/or leaner mixtures to improve their efficiencies and reduce emissions, and such conditions leads to combustion devices that operate at higher Karlovitz numbers. When the turbulent length scales are smaller than the reaction layer thickness it is expected that small vortices may enter the reaction zone, thereby disrupting the flame structure. Modelling of the high Karlovitz number flames can therefore be challenging and there is a need to explore which types of models, both detailed and simple, can be applied at the high-Ka regime.

It has been observed in a recent study [14] that the *unfiltered* chemical source term has large local fluctuations and thus is difficult to model with tabulation methods, while the *filtered* source term is more readily modelled as long as the filter is large enough ($\Delta \geq \delta_{th}$). This implies that a tabulated chemistry approach based on flamelets can still be useful in the high Karlovitz number regimes of combustion. Moreover, it is suggested in [15] that tabulation can be improved by including effects of strain on the flamelet, an effect that is well understood for the RANS framework but not as well established for the LES framework [16, 17]. In [14] it was also noted that unstrained flamelet modelling can work for low and high Karlovitz number ($\mathrm{Ka}_\delta < 0.1$ or $\mathrm{Ka}_\delta > 100$) while at intermediate Ka the strain, curvature and differential diffusion effects can be important.

Thus, this work proposes to assess a presumed-PDF model within the framework of LES for various Karlovitz numbers. It is representative of a class of statistical models for premixed combustion that has been discussed and applied in many previous studies, from early developments [9–11] to more recent works [12, 16, 18–22]. The specific model discussed here assumes that the sub-grid PDF is a beta-distribution and that a single reaction progress variable is enough to describe the flame locally. The goal is to perform an a priori evaluation of a model for the reaction rate, in particular its dependence on the filter size and the Karlovitz number. For this purpose, a set of DNS premixed flames with increasing complexity are used: a one-dimensional laminar with complex chemistry, a turbulent flame with single-step chemistry and 5 different turbulent flames with complex chemistry at different Karlovitz numbers.

First, the use of a presumed beta-PDF for the sub-grid distribution of the reaction progress variable and the accuracy of the resulting modelled reaction rate is investigated. The analysis is performed for two cases where the flamelet assumption can be eliminated. Based on the analysis of a filtered one-dimensional flame a correction factor is defined to impose a consistent consumption speed. Second, the flamelet assumption is assessed for high Ka conditions. Unfiltered flames with multi-step chemistry are used to quantify the error from the flamelet assumption. Finally, filtering is used to show how the combination of the two assumptions, presumed PDF and flamelet, depends on filter size and Ka and highlights the effect of the suggested correction factor.

2. Methodology

2.1. Filtering of the DNS data

In order to perform an a priori analysis of LES models on DNS data a filter operation has to be defined. In this work filtering is defined as a convolution with a Gaussian filter kernel. A filtered quantity is denoted by an over-bar, such as $\overline{\psi}$, and it is computed as

$$\overline{\psi}(\mathbf{x},t) = \iiint_V \psi(\mathbf{r},t) G(\mathbf{x}-\mathbf{r};\Delta)\ \mathrm{d}\mathbf{r}, \tag{1}$$

where V is the computational domain and $G(\mathbf{x};\Delta)$ is a Gaussian filter kernel with filter width Δ. Conventionally the filter width is defined as $\Delta^2 = s^2/12$ where s^2 is the variance of the Gaussian distribution [23]. Favre filtered (density weighted) quantities are also needed. These are denoted by a tilde and are defined as $\widetilde{\psi} = \overline{\rho\psi}/\overline{\rho}$.

The convolution product in Eq. (1) is computed in wave space as $\widehat{\overline{\psi}}(\mathbf{k}) = \widehat{\psi}(\mathbf{k})\widehat{G}(\mathbf{k})$ by the use of a Fourier transform. Here, $\widehat{\ }$ denotes a Fourier transform coefficient and $\mathbf{k}$ is the wave number vector. This is done for efficiency reasons but also to avoid the need to truncate the filter kernel in space. As the transform cannot be applied to data that is not periodic in all spatial dimensions and thus a mirrored copy of the data is attached in the non-periodic direction.

Note that the filter operation defined by Eq. (1) is used only to compute localized filtered values representative of what would come out of a LES. This should not be confused with ensemble averaging (represented by time averaging in the case of statistically stationary systems) which is used to obtain statistics.

2.2. Presumed-PDF model for the reaction rate

In combustion, the progress of reaction from reactants to products can be described by a reaction progress variable, c. In the case on single-step chemistry c is solved for directly, but in the case of multi-step chemistry many possibilities exist for the definition of c. Here, c is defined as the normalized mass fraction of H_2O since this is one of the few species that can be found throughout the entire flame structure including preheat and post flame zones. c can thus be expressed as

$$c(\mathbf{x},t) = \frac{Y_{\mathrm{H2O}}(\mathbf{x},t) - Y_{\mathrm{H2O},u}}{Y_{\mathrm{H2O},b} - Y_{\mathrm{H2O},u}}. \tag{2}$$

Subscripts u and b denote the unburnt and burnt states, respectively. The Favre filtered progress variable is then defined as $\tilde{c} = \overline{c\rho}/\overline{\rho}$ where the filter operation is given by Eq. (1). The transport equation for the filtered progress variable, $\tilde{c}$, follows directly from the transport equation for $\widetilde{Y}_{\mathrm{H2O}}$ and is given by

$$\frac{\partial \overline{\rho}\tilde{c}}{\partial t} + \nabla \cdot (\overline{\rho}\tilde{\mathbf{u}}\tilde{c}) = \overline{\mathcal{D}} - \nabla \cdot (\overline{\rho \mathbf{u} \mathbf{c}} - \overline{\rho}\tilde{\mathbf{u}}\tilde{c}) + \overline{\dot{\omega}}. \tag{3}$$

In Eq. (3), $\mathbf{u}$ is the velocity vector, ρ is the density, $\dot{\omega}$ is the chemical reaction rate and $\mathcal{D}$ is the diffusion term (the details of which depends on the transport model, see section 3). The three terms on the right hand side represent molecular diffusion, sub-grid transport and chemical reaction, respectively. All three require further modelling and the focus here is on the reaction term.

The sub-grid PDF of the reaction progress variable is defined as [24]

$$P(\varsigma; \mathbf{x}, t) = \iiint_V \delta(c(\mathbf{r}, t) - \varsigma) G(\mathbf{x} - \mathbf{r}) \; \mathrm{d}\mathbf{r}, \tag{4}$$

where G is the filter function, δ is the Dirac delta-function and the volume V includes the support of G which here taken to be the computational domain.

The presumed-PDF model to be evaluated is now formulated as

$$\overline{\dot{\omega}}(\mathbf{x}, t) \approx \int_0^1 \dot{\omega}(\varsigma) P(\varsigma; \mathbf{x}, t) \; \mathrm{d}\varsigma \approx \overline{\rho}(\mathbf{x}, t) \int_0^1 \frac{\dot{\omega}(\varsigma)}{\rho(\varsigma)} P_\beta(\varsigma; \tilde{c}(\mathbf{x}, t), \sigma^2(\mathbf{x}, t)) \; \mathrm{d}\varsigma, \tag{5}$$

where $\sigma^2 = \widetilde{cc} - \tilde{c}\tilde{c}$ is the Favre sub-grid variance of c, and P_β is the presumed Favre-filtered sub-grid PDF. This model is based on the following two assumptions:

(i) The functional form of the Favre-filtered sub-grid PDF is presumed to be a beta-distribution, parametrized by $\tilde{c}$ and σ^2. This is expressed as

$$P(\varsigma; \mathbf{x}, t) \frac{\rho(\varsigma)}{\overline{\rho}(\mathbf{x}, t)} \approx P_\beta(\varsigma; \tilde{c}(\mathbf{x}, t), \sigma^2(\mathbf{x}, t)).$$

and corresponds to the second step in equation (5).

(ii) The unfiltered reaction rate is assumed to be a function of only c, that is, $\dot{\omega}(Y_i, T) \approx \dot{\omega}(c)$. This corresponds to the first step in equation (5). The function $\dot{\omega}(c)$ is given by a separate calculation of a steady one-dimensional flame.

In Eq. (5), the last integral is a 1D integral in composition space which makes it possible to pre-compute and tabulate the integral as a function of $\tilde{c}$ and σ^2. It is this possibility to tabulate that makes this model computationally efficient. For the present study a table is constructed based on 300 linearly distributed points in both $\tilde{c}$ and σ^2. The resulting two-dimensional table is illustrated in Fig. 1. In the set of flames considered in the present study, pressure, equivalence ratio and unburnt temperature, are constant. To be able to

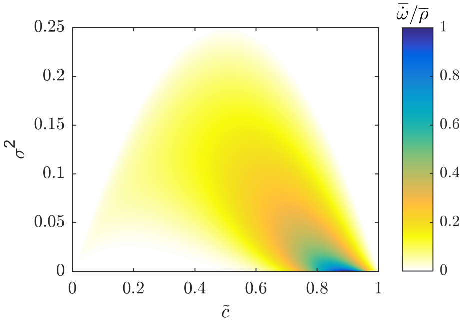

Figure 1: Modelled reaction rate, $\bar{\dot{\omega}}/\bar{\rho}$, as a function of $\tilde{c}$ and σ^2. Normalization is done using the peak values of the one-dimensional unfiltered flame.

model flames where these parameters are not constant, additional dimensions have to be added to the table and corresponding sets of additional one-dimensional flames would have to be computed.

It should also be noted that there exists a method where the PDF is obtained by filtering of one-dimensional flames instead of using a beta-distribution [25]. This was recently investigated in [14] but since no significant improvement was reported over the beta-distribution for three-dimensional flames this method will not be pursued here.

To compute $\bar{\dot{\omega}}$, an additional model for the unknown sub-grid variance σ^2 needs to be supplied. In LES this can be done either by an algebraic expression or by solving a transport equation for σ^2 [26, 27]. In this work the focus is on the two assumptions (i) and (ii) mentioned above and the modelling of σ^2 is thus not considered. Assessing the modelling of σ^2 for high Ka flames will be the topic of a separate study. Instead, the exact value of σ^2 is extracted from DNS and used directly in Eq. (5).

2.3. Error and correlation

To quantify the model error, two different metrics will be used. The first one is the integrated error, denoted by E. It is defined as

$$E = \left\langle \frac{|\bar{\dot{\omega}}_e - \bar{\dot{\omega}}|}{|\bar{\dot{\omega}}_e|} \right\rangle, \tag{6}$$

where the symbol $\dot{\omega}_e$ is introduced to denote the exact filtered reaction rate, obtained through a direct filtering of the fully resolved data, and $\langle \cdot \rangle$ denotes time and space average (not to be confused with the filtering). The index i runs over data points (computational cells) sampled uniformly in space and over time in a statistically stationary flame. The choice of this error metric is motivated by the fact that in finite volume methods, commonly used to discretise the Navier-Stokes equations, it is not omega itself but its integral over a cell volume that is used. Typical cell sizes are of the same order as Δ, and since Δ can be larger than δ_{th} the integrated error E becomes a relevant quantity in the LES, at least in the context of finite volume methods.

The second metric is the weighted Pearson correlation coefficient [28], r, which is based on weighted covariances and is defined as

$$r = \frac{\left\langle w(\overline{\dot{\omega}}_e - \langle\overline{\dot{\omega}_e}\rangle_w)(\overline{\dot{\omega}} - \langle\overline{\dot{\omega}}\rangle_w)\right\rangle}{\left\langle w(\overline{\dot{\omega}}_e - \langle\overline{\dot{\omega}_e}\rangle_w)^2\right\rangle^{1/2}\left\langle w(\overline{\dot{\omega}} - \langle\overline{\dot{\omega}}\rangle_w)^2\right\rangle^{1/2}}. \tag{7}$$

Here, $\langle\cdot\rangle_w$ denotes weighted averages and w is the weight. The weight is set equal to the reaction rate itself, $w = \overline{\dot{\omega}}$, and this choice is made to prevent the large non-reacting zones outside the flame from affecting r. This way, data points with large reaction rate will contribute more to r than points with low rate. Note that a high correlation can exist even if E is large.

2.4. Scaled model

It is commonly known (and will be seen in section 4.2.1) that for a one-dimensional flame, Eq (5) tends to over-predicts the filtered rate. This happens when the filter is large enough that $\sigma^2 > 0$ and comes from the fact that the presumed shape PDF is not able to exactly produce the right sub-grid distribution. As a result, the correct laminar flame speed is not guaranteed for $\sigma^2 > 0$. However, for a one-dimensional laminar flame the model can be improved by introducing a correction factor f defined as

$$f(\Delta) = \frac{\int_{-\infty}^{\infty} \overline{\dot{\omega}}_e(Y_i, T; \Delta)\ \mathrm{d}x}{\int_{-\infty}^{\infty} \overline{\dot{\omega}}(\tilde{c}, \sigma^2; \Delta)\ \mathrm{d}x} \tag{8}$$

where $\overline{\dot{\omega}}_e$ is the exact rate evaluated for the one-dimensional flame and $\overline{\dot{\omega}}$ is the modelled rate as in Eq. 5. The scaled model is then obtained as $f \cdot \overline{\dot{\omega}}(\tilde{c}, \sigma^2)$.

Under the flamelet assumption a three-dimensional flame is assumed to locally have the same structure as a one-dimensional flame. It is therefore motivated to compute the factor f a priori (using a one-dimensional flame) and store it for use when modelling three-dimensional flames. Also, since the f only depends on Δ, it can be pre-multiplied in the table and its use will thus add no extra computational cost to an LES.

The factor f is defined as in Eq. (8) to ensure that the following condition is respected:

$$\int_{-\infty}^{\infty} \overline{\dot{\omega}}_e(x)\ \mathrm{d}x = \int_{-\infty}^{\infty} f\overline{\dot{\omega}}(x)\ \mathrm{d}x \tag{9}$$

Physically the correction corresponds to enforcing the correct consumption speed for a one-dimensional flame. Indeed, the inability of a presumed beta-distribution to produce the correct flame speed is a known problem [29]. Moreover, f increases with the filter size, Δ, which is an important characteristics as will be shown in section 4.2. It should also be noted that, while the correction factor can reduce the error E, it does not affect the correlation r.

3. Numerics and DNS data

The current study uses a DNS dataset of turbulent, statistically planar, premixed flames. The computational domain is a rectangular box in an inlet-outlet configuration, discretised on a uniform grid. A planar premixed flame is in the centre of the domain at time $t = 0$ and it propagates towards the inlet at $t > 0$. Periodic boundary conditions are imposed in the cross-stream directions and a convective outflow boundary condition is used at the outlet. On the inlet boundary, a constant value for temperature ($T = 298$ K) and species is imposed while a turbulent time-varying boundary condition is used for the velocity. An instantaneous picture of the $c = 0.8$ iso-surface is shown in Fig. 2 for each simulation at a random time instant within the statistically stationary state. The wrinkled and distorted shape of the flames can be seen and the variation of $\dot{\omega}$ along the flame surface is shown by the colour scale. For higher Ka the variations are generally larger, but not for case D which has no variations since $\dot{\omega}$ in this case only depends on c.

Five of the cases, referred to as A1, A2, A3, B anc C, are lean methane-air flames at atmospheric pressure and temperature. These simulations use multi-step chemistry and include differential diffusion. The methane/air chemistry is modelled with the skeletal mechanism of Smooke and Giovangigli [30], which contains 16 species and 35 reactions. The equivalence ratio is 0.6. Transport properties, i.e. species diffusion coefficients, thermal conductivity, and viscosity, are mixture averaged based on the detailed properties for individual species obtained from the CHEMKIN thermodynamic database. Diffusion velocities of individual species are modelled using the Curtiss-Hirschfelder approximation. Note that case B has been analysed in a previous work [31].

The sixth case, referred to as case D, uses a single global reaction with an Arrhenius rate expressed as $\dot{\omega} = (1 - c)^{1.6}/\tau_0 \times \exp(-E_a T_b/T)$ where $\tau_0 = 5 \times 10^{-10}$ s^{-1} and $E_a = 9$, unity Lewis number and a Prandtl number of 0.3. These parameters were chosen to get a laminar flame speed and thickness comparable to the methane-air flames. Important parameters for all six cases are summarised in Table 1.

3.1. Numerical methods and turbulence generation

During the simulation, to keep the flame near the centre of the domain, the mean inlet velocity u_{in} is adjusted to match the propagation speed of the flame front. A fluctuating velocity component $u'(y, z)$ is also added at the inlet boundary plane. This component is obtained by extracting a plane from a pre-generated turbulent velocity field. The pre-generated turbulence is also used to set the initial conditions. For this purpose, a homogeneous isotropic turbulence field is generated as follows: a flow field with desired turbulence intensity and length scale is synthesized in a fully periodic cubic box by sampling sine waves of suitable wave numbers and amplitudes. The flow in this box is then simulated until a statistically stationary state is reached, quantified by convergence of the energy spectrum, the energy dissipation rate and the integral length scale. During this simulation the turbulence intensity and length scale is maintained by low-wavenumber forcing.

The low-wavenumber forcing strategy works by injecting energy to low wavenumber modes through the addition of a source term in the momentum equation. In wave space

Table 1: Parameters for the simulated cases. L_y is the cross-stream domain height, L_{11} the upstream integral length scale, h the grid spacing, δ_{th} the laminar thermal flame thickness, η the upstream Kolmogorov length scale, u' the upstream velocity fluctuation and S_L the laminar flame speed. The number of grid points is $N_x \times N_y \times N_z$. In the case of methane/air chemistry at equivalence ratio 0.6 the laminar flame speed and thickness are $\delta_{th} = 0.92$ mm and $S_L = 0.12$ m/s.

Case	A1	A2	A3	B	C	D
N_x	256	256	512	1024	512	192
N_y, N_z	128	128	256	512	256	64
L_y [mm]	5.0	5.0	5.0	5.0	14	2.9
L_y/δ_{th}	5.5	5.5	5.5	5.5	15.3	5.5
L_{11}/δ_{th}	1.3	1.0	1.0	0.48	2.4	1.2
δ_{th}/h	23.5	23.5	47.0	93.9	16.8	11.6
η/h	2.5	0.83	0.64	0.48	0.63	0.62
δ_{th}/η	9.5	28	74	220	27	19
u'/S_L	3.7	18	66	210	24	13
Ka	6.0	74	540	4100	75	40
Da	0.38	0.060	0.015	0.0025	0.11	0.098
Re_t	32	120	390	660	390	80
Chemistry	Multi-step					Global

for wavenumber κ the source term is

$$\hat{\mathbf{f}}_\kappa(t) = \frac{\rho \langle \varepsilon \rangle I^R_{\kappa \le \kappa_f}}{2\rho_u k_f(t)} \hat{\mathbf{u}}_\kappa(t) \tag{10}$$

where ρ is the local density, ρ_u is the density of the unburned mixture, $\langle \varepsilon \rangle = \langle 2\nu S_{ij} S_{ij} \rangle$ is the space averaged dissipation rate of turbulent kinetic energy, ν is the viscosity, S_{ij} is the strain rate tensor, $\hat{\mathbf{u}}_\kappa$ is the Fourier transform of the velocity $\mathbf{u}$ and $k_f = \sum_{|\kappa| \le \kappa_f} \hat{\mathbf{u}}_\kappa \cdot \hat{\mathbf{u}}_\kappa / 2$ is the kinetic energy contained in the set of modes with $|\kappa| \le \kappa_f$. The largest forced wavenumber, κ_f, is 3 for case B and 1 for all other cases. The function $I^R_{\kappa \le \kappa_f}$ is stochastic and for every time step it is set to 1 for a randomly selected wavenumber in the shell $|\kappa| \le \kappa_f$ and to 0 for all others. When used in a reacting flow simulation the density ratio ρ/ρ_u appearing in Eq.(10) is introduced to ensure a weaker forcing in the flame and post-flame regions. Further details on this forcing method are given in [32, 33].

The DNS solver is based on the governing equations for conservation of mass, momentum, energy and chemical species at low Mach number discretized on a uniform Cartesian grid, see Yu et al. [34] for a detailed description and validation. A 5th order weighted essentially non-oscillatory (WENO) finite difference method is used for convective terms and a 6th order central difference scheme is used for all other terms. For time discretisation a second-order operator splitting scheme [35] is employed by performing integration of the chemical source terms between two half time-step integrations of the diffusion term. The integration of the diffusion term is further divided into smaller explicit steps to ensure stability and the overall time step is set to ensure that the CFL number remains smaller than 0.1. In cases

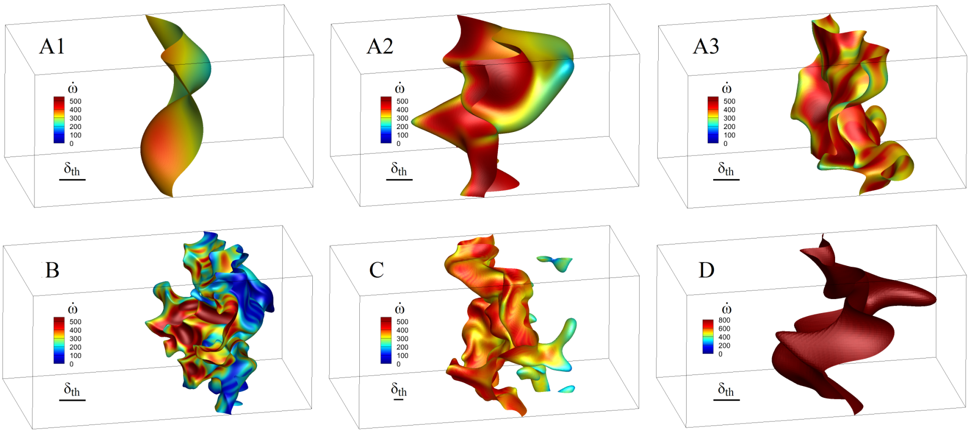

Figure 2: Iso-surfaces of $c = 0.8$ for the different cases. The surfaces are coloured by the reaction rate of c. The laminar flame thickness δ_{th} is indicated in each figure. In the figures the inlet is on the left.

with complex chemistry the chemical source terms are integrated using the stiff DVODE solver [36]. The variable coefficient Poisson equation for pressure difference is solved using a multigrid method [37].

3.2. Summary of cases

Dimensionless parameters given in Table 1 are defined as follows: Karlovitz number $\mathrm{Ka} = (u'/S_L)^{1.5}(\delta_{th}/L_{11})^{0.5}$, Damköhler number $\mathrm{Da} = L_{11}S_L/(\delta_{th}u')$ and turbulent Reynolds number $\mathrm{Re}_t = u'L_{11}/\nu_u$ where u' is the root mean square velocity fluctuation, L_{11} is the integral length scale, S_L is the laminar flame speed, $\delta_{th} = (T_b - T_u)/|\nabla T|_{\max}$ is the laminar flame thermal thickness and ν_u is the viscosity. The Kolmogorov length scale is computed as $(\nu^3/\varepsilon)^{1/4}$ where ε is the dissipation rate of turbulent kinetic energy. All turbulence quantities used in Table 1 are evaluated in the homogeneous non-reactive turbulence field that was used to set the initial and boundary conditions.

For cases A1, A2 and A3 the intention is to investigate the dependency on Ka while maintaining the domain size constant. The only parameter that was changed between these cases is therefore the turbulence intensity u' resulting in Karlovitz numbers 6, 74 and 540. However, although the aim was to also keep the integral length scale constant in those cases, it was found by autocorrelation, L_{11}, to decrease with u' and as result the cases have somewhat different length scales as seen in Table 1. To provide a case with very high Ka, case B with $\mathrm{Ka} = 4100$ from [31] is used. This case has the same set-up as cases A1-3 except for the forcing radius κ_f which is 3 instead of 1. To investigate if the integral length scale is an important parameter, case C is introduced. This case has the same Karlovitz number as A2 ($\mathrm{Ka} = 74$) but a larger domain size giving a 2.4 times larger integral length scale. Case C is used to verify that trends observed for cases A1-3 and B are due the turbulence intensity and not due to the turbulent length scale. Finally, case D is introduced to provide a suitable test case for assumption (i). Therefore, case D was chosen to have a single-step reaction scheme and unity Lewis number, a set-up which ensures that assumption (ii) is always verified.

4. Results

The results section is organized as follows: in section 4.1 the parametrization of $\overline{\dot{\omega}}$ as a function of $\tilde{c}$ and σ^2 is investigated. In section 4.2 assumption (i) is evaluated, first for a steady one-dimensional flame and then for the simplified-chemistry case D. In section 4.3 assumption (ii) is evaluated using unfiltered data from cases A1, A2, A3, B and C and finally, the combined effect of both assumptions is discussed in section 4.4.

4.1. Filtering and parametrization of the reaction rate

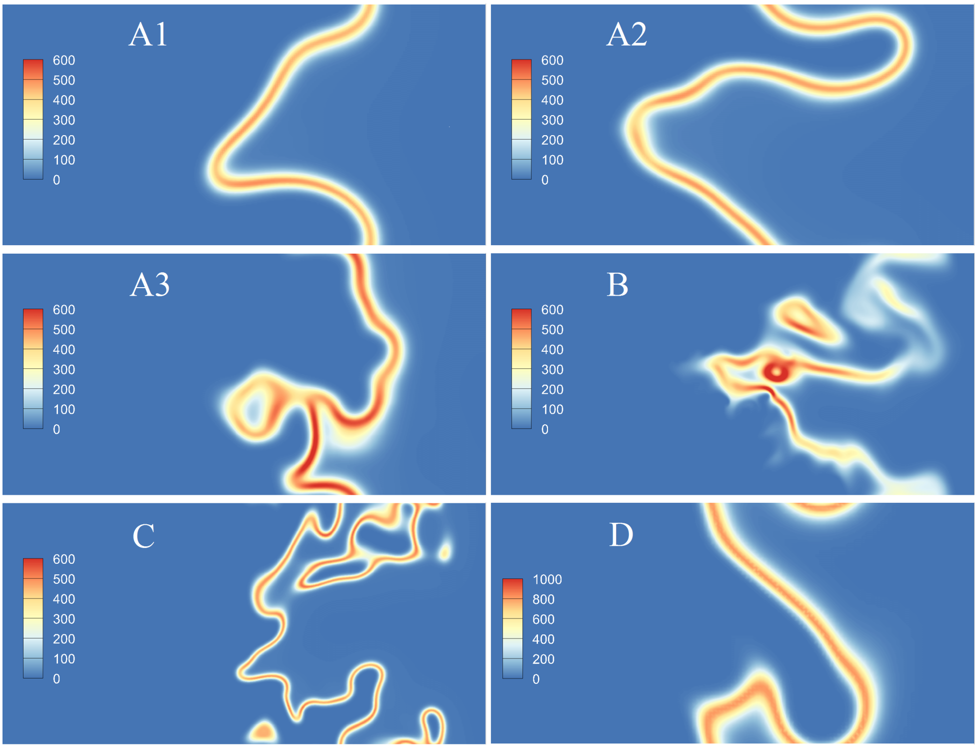

Figure 3: Instantaneous picture of the reaction rates $\dot{\omega}$ computed directly from DNS data for all cases. The unit of reaction rate is kg/m^3/s.

Before investigating the model, the effect of the filter operation on the reaction rate is illustrated. Instantaneous pictures of the unfiltered reaction rate $\dot{\omega}$ from the DNS data is shown in Figure 3 for all cases. As observed from the figure a local flamelet structure is not preserved everywhere for case B because of the appearance of holes and irregularities in the reaction layer. Some perturbations can also be seen for case A3 but in the other cases the reaction rate is not significantly perturbed.

The model given by Eq. (5) gives the reaction rate as a function of the mean and variance of the reaction progress variable, $\overline{\dot{\omega}} = \overline{\dot{\omega}}(\tilde{c}, \sigma^2)$. It is therefore appropriate to study how well the reaction rate is parametrized by $\tilde{c}$ and σ^2. Fig. 4 shows scatter plots of $\overline{\dot{\omega}}$ as a function of $\tilde{c}$ and σ^2 where colours indicate the magnitude of the filtered reaction rate, and Fig. 5 shows the standard deviation of the doubly conditioned reaction rate $\langle \overline{\dot{\omega}} | c, \sigma^2 \rangle$. The standard deviation is normalized for clarity by the peak of the single conditional average, $\max\langle \overline{\dot{\omega}} | c \rangle$. The precise quantity shown in the figure is thus

$$\frac{\left\langle [\overline{\dot{\omega}} - \langle \overline{\dot{\omega}} \mid \tilde{c}, \sigma^2 \rangle]^2 \mid \tilde{c}, \sigma^2 \right\rangle^{1/2}}{\max\langle \overline{\dot{\omega}} \mid c \rangle} \tag{11}$$

Low values indicate that $\overline{\dot{\omega}}$ is parametrized well by $\tilde{c}$ and σ^2. The figures show the two representative cases A2 and B for the two normalized filter sizes $\Delta^+ = \Delta/\delta_{th} = 1$ and 3.5.

Both figures indicate that the parametrization works well for case A2 and for case B with filter size $\Delta^+ = 3.5$ since the normalized standard deviation is below 0.1 for the most part. For case B with $\Delta^+ = 1$, however, vastly different values of $\overline{\dot{\omega}}$ are sometimes found for the same values of $\tilde{c}$ and σ^2, and standard deviation as high as 0.15 are common for this condition in Fig 5. For both cases the standard deviation is lower when the larger filter size is used indicating that correlation between model and DNS can be expected for large filters. Low standard deviation is necessary for the model to be accurate because the model provides only one value for each given combination of c and σ^2. For the high Karlovitz number, case B, the scatter is larger and thus the local and instantaneous value of the modelled reaction rate may be inaccurate.

At large filter sizes the local variations of the reaction rate are smoothed out as shown in Fig. 5. This suggests that a flamelet model with presumed PDF may perform satisfactorily at high Karlovitz numbers even if assumption (ii) does not strictly hold, as long as the filter size is sufficiently large. However, larger filter sizes introduce errors that also need to be investigated which will be done next.

4.2. Evaluation of assumption (i)

Assumption (i), which states that the sub-grid PDF is a beta-distribution, and its effect on $\overline{\dot{\omega}}$ are evaluated in this section. Two conditions are chosen for this purpose: a filtered steady one-dimensional flame with multi-step chemistry, and the filtered three-dimensional case D which uses single-step chemistry. Under these conditions, assumption (ii) is verified exactly because the reaction rate is only a function of c, thus providing clean test cases for assumption (i). The two conditions are complementary since case D contains turbulence effects while the one-dimensional flame contains multi-step chemistry effects.

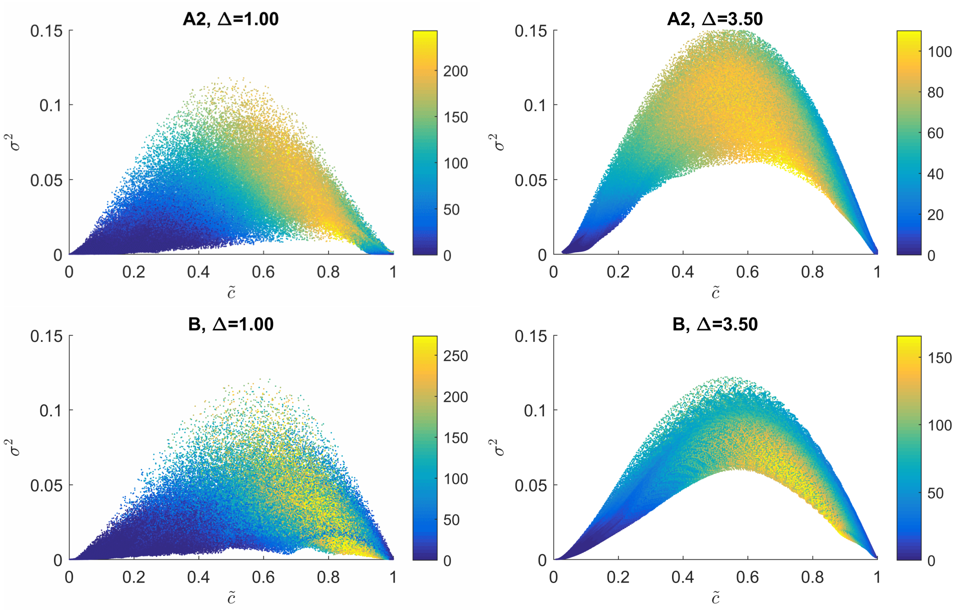

Figure 4: Scatter plot of $\tilde{c}$ and its sub-grid variance σ^2 for cases A2 and B. The colour scale shows the value of filtered reaction rate $\overline{\dot{\omega}}$ (kg/m^3/s).

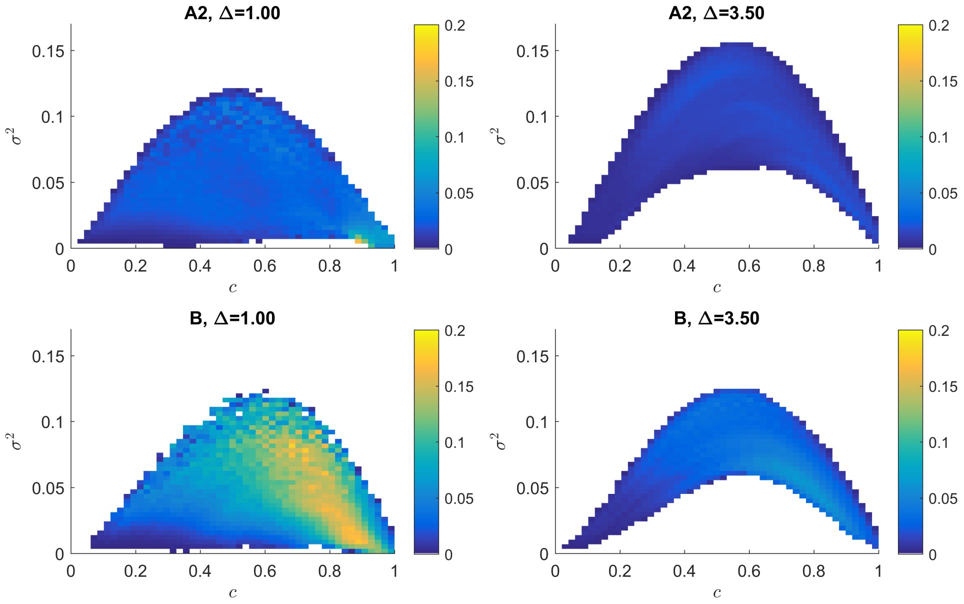

Figure 5: Standard deviation of the doubly conditioned reaction rate $\langle\bar{\omega}|c,\sigma^2\rangle$ for cases A2 and B at two different filter sizes. The standard deviation is normalized by $\max\langle\bar{\omega}|c\rangle$.

4.2.1. One-dimensional steady flame

In this section equation (5) is evaluated for a laminar one-dimensional (1D) flame. For this case assumption (ii) holds exactly since c is a monotonic function of the spatial coordinate. The only source of error in the modelled filtered reaction rate is due to assumption (i), i.e. differences between the sub-grid PDF from DNS and the presumed beta-distribution.

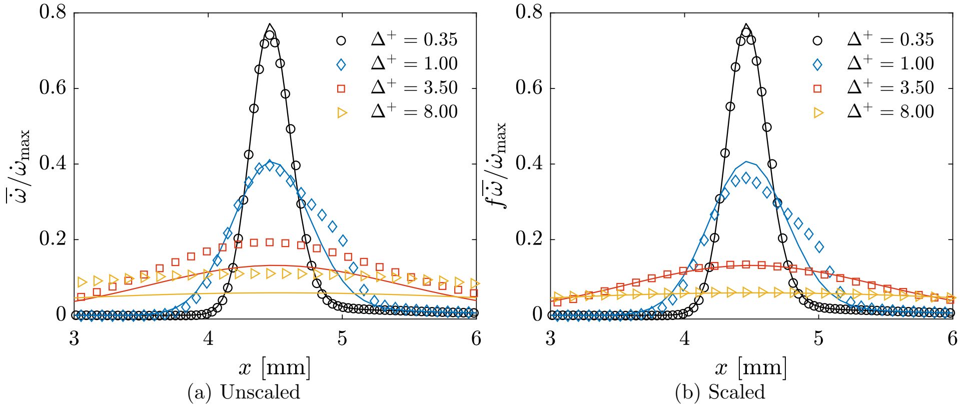

(a) Unscaled

(b) Scaled

Figure 6: Filtered reaction rate in a one-dimensional flame (lines). Symbols show the corresponding results obtained from the presumed-PDF model. In (a) the model is unscaled and in (b) it is scaled following Eq. (8).

Figure 6a shows the exact filtered reaction rate $\overline{\dot{\omega}}_e$ (lines) and the corresponding presumed-PDF model (symbols) for normalized filter sizes Δ^+ ranging from 0.35 to 8. From the figure it is seen that the model captures the shape of the profiles at the different filter sizes but for filters with $\Delta^+ > 1$ the magnitude is over-predicted. The level of over-prediction can be reduced by using the correction factor f introduced by Eq. (8) which is shown as a function of Δ^+ in Fig. 7a. The result after applying the correction factor f is shown in Fig. 6b where over-predication has been mitigated. Although the match is good (the maximum error is below 9% of $\dot{\omega}_{\max}$ and much less for the two largest filter sizes), the shape of the modelled rate profile for $\Delta^+ = 1$ (blue curve) does not entirely match the correct shape even after the correction factor has been applied, this is due to the restriction from a presumed shape PDF.

In Fig. 7b the integrated error E and weighted correlation coefficient r (defined in Eqs. (6) and (7), respectively) are shown as functions of Δ^+. The error E is shown both with and without the correction factor applied to the modelled reaction rate (denoted by scaled and unscaled, respectively). Using the correction factor does not reduce the error to zero because it does not affect the shape of the reaction rate profile, but only its magnitude. The error in the unscaled model increases monotonically with Δ while the correlation r has a minimum at $\Delta^+ = 1.5$. There is also a corresponding maximum in the error of the scaled model for this filter size so this represents the least favourable filter size for the model according to

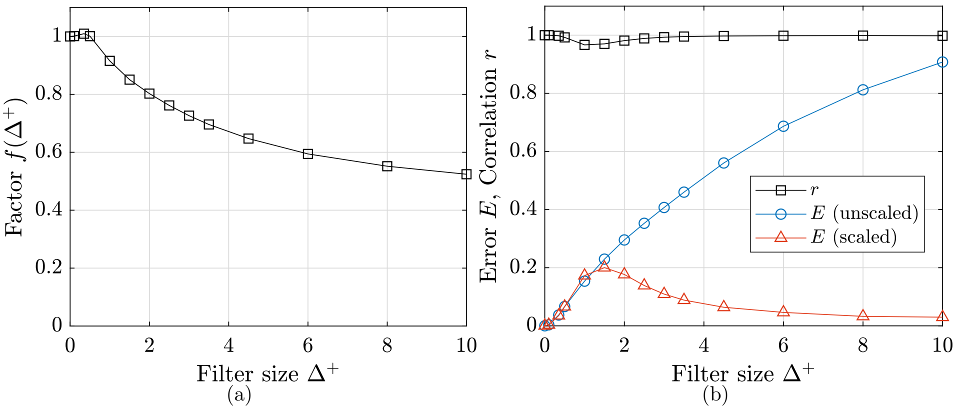

Figure 7: (a) Correction factor computed from Eq. (8) using the 1D flame. (b) Error E and correlation r for a one-dimensional laminar flame. Filters range from 0.1 to 10 times the thermal flame thickness. Circles shows the unscaled model from Eq. (5) and triangles shows the scaled model.

the metrics used. The source of the seen error has to do with the use of a presumed PDF as this is the only approximation that is employed. In principle the error cannot be entirely mitigated unless the actual sub-grid PDF is extracted and used in place of the beta-PDF.

The actual sub-grid PDFs of c computed for the filtered one-dimensional flame are presented in Fig. 8 for the point with $\tilde{c} = 0.5$ and 0.7 at filter levels $\Delta^+ = 0.35$, 1.0 and 3.5, and compared with beta-PDFs obtained for the same c and σ^2. These values were selected as a representative locations where the filtered reaction rate is significant for all filter levels. The dashed lines show the beta-distributions and the solid lines show the corresponding distribution that results from applying the density weighted filter to the actual flame. For the one-dimensional case the sub-grid PDF in x-space is equal to the Favre filter and can be transformed to c-space via $P(x)\mathrm{d}x = P(c(x))\mathrm{d}c$ since c is a monotonic function of x.

Table 2: Kullback–Leibler divergence $D(P||P_\beta)$ for all cases at $\tilde{c} = 0.5$ and $\tilde{c} = 0.7$.

Case	1D	A1	A2	A3	B	C	D
$\tilde{c} = 0.5, \Delta^+ = 0.35$	0.0095	0.0089	0.042	0.12	0.081	0.034	0.034
$\tilde{c} = 0.5, \Delta^+ = 1.0$	0.030	0.024	0.036	0.072	0.050	0.040	0.051
$\tilde{c} = 0.5, \Delta^+ = 2.5$	0.35	0.28	0.18	0.087	0.062	0.20	0.12
$\tilde{c} = 0.5, \Delta^+ = 3.5$	0.65	0.41	0.25	0.12	0.080	0.28	0.16
$\tilde{c} = 0.7, \Delta^+ = 0.35$	0.0074	0.0019	0.0029	0.024	0.059	0.0030	0.0031
$\tilde{c} = 0.7, \Delta^+ = 1.0$	0.096	0.096	0.087	0.035	0.041	0.091	0.034
$\tilde{c} = 0.7, \Delta^+ = 2.5$	0.68	0.55	0.38	0.17	0.11	0.40	0.22
$\tilde{c} = 0.7, \Delta^+ = 3.5$	1.1	0.72	0.46	0.24	0.16	0.48	0.33

To quantify the match between the modelled PDF and the beta-distribution, the Kullback–Leibler (KL) divergence $D(P||P_\beta)$ is computed and listed in Table 2 for all cases. The

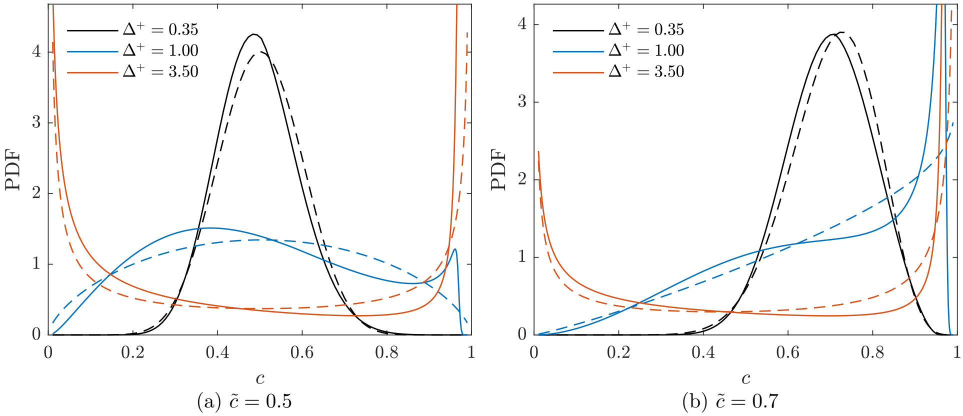

(a) $\tilde{c} = 0.5$

(b) $\tilde{c} = 0.7$

Figure 8: Sub-grid probability density of the reaction progress variable for different filter levels for the one-dimensional laminar flame. Solid lines show $P(c)$ and dashed lines show the model beta-distribution $P_\beta(c)$. (a) and (b) show $P(c \mid \widetilde{c} = 0.5)$ and $P(c \mid \widetilde{c} = 0.7)$, respectively.

KL divergence is defined as

$$D(P||P_\beta) = \int_0^1 P(\varsigma) \ln\left(\frac{P(\varsigma)}{P_\beta(\varsigma)}\right) \mathrm{d}\varsigma \tag{12}$$

where P is the PDF extracted from simulations and P_β is the presumed beta-distribution. In the table, the KL divergence is listed for $\tilde{c} = 0.5$ and $\tilde{c} = 0.7$. For the one-dimensional laminar flame (1D) the divergence increases with filter size indicating a worse match of the beta-PDF for larger filters.

Overall, the beta-PDF reproduces reasonably well the trends of the filtered PDF, at least for filter sizes $\Delta^+ \leq 1$. However, discrepancies between the two PDFs in the high reactivity range of c values might cause large errors in reaction rate estimations, as shown in Fig. 7b. In particular, at filter size $\Delta^+ = 1$ there is non-negligible error in the PDF which explains the discrepancy in the reaction rate profile in Fig. 6.

As was mentioned previously, the physical motivation for introducing the correction factor f is to make the model consistent by preserving the integrated reaction rate and thereby the consumption speed (c.f. section 2.4). This leads to a decrease in E for the one-dimensional flame and the reduction is substantial for large Δ. This is relevant for finite volume methods as explained earlier and thus f may effectively reduce the over-prediction that can occur for $\Delta^+ > 1$. It is anticipated that the same sort of over-prediction will be prevalent also in three-dimensional wrinkled or turbulent flames. Applying the correction factor for such flames may also lead to error reduction and this will be explored in the next section.

4.2.2. Turbulent flame with simplified chemical kinetics

After having studied the one-dimensional flame the next step is to investigate the three-dimensional turbulent flame of case D. This case uses a simplified chemical model based on a single global reaction and unity Lewis number, and it has a Karlovitz number of 40. Simple linear relations exist between local species mass fractions and the temperature because of the absence of intermediate species and differential diffusion. Therefore, only one scalar transport equation needs to be solved, and this scalar is equivalent to a progress variable c. Thus, $\dot{\omega}$ can be expressed as a function of only c, meaning that assumption (ii) holds making case D suitable to study the accuracy of assumption (i) in three-dimensional filtered flames.

A one-dimensional laminar flame based on the simplified chemistry is first analysed in order to obtain the correction factor f. Analogous to Fig. 7 the factor f, error E and correlation coefficient r are shown in Fig. 9 for this laminar flame. The trends for all these quantities are qualitatively similar to those of the previously discussed complex chemistry laminar flame with, but there are some quantitative differences owing to the somewhat different flame structure.

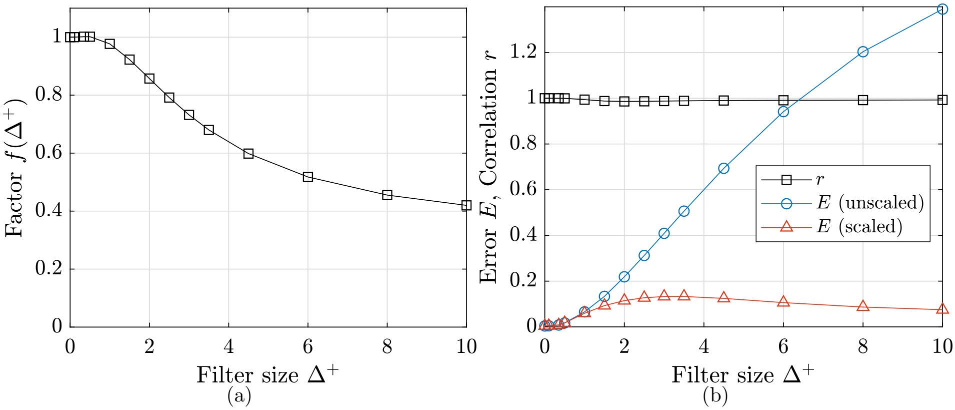

Figure 9: (a) Correction factor f and (b) error E and correlation coefficient r for a one-dimensional laminar flame with single-step chemistry. Error E is shown both for the unscaled model (circles) and the scaled model (triangles).

For the tree-dimensional case D the error and correlation are shown in Fig. 10a. When filter size is increased the error increases monotonously (both with and without correction factor) and the correlation r decreases. This means that the approximation of the PDF by a beta-distribution becomes worse as the filter size increases, in contrast to the one-dimensional case (Fig. 9) where the correlation is high also for large filters and the correction factor can effectively reduce the integrated error (c.f. the Kullback-Leibler divergence shown in Table 2). But still, for case D, the scale factor is found to reduce the error by up to 50%. A comparison of sub-grid PDFs from model and DNS is also shown in Fig 10 for three filter sizes and conditioned on for $\tilde{c} = 0.5$. A reasonably good match is seen, although not quite as good as in the one-dimensional case. However, a good match of the average PDF does not guarantee a low error in the local $\bar{\dot{\omega}}$.

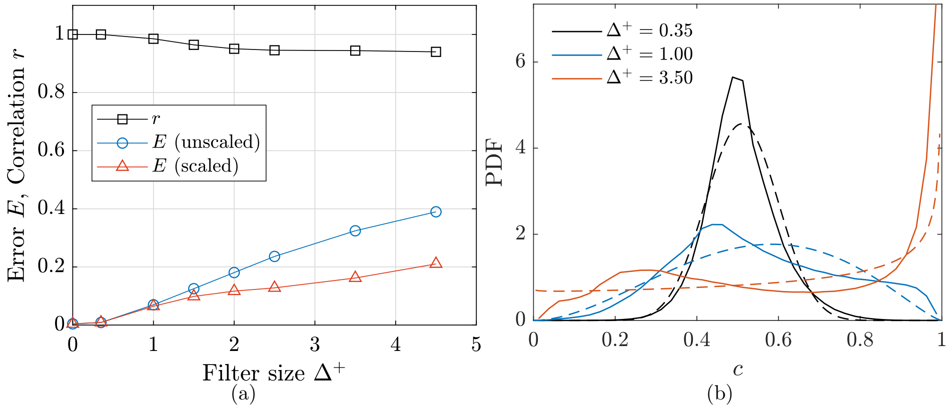

Figure 10: (a) Error E and correlation coefficient r for case D. Error E is shown both for the unscaled model (circles) and the scaled model (triangles). (b) Comparison of PDFs from the model (dashed lines) and DNS (solid lines) for $\tilde{c} = 0.5$ in case D.

4.3. Evaluation of assumption (ii)

The previously observed behaviour that the error due to assumption (i) grows with Δ^+ for a three-dimensional flame must occur also when multi-step chemistry is used, and likely also at higher Re and Ka numbers. However, at these conditions, errors due to assumption (ii) may be present and thus an assessment on this assumption is needed. Assumption (ii) states that the unfiltered reaction rate is a function of only the progress variable, $\dot{\omega} = \dot{\omega}(c)$. To provide a clean test case, conditions have to be chosen such that assumption (i) is satisfied exactly. Assumption (i) states that the sub-grid PDF is a beta-distribution, and the condition where this assumption is satisfied is $\Delta^+ = 0$. At this condition the sub-grid PDF (both modelled and exact) will collapse to a delta function. The progress-variable used in the case of methane/air flames is based on the mass fraciton of H_2O.

The unfiltered raw data, $\dot{\omega}$, shows large differences between model and DNS in most cases. This is illustrated in Fig. 11 which shows the joint PDF of the exact and modelled reaction rate. Under these conditions of zero variance the model is just the reaction rate from the one-dimensional laminar flame at a given c. For the cases with lower Ka, cases A1, A2 and C, two branches can be seen in the figures. These are marked by "A" and "B" in Fig. 11a and they correspond to relatively low (0.6-0.8) and high (0.9) c-values, respectively. The two branches results from a shift of the reaction rate profile in the c-coordinate as will be discussed later. No such clear branches can be identified in cases A3 and B. In case B, which has the highest Ka, a particularly large spread is seen. Case D has no spread at all. In this case the model rate is equal to the exact rate and assumption (ii) is fulfilled exactly as discussed before, and the case is included here only for completeness.

Quantitative measures of the accuracy of assumption (ii) are provided by the error E and the correlation coefficient r. These are listed in Table 3 for cases A1-3, B and C. Karlovitz

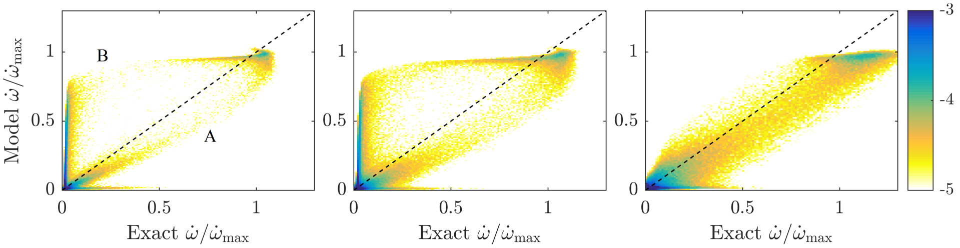

(a) Case A1 (b) Case A2 (c) Case A3

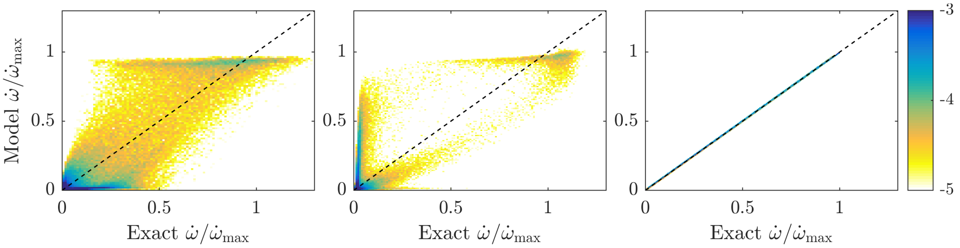

(d) Case B (e) Case C (f) Case D

Figure 11: The colour scale shows the joint PDF of the exact (DNS) and modelled reaction rate for unfiltered data from all cases. To make the scatter more visible the colour scale is logarithmic, numbers indicate the exponent of 10.

Table 3: Error and correlation coefficient of the presumed-PDF model when applied to unfiltered data.

	A1	A2	A3	B	C
E	0.64	0.56	0.31	0.46	0.59
r	0.79	0.75	0.89	0.71	0.76
Ka	6	74	540	4100	75

numbers are also listed for reference. The two cases that have the same Ka, cases A2 and C, have nearly the same values of both E and r which confirms that the 2.4 times difference in integral length scale does not affect E and r.

As a function of Ka the error has a minimum for case A3 (Ka = 540). Similarly, the correlation coefficient has a maximum for the same case. The trend of decreasing error with increasing Ka that is seen for cases A1-3 and the particularly low error in case A3 is in agreement with the findings of [14] where the effects of strain and curvature were seen to be less important for Ka > 100. Cases A1 and A2 fall in the regime where strain and curvature may have an effect. For these cases, modelling based on unstrained flamelets may not be suitable. Flamelet modelling of low Ka flames is however a well-known subject and only a short discussion will be given here; the focus is rather on the high Ka flames.

In Fig. 12 (a-c) the joint PDF of c and $\dot{\omega} - \dot{\omega}_e$ is shown for cases A1, A3 and B. The line shows the conditional average $\langle(\dot{\omega} - \dot{\omega}_e)|c\rangle$. In the low Ka case A1 the difference between $\dot{\omega}$ and $\dot{\omega}_e$ is largest in the range $0.9 < c < 1$, while in the high Ka case B large difference is found in a wider range of c. Figure 12 (d-i) shows scatter plots of c and the exact rate $\dot{\omega}_e$, coloured by the local curvature and tangential strain rate. Curvature is defined as $0.5\nabla \cdot \mathbf{n}$ where the normal vector $\mathbf{n} = \nabla c/|\nabla c|$ points toward the product side, so positive curvature means that the centre of curvature is on the reactant side. The lines in these figures show the model predicted rate. At Ka = 6 (case A1) there is a clear connection between curvature and reaction rate; for points with positive curvature the rate profile is shifted to the left and for points with negative curvature the profile is shifted to the right. At Ka = 540 (case A3) a distinction between points of opposite curvature can still be seen. It is known that curvature and strain does affect flame structure in the flamelet regime, as seen for case A1. A possible explanation for the high correlation r that is observed in case A3 can be the short turbulent time scale: the local curvature/strain changes rapidly and the flame structure does not have time to respond the same way as in the flamelet regime. At Ka = 4100 (case B) there is no relation between curvature/strain and reaction rate indicating that the time scale of changes in curvature/strain is so short that the flame has no time to respond to the rapidly changing curvature/strain. Similar observations were made in [38] where it was shown that the response of a flame to strain is reduced at low Da. The model error E seen in case B is larger than that of case A3 and cannot be explained by any correlation with local curvature and strain. It could be due to the larger level of turbulence which induces faster random perturbations on the flame structure.

To conclude, it seems that the model error E due to assumption (ii) as a function of Ka behaves as follows: For a one-dimensional (planar) flame E is relatively small. When the flame becomes wrinkled (case A1 and A2) E increases due to the growing curvature effects. When high Karlovitz numbers are reached (case A3) E drops to a smaller value due to weaker influence of curvature on the reaction zone. Finally, at very high Karlovitz number (case B) E increases again which might be an effect of convection driven mixing.

4.4. Combined effect of both assumptions

The model is now evaluated for cases A1-3, B and C with non-zero filter size. When these flames are filtered, neither assumption (i) nor (ii) holds exactly and both can contribute to

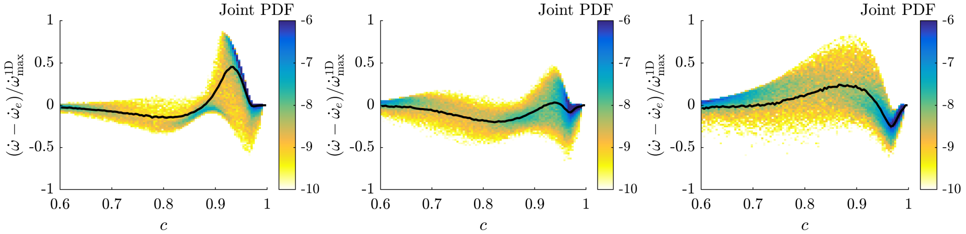

(a) Case A1 (b) Case A3 (c) Case B

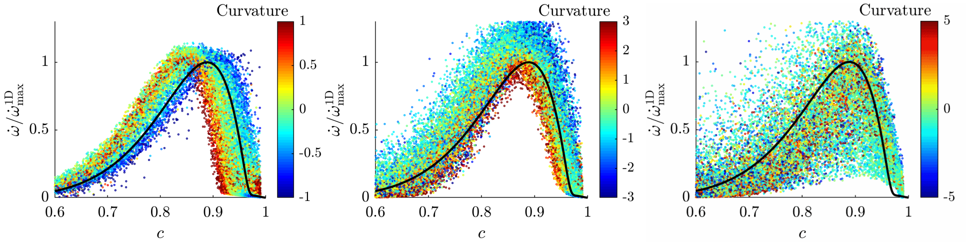

(d) Case A1 (e) Case A3 (f) Case B

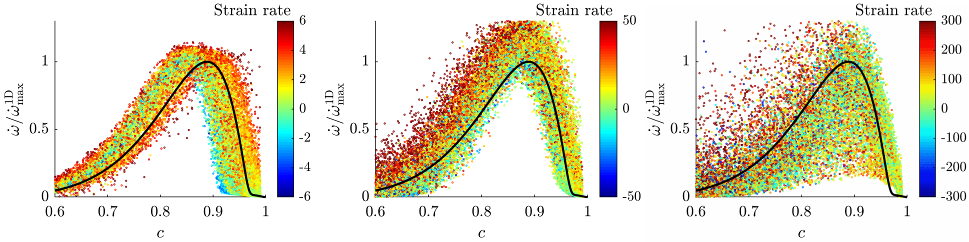

(g) Case A1 (h) Case A3 (i) Case B

Figure 12: (a-c): Joint PDF of c and the difference between modelled and exact reaction rate $\dot{\omega}-\dot{\omega}_e$. The colour scale is logarithmic and the numbers give the exponent of 10. The black line shows the conditional average $\langle(\dot{\omega}-\dot{\omega}_e)|c\rangle$. (d-i): Scatter plots of c and exact reaction rate. The colour scale shows mean curvature normalized by $1/\delta_{th}$ in (d-f) and tangential strain rate normalized by S_L/δ_{th}. The black line shows the modelled reaction rate.

errors. Under these conditions it is not possible to discern how much of the error can be attributed to either assumption. The conclusions from previous sections can however provide an indication.

A direct comparison of modelled sub-grid PDFs and PDFs extracted from DNS are shown in Fig. 13 for cases A1, A2, A3 and B using three filter sizes and three values of $\tilde{c}$. Case C is not shown here since its PDFs are very similar to that of case A2. In Table 2 the match between the PDFs and beta-distribution is quantified by the Kullback-Leibler divergence. The match is generally better for higher Ka and smaller filter size. As seen in the figure the error can sometimes be significant near the reaction region when the filter size is ≥ 1.

The mean error E and the correlation coefficient r are shown in Fig. 14 as functions of filter size for all three-dimensional cases. For most cases (A3 is the exception, as was discussed in the previous section) the correlation coefficient starts around 0.8 for the unfiltered flame, decreases to a minimum near $\Delta^+ = 1$ and then increases for larger filters.

The error E for the scaled model generally decreases with filter size while the error of the unscaled model tends to have a minimum for some filter size $\Delta^+ > 1$, consistently with the observations from the one-dimensional flame in section 4.2.1. The relatively large error and low correlation in the unfiltered flames is due only to assumption (ii), i.e. $\dot{\omega}$ is not well described by the one-dimensional flame as discussed in the previous section. When the Δ^+ increases the effects responsible for the deviations from assumption (ii) are averaged over. The result of this is that the filtered field contains fewer deviations so that a larger filter helps improving the model predictions at high Ka. Furthermore, the sub-grid PDF is likely to be predicted with similar accuracy here as it was in the simplified-chemistry case D for which the correlation was always high (c.f. Fig. 10). Overall the non-monotonic error and correlation curves in Fig. 14 are consistent with a balance between the errors from the two assumptions that were previously discussed individually. Most of the error seen in these complex chemistry cases is however probably due to assumption (ii) which is related to the presence of intermediate species, curvature and strain. It is also noted that the correction factor f is effective in reducing the error also when the two assumptions are combined.

Cases A2 and C again have nearly identical values of E and r. Since these two cases only differ by their integral length scale it can be concluded that E and r do not have a major dependence on this parameter.

5. Conclusions

DNS data of premixed flames, both with single-step reaction and complex methane/air chemistry, at high Karlovitz numbers have been used for a priori evaluation of a presumed-PDF combustion model with flamelet tabulation. Filtered reaction rates of a reaction progress variable were computed from the model and compared with the corresponding rates obtained by direct filtering of DNS data. The main conclusions are summarized in the following:

- For flames with complex transport and chemistry the presumed-PDF model works better for large filter sizes than for small ones. For such flames most of the error stems

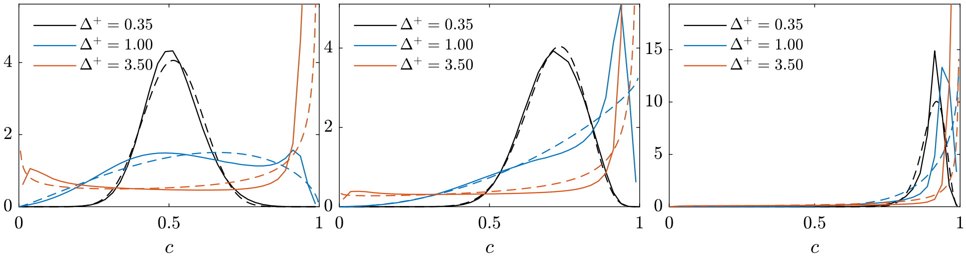

(a) A1, $\tilde{c} = 0.5$ (b) A1, $\tilde{c} = 0.7$ (c) A1, $\tilde{c} = 0.9$

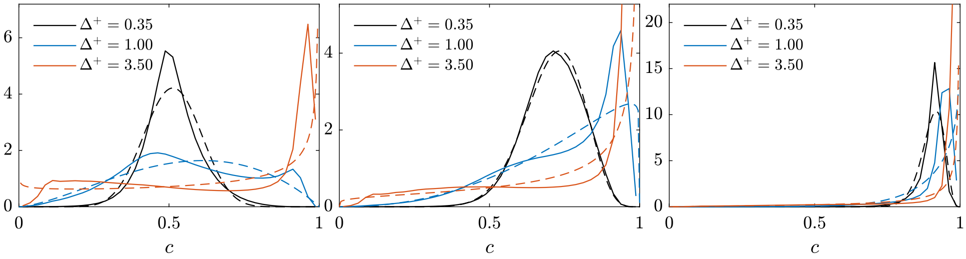

(d) A2, $\tilde{c} = 0.5$ (e) A2, $\tilde{c} = 0.7$ (f) A2, $\tilde{c} = 0.9$

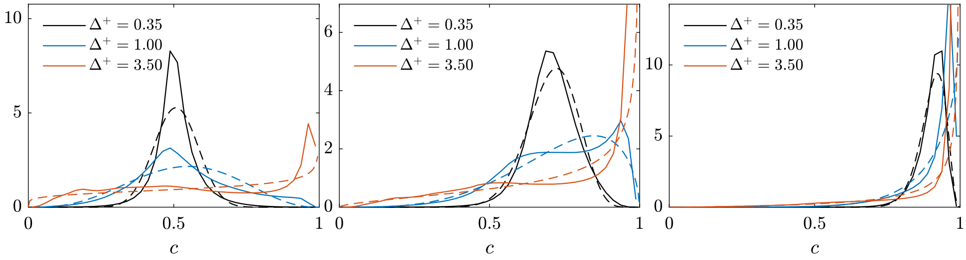

(g) A3, $\tilde{c} = 0.5$ (h) A3, $\tilde{c} = 0.7$ (i) A3, $\tilde{c} = 0.9$

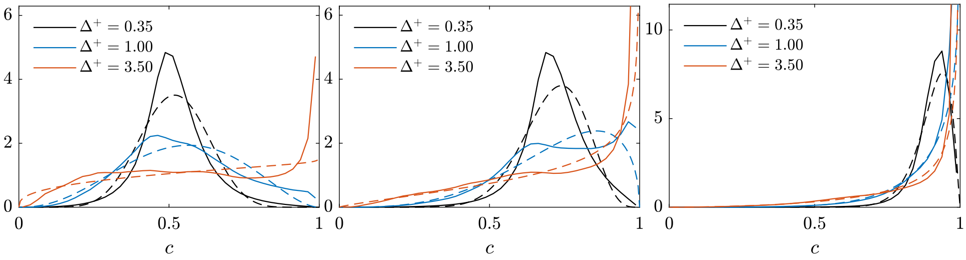

(j) B, $\tilde{c} = 0.5$ (k) B, $\tilde{c} = 0.7$ (l) B, $\tilde{c} = 0.9$

Figure 13: Sub-grid probability density of c at selected values of the filtered progress variable $\tilde{c}$. Different cases and filter sizes are shown as indicated in the figure. Symbols show the PDF from DNS and lines show the model beta-distribution.

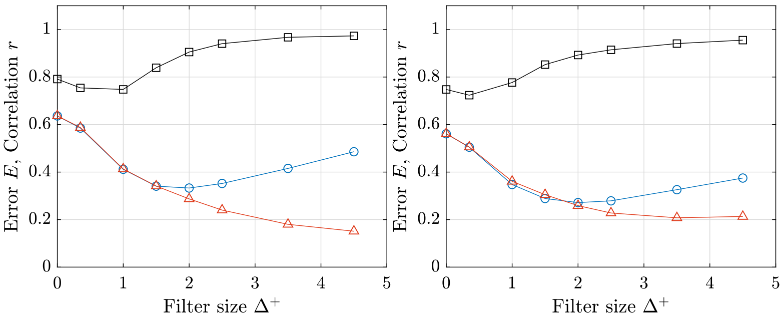

(a) Case A1 (b) Case A2

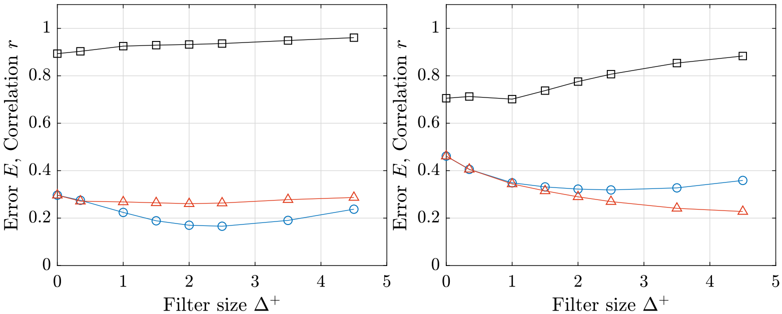

(c) Case A3 (d) Case B

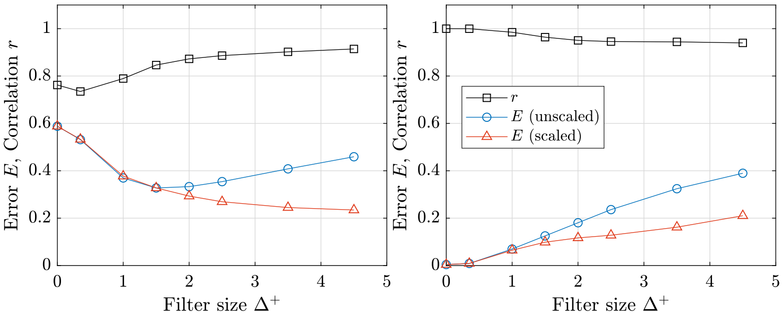

(e) Case C (f) Case D

Figure 14: Error E and correlation coefficient r of the presumed-PDF model applied to a the filtered reaction rate of turbulent flames. Error E is shown both for the unscaled (circles) and scaled (triangles) versions of the model. Figures (a-e) shows cases A1, A2, A3, B, C and D, respectively.

from assumption (ii), i.e. the representation of the local rates by a flamelet through $\dot{\omega} = \dot{\omega}(c)$, and is therefore tied to the complex chemistry. The error at small filter sizes, however, is found to have a minimum for the case with Ka = 540 and larger error is seen for both larger (4100) and smaller (6 and 74) Ka. At low Ka this is believed to be due to the strong correlation observed between curvature/strain and shift in the reaction rate profile in the reaction progress variable coordinate. This correlation disappears for very high Ka.

- At high Karlovitz numbers a large filter has a smoothing effect which helps reduce the error from the flamelet assumption. This is an interesting behaviour for example for LES of gas turbines, where filter sizes can be relatively large compared to the flame thickness.

- The match between sub-grid probability distribution and the beta-distribution varies from acceptable to rather poor depending on Karlovitz number, filter size and location in the flame. The corresponding error in the filtered rate does increase with filter size which can be problematic for practical LES where the filter size cannot be too small if the computation should be kept affordable. This was established by studying a flame with simplified chemistry where the flamelet assumption holds. For flames with complex chemistry and transport this error seems to be small compared with the one from the flamelet assumption.

- A filter size dependent scaling factor for the model was defined using a filtered one-dimensional flame. The factor ensures that the flame speed is unaffected by filtering for the one-dimensional flame. This factor results in a substantial reduction of the model error for filter sizes larger than the thermal flame thickness, which is relevant for practical LES. The same factor can be used in three-dimensional flames which makes it inexpensive to use in LES since the factor can be pre-computed and stored.

This work has been concerned only with the flamelet assumption and the presumed PDF. When used in practical LES, the result will also be influenced by the choice of model for the sub-grid variance. Future follow-up studies should therefore contain both a priori analysis of models for the sub-grid variance and a posteriori analysis where a complete LES model is compared with a similar DNS.

Acknowledgements

The authors at Lund University acknowledges funding from the Swedish Research Council (VR) and the national Centre for Combustion Science and Technology (CeCOST). We acknowledge PRACE for awarding us access to MareNostrum at Barcelona Supercomputing Center (BSC), Spain and SuperMUC at LRZ, Germany. Computations were also performed on resources provided by the Swedish National Infrastructure for Computing (SNIC) at PDC and HPC2N. N.A.K. Doan acknowledges the support of the Technical University of Munich - Institute for Advanced Study, funded by the German Excellence Initiative and the European Union Seventh Framework Programme under grant agreement no. 291763.

[1] B. Fiorina, D. Veynante, S. Candel, Modeling combustion chemistry in large eddy simulation of turbulent flames, Flow Turbulence Combust. 94 (2015) 3–42.

[2] N. Peters, Turbulent Combustion, Cambridge University Press, 2000.

[3] H. Pitsch, A consistent level set formulation for large-eddy simulation of premixed turbulent combustion, Combust. Flame 143 (2005) 587–598.

[4] O. Colin, F. Ducros, D. Veynante, T. Poinsot, A thickened flame model for large eddy simulations of turbulent premixed combustion, Phys. Fluids 12 (2000) (2000) 1843–1863.

[5] B. F. Magnussen, On the Structure of Turbulence and a Generalized Eddy Dissipation Concept for Chemical Reaction in Turbulent Flow, 19th AIAA Aerospace Science Meeting, St.Louis, Missouri.

[6] M. Berglund, E. Fedina, C. Fureby, J. Tegner, V. Sabel'nikov, Finite Rate Chemistry Large-Eddy Simulation of Self-Ignition in a Supersonic Combustion Ramjet, AIAA J. 48 (2010) 540–550.

[7] A. R. Kerstein, Linear eddy modelling of turbulent transport. Part 7. Finite-rate chemistry and multi-stream mixing, J. Fluid Mech. 240 (1992) 89–313.

[8] S. B. Pope, PDF methods for turbulent reactive flows, Prog. Energy Combust. 11 (1985) 119–192.

[9] R. Borghi, P. Moreau, Turbulent combustion in a premixed flow, Acta Astronautica 4 (1977) 321–341.

[10] D. Bradley, L. K. Kwa, A. K. C. Lau, M. Missaghi, Laminar flamelet modeling of recirculating premixed metahne and propane-air combustion, Combust. Flame (71) (1988) 109–122.

[11] A. W. Cook, J. J. Riley, A subgrid model for equilibrium chemistry in turbulent flows, Phys. Fluids (6) (1994) 2868–2870.

[12] J. A. van Oijen, A. Donini, R. J. M. Bastiaans, J. H. M. ten Thije Boonkkamp, L. P. H. de Goey, State-of-the-art in premixed combustion modeling using flamelet generated manifolds, Progress in Energy and Combustion Science (2016) 30–74.

[13] O. Gicquel, N. Darabiha, D. Thevenin, Laminar premixed hydrogen/air counterflow flame simulations using flame prolongation of ILDM with differential diffusion, Proceedings of the Combustion Institute 28 (2000) 1901–1908.

[14] S. Lapointe, G. Blanquart, A priori filtered chemical source term modeling for LES of high Karlovitz number premixed flames, Combust. Flame 176 (2017) 500–510.

[15] P. Trisjono, K. Kleinheinz, E. R. Hawkes, H. Pitsch, Modeling turbulence-chemistry interaction in lean premixed hydrogen flames with a strained flamelet model, Combust. Flame 174 (2016) 194–207.

[16] I. Langella, N. Swaminathan, Unstrained and strained flamelets for LES of premixed combustion, Combust. Theory Model. 20 (2016) 410–440.

[17] N. A. K. Doan, N. Swaminathan, N. Chakraborty, Multiscale analysis of turbulence-flame interaction in premixed flames, Proc. Combust. Inst. 36 (2017) 1929–1935.

[18] P. Domingo, L. Vervisch, D. Veynante, Large-eddy simulation of a lifted methane jet flame in a vitiated coflow, Combust. Flame (152) (2008) 415–432.

[19] J. Floyd, A. M. Kempf, A. Kronenburg, R. H. Ram, A simple model for the filtered density function for passive scalar combustion LES, Combust. Theory Model. 13 (4) (2009) 559–588.

[20] S. Nambully, P. Domingo, V. Moreau, L. Vervisch, A filtered-laminar-flame PDF subgrid scale closure for LES of premixed turbulent flames. Part I: Formalism and application to a bluff-body burner with differential diffusion, Combust. Flame (161) (2014) 1756–1774.

[21] I. Langella, N. Swaminathan, R. W. Pitz, Application of unstrained flamelet SGS closure for multi-regime premixed combustion, Combust. Flame 173 (2016) 161–178.

[22] S. Lapointe, G. Blanquart, A priori filtered chemical source term modeling for LES of high Karlovitz number premixed flames, Combust. Flame 176 (2017) 500–510.

[23] S. B. Pope, in: Turbulent Flows, Cambridge University Press, Cambridge, 2000, Ch. 13.

[24] F. Gao, E. E. O'Brien, A large-eddy simulation scheme for turbulent reacting flows, Physics of Fluids A: Fluid Dynamics 5 (1993) 1282–1284.

[25] S. Nambully, P. Domingo, V. Moureau, L. Vervisch, A filtered-laminar-flame PDF subgrid scale closure for LES of premixed turbulent flames. Part I: Formalism and application to a bluff-body burner with differential diffusion, Combust. Flame 161 (2014) 1756–1774.

[26] C. Jimenez, F. Ducros, B. Cuenot, B. Bedat, Subgrid scale variance and its dissipation of a scalar field in large eddy simulations, Phys. Fluids 13 (2001) 1748–1754.

[27] T. Nilsson, I. Langella, N. Doan, N. Swaminathan, R. Yu, X. Bai, A priori analysis of sub-grid variance of a reactive scalar using dns data of high ka flames, Combustion Theory and Modelling 0 (0) (2019) 0. doi:10.1080/13647830.2019.1600033.

[28] J. M. Bland, D. G. Altman, Calculating correlation coefficients with repeated observations: Part 2—correlation between subjects, BMJ 310 (1995) 633.

[29] B. Fiorina, R. Vicquelin, P. Auzillon, N. Darabiha, O. Gicquel, D. Veynante, A filtered tabulated chemistry model for les of premixed combustion, Combust. Flame 157 (2010) 465–475.

[30] M. Smooke, V. Giovangigli, Reduced Kinetic Mechanisms and Asymptotic Approximation for methane-air Flames, Springer-Verlag, Berlin, 1991.

[31] T. Nilsson, H. Carlsson, R. Yu, X. S. Bai, Structures of turbulent flames in the high Karlovitz number regime - DNS analysis, Fuel 216 (2018) 627–638.

[32] R. Yu, N. Lipatnikov, DNS study of dependence of bulk consumption velocity in a constant-density reacting flow on turbulence and mixture characteristics, Phys. Fluids 29 (2017) 065116.

[33] S. Ghosal, T. S. Lund, P. Moin, K. Akselvoll, A dynamic localization model for large-eddy simulation of turbulent flows, J. Fluid Mech. 286 (1995) 229–255.

[34] R. Yu, J. Yu, X. S. Bai, An improved high-order scheme for DNS of low mach number turbulent reacting flows based on stiff chemistry solver, J. Comp. Phys. 231 (2012) 5504–5521.

[35] G. Strang, On the construction and comparison of difference schemes, Siam J. on Num. Anal. 5 (1968) 506–517.

[36] P. N. Brown, G. D. Bryne, A. C. Hindmarsch, VODE, a variable-coefficient ode solver, Siam J. Sci. Stat. Comp. 10 (1989) 1038–1051.

[37] R. Yu, X. S. Bai, A semi-implicit scheme for large eddy simulation of piston engine flow and combustion, Int. J. Numerical Methods in Fluids 71 (2013) 13–40.

[38] E. R. Hawkes, J. H. Chen, Comparison of direct numerical simulation of lean premixed methane-air flames with strained laminar flame calculations, Combust. Flame 144 (2006) 112–125.

Paper IV

Evolution of averaged local premixed flame thickness in a turbulent flow

Rixin Yu[a], Thommie Nillson[a], Xue-Song Bai[a], Andrei N. Lipatnikov[b]

[a]*Div. of Fluid Mechanics, Dep. of Energy Sciences, Lund University, Sweden*

[b]*Department of Mechanics and Maritime Sciences, Chalmers University of Technology, Göteborg, 412 96, Sweden.*

Abstract

In the combustion literature, contradictory results on the influence of turbulence on the local thickness of a premixed flame can be found and the present paper aims at contributing to reconcile this issue. First, different measures of local flame thickness in a turbulent flow, e.g. area-weighted and unweighted surface-averaged values of (i) $|\nabla c|$ the absolute value of 3D gradient of the combustion progress variable c or (ii) $1/|\nabla c|$, are studied and analytical relationships/inequalities between them are obtained. Second, the evolution of the different flame thickness measures is explored by numerically evaluating them, as well as various terms in relevant evolution equations derived analytically. To do so, various measures and terms are extracted from DNS data obtained from (i) a highly turbulent, constant-density, dynamically passive, single-reaction wave, (ii) moderately and highly turbulent, single-step-chemistry flames, and (iii) moderately and highly turbulent, complex-chemistry lean methane-air flames. In all those cases, all studied flame thickness measures are reduced during an early stage of premixed turbulent flame development, followed by local flame re-broadening at later stages. Analysis of various terms in the aforementioned evolution equations shows that the initial local flame thinning is controlled by turbulent strain rates. The subsequent local flame re-broadening is controlled by (i) curvature contribution to the stretch rate, which counter-balances the strain rate, (ii) spatial non-uniformities of the normal diffusion contribution to the local displacement-velocity vector $S_d\boldsymbol{n}$, and (iii) dilatation, which plays an important role in moderately turbulent flames, but a minor role in highly turbulent flames. Moreover, the present study shows that differently defined measures of a local flame thickness can be substantially different. This difference should also be borne in mind when comparing data that indicate local flame thinning with data that indicate local flame broadening.

Keywords: Turbulent reacting flow, turbulent combustion, flame thickness, DNS, conditioned statistics

---

1. Introduction

When a premixed flame propagates in a turbulent flow, the turbulence not only wrinkles the flame surface, consequently increasing its area and burning rate, but can also substantially affect the inner structure of the instantaneous flame as well as the local heat release rate within it. One of the most discussed manifestations of the latter (structure) effects consists of variations in the local flame thickness under the influence of turbulent eddies. While such thickness variations have been attracting significant attention, this fundamental issue is still intricate and the available data are controversial. Indeed, on the one hand there are experimental [1, 2] and Direct Numerical Simulation (DNS) data [3] that indicate local thinning of flames in turbulent flows. On the other hand, there are experimental [4–6] and DNS data [7–12] that show the opposite trend. Moreover, in certain experimental studies of methane-air flames [13, 14], both local thinning and local broadening of flames was documented at lower and larger, respectively, equivalence ratios.

As discussed in detail by Driscoll [15], there are several possible explanations for the aforementioned opposite trends. For instance, they were argued [13, 16] to stem from the opposite effects of a positive strain rate on the thicknesses of lean methane-air (thinning) or lean propane-air (broadening) laminar flames. Accordingly, both local thinning and local broadening of a flame in a turbulent flow were considered [13] to be controlled by the local stretch rate, rather than by penetration of turbulent eddies into the flame. However, such a clear and plausible explanation is not supported by recent DNS data that indicate local broadening of lean methane-air flames [11, 12].

Thus, the discussed issue is not resolved and the behaviour of local flame thickness in a turbulent flow still requires further research. The present work aims at addressing this request both analytically, see Section 2 where different measures of the local flame thickness and relevant evolution equations are dicussed, and numerically, i.e. by analyzing DNS data, see Sections 3 and 4 where the DNSs are described and the computed results are analyzed. Conclusions are summarized in Section 5.

2. Analysis

2.1. Different measures of local flame thickness

To explore the behaviour of a local flame thickness in a turbulent flow, this thickness should be defined. In the literature, different measures of the thickness can be found, but, most often, it is evaluated using the absolute value of the gradient of the temperature, density, or mass fraction of a major species. In the present paper, the thickness is quantified using the spatial gradient of the combustion progress variable c, which is equal to zero and unity in reactants and products, respectively. Accordingly, the local flame thickness is equal to $1/|\nabla c|$. Even in this simplest case, there are different definitions of the mean local flame thickness, i.e. $1/|\nabla c|$ conditionally averaged over a certain flame zone $c_1 < c(t, \boldsymbol{x}) < c_2$ or along a certain flame surface $c(t, \boldsymbol{x}) = \hat{c}$.

For any local flame or flow characteristic $\phi(t,\boldsymbol{x})$, its surface-averaged value measured at time instant t can be either area-weighted [17], i.e.

$$\langle\phi\rangle_s|_{\hat{c},t} \equiv \overline{\phi|\nabla c|\delta(c-\hat{c})} \;/\; \overline{|\nabla c|\delta(c-\hat{c})}, \tag{1}$$

or unweighted, i.e.

$$\langle\phi\rangle_v|_{\hat{c},t} \equiv \overline{\phi\delta(c-\hat{c})} \;/\; \overline{\delta(c-\hat{c})}. \tag{2}$$

Here, $\delta(c-\hat{c})$ is the Dirac delta function, overline designates both ensemble and spatial averages taken consecutively, i.e.

$$\overline{\phi} \equiv \lim_{M\to\infty} \frac{1}{M}\sum_{i=1}^{M}\frac{1}{V}\iiint \phi_{(i)}(t,\boldsymbol{x})\,\mathrm{d}\boldsymbol{x}, \tag{3}$$

M is the number of realizations in the ensemble, $\phi_{(i)}$ pertains to the i-th realization, and V is the considered volume, i.e. the volume of the computational domain in numerical simulations or the volume of the burner in an experiment. By using a smaller volume bounded by two mean iso-scalar surfaces, the above definitions can be extended to study surface-averaged quantities conditioned to a particular zone of the mean flame brush, with quantities conditioned to different zones being different. However, the present analysis is restricted to bulk quantities conditioned to the entire surface of $c(t,\boldsymbol{x}) = \hat{c}$, i.e. conditionally averaged over the entire flame-brush volume. Indeed, in Eqs. (1) and (2), integration over the volume is equivalent to integration over the surface due to the appearance of a Dirac delta function in the numerator and denominator of both equations.

Using an equality of $\iiint \phi|\nabla c|\delta(c-\hat{c})\,\mathrm{d}\boldsymbol{x} = \iint_{S|_{\hat{c},t}} \phi\,\mathrm{d}s$ [18–20], the area-weighted surface-average can be re-expressed as follows

$$\langle\phi\rangle_s|_{\hat{c},t} = \widehat{\iint_{S|_{\hat{c},t}} \phi\,\mathrm{d}s} \Big/ \widehat{A|_{\hat{c},t}}, \tag{4}$$

where $S|_{\hat{c},t}$ denotes the iso-surface of $c(\boldsymbol{x},t) = \hat{c}$, whose total area is $A|_{\hat{c},t} \equiv \iint_{S|_{\hat{c},t}} \mathrm{d}s$, and the long-hat operator over any expression ψ represents the ensemble average, i.e. $\widehat{\psi} \equiv \lim_{M\to\infty}\frac{1}{M}\sum_{i=1}^{M}\psi_{(i)}$ and, consequently, $\overline{\psi} = \frac{1}{V}\widehat{\iiint \psi\,\mathrm{d}\boldsymbol{x}}$, see Eq. (3).

Similarly, area-weighted and unweighted quantities conditioned to a certain flame zone can be introduced as

$$\begin{aligned}
\langle\phi\rangle_S|_{\hat{c},\epsilon,t} &\equiv \frac{\overline{\phi|\nabla c|1_{\hat{c},\epsilon}}}{\overline{|\nabla c|1_{\hat{c},\epsilon}}} = \lim_{M\to\infty}\frac{\sum_{i=1}^{M}\iiint_V \phi_{(i)}|\nabla c_{(i)}|1_{\hat{c},\epsilon}\,\mathrm{d}\boldsymbol{x}}{\sum_{i=1}^{M}\iiint_V |\nabla c_{(i)}|\,1_{\hat{c},\epsilon}\,\mathrm{d}\boldsymbol{x}};\\
\langle\phi\rangle_V|_{\hat{c},\epsilon,t} &\equiv \frac{\overline{\phi 1_{\hat{c},\epsilon}}}{\overline{1_{\hat{c},\epsilon}}} = \lim_{M\to\infty}\frac{\sum_{i=1}^{M}\iiint_V \phi_{(i)}\cdot 1_{\hat{c},\epsilon}\,\mathrm{d}\boldsymbol{x}}{\sum_{i=1}^{M}\iiint_V 1_{\hat{c},\epsilon}\,\mathrm{d}\boldsymbol{x}},
\end{aligned} \tag{5}$$

respectively. Here, the sifting function $1_{\hat{c},\epsilon} \equiv H(c-\hat{c}) - H(c-\hat{c}-\epsilon)$ allows us to select c within an interval of $[\hat{c},\hat{c}+\epsilon]$, ϵ is a positive number, and $H(c)$ is Heaviside function. Then, the quantities $\langle\phi\rangle_s|_{\hat{c},t}$ and $\langle\phi\rangle_v|_{\hat{c},t}$ may be interpreted to be "fine-grained" values of ϕ, whereas $\langle\phi\rangle_S|_{\hat{c},\epsilon,t}$ and $\langle\phi\rangle_V|_{\hat{c},\epsilon,t}$ are its "coarse-grained" values. Even if one would expect that

$$\langle\phi\rangle_s|_{\hat{c},t} = \lim_{\epsilon\to 0}\langle\phi\rangle_S|_{\hat{c},\epsilon,t} \;\; ; \;\; \langle\phi\rangle_v|_{\hat{c},t} = \lim_{\epsilon\to 0}\langle\phi\rangle_V|_{\hat{c},\epsilon,t}, \tag{6}$$

the fine-grained and coarse-grained values of ϕ can be different for a finite ϵ. Therefore, the relationship between $\langle\phi\rangle_s|_{\hat{c},t}$ and $\langle\phi\rangle_S|_{\hat{c},\epsilon,t}$ or between $\langle\phi\rangle_v|_{\hat{c},t}$ and $\langle\phi\rangle_V|_{\hat{c},\epsilon,t}$ should be studied. This issue was addressed in recent papers [21, 22], where a good match of fine-grained and coarse-grained values of various ϕ was demonstrated by analyzing DNS data and using a sufficiently small $\epsilon \leq 0.02$.

It is worth remembering that both area-weighted and unweighted, fine-grained and coarse-grained values of various quantities ϕ appear to be used in the literature, while methods applied to obtain a conditioned value of ϕ are seldom discussed in detail. We may note that unweighted coarse-grained surface-averaged quantities appear to be addressed in experimental papers aiming at evaluation of local flame thickness [1, 2, 5, 13, 14, 23, 24] by measuring $|\nabla c|$, local flame curvature [14, 24–26], local strain rate [27], etc. Area-weighted surface-averaged quantities ϕ were reported in some DNS papers, e.g. see Ref. [28]. In the following, symbol $\langle\phi\rangle_{?,\hat{c}}$ is used when discussing a surface-averaged quantity whose definition has not been specified properly or is of minor importance for the discussed subject.

In addition to the aforementioned sources of ambiguities (i.e. different definitions of surface-averaged quantities), there is also another ambiguity. The point is that the behavior of the local flame thickness is often discussed either by comparing $\langle|\nabla c|\rangle_{?,\hat{c}}$ with the counterpart value $|\nabla c_L|(\hat{c})$ obtained from the unperturbed laminar flame (i.e. fully-developed, planar, 1D laminar premixed flame) or by comparing $\langle 1/|\nabla c|\rangle_{?,\hat{c}}$ with $1/|\nabla c_L|(\hat{c})$. However, $1/\langle|\nabla c|\rangle_{?,\hat{c}}$ does not equal to $\langle 1/|\nabla c|\rangle_{?,\hat{c}}$ and the difference in these two quantities should be studied.

While some of the quantities defined above can be related using simple equations, other quantities can be significantly different. Indeed, on the one hand, a comparison of Eqs. (1) and (2) results directly in

$$\langle\phi\rangle_s = \langle\phi|\nabla c|\rangle_v / \langle|\nabla c|\rangle_v \quad \text{and} \quad \langle\phi\rangle_v = \langle\phi/|\nabla c|\rangle_s \langle|\nabla c|\rangle_v, \tag{7}$$

and similar relationships can be derived for coarse-grained surface-averaged quantities. On the other hand, the difference between area-weighted and unweighted surface averages is

$$\langle\phi\rangle_s - \langle\phi\rangle_v = R_{\phi,|\nabla c|}|_v \cdot \sqrt{\langle\phi'^2\rangle_v}\sqrt{\langle|\nabla c|'^2\rangle_v}/\langle|\nabla c|\rangle_v, \tag{8}$$

where $R_{\phi,|\nabla c|}|_v \equiv \langle\phi'|\nabla c|'\rangle_v / \sqrt{\langle\phi'^2\rangle_v \langle|\nabla c|'^2\rangle_v}$ designates the correlation between ϕ and $|\nabla c|$, the prime symbol represents fluctuations in the unweighted framework, i.e., $\phi' \equiv \phi - \langle\phi\rangle_v$, and $\sqrt{\langle\phi'^2\rangle_v}$ is the standard deviation of ϕ within the same framework. Equation (8) shows that the difference in area-weighted and unweighted values can vanish either in an unlikely case of zero correlation between ϕ and $|\nabla c|$ or in the trivial case of zero fluctuations, i.e., $\sqrt{\langle \phi'^2 \rangle_v} = 0$. Such a trivial case could be relevant in a weakly turbulent environment associated with negligible perturbations of the local flame structure. However, in a flame strongly perturbed by turbulence, fluctuations in $|\nabla c|$ along an iso-scalar surface can be significant, thus making $\langle \phi \rangle_s$ and $\langle \phi \rangle_v$ substantially different.

For instance, if $\phi = |\nabla c|$, then, $\langle |\nabla c| \rangle_s - \langle |\nabla c| \rangle_v = \langle |\nabla c|'^2 \rangle_v / \langle |\nabla c| \rangle_v \geq 0$, because $R_{|\nabla c|,|\nabla c|} = 1$. On the contrary, if $\phi = 1/|\nabla c|$, the difference $\langle 1/|\nabla c| \rangle_s - \langle 1/|\nabla c| \rangle_v \leq 0$ due to negative correlation of $R_{|\nabla c|,1/|\nabla c|} \leq 0$ by virtue of Cauchy-Schwartz inequality.If we introduce other measures of the local flame thickness, e.g. $1/\exp\left(\langle \ln(|\nabla c|) \rangle_s\right)$ and $1/\exp\left(\langle \ln(|\nabla c|) \rangle_v\right)$, which characterize the area-weighted and unweighted, respectively, geometrical means of $|\nabla c|$ as discussed in section 1 in supplemental material, then the following inequalities hold

$$\frac{1}{\langle |\nabla c| \rangle_s} \leq \frac{1}{\exp\left(\langle \ln(|\nabla c|) \rangle_s\right)} \leq \frac{1}{\langle |\nabla c| \rangle_v} = \left\langle \frac{1}{|\nabla c|} \right\rangle_s \leq \frac{1}{\exp\left(\langle \ln(|\nabla c|) \rangle_v\right)} \leq \left\langle \frac{1}{|\nabla c|} \right\rangle_v, \tag{9}$$

see Eqs. (7), (8) and section 1 in supplemental material.

Therefore, if the local wave thickness is characterized with a surface-averaged value of $|\nabla c|$ or $1/|\nabla c|$, then, results of evaluation of the area-weighted $\langle |\nabla c| \rangle_s$ or $\langle 1/|\nabla c| \rangle_s$, respectively, are associated with a smaller thickness when compared to results found for the unweighted $\langle |\nabla c| \rangle_v$ or $\langle 1/|\nabla c| \rangle_v$, respectively. This difference should be borne in mind when qualitatively comparing published data on the thickness. Such a difference is unlikely to be the major cause of opposite trends reported for the influence of turbulence on the local flame thickness, but it can contribute to the inconsistency of some reported data.

Another commonly disregarded effect, i.e. transient development of premixed turbulent flames that were studied in most experiments [29, 30] and in some DNSs, e.g. see Ref. [3], appears to be of much more importance, as will be shown in Section 4.1. To explore this effect more profoundly, various terms in recently derived [22] evolution equations for differently defined bulk surface-averaged measures of the local flame thickness will be analyzed in Section 4.2. For completeness, those evolution equations and derivation of them are briefly summarized in the next subsection.

2.2. Derivation of evolution equations

After defining several statistical measures of the local flame thickness in a turbulent flow, let us derive evolution equations for them starting from the following well-known transport equation for a reaction progress variable

$$\frac{\partial c}{\partial t} + \boldsymbol{u} \cdot \nabla c = \mathbb{D} + \mathbb{W}. \tag{10}$$

Here, t, $\boldsymbol{u}$, $\mathbb{D}$, and $\mathbb{W}$ are the time, flow velocity vector, diffusion term (e.g. $\rho^{-1}\nabla \cdot \rho\mathcal{D}\nabla c$, where $\mathcal{D}$ is the molecular diffusivity of c) and the rate of product formation, respectively. By defining the unit normal vector $\boldsymbol{n} \equiv \boldsymbol{\nabla} c/|\nabla c|$, the local displacement speed $S_d \equiv (\mathbb{D}+\mathbb{W})/|\nabla c|$, and the "total flame speed" [31] $\boldsymbol{u}^* \equiv \boldsymbol{u} - \boldsymbol{n}S_d$ respectively, the "convective derivative based on the total flame speed" [31] can be defined as

$$\frac{d^*}{d^*t}\phi \equiv \frac{\partial}{\partial t}\phi + \boldsymbol{u}^* \cdot \boldsymbol{\nabla}\phi, \tag{11}$$

Eq. (10) can be rewritten in the following "kinematic" form

$$\frac{\partial c}{\partial t} + \boldsymbol{u} \cdot \nabla c = S_d|\nabla c|, \quad \text{or} \quad \frac{d^*}{d^*t}c = 0. \tag{12}$$

Within the adopted analytical framework, the following transport equation for $|\nabla c|$

$$\frac{1}{|\nabla c|}\frac{d^*}{d^*t}|\nabla c| = -a_n + \boldsymbol{n} \cdot \boldsymbol{\nabla} S_d = a_t - \nabla\cdot\boldsymbol{u} + \nabla\cdot(S_d\boldsymbol{n}) - S_d\boldsymbol{\nabla}\cdot\boldsymbol{n} = \mathcal{K} - \nabla\cdot\boldsymbol{u} + \nabla\cdot(S_d\boldsymbol{n}) \tag{13}$$

is well known, see for example Eq. (38) in the seminal paper by Candel and Poinsot [31], where notation is different, e.g. the unit normal vector points to the opposite direction. Here, $a_n \equiv \boldsymbol{nn} : \nabla\boldsymbol{u}$ is the normal strain rate, $a_t = \nabla\cdot\boldsymbol{u} - a_n$ is the tangential stain rate, and $\mathcal{K} = a_t - S_d\nabla\cdot\boldsymbol{n}$ is the stretch rate.

The stretch rate is well known [31, 32] to control the rate of change in the area $\mathrm{d}s$ of an infinitesimal element of an iso-scalar surface. For instance, using the following transport theorem

$$\frac{d}{dt}\iint\limits_{S(t)} \boldsymbol{G}\cdot\boldsymbol{n}\,\mathrm{d}s = \iint\limits_{S(t)} \left[\frac{\partial}{\partial t}\boldsymbol{G} + (\boldsymbol{u}^*\cdot\boldsymbol{\nabla})\boldsymbol{G} - (\boldsymbol{G}\cdot\boldsymbol{\nabla})\boldsymbol{u}^* + \boldsymbol{G}\boldsymbol{\nabla}\cdot\boldsymbol{u}^*\right]\cdot\boldsymbol{n}\,\mathrm{d}s \tag{14}$$

with $\boldsymbol{G} = \boldsymbol{n}$, Candel and Poinsot [31] have shown that, for any iso-scalar surface, $\frac{d}{dt}\iint_{S(t)} \mathrm{d}s = \iint_{S(t)}(-\boldsymbol{nn} : \boldsymbol{\nabla}\boldsymbol{u}^* + \boldsymbol{\nabla}\cdot\boldsymbol{u}^*)\,\mathrm{d}s = \iint_{S(t)} \mathcal{K}\,\mathrm{d}s$. Substitution of $\boldsymbol{G} = \boldsymbol{n}\phi$ into Eq. (14) written for an iso-scalar surface of $c(\boldsymbol{x}, t) = \hat{c}$ results in

$$\begin{aligned}\frac{d}{dt}\iint\limits_{S|_{\hat{c},t}} \phi\,\mathrm{d}s &= \iint\limits_{S|_{\hat{c},t}} \left[\frac{\partial}{\partial t}\phi + \boldsymbol{u}^*\cdot\boldsymbol{\nabla}\phi\right]\mathrm{d}s + \iint\limits_{S|_{\hat{c},t}} \left[-\boldsymbol{nn} : \boldsymbol{\nabla}\boldsymbol{u}^* + \boldsymbol{\nabla}\cdot\boldsymbol{u}^*\right]\phi\,\mathrm{d}s \\ &= \iint\limits_{S|_{\hat{c},t}} \frac{d^*}{d^*t}\phi\,\mathrm{d}s + \iint\limits_{S|_{\hat{c},t}} \phi\mathcal{K}\,\mathrm{d}s.\end{aligned} \tag{15}$$

Finally, combining this equation written for $\phi = 1$ with the definition of area-weighted, surface-averaged stretch rate, given by Eq. (4) with $\phi = \mathcal{K}$, and taking ensemble average, we arrive at

$$\langle\mathcal{K}\rangle_s|_{\hat{c},t} = \frac{1}{\widehat{A}|_{\hat{c},t}}\frac{\partial}{\partial t}\widehat{A}|_{\hat{c},t}. \tag{16}$$

Equations (4) and (16) allow us to easily derive an evolution equation for the area-weighted surface-averaged value $\langle\phi\rangle_s$ of the quantity ϕ. Indeed, let us rewrite Eq. (4) as follows

$$\widehat{A}\,\langle\phi\rangle_s = \widehat{\iint_S \phi\,\mathrm{d}s}. \tag{17}$$

Henceforth, subscript $\hat{c}, t$ is skipped for brevity. Differentiation of this equality with respect to time followed by multiplication with $1/\widehat{A}$ yields

$$\frac{\partial}{\partial t}\langle\phi\rangle_s + \langle\phi\rangle_s \frac{1}{\widehat{A}}\frac{\partial}{\partial t}\widehat{A} = \frac{1}{\widehat{A}}\widehat{\iint_S \tfrac{d^*\phi}{d^*t}\,\mathrm{d}s} + \frac{1}{\widehat{A}}\widehat{\iint_S \phi\mathcal{K}\,\mathrm{d}s} \tag{18}$$

using Eq. (15). Here, the symbol of partial derivative is used instead of d/dt in Eq. (15), because $\langle\phi\rangle_s|_{\hat{c},t}$ and $\widehat{A}|_{\hat{c},t}$ depend not only on time, but also on $\hat{c}$. Finally, using Eqs. (4) and (16), we arrive at the following general evolution equation for the bulk area-weighted surface-averaged value of the quantity ϕ:

$$\frac{\partial}{\partial t}\langle\phi\rangle_s = \left\langle \frac{d^*}{d^*t}\phi \right\rangle_s + \langle\phi\mathcal{K}\rangle_s - \langle\phi\rangle_s\langle\mathcal{K}\rangle_s. \tag{19}$$

The derived evolution Eq. (19) holds (i) for an arbitrary quantity ϕ, (ii) for any iso-surface of $c(\boldsymbol{x},t) = \hat{c}$ with $\hat{c} \in (0,1)$, and (iii) for any time instant t.

If $\phi = |\nabla c|$, Eqs. (13) and (19) read

$$\frac{\partial}{\partial t}\langle|\nabla c|\rangle_s = 2\langle|\nabla c|\mathcal{K}\rangle_s + \langle|\nabla c|\nabla\cdot(S_d\boldsymbol{n})\rangle_s - \langle|\nabla c|\nabla\cdot\boldsymbol{u}\rangle_s - \langle|\nabla c|\rangle_s\langle\mathcal{K}\rangle_s. \tag{20}$$

If $\phi = 1/|\nabla c|$, Eqs. (13) and (19) give $\frac{\partial}{\partial t}\langle 1/|\nabla c|\rangle_s = -\langle 1/|\nabla c|\nabla\cdot(S_d\boldsymbol{n})\rangle_s + \langle 1/|\nabla c|\nabla\cdot\boldsymbol{u}\rangle_s - \langle 1/|\nabla c|\rangle_s\langle\mathcal{K}\rangle_s$, which can be rewritten in another form

$$\frac{\partial}{\partial t}\ln\langle|\nabla c|\rangle_v = \langle\mathcal{K}\rangle_s + \langle\nabla\cdot(S_d\boldsymbol{n})\rangle_v - \langle\nabla\cdot\boldsymbol{u}\rangle_v = \langle\mathcal{K}\rangle_s - \langle\nabla\cdot\boldsymbol{u}^*\rangle_v, \tag{21}$$

by substituting $1/|\nabla c|$, $\nabla\cdot(S_d\boldsymbol{n})/|\nabla c|$, and $\nabla\cdot\boldsymbol{u}/|\nabla c|$ into Eq. (7).

If $\phi = \ln|\nabla c|$, Eqs. (13) and (19) read

$$\frac{\partial}{\partial t}\langle\ln|\nabla c|\rangle_s = \langle\mathcal{K}\rangle_s + \langle\nabla\cdot(S_d\boldsymbol{n})\rangle_s - \langle\nabla\cdot\boldsymbol{u}\rangle_s + \langle\ln|\nabla c|\mathcal{K}\rangle_s - \langle\ln|\nabla c|\rangle_s\langle\mathcal{K}\rangle_s. \tag{22}$$

Equations (20), (21), and (22) hold at all iso-surfaces of $c(\boldsymbol{x},t) = \hat{c} \in (0,1)$, for all time instants, and also for a general premixed flame. In Section 4.1, behavior of each term in these equations is explored by analyzing DNS data with the focus of the analysis being placed on (i) transient effects during flame development, (ii) physical mechanisms that control the transient effects, and (iii) differences between differently defined measures of the local flame thickness.

2.3. Statistically stationary relationships

By definition, when a reaction wave evolves into a statistically stationary state (denoted by t_∞ in the following), the time derivative of any statistical quantity becomes zero. Moreover, Eq. (16) shows that the fully-developed bulk conditioned stretch rate vanishes, i.e. $\langle \mathcal{K} \rangle_s |_{\hat{c},t_\infty} = 0$. Consequently, Eqs. (20), (21) and (22) at t_∞ reduces to three relations for all $\hat{c} \in (0,1)$, respectively, as

$$\begin{gathered}
2\,\langle |\nabla c| \mathcal{K} \rangle_s |_{\hat{c},t_\infty} + \langle |\nabla c| \nabla\cdot(S_d \boldsymbol{n}) \rangle_s |_{\hat{c},t_\infty} = \langle |\nabla c| \nabla\cdot\boldsymbol{u} \rangle_s |_{\hat{c},t_\infty} \\
\langle \nabla\cdot(S_d \boldsymbol{n}) \rangle_s |_{\hat{c},t_\infty} - \langle \nabla\cdot\boldsymbol{u} \rangle_s |_{\hat{c},t_\infty} = -\,\langle \ln|\nabla c| \mathcal{K} \rangle_s |_{\hat{c},t_\infty}, \\
\langle \nabla\cdot(S_d \boldsymbol{n}) \rangle_v |_{\hat{c},t_\infty} = \langle \nabla\cdot\boldsymbol{u} \rangle_v |_{\hat{c},t_\infty}. \left\langle \frac{1}{|\nabla c|} \nabla\cdot(S_d \boldsymbol{n}) \right\rangle_s |_{\hat{c},t_\infty} = 0 \ll | \left\langle \frac{1}{|\nabla c|} \mathcal{K} \right\rangle_s |_{\hat{c},t_\infty}.
\end{gathered} \tag{23}$$

3. Computational setup

In the rest of the paper, behaviour of various measures of the local flame thickness will be discussed by analyzing five representative cases selected from three different 3D DNS databases obtained from statistically 1D planar turbulent flames. The first database (a single representative highly turbulent case C) addresses the simplest relevant problem, i.e. propagation of a dynamically passive single-reaction wave in constant-density turbulent flow. As will be discussed later, these simplifications allow us to significantly extend the statistical sampling as well as to facilitate investigations on a number of issues. The second database (one moderately turbulent case F and one highly turbulent case G) was obtained in simulations of complex-chemistry methane-air flames. The third, intermediate database (one moderately turbulent case D and one highly turbulent case E) deals with singe-step chemistry, but variable-density flames. A comparison of results extracted from the three significantly different databases will offer an opportunity to explore effects of density variations and combustion chemistry on trends revealed in the simulations.

Since the first and second DNS sets were discussed in detail in Refs. [33–38] and [39, 40], respectively, and the third DNS set was performed by simplifying the chemical mechanism invoked in the second DNS set, we will restrict ourselves to a very brief summary of the simulations and refer the interested reader to the cited papers for further numerical information.

3.1. Governing equations for reacting flows at low Mach numbers

At low Mach numbers, the pressure can be decomposed into a spatially uniform thermodynamic pressure $P(t)$ and a hydrodynamic pressure $p(\boldsymbol{x}, t)$ [41]. In unconfined flows addressed in the rest of the present paper, $P(t)$ is constant. If Soret/Dufort effects and radiation heat transfer are not considered, then, a reacting flow containing N_{sp} species is governed by the following transport equations which describe, respectively, the conservation of total mass, species mass, energy, and momentum:

$$\frac{\partial \rho}{\partial t} + \boldsymbol{\nabla} \cdot (\rho \boldsymbol{u}) = 0, \tag{24}$$

$$\frac{\partial \rho Y_k}{\partial t} + \boldsymbol{\nabla} \cdot (\rho \boldsymbol{u} Y_k) = -\nabla \cdot (\rho Y_k \boldsymbol{V}_k) + \dot{\omega}_k, \quad \text{for } \ k \in [1, ..., N_{sp} - 1], \tag{25}$$

$$\rho C_p \left(\frac{\partial T}{\partial t} + \boldsymbol{u} \cdot \boldsymbol{\nabla} T \right) = E_T + \nabla \cdot (\lambda \boldsymbol{\nabla} T) - \sum_{k=1}^{N_{sp}} h_k \dot{\omega}_k, \tag{26}$$

$$\frac{\partial \rho \boldsymbol{u}}{\partial t} + \nabla \cdot (\rho \boldsymbol{u} \boldsymbol{u}) = -\nabla p + \nabla \cdot \boldsymbol{\tau} + \mathbf{f} \tag{27}$$

and the equation of state reads $P = \rho \mathcal{R} T \sum_{k=1}^{N_{sp}} Y_k / W_k$. Here, T is the temperature, $\mathcal{R}$ is the universal gas constant, λ is the molecular heat conductivity of the mixture, Y_k, W_k, and $\dot{\omega}_k$ are, respectively, mass fraction, molecular weight, and rate of production or consumption of the k-th species. The diffusion velocity is modeled using the Curtiss-Hirschfelder approximation $\boldsymbol{V}_k = -(D_k/X_k) \boldsymbol{\nabla} X_k + \sum_{m=1}^{N_{sp}} D_m (Y_m/X_m) \boldsymbol{\nabla} X_m$, where $X_k \equiv Y_k (\sum_{m=1}^{N_{sp}} W_m)/W_k$ is the mole fraction of the k-th species, D_k is its molecular diffusivity, the transport term $E_T = \rho \boldsymbol{\nabla} T \cdot \sum_{k=1}^{N_{sp}} C_{p,k} Y_k \boldsymbol{V}_k$, $C_{p,k}$ is the specific heat capacity of the k-th species under constant-pressure, $C_p = \sum_{k=1}^{N_{sp}} Y_k C_{p,k}$ is the specific heat capacity of the mixture, $h_k = h_k^{298} + \int_{298}^{T} C_{p,k} dT$ is the enthalpy of the k-th species, and h_k^{298} is its enthalpy of formation. In the momentum Eq. (27), $\mathbf{f}$ is an external forcing term, which will be described later, and the viscous stress tensor is modeled as follows $\boldsymbol{\tau} = \mu(\boldsymbol{\nabla u} + (\boldsymbol{\nabla u})^T - \frac{2}{3} \boldsymbol{I} (\nabla \cdot \boldsymbol{u}))$, where $\boldsymbol{I}$ is the identity matrix.

3.1.1. Methane-air flame

A lean (the equivalence ratio is equal to 0.6) premixed methane-air flame considered in this work burns at atmospheric pressure ($P = 1$ bar). The flame chemistry is modeled using a mechanism by Smooke and Giovangigli [42], which contains 35 reactions and $N_{sp} = 16$ species. All the mixture and species characteristics, i.e. W_k, $C_{p,k}$, C_p, D_k, λ, and ν, are evaluated using the NASA polynomials.

For a complex chemistry flame, various reaction progress variables can be defined, e.g. $c = (Y_k - Y_{k;u})/(Y_{k;b} - Y_{k;u})$ using mass fractions of different major species. Here, subscript u and b designate unburned mixture and equilibrium combustion products, respectively. In the present work, a progress variable c_p based on a product (H_2O) mass fraction, will be used. Accordingly, in Eq. (10), $\mathbb{D} = -\nabla \cdot (\rho Y_{\mathrm{H_2O}} \boldsymbol{V}_{\mathrm{H_2O}})/\rho/(Y_{\mathrm{H_2O};b} - Y_{\mathrm{H_2O};u})$ and $\mathbb{W} = \dot{\omega}_{\mathrm{H_2O}}/\rho/(Y_{\mathrm{H_2O};b} - Y_{\mathrm{H_2O};u})$.

3.1.2. Single-reaction exothermic flames

In the case of the single-step chemistry, there are two species ($N_{sp} = 2$), fuel and product, whose mass fractions are designated with Y_1 and $Y_2 = 1 - Y_1$, receptively. In this case, the thermodynamic and transport proprieties are assumed to be constant for both the fuel and product. In particular, $W_1 = W_2$ =0.029 kg/mole, $\rho D_1 = \rho D_2 = \mu/Pr/Le$, $C_{p,1} = C_{p,2} = C_p = 7R/(2W_1)$, $\mu = 1.82 \times 10^{-5}$ m^2/s, the Lewis number $Le = \lambda/(\rho C_p D_1) = 1$, and the Prandtl number $Pr = C_p\mu/(\rho\lambda) = 0.3$. The single reaction of $Y_1 \rightarrow Y_2$ is considered to be irreversible and to have Arrhenius rate $\dot{\omega}_1 = -\rho Y_1^{1.6}/\tau_R \cdot \exp\left[-Ze\Theta^2 T_u/(\Theta-1)/T\right]$ and a prescribed heat release $h_2^{298} - h_1^{298} = (\Theta-1)T_u C_p$. Here, T_u=300 K is the temperature on the fresh fuel side, $\tau_R = 5 \times 10^{-10}$ s is the reaction time scale, the density ratio $\Theta = \rho_u/\rho_b = 5.6$ (as in the lean methane-air flame), and $Ze = 9(\Theta-1)/\Theta$ is the Zeldovich number. The combustion progress variable is defined as follows $c = Y_2 = 1 - Y_1$.

3.1.3. Constant-density, single-reaction wave

When considering a dynamically passive, single-reaction wave propagating in an equidiffusive, constant-density mixture, the governing Eqs. (24), (25) and (26) are reduced to

$$\nabla\cdot\boldsymbol{u} = 0, \tag{28}$$

and

$$\frac{\partial c}{\partial t} + \mathbf{u}\cdot\nabla c = \mathcal{D}\nabla^2 c + \dot{\omega}, \tag{29}$$

where c is the reaction progress variable and the diffusivity $\mathcal{D} = const$. The reaction rate is modeled as $\dot{\omega} = (1-c)/(1+\theta)/\tau_R \cdot \exp\left[-Ze(1+\theta)^2/\theta/(1+\theta c)\right]$ where τ_R is a constant reaction time scale, $\theta = 6$ and $Ze = 6$. Note that Eq. (29) is a simplified form of Eq. (10) with $\mathbb{D} = \mathcal{D}\nabla^2 c$ and $\mathbb{W} = \dot{\omega}$. The momentum Eq. (27) reads

$$\frac{\partial \mathbf{u}}{\partial t} + (\mathbf{u}\cdot\nabla)\mathbf{u} = -\rho^{-1}\nabla p + \nu\nabla^2\mathbf{u} + \rho^{-1}\mathbf{f}_u, \tag{30}$$

where the density ρ, dynamic viscosity μ, and kinematic viscosity $\nu = \mu/\rho$ are uniform within the entire reaction wave, i.e. the reaction does not affect them. The vector-function $\mathbf{f}_u = \mathbf{f}/\rho$ is a low-wavenumber forcing function, which was used in the present simulations following Lamorgese et al. [43].

To emphasize that this constant-density reaction wave differs significantly from a flame, we will often use terms “reaction wave”, “reaction progress variable”, etc. in the rest of the paper. Nevertheless, for brevity, we will also use the term “flame” when referring to results obtained in all studied cases.

3.2. Boundary/initial conditions and turbulence forcing

All DNSs under consideration address propagation of statistically one-dimensional, planar reaction wave or premixed flames in the x-direction in a rectangular domain of dimensions $\Lambda_x \times \Lambda \times \Lambda$ represented using a uniform grid of $N_x \times N \times N$ cubic cells. The transverse boundary ($y = 0$, $y = \Lambda$, $z = 0$, or $z = \Lambda$) conditions are periodic. In the simulations of the constant-density reaction wave, an additional periodic condition

Table 1: Five representative DNS cases

Case	Reactions	ρ_b/ρ_u	$\frac{\Lambda_x}{\Lambda}$	N_x	$\frac{u_0}{S_L}$	$\frac{L_{11}}{\delta_F}$	$\frac{\delta_F}{\Delta x}$	$\frac{\eta}{\Delta x}$	Da	Ka	Re_t
C	1	1	8	2048	60	1.2	24	1.07	0.02	390	89
D	1	5.6	3	192	13	1.2	12	0.62	0.098	70	80
E	1	5.6	3	768	56	0.9	47	0.82	0.016	640	260
F	35	5.6	2	256	18	1.1	23	0.83	0.060	130	120
G	35	5.6	2	1024	210	0.5	94	0.43	0.0025	7660	660

is set at the inlet ($x = 0$) and outlet ($x = \Lambda_x$) boundaries. In other words, when a constant-density reaction wave reaches the left boundary ($x = 0$) of the computational domain, the identical reaction wave enters the domain through its right boundary ($x = \Lambda_x$). Such a method discussed in detail elsewhere [34–36] allows us to improve sampling statistics by simulating many cycles of wave propagation through the computational domain, but the method may only be used in the case of ρ =const and ν =const. Accordingly, in the simulations of flames, inlet and convective outlet boundary conditions are set at $x = 0$ and $x = \Lambda_x$, respectively. The axial-velocity averaged over the inlet boundary, i.e. $U_{In}(t) = \frac{1}{\Lambda^2}\iint_{0,0}^{\Lambda,\Lambda} u(0, y, z, t)dydz$, is adjusted during each simulation to keep the flame close to the domain center, i.e. $\frac{1}{\Lambda^2}\iiint_{0,0,0}^{\Lambda_x,\Lambda,\Lambda} c_f(x, y, z, t)dxdydz \approx \Lambda_x/2$.

In all cases, the initial ($t = 0$) turbulence fields are generated as follows. A fluctuating velocity field is first synthesized from prescribed Fourier waves [44] with an initial rms velocity u_0, an integral scale $\ell_0 = \Lambda/4$, and Reynolds number $Re_0 = u_0\ell_0\rho_u/\mu_u$. Subsequently, a non-decaying incompressible turbulent field is simulated by integrating Eqs. (28) and (30) using a forcing function $\mathbf{f}_u$. Turbulence fields characterized by the same rms velocity $u' \approx u_0$, but different longitudinal integral length scales L_{11} are generated [36] by appropriately adjusting $\mathbf{f}_u$ following Lamorgese et al. [43]. At $t > 3.5\tau_t^0$, where $\tau_t^0 = \ell_0/u'$, the generated turbulence is homogeneous (see Fig. 2 in Ref. [33]), isotropic (see Fig. 1 in Ref. [35]), and statistically stationary (see Fig. 2 in Ref. [36]), with volume-averaged values of u' or the dissipation rate of the turbulent energy being very close to u'_0 or weakly oscillating around $1.6{u'_0}^3/\ell_0$, respectively, see Fig. 1 in Ref. [34]. A ratio of L_{11}/Λ is always less than 0.20 [36]. To simulate variable-density flames, the initial turbulence field is also continuously fed into the computation domain through the inlet boundary to supply the upstream fluctuating velocity during the computations.

At $t > 0$, the flow simulation is performed solving Eqs. (28) and (30) in the case of a constant-density reaction wave. When simulating flow in flames, Eqs. (24) and (27) are solved with $\mathbf{f} = \rho\mathbf{f}_u/\rho_u$. This forcing term $\mathbf{f}$ inhibits artificial energy injection on the burned side of a flame due to a lower density of combustion products.

3.3. DNS cases

Major characteristics of the five cases analyzed in the following are summarized in Table 1, where $Da = \tau_t/\tau_F$ and $Ka = \tau_F/\tau_\eta$ are the Damköhler and Karlovitz numbers, respectively, the thickness δ_F is calculated as follows $\delta_F = \mathcal{D}/S_L$ in the constant-density case C or $\delta_F = (T_{L,b} - T_{L,u})/|\nabla T_L|_{\max}$ in the flames D-G, $\tau_F = \delta_F/S_L$ is the laminar flame time scale, $\tau_t = L_{11}/u'$ and $\tau_\eta = (\nu/\overline{\varepsilon})^{1/2}$ are integral and Kolmogorov time scales of the turbulence, respectively, the dissipation rate $\overline{\varepsilon} = 2\nu\overline{S_{ij}S_{ij}}$, the Kolmogorov length scale $\eta = (\nu^3/\overline{\varepsilon})^{1/4}$, and the turbulent Reynolds number $Re_t = u'L_{11}/\nu$ are evaluated in the constant-density turbulent flow of fresh reactants, and Δx is the grid cell size. Case C addresses a constant-density single reaction wave, cases D and E deal with single-step-chemistry premixed turbulent flames, and cases G and F are complex-chemistry cases. Flames D and E propagate into moderately intense turbulence, whereas three other cases are highly turbulent cases.

It should be noted that an "effective" Karlovitz number experienced by local heat-release zones in a premixed turbulent flame can be significantly lower than Ka evaluated in the upstream turbulent flow and reported in Table 1. This difference results from (i) dilation, (ii) an increase in the mixture viscosity due to heat release, and (iii) inhibition of the turbulence forcing term toward the burned product side. Accordingly, in spite of a very large value of $Ka = 7660$ in case G (a lower Karlovitz number $Ka' = (u'/S_L)^{3/2}(\delta_F/L_{11})^{1/2}$=4100 is reported in an earlier paper [40]), this flame is associated with transition from thin reaction zone to distributed reaction regimes of premixed turbulent combustion.

3.4. Solution methods

The governing equations are numerically integrated using an in-house DNS solver [45]. Temporal integration of the transport equations is based on a 2nd order symmetrical Strang splitting method [46], i.e. a full time step of chemistry integration is placed between two half-time-step integrations of a sum of the diffusion and convection terms. The diffusion term calculation is further split into multiple sub-steps of explicit integration starting with a Runge-Kutta scheme and followed by an Adam-Bashforth scheme. In the case of complex-chemistry flames, the thermodynamic and transport coefficients are evaluated at each full time step and are interpolated to each sub time-step for the diffusion calculations. The size of the full and sub time-steps are given by the CFL condition and the diffusive stability limit, respectively. The stiff chemistry integration is performed with a high order ODE solver [47].

A 6th order central difference scheme is used for all terms containing spatial derivatives with the exception of the convection terms in Eq. (25), (26), or (29) ,which are discretized using a 5th order WENO scheme [48] to avoid numerical overshooting. In flames, the resulted variable-coefficient Poisson equation for pressure fluctuations is solved adopting an efficient multi-grid method [49]. When exploring constant-density reaction waves, the pressure equation reduces to a fully-periodic constant-coefficient Poisson equation, which is solved using FFTW [50]. The reacting-flow solver was successfully applied to studies of complex-chemistry flames [39, 40, 51–54], single-step-chemistry flames [55], and constant-density reaction waves [33–38, 56].

3.5. Sampling statistics from the constant-density reaction wave

The simplifications of constant density offers an opportunity to sample various statistics with a high accuracy, as described below. Both fully-developed and transient reaction waves were simulated starting from the pre-computed laminar-wave profile of $c_L(\xi)$ with $dc_L/d\xi > 0$. In order to study a fully-developed turbulent reaction wave, a planar wave $c^s(x,0) = c_L(\xi)$ was initially ($t = 0$) released at $x_0 = \Lambda_x/2$ such that $\int_{-\infty}^{0} c_L(\xi)d\xi = \int_0^{\infty}[1 - c_L(\xi)]d\xi$ and $\xi = x - x_0$. Subsequently, evolution of this field $c^s(x,t)$ was simulated by solving Eq. (29). Computations of the fully-developed statistics with sampling every 100 time steps Δt were started after $t > 5\tau_t^0$ and were performed over a time interval longer than $50\tau_t^0$.

In order to study the transient phase of constant-density wave evolution, several copies of the same pre-computed laminar wave profile $c_L(\xi)$ were simultaneously embedded into the turbulent flow in $\mathcal{M}$ equidistantly separated planar zones centered around $x_m/\Lambda_x = (m - 0.5)/\mathcal{M}$, i.e., $c_m^t(x,t^*) = c_L(\xi_m)$, where coordinates $\xi_m = x - x_m$ were set using $\int_{-\infty}^{0} c_L(\xi_m)d\xi_m = \int_0^{\infty}[1 - c_L(\xi_m)]d\xi_m$ and m was an integer number ($1 \leq m \leq \mathcal{M} = 15$). Subsequently, evolutions of $\mathcal{M}$ transient fields $c_m^t(\mathbf{x},t)$ were simulated by solving $\mathcal{M}$ independent Eq. (29), with these fields affecting neither each other nor the turbulent flow in the studied case of ρ=const and ν=const. Accordingly, all $\mathcal{M}$ transient fields $c_m^t(\mathbf{x},t)$ were independent from each other and a distance between iso-surfaces of two different transient fields did not affect computed results. The transient simulations were run over $2\tau_t^0$ before being reset. Subsequently, at $t = t^* + 2j\tau_t^0$ with $1 \leq j \leq J$, the flow was again populated by $\mathcal{M}$ new profiles of $c_L(\xi_m)$ and the transient simulations were repeated. Therefore, the total duration of the simulations was $t^* + 2J\tau_t^0$.

The time-dependent statistics was restricted to a time interval of $2\tau_t^0$ and was computed by averaging the DNS data over the entire ensemble ($m = 1, ..., \mathcal{M}$) of $\mathcal{M}$ different $c_m^t(\boldsymbol{x},t)$-fields and over J time intervals of $t^* + 2(j-1)\tau_t^0 \leq t \leq t^* + 2j\tau_t^0$, where $j = 1, ...J$. Accordingly, the total number of realizations was equal to $M = \mathcal{M} \times J$. For comparison, the fully-developed statistics sampled from a single $c^s(\boldsymbol{x},t)$-field is associated with $M = 2J\tau_t^0/(100\Delta t)$ realizations. Such a method, i.e. simulations of $\mathcal{M}$ independent transient fields, significantly increased the sampling counts for calculating transient statistics and was already applied to studying self-propagation of an infinitely thin front in homogeneous isotropic turbulence [33, 34]. In supplementary material, the top image in Fig. 14 shows simultaneous snapshots of a few non-interfering c^t-waves and the c^s-wave, which evolve in the same background turbulence, see the second image in Fig. 14.

Statistics were computed on the fly while running the constant-density simulations.

3.6. Sampling statistics from exothermic flames

Unlike the constant-density reaction wave, the reactions and flow are coupled in a flame. Accordingly, a standard setup was used to obtain statistics. Each flame simulation was initialized by embedding a single pre-computed laminar flame with profiles of $Y_{k;L}(\xi)$, $\rho_L(\xi)$, and $T_L(\xi)$ into the forced turbulence field. The profiles were centered at $x_0 = \Lambda_x/2$.

Subsequently, a single realization of each flame was simulated and statistics were computed by post-processing data snapshots that were stored every $500\Delta t$. When discussing results obtained from flames D, E, and F, the term "fully-developed" will refer to statistics averaged over $t > 5\tau_t$. In cases D and E, such statistics were computed during a time interval of $40\tau_t$. In case F, the fully-developed statistics were sampled during a time interval of $15\tau_t$. Due to (i) high computational costs of the DNS of the highly turbulent complex-chemistry case G and (ii) a large ratio of t/τ_t required for that flame to become fully developed,[1] the fully-developed stage of flame development was not reached in this case. Nevertheless, due to a very high Karlovitz number and complex chemistry, case G appears to be of great interest. Accordingly, when discussing results obtained from fully-developed flames, data averaged from $12\tau_t$ to $22\tau_t$ in case G will also be reported for qualitative comparison in certain figures in Sections 4.2.2 and 4.2.3. The bottom image in Fig. 14 in supplementary material shows a snapshot of flame G.

3.7. Computation of surface-averaged qantities

Due to the lack of Dirac-delta functions, Eq. (4) provides a direct method for numerically calculating the surface-averaged values of various ϕ, including $|\nabla c|$ or $1/|\nabla c|$. In a practical CFD code, which deals with a discrete grid, the fields of $c_{(i)}(t, \boldsymbol{x})$ are often represented using an iso-surface extraction algorithm such as the marching cube method. Accordingly, the implicit surface $S_{(i)}$ of $c_{(i)}(t, \boldsymbol{x}) = \hat{c}$ can be extracted as a collection of triangulated surface elements. Subsequently, the area-weighted integration in Eq. (4) can be approximated by summing the product of each triangular area with the value of ϕ interpolated to the triangle center.

At the same time, Eqs. (5) and (6) suggest an alternative numerical approach to calculate the fine-grained area-weighted surface averages. The spatial integration ($\iiint \phi_{(i)}|\nabla c_{(i)}|\, 1_{\hat{c},\epsilon}\, \mathrm{d}\boldsymbol{x}$) in Eq. (5) can be approximated by summing the product of each grid cell volume with the value ($\phi|\nabla c|1|_{\hat{c},\epsilon}$) at the cell center. This approach is simple and is adopted in the present work for numerically extracting fine-grained area-weighted surface averages. A recent analysis [21, 22] of DNS data obtained from the reaction wave C shows that, even in such a highly turbulent case, the two aforementioned approaches yield very close values of $\langle\phi\rangle_s$ for various relevant quantities ϕ provided that ϵ in Eqs. (5) and (6) is sufficiently small, e.g. $\epsilon \le 0.02$, and the realization number is sufficiently large, e.g. $M > 100$.

Similarly, the fine-grained unweighted surface-averaged values of various ϕ are evaluated using Eqs. (5) and (6). In case C, the total number of realizations was set $M > 1000$ (or $M > 400$) when computing the fully-developed averages (or transient averages at $0 \le t \le 2\tau_t^0$, respectively). Other numerical details are discussed elsewhere [21, 22].

---

[1] Figure 3a in Ref. [12] clearly shows that an increase in Ka results in increasing time required for a complex-chemistry premixed turbulent flame to become fully developed.

4. Result and Discussion

4.1. Thinning/broadening of flames

To explore behavior of the local flame thickness, three different quantities, i.e., $1/\langle|\nabla c|\rangle_s$, $1/\langle|\nabla c|\rangle_v$ and $1/\exp(\langle\ln|\nabla c|\rangle_s)$, are considered in the present section. They are different measures of the thickness and are directly relevant to the separation distance between neighboring iso-surfaces. In the rest of this section, each of these three quantities will be called a thickness for brevity and will be normalized with the corresponding laminar value, which is the same and is equal to $1/\langle|\nabla c_L|\rangle_s$ for each of them. Accordingly, the same symbol δ_c will be used to designate any of the normalized thicknesses when discussing trends common for all of them.

Figures 1a and 1b show the temporal evolution of the normalized thicknesses conditioned to either $c(\boldsymbol{x},t) = 0.3$ associated with the mixing zone or $c(\boldsymbol{x},t) = 0.88$ associated with the reaction zone, respectively, in the constant-density case C. These data were averaged over many realizations of the studied process.

Plotted in Fig. 2 are similar results conditioned to $c(\boldsymbol{x},t) = 0.2$ and 0.8, respectively, and simulated in the variable-density cases D-G. Due to high computational costs, each of the figure panels show results obtained from a single realization.

Finally, Fig. 1c reports dependencies of the three thicknesses on $\hat{c}$ in the developing constant-density reaction wave C and Fig. 3 shows such dependencies obtained from the fully-developed flames (at t_∞) in cases C, D, E, and F. In the variable-density cases D-F, the fully-developed thicknesses were evaluated by averaging their time-dependent values at $t > 5\tau_t$. As indicated in Figs. 2a-c and 2e-g, the thicknesses do show the fully-developed behavior in these three cases at $t > 5\tau_t$. When discussing fully-developed flames, the highly turbulent case G is excluded from the consideration, because a too long time is required to reach a statistically stationary state at so high Ka, see Figs. 2d and 2h.

The following trends observed in Figs. 1-3 are worth noting. First, in line with Eq. (9), the inequalities $1/\langle|\nabla c|\rangle_s \leq 1/\exp(\langle\ln|\nabla c|\rangle_s) \leq 1/\langle|\nabla c|\rangle_v$, hold for each iso-surface $c(\boldsymbol{x},t) = \hat{c} \in (0,1)$, in each case, and at various t. Second, the major features of the transient evolutions of all thicknesses are similar in different (constant density and single-step-chemistry, variable density and single-step chemistry, variable density and complex chemistry) cases. At early instants, the thicknesses are decreased, but the trend is opposite at a later stage of the reaction-wave or flame development. In the high Ka cases C (constant density and single-step chemistry), E (variable density and single-step chemistry), and G (variable density and complex chemistry), the normalized thickness $|\nabla c_L|/\langle|\nabla c|\rangle_s$ can be as low as 0.2 in the mixing zone.

Nevertheless, third, there are minor differences between the cases. In particular, in the constant-density case C, the temporal evolutions of the thicknesses show only minor differences between the mixing and reaction zones, see Figs. 1a and 1b. Accordingly, at various instants, each normalized thickness depends weakly on $\hat{c} \in (0,1)$, see Figs. 1c and

3a. In the variable-density cases D-G, the transient behavior of the thicknesses depends on $\hat{c}$, cf. the top and bottom rows in Fig. 2. In particular, the local minima of the $\delta_c(t)$-curves are much more pronounced for the preheat zone ($\hat{c} = 0.2$) when compared to the reaction zone ($\hat{c} = 0.8$). This difference between case C and cases D-G could be attributed to reduction of the influence of turbulence on iso-scalar surfaces at larger $\hat{c}$ due to dissipation of the smallest-scale turbulent eddies, caused by combustion-induced dilatation and an increase in the local viscosity of the mixture with $\hat{c}$ [15].

Fourth, while certain influence of thermal expansion on the evolution of $\delta_c(t)$ is observed, comparison of Figs. 2a,b,e and f and Figs. 2c and g does not indicate any notable influence of combustion chemistry on the evolution of $\delta_c(t)$.

Fifth, an increase in Ka results in increasing duration of an early "thinning" stage characterized by $\delta_c(t) < 1$, cf. Figs. 2d and h with Figs. 2c and g. This effect appears to be a manifestation of an increase in the duration of flame-development stage by Ka (if the duration is measured in terms of integral time scales). It is worth remembering, however, that the integral time scale is very small at high Ka due to large values of u'.

Sixth, as far as fully-developed thicknesses $\delta_c(t_\infty)$ are concerned, the difference between $\langle|\nabla c_L|\rangle_s / \langle|\nabla c|\rangle_s$, $\langle|\nabla c_L|\rangle_s / \langle|\nabla c|\rangle_v$, and $\langle|\nabla c_L|\rangle_s / \exp(\langle \ln|\nabla c|\rangle_s)$ is significantly larger in the constant-density case C when compared to variable-density cases D-F provided that $\hat{c} > 0.5$ in cases D and E (single-step chemistry) or $0.5 < \hat{c} \leq 0.8$ in case F (complex chemistry), see Fig. 3. This effect is also associated with the aforementioned dissipation of the smallest-scale turbulent eddies within local flames.

Seventh, the difference between $\langle|\nabla c_L|\rangle_s / \langle|\nabla c|\rangle_s$, $\langle|\nabla c_L|\rangle_s / \langle|\nabla c|\rangle_v$, and $\langle|\nabla c_L|\rangle_s / \exp(\langle \ln|\nabla c|\rangle_s)$ depends weakly on $0 < \hat{c} < 1$ in the constant-density case C, see Fig. 3a. In cases D and E (variable density and single-step chemistry), the difference depends weakly on $\hat{c}$ at large $\hat{c} > 0.6$, but the difference increases with decreasing $\hat{c}$ at lower $\hat{c}$, see Figs. 3b and 3c. The latter trend is also observed in the complex-chemistry case F, see Fig. 3d, but, in this case, the difference is strongly increased at large $\hat{c}$. This effect is associated with the appearance of relatively thick recombination zones within complex-chemistry premixed flames [57]. Such thick recombination zones seem to be more prone to local broadening by small-scale turbulent eddies that are still too large to broaden the thin reaction zones.

Eighth, differently defined thicknesses can indicate opposite trends regarding thinning or broadening of the flames. For instance, Fig. 3a shows that, at various $\hat{c}$ in the fully-developed reaction wave C, $\langle|\nabla c_L|\rangle_s / \langle|\nabla c|\rangle_s |_{t_\infty}$ is less than unity implying a local thinning effect, whereas $\langle|\nabla c_L|\rangle_s / \langle|\nabla c|\rangle_v |_{t_\infty}$ is larger than unity implying a local broadening effect. The same trend is seen in the variable-density case E at $0.2 < \hat{c} < 0.6$, see Fig. 3c. It is also worth noting that, by applying other diagnostic tools to the same DNS data, it was recently demonstrated [21] that the use of $\langle 1/|\nabla c|\rangle_v$ for characterizing the local thickness of the fully-developed reaction wave C yielded even more significant local broadening, in line with Eq. (9).

Finally, while the "geometrical mean" thickness $1/\exp(\langle \ln|\nabla c|\rangle_s)|_{t_\infty}$ was rarely reported in the literature, it is closest to the laminar reference value at almost all $\hat{c}$ in all four fully-developed cases C-F.

4.2. *Evolution equations for thinning/broadening of reaction wave*

In this section, the behavior of various terms in Eqs. (20), (21), and (22), which describe the evolution of $\Psi = \langle|\nabla c|\rangle_s|_{\hat{c},t}$, $\Psi = \ln\langle|\nabla c|\rangle_v|_{\hat{c},t}$, and $\Psi = \langle\ln|\nabla c|\rangle_s|_{\hat{c},t}$, respectively, will be discussed by analyzing the DNS data. More specifically, the transient behavior of the terms will be addressed in Sect. 4.2.1. Then, dependencies of various terms on $\hat{c}$ in the fully-developed wave C, fully-developed flames D-F, and moderately developed flame G will be considered in Sect. 4.2.2. Finally, terms that contain the displacement speed S_d will be decomposed into three subterms, which describe the contributions due to curvature, normal diffusion, and reaction [58, 59], and each sub-term will be considered in Sect. 4.2.3.

Before presenting these results, it is worth stressing that, for all three evolution equations, the residual magnitudes are much less than the magnitudes of the lhs term or the sum of the rhs terms for almost all iso-surfaces of $\hat{c} \in (0,1)$ and at almost all studied instants, as discussed in detail in a recent paper [22], where the DNS data obtained in case C are analyzed.

4.2.1. *Evolution of various terms in constant-density single-reaction wave*

Since (i) the $\delta_c(t)$-curves obtained from the constant-density reaction wave C and flames D-G look qualitatively similar, cf. Figs. 1a and 1b with Fig. 2, and (ii) computing statistically solid values of the discussed terms is highly expensive when simulating developing flames, the contents of this subsection will mainly be restricted to case C. In this case, reliable statistics were obtained by averaging numerical data over many realizations ($M > 400$).

Shown in the left and middle panels in Figs. 4, 5, and 6 are the transient behaviors of various terms in Eqs. (20), (21), and (22), respectively, which describe the evolution of $\Psi = \langle|\nabla c|\rangle_s|_{\hat{c},t}$, $\Psi = \ln\langle|\nabla c|\rangle_v|_{\hat{c},t}$, and $\Psi = \langle\ln|\nabla c|\rangle_s|_{\hat{c},t}$, respectively. Results conditioned to $\hat{c} = 0.3$ and $\hat{c} = 0.88$ associated with the mixing and reaction zones, respectively, are plotted in the left and middle panels, respectively. For any Ψ, the time derivative $\frac{\partial}{\partial t}\Psi$ (red dots in the aforementioned figures) was evaluated by (i) taking a sequence of transient Ψ calculated at 20 sampling instants, i.e. $t_i = (i^2/200)\tau_t^0$ with $i = (1,..,20)$, and (ii) applying a discrete approximation of time derivative to this sequence. Moreover, dependencies of the terms on $\hat{c}$, extracted at a single representative instant $t = 0.74\tau_t$, are reported in the right panels. Furthermore, the transient behaviors of various terms in Eq. (20) obtained from flames F and G are shown in Fig. 15 of supplemental material for qualitative comparison. Since these results are limited to a single realization, they should be interpreted with care.

Red points in the left and middle panels in Figs. 4, 5, and 6 show that the evolutions of the time derivatives $\frac{\partial}{\partial t}\Psi$ is consistent with the evolutions of $\Psi = \langle|\nabla c|\rangle_s|_{\hat{c},t}$, $\Psi = \ln\langle|\nabla c|\rangle_v|_{\hat{c},t}$, and $\Psi = \langle\ln|\nabla c|\rangle_s|_{\hat{c},t}$, respectively, reported in Figs. 1a and 1b. All three time derivatives start at zero at $t = 0$ and rise rapidly to a peak value of the positive magnitude, thus, indicating the local thinning of the reaction wave (its local thickness is inversely proportional to $|\nabla c|$).

Subsequently, the time derivatives decrease, change their sign, reach a local minimum, and, finally, relax back to zero in the fully-developed wave.

To explain such a behavior of $\frac{\partial}{\partial t}\Psi$, let us begin with exploring the evolutions of various terms on the rhs of Eq. (21), because, in the considered constant-density case C, there are only two terms on the rhs. Figures 5a and 5b show that, at the early stage, i.e. $t/\tau_t < 0.2$ if $\hat{c} = 0.88$ or $t/\tau_t < 1.0$ if $\hat{c} = 0.30$, term $\langle \nabla \cdot (S_d \boldsymbol{n}) \rangle_v$ (squares) is close to zero, because the surface is weakly wrinkled. On the contrary, the stretch-rate term $\langle \mathcal{K} \rangle_s$ (pentagrams) rapidly grows and results in increasing $\Psi = \ln \langle |\nabla c| \rangle_v |_{\hat{c},t}$. Accordingly, $\frac{\partial}{\partial t} \ln \langle |\nabla c| \rangle_v \approx \langle \mathcal{K} \rangle_s$ during this stage and the observed thinning of the wave is consistent with Batchelor's classical theory of turbulent stretching of material lines [60].

At larger t/τ_t, the stretch-rate term $\langle \mathcal{K} \rangle_s$ decreases from its peak value to zero, whereas term $\langle \nabla \cdot (S_d \boldsymbol{n}) \rangle_v$ begins to play an important role when the surface is sufficiently perturbed by turbulent eddies. The latter term decreases from zero at a low t/τ_t to a minimum value and, then, relaxes back to zero. Thus, each of the two terms reaches a single extreme value (maximum for $\langle \mathcal{K} \rangle_s$ and minimum for $\langle \nabla \cdot (S_d \boldsymbol{n}) \rangle_v$) during its evolution. Accordingly, at a sufficiently large t/τ_t, the derivative $\frac{\partial}{\partial t} \ln \langle |\nabla c| \rangle_v |_{\hat{c},t}$ begins to decrease with time and becomes negative at a larger t/τ_t, thus, indicating the local reaction-wave broadening. An instant associated with the change in sign of the derivative from plus to minus depends on $\hat{c}$, because term $\langle \nabla \cdot (S_d \boldsymbol{n}) \rangle_v$ depends on $\hat{c}$, see squares in Fig. 5c.

Let us consider the behaviors of various terms on the rhs of Eq. (20), which describes the evolution of $\Psi = \langle |\nabla c| \rangle_s |_{\hat{c},t}$. Figure 4a and 4b show that, at $0 < t/\tau_t < 0.2$, term $\langle |\nabla c| \nabla \cdot (S_d \boldsymbol{n}) \rangle_s \approx 0$ (squares), and the early thinning of the reaction wave is controlled by the difference between a larger positive term $2 \langle |\nabla c| \mathcal{K} \rangle_s$ (pentagrams) and a smaller negative term $- \langle |\nabla c| \rangle_s \langle \mathcal{K} \rangle_s$ (triangles). During this stage, the lhs term $\frac{\partial}{\partial t} \langle |\nabla c| \rangle_s$ looks like a mirror of the small negative term $- \langle |\nabla c| \rangle_s \langle \mathcal{K} \rangle_s$ in Figs. 4a and 4b. This observation implies that $\frac{\partial}{\partial t} \ln \langle |\nabla c| \rangle_s \approx \langle \mathcal{K} \rangle_s$ during the discussed early stage.

At larger t/τ_t, the negative term $- \langle |\nabla c| \rangle_s \langle \mathcal{K} \rangle_s$ has a low magnitude, but term $\langle |\nabla c| \nabla \cdot (S_d \boldsymbol{n}) \rangle_s$ begins to play an important role by reducing $\frac{\partial}{\partial t} \langle |\nabla c| \rangle_s$. For the corresponding wave thickness, the fully-developed data plotted in red circles in Fig. 3a indicate the local broadening of the wave, thus, implying that term $\langle |\nabla c| \nabla \cdot (S_d \boldsymbol{n}) \rangle_s$ makes the derivative $\frac{\partial}{\partial t} \langle |\nabla c| \rangle_s$ negative at sufficiently large t/τ_t, but this effect is not observed in Figs. 4a and 4b, probably, because such an evolution stage was not reached in the present transient simulations. It is also worth noting that, contrary to Eq. (21), all terms on the rhs of Eq. (20) depend on $\hat{c}$, see Fig. 4c.

Figures 6a and 6b show that, at $0 < t/\tau_t < 0.2$, the time derivative $\frac{\partial}{\partial t} \langle \ln |\nabla c| \rangle_s$ (dots) is also close to the surface-averaged stretch rate $\langle \mathcal{K} \rangle_s$ (pentagrams), but, due to a small positive difference $\langle \ln |\nabla c| \mathcal{K} \rangle_s - \langle \ln |\nabla c| \rangle_s \langle \mathcal{K} \rangle_s$ (triangles) on the rhs of Eq. (22), the difference between $\frac{\partial}{\partial t} \langle \ln |\nabla c| \rangle_s$ and $\langle \mathcal{K} \rangle_s$ is larger than the difference between $\frac{\partial}{\partial t} \ln \langle |\nabla c| \rangle_v$ and $\langle \mathcal{K} \rangle_s$ in Fig. 5. At larger t/τ_t, the positive difference $\langle \ln |\nabla c| \mathcal{K} \rangle_s - \langle \ln |\nabla c| \rangle_s \langle \mathcal{K} \rangle_s$ is much larger than the stretch rate $\langle \mathcal{K} \rangle_s$. All terms on the rhs of Eq. (22) depend weakly on $\hat{c}$ during the wave development, see Fig. 6c.

The major trend observed in Figs. 15a and c in supplemental material, where results obtained from flames F and G are reported, are consistent with the already discussed behaviors of terms $-\langle|\nabla c|\rangle_s \langle\mathcal{K}\rangle_s$, $\langle|\nabla c|\nabla\cdot(S_d\boldsymbol{n})\rangle_s$, and $2\langle|\nabla c|\mathcal{K}\rangle_s$ in the constant-density wave C. The initial thinning of the flames is controlled by the positive stretch-rate term $2\langle|\nabla c|\mathcal{K}\rangle_s$ (pentagrams). Subsequently, the negative term $\langle|\nabla c|\nabla\cdot(S_d\boldsymbol{n})\rangle_s$ (squares) in the highly turbulent case G and also the negative term $-\langle|\nabla c|\rangle_s \langle\mathcal{K}\rangle_s$ (triangles) in moderately turbulent case F overwhelm the stretch-rate term and result in decreasing the time derivative $\frac{\partial}{\partial t}\langle|\nabla c|\rangle_s$, i.e. the local flame broadening. The dilatation term $-\langle|\nabla c|\nabla\cdot\boldsymbol{u}\rangle_s$ (circles) is negative during the flame development and works to locally broaden the flame. However, this term, as well as term $-\langle|\nabla c|\rangle_s \langle\mathcal{K}\rangle_s$, plays a minor role in the highly turbulent case G. Thus, in both highly turbulent constant-density reaction wave C and highly turbulent complex-chemistry flame G, the evolution of $\langle|\nabla c|\rangle_s$ is mainly controlled by the two terms; $2\langle|\nabla c|\mathcal{K}\rangle_s$ and $\langle|\nabla c|\nabla\cdot(S_d\boldsymbol{n})\rangle_s$. In both cases, these two dominating terms depend on $\hat{c}$, see Figs. 4c and 15f in supplemental material.

All in all, the discussed results show that the local thicknesses of the reaction wave and flames are decreased due turbulent stretching during an earlier development stage, but effects caused by the wave or flame propagation, i.e. terms $\langle|\nabla c|\nabla\cdot(S_d\boldsymbol{n})\rangle_s$, $\langle\nabla\cdot(S_d\boldsymbol{n})\rangle_v$, and $\langle\nabla\cdot(S_d\boldsymbol{n})\rangle_s$ in Eqs. (20), (21) and (22), respectively, begin to play a more important role when the local wave or flame surface is sufficiently complicated at a later stage. Accordingly, the latter effects result in increasing the local thicknesses.

4.2.2. Fully-developed relations

The $\hat{c}$-dependencies of all fully-developed (t_∞) terms in Eqs. (20), (21), and (22) are reported in Fig. 7 for $\Psi = \langle|\nabla c|\rangle_s$, Fig. 8 for $\Psi = \ln\langle|\nabla c|\rangle_v$, and Fig. 9 for $\Psi = \langle\ln|\nabla c|\rangle_s$, respectively. In addition to data obtained in cases C-F, results computed by simulating the 1D reference laminar CH_4-air flame L (associated with case F and G) are also presented in these figures. As fas as the high-Ka flame G is concerned, results discussed in the following were averaged from $12\tau_t$ to $22\tau_t$, whereas the fully-developed stage of the flame development was not reached in case G in the present DNS study.

As discussed in Sect. 2.3, for a fully-developed wave at t_∞, the surface-averaged Eqs. (20), (21), and (22) reduce to three relations in Eq. (23). Accordingly, for each equation, the sum of the rhs terms vanishes, see solid lines with pluses. Moreover, in line with the contents of Sect. 2.3, terms $\langle|\nabla c|\rangle_s \langle\mathcal{K}\rangle_s$ (triangles in Fig. 7), $\langle\mathcal{K}\rangle_s$ (pentagrams in Figs. 8 and 9), and $\langle\ln|\nabla c|\rangle_s \langle\mathcal{K}\rangle_s$ (left-pointing triangles in Fig. 9) also vanish. Furthermore, in line with second relation in Eq. (23), terms $\langle\nabla\cdot(S_d\boldsymbol{n})\rangle_v|_{t_\infty,\hat{c}}$ and $\langle\nabla\cdot\boldsymbol{u}\rangle_v|_{t_\infty,\hat{c}}$ on the rhs of Eq. (21) counterbalance one another almost completely, see the squares and circles in Fig. 8.

It is of interest to note that differences between the $\hat{c}$-dependencies of various fully-developed terms, obtained in different cases (constant-density single-reaction wave C, single-step-chemistry flames D and E, laminar complex-chemistry flame L, and turbulent complex-chemistry flames F and G), manifest themselves differently for different equations. In particular, first, the fully-developed terms on the rhs of Eq. (21) show a similar behavior in laminar and turbulent or in single-step and complex chemistry flames. In all these cases, there are two dominating terms $\langle \nabla\boldsymbol{\cdot}(S_d\boldsymbol{n})\rangle_v|_{t_\infty,\hat{c}}$ and $\langle \nabla\boldsymbol{\cdot}\boldsymbol{u}\rangle_v|_{t_\infty,\hat{c}}$, which counterbalance one another, as already noted above. On the contrary, in the fully-developed constant-density single-reaction wave C, these terms vanish, as well as other terms on the rhs of Eq. (21).

Second, various terms on the rhs of Eq. (20) show similar behavior in the three very different highly-turbulent cases C (constant-density single-reaction wave), E (single-step-chemistry flame), and G (complex-chemistry flame), see Fig. 7. In each of these three cases, there are two dominating terms, $2\,\langle|\nabla c|\mathcal{K}\rangle_s$ (pentagrams) and $\langle|\nabla c|\nabla\boldsymbol{\cdot}(S_d\boldsymbol{n})\rangle_s$ (squares), which counterbalance one another. In two other turbulent cases D and F characterized by significantly lower Ka, these two terms are of significant importance, but the dilatation term $\langle|\nabla c|\nabla\boldsymbol{\cdot}\boldsymbol{u}\rangle_s$ plays a substantial role also. In the laminar case L, the stretch term $2\,\langle|\nabla c|\mathcal{K}\rangle_s$ vanishes and term $\langle|\nabla c|\nabla\boldsymbol{\cdot}(S_d\boldsymbol{n})\rangle_s$ is counterbalanced by the dilatation term. Thus, as far as the fully-developed terms on the rhs of Eq. (20) are concerned, (i) thermal expansion effects manifest themselves in appearance of the negative dilatation term $\langle|\nabla c|\nabla\boldsymbol{\cdot}\boldsymbol{u}\rangle_s$, which (ii) plays the dominating role in the laminar flame, but (iii) is of minor importance at high Ka. Figure 7 does not indicate a significant effect associated with complex chemistry.

Third, various fully-developed terms on the rhs of Eq. (22) show similar behavior in turbulent single-step (D and E) and complex-chemistry (F and G) flames, cf. Figs. 9b and 9c with Figs. 9e and 9f, respectively, but the behavior of these terms in constant-density single-reaction wave C or the complex-chemistry laminar flame L are very different. Again, (i) role played by the dilatation is reduced with increasing Ka, cf. Figs. 9b and 9c or Figs. 9d, 9e, and 9f, and (ii) no significant effect associated with complex chemistry is observed, cf. Figs. 9b and 9e or Figs. 9c and 9f.

4.2.3. Decomposition of the displacement speed

In the combustion literature, DNS data are often analyzed by decomposing the displacement speed S_d into three contributions due to curvature S_d^c, normal diffusion S_d^n, and reaction S_d^W [58, 59], i.e. $S_d = S_d^c + S_d^n + S_d^W$, where $S_d^W \equiv \mathbb{W}/|\nabla c|$, $S_d^c \equiv \mathcal{D}\nabla\boldsymbol{\cdot}\boldsymbol{n}$ and $S_d^n = \mathcal{D}\boldsymbol{n}\cdot\nabla(\boldsymbol{n}\cdot\nabla c)/|\nabla c|$ in cases C-E or $S_d^n \equiv S_d - S_d^W - S_d^c$ in complex-chemistry flames F and G. Accordingly, the stretch rate term $\langle\mathcal{K}\rangle_s$ on the rhs of Eq. (21) can be presented as a sum of the four terms $\langle\mathcal{K}_t\rangle_s$, $\langle S_d^c\nabla\boldsymbol{\cdot}\boldsymbol{n}\rangle_s$, $\langle S_d^n\nabla\boldsymbol{\cdot}\boldsymbol{n}\rangle_s$, and $\left\langle S_d^W\nabla\boldsymbol{\cdot}\boldsymbol{n}\right\rangle_s$

Shown in Fig. 10 are evolutions of the bulk surface-averaged stretch rate $\langle\mathcal{K}\rangle_s$ and various contributions to it in the constant-density single-reaction wave C. At an early stage of the wave development, the evolution of $\langle\mathcal{K}\rangle_s$ (pentagrams) is controlled by the tangential strain rate $\langle\mathcal{K}_t\rangle_s$ (right-pointing triangles), in line with Batchelor's classical theory [60]. At low t/τ_t, term $\langle\mathcal{K}_t\rangle_s$ rapidly grows with time, reaches a peak value at $t/\tau_t \approx 0.4$ and, then, decreases. The curvature term $\langle S_d^c\nabla\boldsymbol{\cdot}\boldsymbol{n}\rangle_s$ (circles), which is small at low t/τ_t, monotonously grows with time, and counterbalance the strain term $\langle\mathcal{K}_t\rangle_s$ in the fully-developed wave, all other terms are negligible at various t/τ_t. Thus, the evolution of the surface-averaged stretch rate $\langle\mathcal{K}\rangle_s$ is controlled by the surface-averaged tangential strain rate $\langle\mathcal{K}_t\rangle_s$ and the surface-averaged curvature term $\langle S_d^c\nabla\boldsymbol{\cdot}\boldsymbol{n}\rangle_s$. Note that the latter term is never negative, because

$\langle S_d^c \nabla\cdot \boldsymbol{n}\rangle_s = \mathcal{D}\,\langle(\nabla\cdot\boldsymbol{n})^2\rangle_s \geq 0$. Therefore, the curvature contribution $-\langle S_d^c \nabla\cdot \boldsymbol{n}\rangle_s$ to the stretch rate $\langle\mathcal{K}\rangle_s$ works to reduce the rate.

Similarly, the term $\langle\nabla\cdot(S_d\boldsymbol{n})\rangle_v$, which counteracts the stretch-rate term $\langle\mathcal{K}\rangle_s$ on the rhs of Eq. (21), can be decomposed as $\langle\nabla\cdot(S_d\boldsymbol{n})\rangle_v = \left\langle\nabla\cdot(S_d^W\boldsymbol{n})\right\rangle_v + \langle\nabla\cdot(S_d^n\boldsymbol{n})\rangle_v + \langle\nabla\cdot(S_d^c\boldsymbol{n})\rangle_v$. The evolution of this term and the three contributions to it are shown in Figs. 11a and 11b in case C. As expected, $\langle\nabla\cdot(S_d\boldsymbol{n})\rangle_v$ is controlled by the normal-diffusion term $\langle\nabla\cdot(S_d^n\boldsymbol{n})\rangle_v$ in the mixing zone ($\hat{c} = 0.30$, squares and triangles in Fig. 11a), because the reaction rate vanishes there, see pluses in Fig. 11c. Even in the reaction zone ($\hat{c} = 0.88$, Fig. 11b), the magnitude of the normal-diffusion contribution $\langle\nabla\cdot(S_d^n\boldsymbol{n})\rangle_v$ is significantly larger than the magnitude of the reaction contribution $\left\langle\nabla\cdot(S_d^W\boldsymbol{n})\right\rangle_v$ during the wave development, but the two contributions counterbalance one another in the fully-developed wave.

Indeed, since $\langle\nabla\cdot(S_d\boldsymbol{n})\rangle_v|_{t_\infty,\hat{c}} = \langle\nabla\cdot\boldsymbol{u}\rangle_v|_{t_\infty,\hat{c}}$ in the fully-developed reaction wave, see Eq. (21) and the second term vanishes if the density is constant, the normal-diffusion and reaction contributions fully counterbalance one another in the fully-developed wave C, see triangles and pluses in Fig. 12a. Even in variable-density cases D-G and L, the two fully-developed terms counterbalance one another almost completely, while small differences due to dilatation are observed in Figs. 12b-12h.

While Figs. 10-12 indicate that the curvature term $\langle\nabla\cdot(S_d^c\boldsymbol{n})\rangle_v$ (circles) has a negligible magnitude, this result does not mean that the curvature term plays a minor role in flame-turbulence interaction. Indeed, while the local flame curvature averaged over the entire flame brush is well known to be close to zero (and this is the cause of a low magnitude of $\langle\nabla\cdot(S_d^c\boldsymbol{n})\rangle_v$), the local flame curvature evaluated at the leading (trailing) edge of the flame brush is positive (negative) for simple topological reasons and such highly curved reaction zones can play an important role in the flame propagation. This issue is beyond the scope of the present paper and is discussed in detail elsewhere [30, 61].

Finally, as far as the curvature contribution $\langle S_d^c\nabla\cdot\boldsymbol{n}\rangle_s$ to the fully-developed surface-averaged stretch rate $\langle\mathcal{K}\rangle_s$ is concerned, Fig. 13 indicates that it is of substantial importance at various $\hat{c}$. As expected, $\langle\mathcal{K}_t\rangle_s$ (right-pointing triangles) and $\langle S_d\nabla\cdot\boldsymbol{n}\rangle_s$ (squares) counterbalance one another in order for $\langle\mathcal{K}\rangle_s$ (pentagrams) to vanish in the fully-developed flames. Note that a comparison of Figs. 13b and 13c with Figs. 13d and 13e, respectively, does not indicate a notable effect of complex chemistry on the behavior of the considered surface-averaged terms.

4.3. Discussion

The reported numerical results appear to shed a light on the inconsistencies between published experimental and DNS data on the local flame thicknesses δ_c in turbulent flows. As already noted in Sect. 1, on the one hand, certain experimental data and simulations of strained complex-chemistry laminar premixed flames imply that the influence of turbulence on δ_c is controlled by turbulent strain rates, with positive strain rates reducing (increasing) the thickness of a lean methane-air (propane-air, respectively) flame [13, 15, 16]. On the other hand, recent DNS data showed local broadening of lean methane-air flames [11, 12].

The present results offer the following explanation of this apparent inconsistency. On the one hand, premixed turbulent flames investigated in the vast majority of laboratory experiments are developing flames, as discussed in detail elsewhere [29, 30]. Accordingly, results plotted in Figs. 1 and 2 do show that the normalized $\delta_c(t)$ is less than unity during an earlier stage of flame development in all studied cases, including complex-chemistry lean methane-air flames. Moreover, Figs. 4-6 indicate that this local flame thinning is controlled by turbulent stretch rates. Furthermore, Fig. 10 shows that the surface-averaged stretch rate is mainly controlled by turbulent strain rates during the discussed stage of flame development.

Thus, all these figures considered together imply that, during an earlier stage of premixed turbulent flame development, local flame thickness is mainly controlled by turbulent strain rates. For single-step-chemistry flames and lean methane-air flames F and G studied in the present work, the thickness is statistically reduced under the influence of the strain rates, but results from simulations of lean propane-air strained laminar flames [13] imply that the local thickness of lean propane-air flames is statistically increased under the influence of turbulent strain rates during an early stage of the flame development. Therefore, the present DNS study supports (does not contradict to) the aforementioned explanation [13, 15, 16] of the experimental data on the local thinning (broadening, respectively) of lean methane-air (propane-air, respectively) premixed turbulent flames.

We may also note that DNS data obtained by Thevenin [3] from three premixed methane-air turbulent flames and reported at $t/\tau_t^0 = 1.66$ for one flame and at $t/\tau_t^0 = 1.0$ for two other flames indicate thinning of local preheat zones, with the effect being more pronounced at smaller t/τ_t^0, see Fig. 5 in the cited paper. These trends are also consistent with the present results and the above interpretation of them.

On the other hand, in the DNS studies [11, 12], long flame evolution time was allowed and the fully-developed state (which was likely to depend on the width of the computational domain) was obtained. In line with those DNSs, Figs. 2 and 3 of the present work indicate local flame broadening during a late stage of development of lean methane-air flames. Figures 4-6 imply that such a local flame broadening is controlled by self-propagation of wrinkled iso-scalar surfaces and also by dilatation (if turbulence is insufficiently strong to overwhelm the dilatation, cf. the top and bottom panels in Fig. 15 in supplemental materials), whereas the surface-averaged stretch rate plays a minor role during the late stage of flame development, e.g., because strain-rate and curvature contributions to $\langle\mathcal{K}\rangle_s$ counterbalance one another almost completely in the constant-density reaction wave C, see Fig. 10. In the fully-developed flames, terms that involve $\nabla\cdot(S_d\boldsymbol{n})$ can work in opposite directions depending on the chosen measure of the local flame thickness. In particular, squares in Fig. 7 show that such terms work to reduce $\langle|\nabla c|\rangle_s$ in turbulent flows (the effect is opposite in the laminar flame L), whereas squares in Fig. 8 indicate the opposite trend for $\langle|\nabla c|\rangle_v$. In the latter case, the local flame broadening is controlled by dilataion, see circles, which significantly affects $1/\langle|\nabla c|\rangle_v = \langle 1/|\nabla c|\rangle_s$ even in highly turbulent flames.

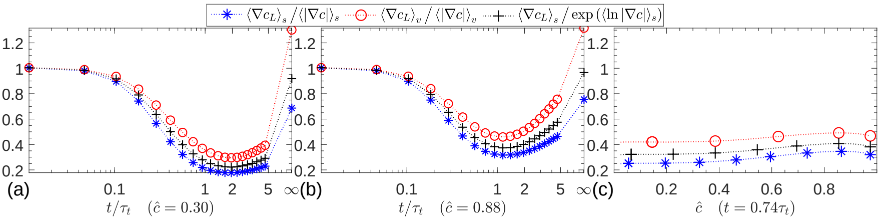

Figure 1: Evolutions of three normalized local thicknesses $\delta_c(t)$ specified in legends conditioned to the mixing zone (a, $\hat{c} = 0.3$) and the reaction zone (b, $\hat{c} = 0.88$), as well as dependencies of the three thicknesses on $\hat{c}$ at $t = 0.32\tau_t^0 = 0.74\tau_t$ (c). Case C.

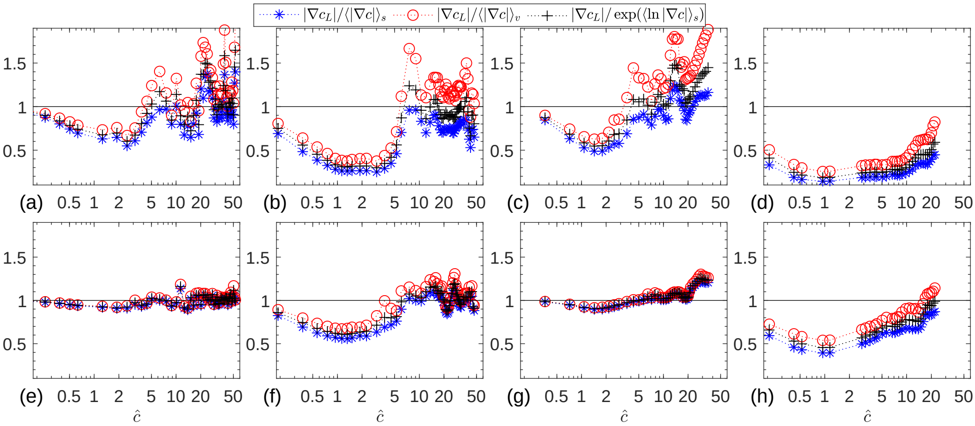

Figure 2: Evolutions of three normalized local thicknesses $\delta_c(t)$ specified in legends conditioned to the preheat zone ($\hat{c} = 0.2$, top row) and the reaction zone ($\hat{c} = 0.8$, bottom row), computed in cases D (a and e), E (b and f), F (c and g), and G (d and h). In cases F and G, the combustion progress variable characterize the normalized mass fraction of H_2O.

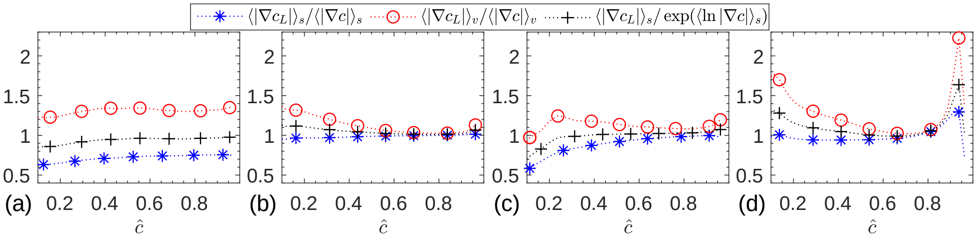

Figure 3: Dependencies of three normalized, fully-developed local thicknesses $\delta_c(t_\infty)$ specified in legends on $\hat{c}$ in cases C (a), D (b), E (c), and F (d).

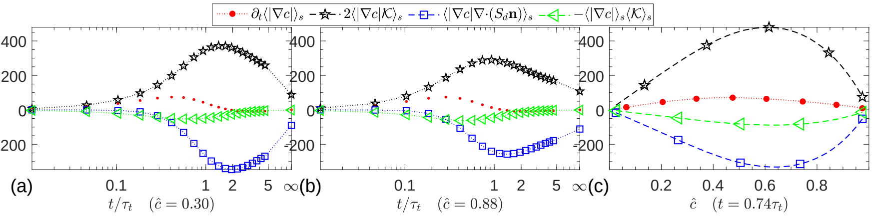

Figure 4: Evolutions of all terms in Eq. (20), specified in legends and conditioned to the mixing zone (a, $\hat{c}=0.3$) and the reaction zone (b, $\hat{c}=0.88$), as well as dependencies of these terms on $\hat{c}$ at $t=0.74\tau_t$ (c). Case C. All terms are normalized by S_L/δ_F.

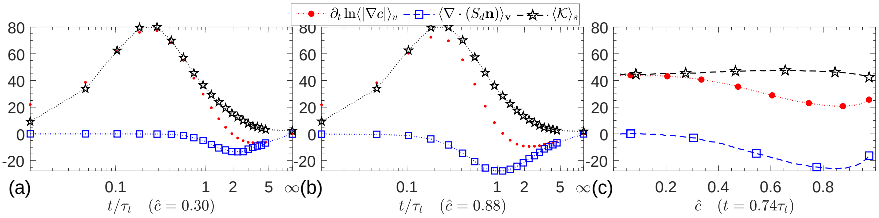

Figure 5: Evolutions of all terms in Eq. (21), specified in legends and conditioned to the mixing zone (a, $\hat{c}=0.3$) and the reaction zone (b, $\hat{c}=0.88$), as well as dependencies of these terms on $\hat{c}$ at $t=0.74\tau_t$ (c). Case C. All terms are normalized by S_L/δ_F.

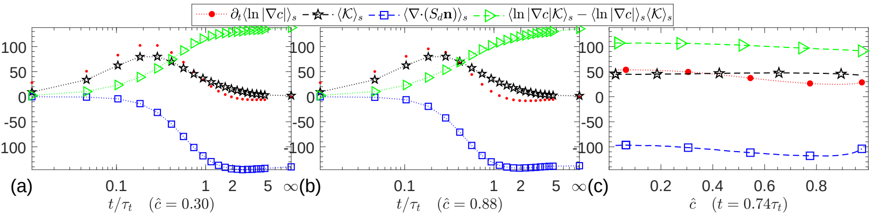

Figure 6: Evolutions of all terms in Eq. (22), specified in legends and conditioned to the mixing zone (a, $\hat{c}=0.3$) and the reaction zone (b, $\hat{c}=0.88$), as well as dependencies of these terms on $\hat{c}$ at $t=0.74\tau_t$ (c). Case C. All terms are normalized by S_L/δ_F.

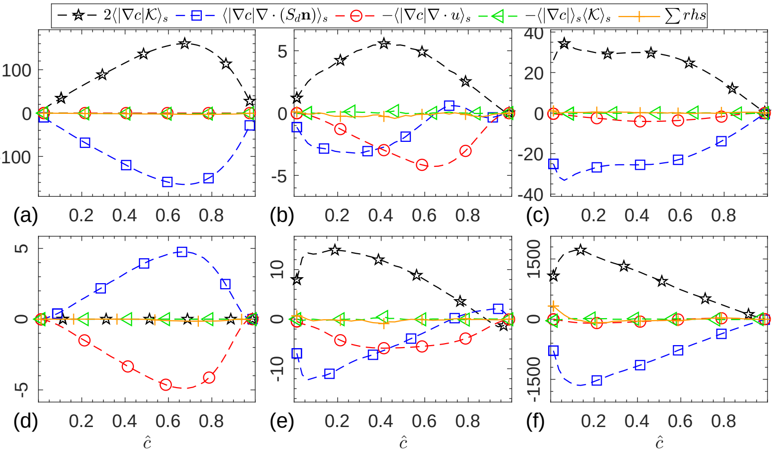

Figure 7: Fully-developed dependencies of all four terms on the rhs of Eq. (20), specified in legends, and the sum of them on $\hat{c}$, obtained in cases C (a), D (b), E (c), L(d), F(e), and G (f). All terms are normalized by S_L/δ_F. Results obtained in single-step and complex-chemistry cases are reported in the first and second row, respectively.

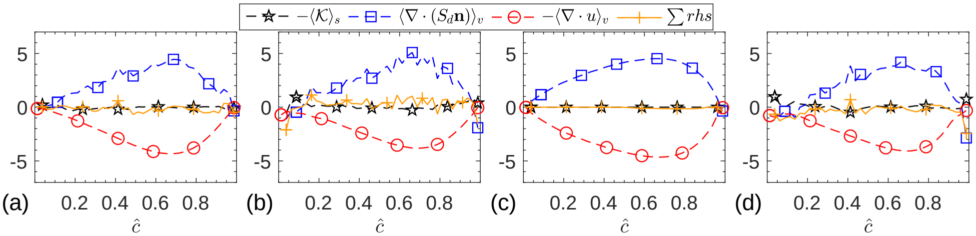

Figure 8: Fully-developed dependencies of all three normalized terms on the rhs of Eq. (21), specified in legends, and the sum of them on $\hat{c}$, obtained in cases D (a), E (b), L(c), and F(d).

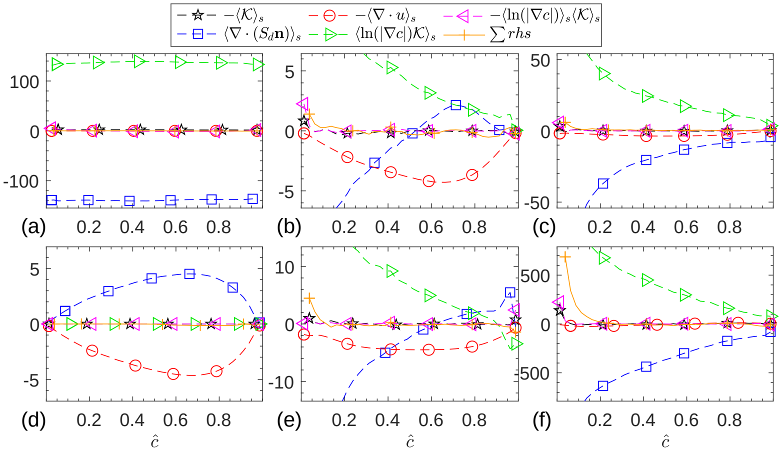

Figure 9: Fully-developed dependencies of all five normalized terms on the rhs of Eq. (22), specified in legends, and the sum of them on $\hat{c}$, obtained in cases C (a), D (b), E (c), L(d), F(e), and G (d).

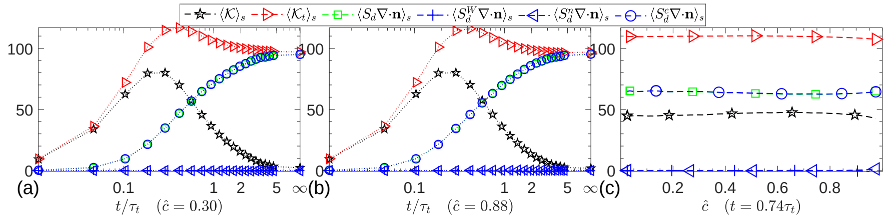

Figure 10: Evolutions of $\langle\mathcal{K}\rangle_s$ and various contributions to it, specified in legends and conditioned to the mixing zone (a, $\hat{c}=0.3$) and the reaction zone (b, $\hat{c}=0.88$), as well as dependencies of these terms on $\hat{c}$ at $t=0.74\tau_t$ (c). Case C. All terms are normalized by S_L/δ_F.

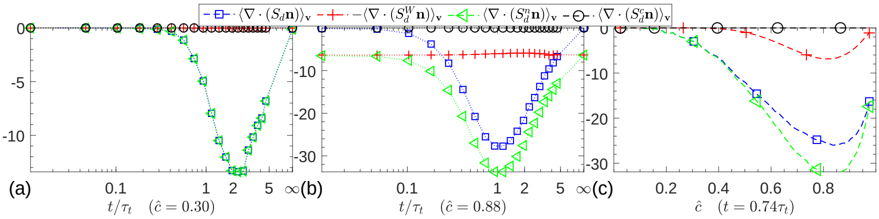

Figure 11: Evolutions of $\langle\nabla\cdot(S_d\boldsymbol{n})\rangle_v$ and various contributions to it, specified in legends and conditioned to the mixing zone (a, $\hat{c}=0.3$) and the reaction zone (b, $\hat{c}=0.88$), as well as dependencies of these terms on $\hat{c}$ at $t=0.74\tau_t$ (c). Case C. All terms are normalized by S_L/δ_F.

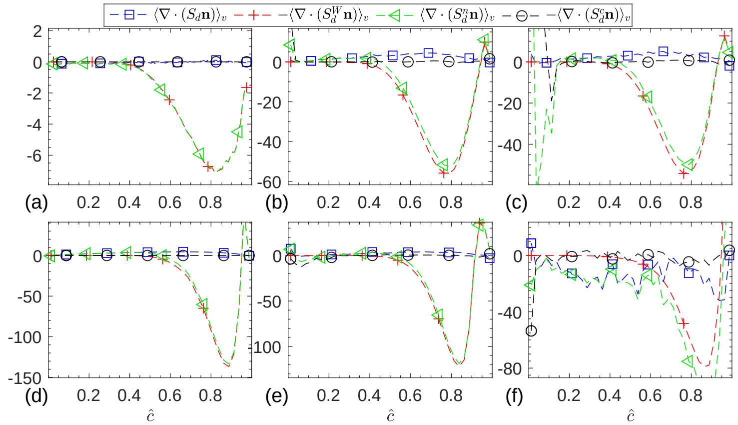

Figure 12: Fully-developed dependencies of $\nabla\cdot(S_d\boldsymbol{n})$ and various contributions to it, specified in legends, on $\hat{c}$, obtained in cases C (a), D (b), E (c), L(d), F(e), and G (f). All terms are normalized by S_L/δ_F.

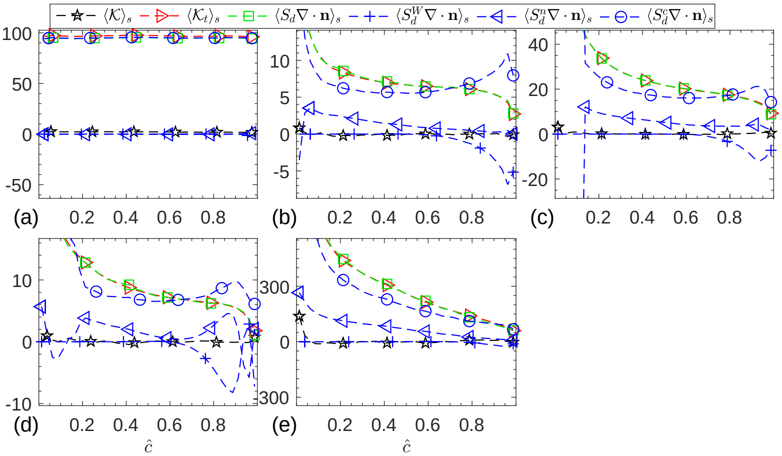

Figure 13: Fully-developed dependencies of $\langle\mathcal{K}\rangle_s$ and various contributions to it, specified in legends, on $\hat{c}$, obtained in cases C(a), D (b), E (c), F (d), and G (e). All terms are normalized by S_L/δ_F.

5. Conclusions

Different measures of local flame thickness in a turbulent flow, e.g. area-weighted and unweighted bulk surface-averaged values of $|\nabla c|$ or $1/|\nabla c|$, were studied and analytical relationship between them, given by Eq. (9), was obtained. Behaviour of different thicknesses and different terms in relevant evolution equations, i.e. Eqs. (20), (21), and (22), were numerically explored by analyzing DNS data obtained from (i) highly turbulent, constant-density, dynamically passive, single-reaction wave C, (ii) moderately and highly turbulent, single-step-chemistry flames D and E, respectively, and (iii) moderately and highly turbulent, complex-chemistry lean methane-air flames F and G, respectively.

In all these cases, all studied surface-averaged local flame thicknesses are reduced during an earlier stage of premixed turbulent flame development, followed by local flame rebroadening at later stages. The magnitude of the initial reduction effect is larger in the constant-density reaction wave C when compared with flames D-G. In the flames, the magnitude of the effect is larger at higher Karlovitz number.

Governing physical mechanisms of such an evolution of the thicknesses were explored by analyzing DNS data obtained from the constant-density reaction wave C. The obtained results show that the initial local wave thinning is controlled by a rapid increase in a positive surface-averaged stretch rate $\langle \mathcal{K} \rangle_s$. In turn, the increase in $\langle \mathcal{K} \rangle_s (t)$ is controlled by an increase in a positive surface-averaged strain rate $\langle \mathcal{K}_t \rangle_s$. At a later wave-development stage, $\langle \mathcal{K} \rangle_s (t)$ begins to decrease with time, because the positive strain rate is counterbalanced by negative surface-averaged stretch rate $\langle S_d \nabla\cdot\boldsymbol{n} \rangle_s$ due to the local wave curvature. In turn, this negative curvature term is controlled by a sub-term $\langle S_d^c \nabla\cdot\boldsymbol{n} \rangle_s$ that involves curvature-induced displacement speed S_d^c. Simultaneously, self-propagation of wrinkled iso-surfaces, i.e. negative terms that involve $\nabla\cdot(S_d\boldsymbol{n})$ in the aforementioned evolution equations, begins to play a more important role by statistically reducing $|\nabla c|$, thus, locally broadening the reaction wave. This effect is mainly controlled by the normal-diffusion contribution S_d^n to S_d, but the reaction contribution also plays a role by partly counterbalancing S_d^n in the reaction zone.

Analysis of DNS data obtained from single-step and complex-chemistry flames indicated trends that were qualitatively similar to the trends in the constant density waves discussed above. Any important effect associated with complex chemistry has not been revealed. Due to density variations, dilatation terms in the studied evolution equations play an important role in moderately turbulent flames, but this role is typically reduced with increasing Karlovitz number. However, at a late stage of flame development, such a reduction effect is not observed for the dilatation term in the evolution equation for the unweighted surface-averaged $\langle |\nabla c| \rangle_v$. For this measure of the local flame thickness (note that $1/\langle |\nabla c| \rangle_v = \langle 1/|\nabla c| \rangle_s$), the dilatation term plays an important role (increases the thickness) in the single-step-chemistry flame E even at a large Ka of 640.

The present study suggests the following explanation of an apparent inconsistency between experimental data that showed local thinning of lean methane-air flames [13, 15, 16] and DNS results that indicated the opposite trend [11, 12]. The point is that rig-dependent experimental data are typically obtained from developing flames, where local flame thinning under the influence of turbulent strain rates can dominate, as demonstrated in the present work. On the contrary, the aforementioned DNS statistics [11, 12] were sampled from well-developed flames where the strain effect was likely to be overwhelmed by local flame broadening due to (i) self-propagation of wrinkled iso-surfaces and (ii) dilatation.

Finally, the present study shows that differently defined measures of a local flame thickness can be substantially different. This difference should be borne in mind when comparing data from different (experimental or DNS) papers and, in particular, when comparing data that indicate local flame thinning with data that indicate local flame broadening.

Acknowledgments

RY, TN and XB gratefully acknowledge financial support by the Swedish Research Council (VR: 2014-5425) and CECOST. AL gratefully acknowledges the financial support by CERC. We acknowledge the PRACE-granted computer access to MareNostrum at Barcelona supercomputing center (BCS), Spain and Leibniz Supercomputing Centre, Germany, as well as the computer facilities provided by the Swedish National Infrastructure for Computing (SNIC) at PDC and HPC2N.

[1] A. Soika, F. Dinkelacker, A. Leipertz, Measurement of the resolved flame structure of turbulent premixed flames with constant Reynolds number and varied stoichiometry, Proc. Combust. Inst. 27 (1998) 785–792.

[2] F. Dinkelacker, A. Soika, D. Most, D. Hofmann, A. Leipertz, W. Polifke, K. Döbbeling, Structure of locally quenched highly turbulent lean premixed flames, Proc. Combust. Inst. 27 (1998) 857–865.

[3] D. Thévenin, Three-dimensional direct simulations and structure of expanding turbulent methane flames, Proc. Combust. Inst. 30 (2005) 629–637.

[4] M. S. Mansour, N. Peters, Y.-C. Chen, Investigation of scalar mixing in the thin reaction zone regime using a simultaneous CH-LIF/Rayleigh laser technique, Proc. Combust. Inst. 27 (1998) 767.

[5] Y. Chen, R. W. Bilger, Experimental investigation of three-dimensional flame-front structure in premixed turbulent combustion – I: Hydrocarbon/air Bunsen flames, Combust. Flame 131 (2002) 400–435.

[6] A. W. Skiba, T. M. Wabel, C. D. Carter, S. D. Hammack, J. E. Temme, J. F. Driscoll, Premixed flames subjected to extreme levels of turbulence part I: Flame structure and a new measured regime diagram, Combust. Flame 189 (2018) 407–432.

[7] R. Sankaran, E. R. Hawkes, J. H. Chen, T. Lu, C. K. Law, Structure of a spatially developing turbulent lean methane-air Bunsen flame, Proc. Combust. Inst. 31 (2007) 1291–1298.

[8] A. Y. Poludnenko, E. S. Oran, The interaction of high-speed turbulence with flames: Global properties and internal flame structure, Combust. Flame 157 (2010) 995–1011.

[9] A. J. Aspden, M. S. Day, J. B. Bell, Turbulence-flame interactions in lean premixed hydrogen: Transition to the distributed burning regime, J. Fluid Mech. 680 (2011) 287–320.

[10] S. Lapointe, B. Savard, G. Blanquart, Differential diffusion effects, distributed burning, and local extinctions in high Karlovitz premixed flames, Combust. Flame 162 (2015) 3341–3355.

[11] R. Sankaran, E. R. Hawkes, C. S. Yoo, J. H. Chen, Response of flame thickness and propagation speed under intense turbulence in spatially developing lean premixed methane-air jet flames, Combust. Flame 162 (2015) 3294.

[12] A. J. Aspden, M. J. Day, J. B. Bell, Three-dimensional direct numerical simulation of turbulent lean premixed methane combustion with detailed kinetics, Combust. Flame 166 (2016) 266.

[13] L. P. H. de Goey, T. Plessing, R. T. E. Hermanns, N. Peters, Analysis of the flame thickness of turbulent flamelets in the thin reaction zone regime, Proc. Combust. Inst. 30 (2005) 859.

[14] P. Tamadonfar, O. L. Gülder, Experimental investigation of the inner structure of premixed turbulent methane/air flames in the thin reaction zones regime, Combust. Flame 162 (2015) 115.

[15] J. F. Driscoll, Turbulent premixed combustion: Flamelet structure and its effect on turbulent burning velocities, Prog. Energy Combust. Sci. 34 (2008) 91.

[16] F. Dinkelacker, Experimental validation of flame regimes for highly turbulent premixed flames, in: European Combustion Meeting, 2003.

[17] D. Veynante, L. Vervisch, Turbulent combustion modeling, Prog. Energy Combust. Sci. 28 (2002) 193–266.

[18] W. Kollmann, J. H. Chen, Dynamics of the flame surface area in turbulent non-premixed combustion, Proc. Combust. Inst. 25 (1994) 1091–1098.

[19] L. Vervisch, E. Bidaux, K. N. Bray, W. Kollmann, Surface density function in premixed turbulent combustion modeling, similarities between probability density function and flame surface approaches, Phys. Fluids 7 (1995) 2496.

[20] V.G. Mazya, Sobolev Spaces, Springer-Verlag, New York, 1985.

[21] R. Yu, A. N. Lipatnikov, Statistics conditioned to iso-scalar surfaces in highly turbulent premixed reacting systems, submitted to Comput. Fluids.

[22] R. Yu, A. N. Lipatnikov, Surface-averaged quantities in turbulent reacting flows and relevant evolution equations, submitted to Phys. Rev. E.

[23] D. A. Knaus, S. S. Sattler, F. C. Gouldin, Three-dimensional temperature gradients in premixed turbulent flamelets via crossed-plane Rayleigh imaging, Combust. Flame 141 (2005) 253.

[24] F. T. C. Yuen, Ö. L. Gülder, Premixed turbulent flame front structure investigation by Rayleigh scattering in the thin reaction zone regime, Proc. Combust. Inst. 32 (2009) 1747.

[25] R. Fragner, F. Halter, N. Mazellier, C. Chauveau, I. Gökalp, Investigation of pressure effects on the small scale wrinkling of turbulent premixed Bunsen flames, Proc. Combust.

Inst. 35 (2015) 1527.

[26] L. Ma, Y. Wu, Q. Lei, W. Xu, C. D. Carter, 3D flame topograpgy and curvature measurements at 5 Hz on a premixed turbulent Bunsen flame, Combust. Flame 166 (2016) 66.

[27] B. R. Chowdhury, B. M. Cetegen, Experimental study of the effects of free stream turbulence on characteristics and flame structure of bluff-body stabilized conical lean premixed flames, Combust. Flame 178 (2017) 311.

[28] H. Wang, E. R. Hawkes, J. H. Chen, B. Zhou, Z. Li, M. Aldén, Direct numerical simulations of a high Karlovitz number laboratory premixed jet flame - An analysis of flame stretch and flame thickening, J. Fluid Mech. 815 (2017) 511–536.

[29] A. N. Lipatnikov, J. Chomiak, Turbulent flame speed and thickness: Phenomenology, evaluation, and application in multi-dimensional simulations, Prog. Energy Combust. Sci. 28 (2002) 1–74.

[30] A. Lipatnikov, Fundamentals of Premixed Turbulent Combustion, CRC Press, 2012.

[31] S. M. Candel, T. J. Poinsot, Flame stretch and the balance equation for the flame area, Combust. Sci. Technol. 70 (1990) 1–15.

[32] S. B. Pope, The evolution of surfaces in turbulence, Int. J. Eng. Sci. 26 (1988) 445–469.

[33] R. Yu, A. N. Lipatnikov, X. Bai, Three-dimensional direct numerical simulation study of conditioned moments associated with front propagation in turbulent flows, Phys. Fluids 26 (2014) 085104.

[34] R. Yu, X. Bai, A. N. Lipatnikov, A direct numerical simulation study of interface propagation in homogeneous turbulence, J. Fluid Mech. 772 (2015) 127–164.

[35] R. Yu, A. N. Lipatnikov, Direct numerical simulation study of statistically stationary propagation of a reaction wave in homogeneous turbulence, Phys. Rev. E 95 (2017) 063101.

[36] R. Yu, A. N. Lipatnikov, DNS study of dependence of bulk consumption velocity in a constant-density reacting flow on turbulence and mixture characteristics, Phys. Fluids 29 (2017) 065116.

[37] R. Yu, A. N. Lipatnikov, A DNS study of sensitivity of scaling exponents for premixed turbulent consumption velocity to transient effects, Flow, Turbul. Combust.doi:10.1007/s10494-018-9982-7.

[38] V. A. Sabelnikov, R. Yu, A. N. Lipatnikov, Thin reaction zones in highly turbulent medium, Int. J. Heat Mass Transf. 128 (2019) 1201–1205.

[39] T. Nilsson, H. Carlsson, R. Yu, X. Bai, Structures of turbulent premixed flames in the high Karlovitz number regime - DNS analysis, Fuel 216 (2018) 627–638.

[40] T. Nilsson, I. Langella, N. A. K. Doan, N. Swaminathan, R. Yu, X. Bai, A priori analysis of sub-grid variance of a reactive scalar using DNS data of high Ka flames, accepted for publication in Combust. Theory Model.

[41] A. Majda, J. Sethian, The derivation and numerical solution of the equations for zero Mach number combustion, Combust. Sci. Technol. 42 (1985) 185.

[42] M. D. Smoke, V. Giovangigli, Formulation of the premixed and nonpremixed test problems, in: Reduced Kinetic Mechanisms and Asymptotic Approximations for Methane-

Air Flames, Springer-Verlag, Berlin/Heidelberg, 1991.

[43] A. G. Lamorgese, D. A. Caughey, S. B. Pope, Direct numerical simulation of homogeneous turbulence with hyperviscosity, Phys. Fluids 17 (2005) 015106.

[44] R. Yu, X. Bai, A fully divergence-free method for generation of inhomogeneous and anisotropic turbulence with large spatial variation, J. Comput. Phys. 256 (2014) 234–253.

[45] R. Yu, J. Yu, X. Bai, An improved high-order scheme for DNS of low Mach number turbulent reacting flows based on stiff chemistry solver, J. Comput. Phys. 231 (2012) 5504.

[46] G. Strang, On the construction and comparison of difference schemes, SIAM J. Numer. Anal. 5 (1968) 506–517.

[47] P. N. Brown, G. D. Byrne, A. C. Hindmarsh, VODE: A variable-coefficient ODE solver, SIAM J. Sci. Stat. Comput. 10 (1989) 1038–1051.

[48] G. S. Jiang, C. W. Shu, Efficient implementation of weighted ENO schemes, J. Comput. Phys. 126 (1996) 202–228.

[49] R. Yu, X. Bai, A semi-implicit scheme for large eddy simulation of piston engine flow and combustion, Int. J. Numer. Methods Fluids 71 (2013) 13–40.

[50] M. Frigo, S. G. Johnson, The design and implementation of FFTW3, Proc. IEEE 93 (2005) 216–231.

[51] J. F. Yu, R. Yu, X. Q. Fan, M. Christensen, A. A. Konnov, X. Bai, Onset of cellular flame instability in adiabatic CH4/O2/CO2 and CH4/air laminar premixed flames stabilized on a flat-flame burner, Combust. Flame 160 (2013) 1276–1286.

[52] R. Yu, X. Bai, Direct numerical simulation of lean hydrogen/air auto-ignition in a constant volume enclosure, Combust. Flame 160 (2013) 1706–1716.

[53] F. Zhang, R. Yu, X. Bai, Direct numerical simulation of PRF70/air partially premixed combustion under IC engine conditions, Proc. Combust. Inst. 35 (2015) 2975–2982.

[54] H. Carlsson, R. Yu, X. Bai, Flame structure analysis for categorization of lean premixed CH4/air and H2/air flames at high Karlovitz numbers: Direct numerical simulation studies, Proc. Combust. Inst. 35 (2015) 1425–1432.

[55] R. Yu, X. Bai, V. Bychkov, Fractal flame structure due to the hydrodynamic Darrieus-Landau instability, Phys. Rev. E 92 (2015) 063028.

[56] T. Elperin, N. Kleeorin, M. Liberman, A. Lipatnikov, I. Rogachevskii, R. Yu, Turbulent diffusion of chemically reacting flows: theory and numerical simulations, Phys. Rev. E 96 (2016) 053111.

[57] F. A. Williams, Progress in knowledge of flamelet structure and extinction, Prog. Energy Combust. Sci. 26 (2000) 657.

[58] J. Chen, H. Im, Correlation of flame speed with stretch in turbulent premixed methane-air flame, Proc. Combust. Inst. 27 (1998) 819.

[59] N. Peters, P. Terhoeven, J. Chen, T. Echekki, Statistics of flame displacement speeds from computations of 2-D unsteady methane-air flames, Proc. Combust. Inst. 27 (1998) 833.

[60] G. K. Batchelor, The effect of homogeneous turbulence on material lines and surfaces,

Proc. R. Soc. A Math. Phys. Eng. Sci. 213 (1952) 349–366.

[61] A. N. Lipatnikov, J. Chomiak, Molecular transport effects on turbulent flame propagation and structure, Prog. Energy Combust. Sci. 31 (2005) 1.

Nomenclature

A	Area
C_p	Heat capacity at constant pressure
$D, \mathcal{D}$	Diffusion coefficient
Da	Damköhler number
$\mathbb{D}$	Diffusion term
H	Heaviside function
I	Identity matrix
J	Number of time intervals
Ka	Karlovitz number
$\mathcal{K}$	Stretch rate
L_{11}	Longitude integral scale
Le	Lewis number
M	Realization number
$\mathcal{M}$	Number of transient waves
N	Cell numbers in y or z
N_x	Cell numbers in x
Pe	Péclet number
Pr	Prandtl number
$R_{a,b}$	Correlation of a and b
Re	Reynolds number
Re_0	Initial Reynolds number
$\mathcal{R}$	Universal gas constant
S_L	Laminar wave speed
S_d	Displacement speed
S_{ij}	Velocity strain tensor
T	Temperature
V	Volume
$\mathbf{V}$	Diffusion velocity
W	Species molecular weight
$\mathbb{W}$, $\dot{\omega}$	Reaction rate
Y	Species mass fraction
Ze	Zeldovich number
a_n	Normal strain rate
a_t	Tangential strain rate
$\hat{c}$	Reference value of c
c	Reaction progress variable
c^*	c value at maximum $\mathbb{W}(c)$
c^s	Fully-developed c-field
c^t	Developing c-field
c_L	c-profile in the laminar wave
c_p	Reaction progress based on H_2O
$\mathrm{d}\boldsymbol{x}$	Infinitesimal small volume
$\mathrm{d}s$	Infinitesimal small area
$\mathbf{f}$	Forcing function
h	Specific enthalpy
h^{298}	Specific enthalpy of formation
ℓ_0	Initial integral scale
$\boldsymbol{n}$	Unit normal vector
p, P	Pressure
t	Time
t^*	Starting sampling time
t_∞	Statistically stationary
$\boldsymbol{u}$	Flow velocity
$\boldsymbol{u}^*$	Total flame speed
u'	rms velocity
u_0	Initial rms velocity
$\boldsymbol{x}$	Space
Δt	Computational time step
Δx	Grid spacing
δ	Dirac delta function
δ_F	Laminar wave thickness
ϵ	Small positive number
ε	Dissipation rate
ϕ, ψ	Arbitrary quantity
Λ	Domain length in y or z
Λ_x	Domain length in x
λ	Thermal conductivity
ρ	Density
$\boldsymbol{\tau}$	Viscous stress tensor
τ_F	Laminar wave time scale
τ_R	Reaction time scale
τ_η	Kolmogorov time scale
τ_t	Integral time scale
τ_t^0	Initial integral time scale
Θ	Density ratio
θ	Reaction parameter
μ	Dynamic viscosity
ν	Kinematic viscosity
$1_{\hat{c},\epsilon}$	Sifting selection function
$\frac{d^*}{d^*t}$	Convective derivative based on total flame speed
$(\cdot)'$	Fluctuation
$(\cdot)_u, (\cdot)_b$	Quantity on unburned/burned state
$\langle\cdot\rangle_S$	Coarse-grained area-weighted average
$\langle\cdot\rangle_V$	Coarse-grained unweighted average
$\widehat{(\cdot)}$	Ensemble average
$\overline{(\cdot)}$	Ensemble and spatial average
$\langle\cdot\rangle_s$	Fine-grained area-weighted average
$\langle\cdot\rangle_v$	Fine-grained unweighted average

Supplementary Material

1. Additional inequalities

If numerical integration over a continuous surface in Eq. (4) is associated with summation over a discrete set of surface elements with the same small area ds, then,

$$\langle \phi \rangle_s = \frac{\sum_{j=1}^{\mathbb{M}} \phi_{(j)} \, \mathrm{d}s}{\sum_{j=1}^{\mathbb{M}} \mathrm{d}s} = \frac{1}{\mathbb{M}} \sum_{j=1}^{\mathbb{M}} \phi_{(j)}, \tag{31}$$

where $\mathbb{M} = \sum_{i=1}^{M} A_{(i)} / \, \mathrm{d}s$ is the total count of the surface elements for all M realizations over the entire surface. Accordingly,

$$\exp\left(\langle \ln |\nabla c| \rangle_s\right) = \exp\left(\frac{1}{\mathbb{M}} \sum_{j=1}^{\mathbb{M}} \ln |\nabla c|_{(j)} \right) = \left(\prod_{j=1}^{\mathbb{M}} |\nabla c|_{(j)} \right)^{1/\mathbb{M}}, \tag{32}$$

i.e. $\exp\left(\langle \ln |\nabla c| \rangle_s\right)$ is the geometrical mean of $|\nabla c|$, whereas

$$\langle |\nabla c| \rangle_s = \frac{1}{\mathbb{M}} \sum_{j=1}^{\mathbb{M}} |\nabla c|_{(j)}, \tag{33}$$

is the arithmetic mean of $|\nabla c|$.

Moreover, Jensen's inequality can be applied to obtain certain relationship between different measures of the conditioned local flame thickness. According to this inequality, if values of a concave function $\Psi(q)$ are measured $\mathbb{M}$ times, then

$$\frac{\sum_{j=1}^{\mathbb{M}} w_{(j)} \Psi\left(q_{(j)}\right)}{\sum_{j=1}^{\mathbb{M}} w_{(j)}} \leq \Psi\left(\frac{\sum_{j=1}^{\mathbb{M}} w_{(j)} q_{(j)}}{\sum_{j=1}^{\mathbb{M}} w_{(j)}} \right) \tag{34}$$

holds for positive weights w. Consequently,

$$\frac{1}{\langle |\nabla c| \rangle_s} \leq \frac{1}{\exp\left(\langle \ln(|\nabla c|) \rangle_s\right)} \leq \left\langle \frac{1}{|\nabla c|} \right\rangle_s. \tag{35}$$

The left (or right) inequality results from substitution of $\Psi(q) = \ln(q)$, $w = 1$, and $q = |\nabla c|$ (or $q = 1/|\nabla c|$, respectively) into Eq. (34), followed by taking exponents of both terms in the obtained inequality.

Similarly, by associating numerical integration in Eq. (2) with summation over a discrete set of equal volumes d$\boldsymbol{x}$ and substituting $\Psi(q) = \ln(q)$, $w = 1$, and $q = |\nabla c|$ or $q = 1/|\nabla c|$ into Jensen's inequality, we arrive at

$$\frac{1}{\langle |\nabla c| \rangle_v} \leq \frac{1}{\exp\left(\langle \ln(|\nabla c|) \rangle_v\right)} \leq \left\langle \frac{1}{|\nabla c|} \right\rangle_v. \tag{36}$$

2. Additional figures

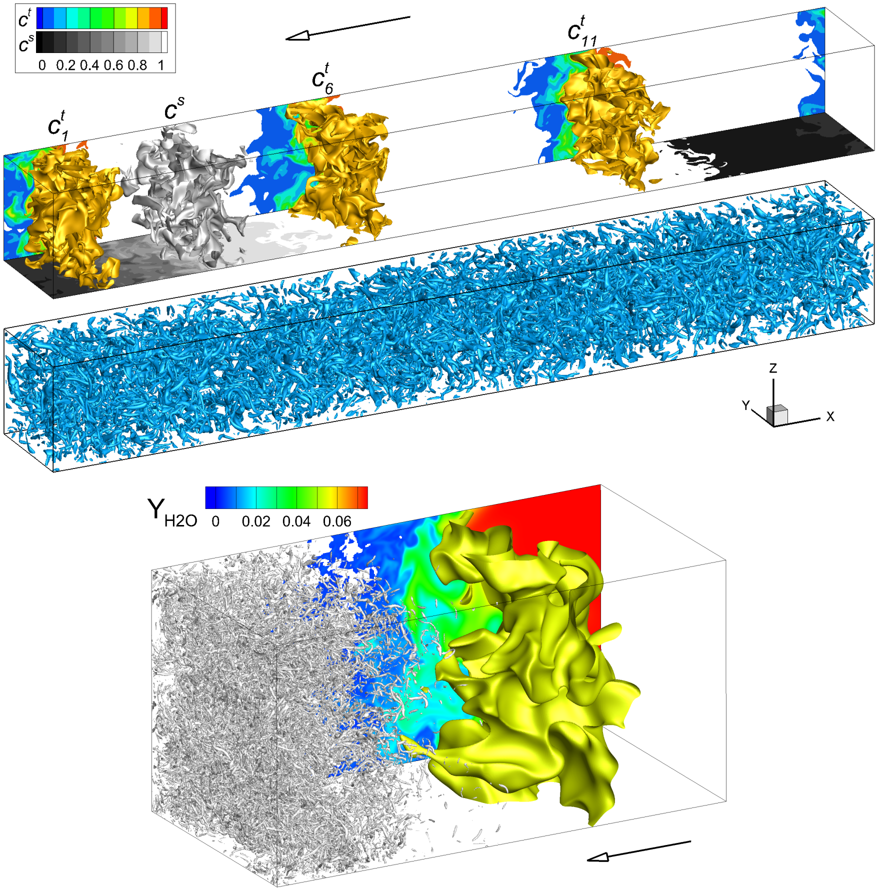

Figure 14: (a) Three simultaneously-embedded, non-interfering, constant-density developing ($t = 0.9\tau_t^0$) reaction waves $c^t_{(i)}(\boldsymbol{x}, t)$ with $i = 1$, 6, and 11 (color iso-surfaces and fields) and the fully-developed reaction wave $c^s(\boldsymbol{x}, t)$ (gray iso-surface and field). Both the peak-reaction-rate iso-surface ($\hat{c} = 0.88$) and 2D image of the c-field on the xz (the transient waves) or xy (the fully-developed wave) boundary surface are shown for each wave. (b) 3D turbulence field visualized using Lambda2-vortex method (i.e. iso-contours of the intermediate eigenvalue of the strain rate tensor in case C. (c) 3D turbulence field (gray Lambda2 vortexes), the iso-surface of $Y_{\mathrm{H2O}}(\boldsymbol{x}, t) = 0.055$, and 2D image of the $Y_{\mathrm{H2O}}(\boldsymbol{x}, t)$-field in case G.

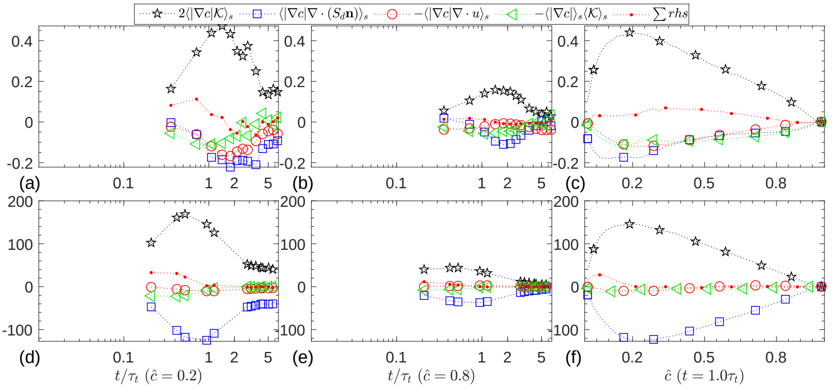

Figure 15: Evolutions (a, b, d, e) of all terms on the rhs of Eq. (20), specified in legends, and the sum of them, as well as dependencies of these terms on $\hat{c}$ at $t=\tau_t$ (c and f). Terms conditioned to the preheat zone ($\hat{c}=0.2$) or the reaction zone ($\hat{c}=0.8$) are reported in panels a and d or b and e, respectively. (a-c) flame F, (d-f) flame G. All terms are normalized by S_L/δ_F.

Printed by Media-Tryck, Lund 2019 NORDIC SWAN ECOLABEL 3041 0903

LUND
UNIVERSITY

Faculty of Engineering
Lund University
ISBN 978-91-7895-109-3
ISSN 0282-1990
ISRN LUTMDN/TMHP-19/1149-SE

9 789178 951093